Incorporation of a vortex tube in thermal systems - refrigerants screening and system integrations

Zheng WANG

A thesis submitted for the degree of Doctor of Philosophy in the Department of Mechanical Engineering, University College London

December 2017

DECLARATION

I, Zheng Wang, confirm that the work presented in this thesis is my own. Where information has been derived from other sources, I confirm that this has been indicated in the thesis.

_____

Zheng WANG

December 2017

Abstract

The temperature separation effect (TSE) is a unique thermal phenomenon occurring in a vortex tube (VT). This creates the possibilities of incorporating a VT in various thermal systems to improve their overall system efficiency. Any improvement will be strongly dependent on the working fluid choices, VT geometric parameters, and the system configurations and operating conditions. However, there appears that no systematic approach for selecting the possible working fluid and for evaluating the performance of a VT when operating in a system is available. Therefore, this research aims at developing a systematic approach to screen possible choices of working fluids, and a system integration procedure to achieve optimal matching of the working fluid choice, the VT geometries and the operation conditions, based on using a combined thermodynamic and CFD simulation analysis.

A 2-D CFD VT model, created using Ansys Fluent, is used to assess the influence of the VT boundary conditions on the TSE, and to provide detailed information on the flow velocities, temperature and shear stress distributions inside the VT, as well as the cooling/heating effect of the VT. The shape of refrigerant's *T-s* diagram is initially used for grouping various refrigerants to either cooling or heating applications of VT. The fluid state at the VT nozzle exit is set as the criterion to identify the suitable VT entry regions on the *T-s* diagram for individual refrigerants. The thermal-physical properties including isentropic expansion exponent, J-T (Joule-Thomson) coefficient, thermal diffusivity, kinematic viscosity and density are employed to appraise the relative heating or cooling performance of individual refrigerants.

One cooling and one heating system are chosen to illustrate the development and implementation of the proposed system integration procedure. In developing the procedure, a boundary line concept is introduced, which allows suitable VT entry conditions in a system be identified for cooling applications. An iteration procedure is designed to identify the best combination of the VT inlet pressure and degree of superheat for the heating applications for individual refrigerants. A guideline for re-selecting alternative refrigerants and re-dimensioning of VT for improving heating or cooling effect is presented, based on examining their thermal-physical properties under system conditions.

The results show that the pressure drop in the VT plays an important role in determining the final heating effect. Key thermal-physical properties, such as thermal diffusivity and kinematic viscosity, are shown to be able to reliably assist the evaluation of the relative cooling/heating performance of different working fluids in closed VT systems. The proposed integration procedure is developed in such a way that it could be easily adapted for evaluation of different system configurations.

Key words: vortex tube, temperature separation effect, refrigerants, thermal systems, integration

Impact Statement

The temperature separation characteristics of the vortex tube, if applied effectively, could enhance the overall thermal efficiency of closed VT thermal systems. However, the development of closed VT thermal systems is still in its infant stage. The use of VT in closed systems also increases the possible choices of working fluids and thus making it difficult to make the right choice for optimum performance. For a given fluid, the thermodynamic analysis on its own is not able to predict reliably the temperature separation effect, and on the other hand the CFD analysis needs to be "told" of the required system operating conditions.

This research proposes and develops a systematic refrigerant screening approach, coupling the thermodynamic calculation with CFD numerical simulation. Both the development and implementation of the procedure are considered successful.

Significant amount of time can be saved for researchers and designers to evaluate possible refrigerant choices, including any newly developed environmental friendly refrigerants, for acquiring the required TSE under the specified system conditions and achieving the ultimate goal of energy saving.

Acknowledgements

First and foremost, I would like to express my great appreciation and sincere gratitude to my supervisor Dr K O Suen for his continuous support for my PhD study. In the past four years, he has showed his great patience to help me to correct my transfer report and final thesis, which brings a huge improvement to my writing and thinking. His immerse knowledge really helped me obtain much more in depth understanding about the thermodynamics fundamentals, and guided me to finish the PhD research. Without his help, I could not have finished the study and the writing of this thesis.

Furthermore, I would like to say thanks to the refrigeration group in the Institute of Refrigeration and Cryogenics from Zhejiang University, and Dr Lijuan HE's refrigeration group from Inner Mongolia University of Science and Technology. They provided me the experimental apparatus and the powerful workstation to help me conduct the CFD validation and run more numerical simulation to finish the research in a short time. In addition, I should thank my colleague Miss. Xizhuo Jiang for her support in solving some thermal issues in the research.

Most importantly, none of this would be possible without the love and the support of my parents. They gave me huge encouragement to live abroad and brightened my life.

List of Content

Nomenclature

A	Area (mm^2)
Bo	Boiler
COP	Coefficient of performance
Cr	Critical point
Co	Compressor
Con	Condenser
CS	Cross section
c_p	Specific heat capacity (kJ/kg·K)
DS	Lowest state point of the boundary line
F	Ending point of boundary line
G	Volume flow rate (m^3/h)
H	Height (mm)
Hx	Heat exchanger
h	Specific enthalpy (kJ/kg)
k	Turbulence kinetic energy (m^2/s^2)
L	Length (mm)
Lp	Liquid pump
$\dot{m}$	Mass flow rate (g/s)
Ma	Mach number
N	Number of nozzles, the point on the boundary line
O	Point on saturated vapour line
p	Pressure (Pa & MPa)
P	Inflection point
Pr	Prandtl number
Q	Heat quantity (kW)
R_g	Specific gas constant (J/kg·K)
r	Radius (mm)
re	Reversed
Ref	Refrigerant
s	Entropy (kJ/kg·K)
T	Temperature (K & °C)

TSE	Temperature separation effect (°C)
Th	Throttle
U	Starting saturated vapour point used to define the suitable VT entry region
v	Velocity (m/s)
VT	Vortex tube
W	Width (mm)
X	Interception point
ΔT_c	Cooling effect (°C)
ΔT_h	Heating effect (°C)
μ_c	$= \dot{m}_c / \dot{m}_{in}$, Cold mass flow ratio

Superscript

*	Sonic condition

Subscript

ada	Adapted VT dimension
c	Cold stream, cold end, cooling
C	Cooling system
cham	VT chamber
co	Cold orifice
e	Equivalent
ex	Exit
h	Hot stream, hot end, isenthalpic
ht	Hot tube
H	Heating system
in	Inlet
max	Maximum
min	Minimum
noz	Nozzle
o	Point on saturated vapour line
out	Outlet
r	Radial
re	Reverse
s	Isentropic

sat	Saturation state
sh	Superheat
sta	Static
stag	Stagnation
t	Turbulent, tangential
w	wall

Greek letters

α	Thermal diffusivity (cm^2/s)
ν	Kinematic viscosity (cm^2/s)
ρ	Density (kg/m^3)
η	Efficiency
Δ	Difference
Φ	Diameter (mm)
γ	Specific heat exponent
ε	Dissipation rate (m^2/s^3)
μ	Mass flow ratio
ω	Angular velocity (rad/s)
μ_{JT}	J-T coefficient (°C/MPa)

List of Tables

List of Figures

1 Introduction

1.1 Background

When a high-pressure gas enters a vortex tube (VT), two streams – a cold stream and a hot stream, with their total temperature respectively lower and higher than that of the entering gas stream[1], can be produced. With this temperature/energy separation effect/characteristic, VTs have been used/proposed in cooling grinding device[2] and comfort heating[3]. When air is chosen as the working fluid, and at an inlet pressure and total temperature of, say, 0.5 MPa and 20 °C respectively, the cold stream could reach a total temperature as low as -25 °C[4] or a hot stream reaching 80 °C total temperature[1][4].

The vortex tube (also known as the Ranque-Hilsch vortex tube[6, 7]) is structurally quite a simple device, typically consisting of five main parts (as shown in Figure 1.1), including a nozzle (multiple nozzles could also be used depending on the design), a cold orifice plate, a vortex chamber, a hot throttle and a hot tube. When a high-pressure gas enters a VT, its velocity can be accelerated through the nozzle to approaching sonic flow. In the vortex chamber, this gas rotates along the periphery (as the primary flow) of the vortex chamber towards the hot end, part of this exits the hot end and becomes the hot stream. The rest rebounds (as the secondary flow) by the hot throttle and flows towards the cold end through the cold orifice, forming the cold stream.

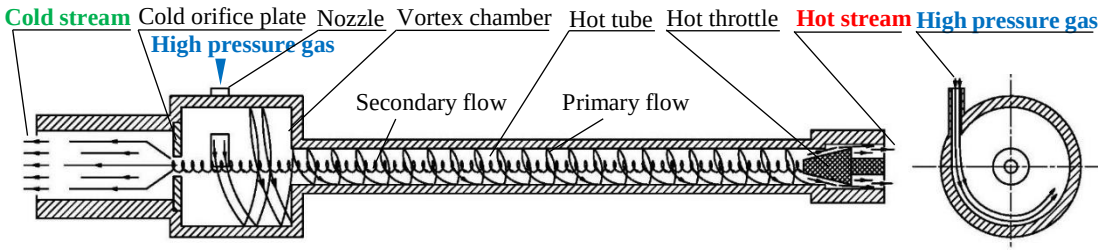

Figure 1.1 Schematic structure of a VT

In general, the temperature separation effect (TSE) is regarded as the combined consequence of adiabatic expansion and fluid friction[4, 8]. At the nozzle outlet, the inertia force attempts to maintain the angular momentum of the fluid entering the VT chamber. The shear force between two adjacent (inner and the outer) rotating layers

[1] Total temperature includes the static temperature and dynamic component related to the kinetic energy of the gas. For a low velocity flow (~20m/s[5]), the static and total temperatures are almost the same

tends to slow down their rotating speed, resulting in a smaller kinetic energy for the inner layer. To conserve the angular momentum, however, one should expect the inner element to have a higher rotating speed and larger kinetic energy, and therefore, the inner layer must have lost certain amount of its kinetic energy to the outer layer[4, 8].

At the same time, due to the pressure difference between the periphery and inner core of the VT, the fluid spirals/expands, leading to a reduction in static temperate (i.e. a decrease in internal energy) towards the VT[8] . Based on the energy conservation, these losses of kinetic and internal energy must be transferred to the outer part of the rotation flow, leading to an increase of total temperature in radially outward direction. After the rebounding, the fluid axially accelerates and expands towards the cold end, thus leading to a further temperature decrease.

In VT, the heat transfer is enhanced by the swirling flow due to the effect of the streamline curvature associated with the tangential velocity component[9]. The swirling/rotating flow can be generally regarded a kind of decaying swirl, as the swirl is generated at the chamber inlet and the velocities decay along the axial flow direction[10, 11].

Many factors could influence the TSE which is generally referred to the cooling effect[2] and the heating effect[3], or the total temperature separation effect[4]. These factors can be put into three groups: the operating conditions, the VT geometric parameters and the choices of the working fluid. The former two have been investigated extensively but primarily using air as the working fluid.

For a given VT and a specified working fluid choice, a number of operating parameters are found to affect the TSE; these include the VT inlet pressure (p_{in}), inlet temperature (T_{in}) and the cold mass flow ratio[5] (μ_c).

In general, for air, a higher p_{in} (up to certain limits) would lead to an increase in mass flow rate $\dot{m}_{in}$, resulting in a larger VT chamber inlet velocity ($v_{cham,in}$) and a stronger rotational flow, thus with the possibility of generating a larger cooling or heating effect.

[2] The difference between inlet fluid temperature and cold end fluid temperature
[3] The difference between hot end fluid temperature and inlet fluid temperature
[4] The difference between hot end fluid temperature and cold end fluid temperature
[5] The cold end fluid mass flow rate divided by the inlet fluid mass flow rate, and this ratio can be adjusted by changing the hot throttle position, reducing the throttle area would lead to an increase in the cold mass flow ratio

On the other hand, the influence of the T_{in} on TSE seems to be dependent on the design of the VT and operating conditions (e.g. VT inlet and outlet pressures), as both a larger and a smaller TSE have been observed when a higher T_{in} is employed[12, 13]. Whether a VT is to function as a cooling or heating device depends on the μ_c; for air, it is generally observed that, a low value of μ_c, say less than 0.5, is suitable for the former and a μ_c value above 0.5 is usually adopted for the heating purpose[14-16].

Regarding VT geometric parameters, the nozzle size/shape, the number of nozzles, the length of the hot tube, the chamber diameter, and the shape/dimensions of the hot end throttle and the cold orifice, all could impact on the cooling or the heating effect. The nozzle size/shape determines how the fluid enters the VT chamber, and it is widely acknowledged that, based on air, the use of convergent nozzles would lead to the generation of stronger rotational flows in the VT chamber[17], thus resulting in a larger TSE. The ratio of the hot tube length to the chamber diameter could also be varied to achieve optimum TSE, depending on the operating conditions[18, 19].

For the working fluids, different choices are expected to generate dissimilar TSEs even when operating under the same conditions, as they have different thermal-physical properties. Compared to the work on air and some of its constituent gases (e.g. N_2, CO_2), the research on the use of refrigerants in VT is still in its infant stages, though preliminary research have suggested that some refrigerants (e.g. R32, R50) could produce better cooling effect than N_2 or CO_2 in VT under certain conditions[20, 21], probably due to their more favourable thermal-physical properties. For example, the J-T coefficient of R32 and air at 20 °C and 0.2 MPa is 26.9 °C/MPa and 2.4 °C/MPa, respectively, which could suggest that R32 could produce a larger temperature drop than air when they are throttled in a VT.

To better understand the development of the flow field and the energy separation process inside a VT, and their dependence of the operating conditions and VT design, numerical simulation methods[22, 23] have been extensively used in recent years, involving setting up 2-D or 3-D models. The associated tasks typically include defining VT geometries, mesh generation, selecting appropriate turbulence models and validating the results.

1.2 Motivation

In the past decade, the potential use of VT in closed systems have been explored by various researchers, to either improve the overall system thermal efficiency or to expand the application domains of VT. Published works[24, 25] show that the cooling effect in a VT is always larger than the isenthalpic temperature drop, thus suggesting that putting a VT in a system could have a chance of increasing the system efficiency[26]. In addition, a VT heating pump could upgrade the temperature of the heat resource (60~80 °C) to a higher level (80~100 °C).

An example of a closed VT system is shown in Figure 1.2a, in which the VT is functioned mainly as a throttling device to replace a typical throttle (Figure 1.2b). Under the same pressure ratio p_3/p_4, as shown in Figure 1.3, the VT cooling system can provide a larger specific refrigerating effect (h_6-h_4) than the typical system ($h_6-h_{4'}$). However, currently VT system performance is often evaluated based on energy balance analysis which takes in no account that the VT may not have the right dimensions to generate the required cooling/heating temperature at design system conditions.

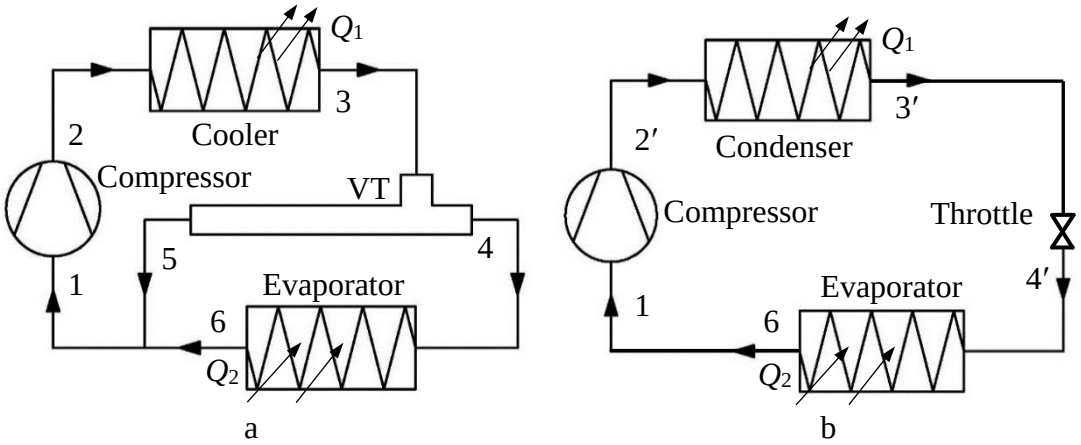

Figure 1.2 Schematic diagram of: a. VT compressor cooling system (adapted from [26], b. typical vapour compressor refrigeration system

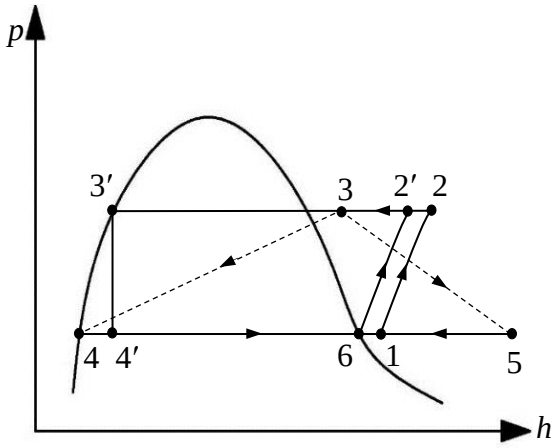

Figure 1.3 Flow process on the *p-h* diagram for the VT compressor cooling system and the typical compressor cooling system

Unlike open systems which mostly employ air, closed systems enable a wider choice of working fluids, including refrigerants, to be considered. However, refrigerants typically have a higher critical point when compared to air, and thus there is a likelihood of liquification when the fluid is undergoing the temperature reduction process within the VT. Liquification could be detrimental or beneficial to the VT performance depending where it occurs which could either be in the nozzle or within the main body of the VT. Therefore it is important to be able to identify the conditions under which no liquification would occur.

To select a suitable working fluid/refrigerant for a specific VT design to achieve optimum performance is a complex matter; other important factors to consider include the system configuration and the operating conditions. Naturally, due to resource and time constrains, it is practically impossible to evaluate experimentally all the different combinations of refrigerant choices, VT designs and system requirements. Therefore, it is highly desirable to have a simple and effective method to screening suitable refrigerants, and more importantly to relate their thermal-physical properties to the VT TSE (cooling or heating performance) under specific operating conditions.

To incorporate a VT in a closed thermal system, it is important to establish if the VT can perform as expected under the system design conditions. Previously approaches based on energy balance analysis cannot always guarantee a given VT could generate the required cooling or heating effect when integrating the VT into a system. Therefore, it would be practically beneficial to have a system integration procedure developed for matching the VT characteristics (cooling or heating effect) with system operating conditions to ensure the required VT performance is achieved. Potentially, this could

also lead to better matching by, if necessary, re-dimensioning of various key VT geometric parameters.

To summarise, this research is motived by the need to develop a systematic refrigerants screening method for the VT, which can reliably and effectively evaluate the VT performance of different refrigerants based on their thermal-physical properties; and establish a closed VT system integration procedure, which can identify the optimal combination of the refrigerants, VT dimensions and the system operating conditions to achieve the desirable cooling/heating temperature.

1.3 Outline of thesis

A brief research background is given in Chapter 1, followed by a comprehensive literature review (Chapter 2) which brings out the relevant research questions and highlights the project objectives.

The main part of the thesis (Chapter 3) describes the work which aims at developing a unique refrigerant screening methodology and a coupling procedure for integrating a VT into thermal systems, comprising optimal matching of the VT geometry with the refrigerant choice and the system operations.

The main analysis (Chapter 4) is CFD based and a simplified axial symmetric 2-D VT model, using Ansys Fluent and the standard *k-epsilon* turbulence model, is created, and used to assess the influence of the VT boundary conditions (inlet mass flow rate, inlet pressure, inlet temperature, cold mass flow ratio) on the TSE for various refrigerants.

Accordingly, the refrigerants are ranked for their TSE performance which are evaluated, as described in Chapter 5, and linked to certain thermal-physical properties (e.g. thermal diffusivity).

The thermodynamic theories and the CFD predictions are used together to develop the novel system integration procedure, as presented in Chapter 6. Two published VT systems are specified to demonstrate the implementation of the procedure, followed by the identification of the optimal refrigerant choices and operating conditions for the chosen VT systems.

Chapter 7 summarises the main contributions and proposes relevant future works.

2 Literature review

In recent years, research efforts regarding VTs have been focusing on the following four main areas; some relevant published literature are reviewed, as presented in Sections 2.1 to 2.4.

- Experimental research aiming at establishing the optimum operating conditions for achieving the maximum TSE and examining how various key geometric parameters influence the VT performance.
- Theoretical analysis of the heat and mass transfer processes in VT, attempting to acquire a better understanding of the temperature separation mechanism.
- Computational Fluid Dynamics (CFD) studies for analysing the flow behaviour and optimising the VT design.
- System integration - exploring the possibility of incorporating VTs in thermal systems for enhancing their overall energy efficiency.

2.1 Experimental research

A number of parameters have been identified to have an impact on the operating characteristics (i.e. TSE) of the VT, including the inlet pressure p_{in}[27], inlet fluid temperature T_{in}[28], cold flow mass ratio μ_c[29], the ratio of cold end pressure p_c to the hot end pressure p_h[30], the VT structures/dimensions[31-37], the properties[21, 38] and the state[39] of the working fluid. They all need to be carefully evaluated in order to deliver good performance for a specific application.

2.1.1 Operating conditions

For a given VT, the inlet pressure p_{in} influences the $\dot{m}_{in}$ of the fluid entering the device. Experimentally[40-42], based on air, it has been shown for a given inlet temperature T_{in}, an increase of the p_{in} would in general lead to an increase in the cooling or heating effect. Among these experiments, Eiamsa-ard[41] believed that the fluid reaches a higher tangential velocity at the chamber inlet under the larger p_{in}, resulting in a bigger momentum transfer from the central to the outer part of the rotating flow and generating a stronger TSE. However, for most of the VTs, convergent nozzles are applied, which limit the maximum nozzle exit velocity. That means any further

increase of p_{in} could not lead to a higher velocity at the VT nozzle outlet (i.e. the chamber inlet) when the Mach number reaches 1 or choked flow occurs. As also noticed by Ahlborn et al[43], the maximum TSE is obtained when the chamber inlet air velocity $v_{cham,in}$ reaches the sonic speed, and by Saidi and Valipour[29] that when the nozzle outlet gets choked by increasing the VT inlet pressure, the TSE keeps almost unchanged and the VT isentropic efficiency η_{VT} [6] decreases.

Based on the definition of the VT isentropic efficiency η_{VT}[44], the cooling effect ΔT_c can be expressed as the efficiency η_{VT} multiplied by the isentropic temperature drop ΔT_s,

$$\Delta T_c = \eta_{VT}[1 - (p_c/p_{in})^{\frac{r-1}{r}}]T_{in} \quad (2.1)$$

where $$\Delta T_s = [1 - (p_c/p_{in})^{\frac{r-1}{r}}]T_{in}$$

p_{in} and p_c are the VT inlet and cold end pressure, respectivley, and T_{in} is the VT inlet temeprature and r is the specific heat ratio. For a chosen fluid, and a given inlet and outlet pressure p_{in} and p_c, the cooling effect therefore relies upon the VT inlet tempertaure T_{in}, as well as the VT isentropic efficiency. Gulyaev[12] observed that for Helium, the η_{VT} is identified as independent of the T_{in} in range between 80 and 295 K, when p_{in}/p_c = 4 and 8, and an increase of the T_{in} brings a larger cooling effect. On the contrary, as experiments on air by Ding[13] show a higher VT inlet temperature (14 ~ 38 °C, p_{in}/p_c = 5) leads to a smaller cooling effect, suggesting that the η_{VT} decreases with increasing T_{in}.

Whether a VT is to produce noticeable cooling effect or heating effect is a function of the cold mass flow ratio μ_c - a small ratio tends to produce cooling while a large ratio tends to generate heating. Aydın and Baki[19] noted that a μ_c = 0.2 always generates the largest cooling effect and μ_c = 0.8 for a maximum heating effect with VT lengths L_{VT} ranging from 250 mm to 750 mm, and at 0.5 MPa p_{in} for air. Stephan et al[45] and Promvonge and Eiamsa-ard[46] achieved the largest cooling effect at respectively around 0.3 and 0.4, and they achieved the largest heating effect at around μ_c = 0.9.

Stephan et al's experiments were conducted when the p_{in} was varied between 1.5 and 0.5 MPa (air) for a 352mm long VT with a 17.6 mm diameter. The results of Promvonge and Eiamsa-ard were obtained in both an insulated and a non-insulated

[6] The ratio of the cooling effect ΔT_c to the isentropic temperature drop ΔT_s[29]

880 mm VT, with a 16 mm diameter and at 0.35 MPa inlet. All the above suggest that the exact μ_c that would produce either the maximum cooling or heating effect appeared to be dependent on specific parameters such as the VT dimensions, the inlet and outlet pressures.

2.1.2 Geometric parameters

Though structurally simple, specific parts of VT have been subjected to detailed investigations into the effect of geometry on the VT cooling or heating effect; these include the nozzle geometry such as the entry angles, shape and number of nozzles, and the ratio of the length of the hot tube to the vortex chamber diameter.

The tangential entry is believed to produce the best TSE, as it can generate a stronger vortex in the chamber, thus leading to a much more intense fluid rotation within the hot tube. As reported by Hamdan et al[17], under the same experimental conditions and based on one nozzle shape (straight rectangle cross section of 2.33mm × 0.86mm), using 4 different entry angles (as shown in Figure 2.1), the tangential nozzle ($\theta_1 = 0°$) could achieve better TSE than the others.

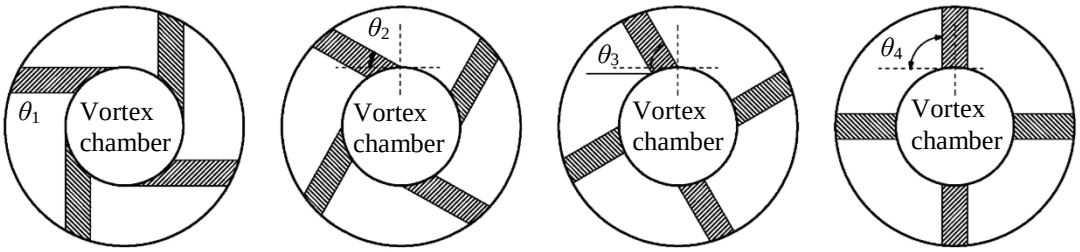

Figure 2.1 Diagram of nozzles with different intake angle ($\theta_1 = 0°$, $\theta_2 = 30°$, $\theta_3 = 60°$, $\theta_4 = 90°$)[17]

Rafiee and Rahimi[47] compared 5 nozzle shapes, each having the same inlet dimension but with the outlet dimensions varied (as shown in Figure 2.2), and the results showed that the convergent nozzles (i.e. $K > 1$) produced a better cooling effect than the straight nozzle ($K = 1$). In addition, an optimum K value ($K = 1.9$, $L_{noz,out} = 1.5$) exists when a 250 mm long VT, with a 18 mm chamber diameter and a 9 mm cold orifice diameter is supplied with 0.25 MPa air. For a constant VT inlet pressure, an increase in the ratio K leads to a higher $v_{cham,in}$, but up to a point when the Mach number reaches 1 or the choked flow exists.

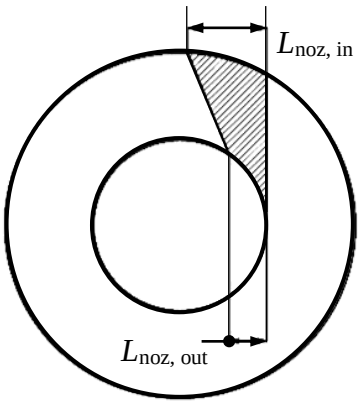

Figure 2.2 Diagram of the nozzle shape ($L_{noz,in}$ = 2.85 mm, $L_{noz,out}$ = 2.85, 2.4, 2.2, 1.5 and 1 mm, $K = L_{noz,in}/L_{noz,out}$)[47]

Results from Rafiee and Rahimi[47], based on 2, 3, 4 and 6 straight tangential nozzles (at 0.25 MPa air supply), and Eiamsa-ard[41], based on 1, 2, 3 and 4 snail nozzles (all at 0.2 or 0.3 MPa air supply), show that, for a given p_{in}, nozzle shape and μ_c, an increase in the nozzle number would generate a stronger swirling flow, resulting in a larger cooling or heating effect (TSE). However, up to certain value, further increase of the nozzle number would be expected to result in a smaller $v_{cham,in}$, thus producing a smaller TSE as observed from Hamdan et al[17], three straight tangential nozzles (2.33 × 0.86 mm) for heating and 4 for cooling are found to produce the best results at a 0.4 MPa inlet pressure when compared to 1, 2, 5 and 6 nozzle numbers. On the contrary, Mohammadi and Farhadi[48] reported that for a given p_{in} and a μ_c, an increase of the straight tangential nozzle number from 2 to 6 (2 mm diameter nozzles at 0.35 MPa inlet air pressure) reduces the TSE, and they suggested this could be caused by an increase in the turbulence level in the chamber.

For a given chamber diameter Φ_{cham}, it is expected that an increase in the VT length L_{VT} (i.e. by increasing the ratio of the L_{VT} to the vortex chamber diameter Φ_{cham}) would have an influence on TSE. A ratio of around 11 (He[39], L_{VT} = 80 - 140mm, Φ_{cham} = 13 mm, air pressure at 0.5 MPa), 15 (Dincer et al[18], L_{VT} / Φ_{cham} = 10, 15 and 18, Φ_{cham} = 9 mm, air at 0.2 - 0.32 MPa) or 20 (Aydın and Baki[19], L_{VT} = 250 - 650mm, Φ_{cham} = 18 mm, air at 0.5 MPa) were found to be an optimal value for cooling or heating, depending on the VT geometries and working conditions. Limited works on assessing the effect of cold orifice diameter Φ_{co} to VT chamber diameter Φ_{cham} ratio (Saidi and Valipou[29], Eiamsa-ard[41], Promvonge and Eiamsa-ard[46]) have revealed that a value of around 0.5 (for air) was regarded as a suitable value to achieve good cooling or heating effect under various working conditions.

2.1.3 Working fluids

Most of the previous work used either air or N_2, though limited research on CO_2, NH_3, HCs and HFCs[20, 39, 49] have been reported.

The work by Martynovskii and Alekseev[20] showed that under the same μ_c of 0.4, R50 (CH_4) has a better cooling effect when compared to R744 (CO_2) and R717 (NH_3). Collins and Lovelace[39] studied the TSE of R290 (propane) in the VT and their experimental results showed that at an inlet temperature of around 40 °C and pressure of 0.79 MPa, the cooling effect could reach 24 °C or the heating effect 15 °C. Han et al[21] experimented on a number of working fluids (at the same inlet pressure of 0.3 MPa), including R728 (N_2), R744 (CO_2), and some HFCs (R32, R161, R22 and R134a), and R32 was found to have the best cooling effect (7.18 °C) and R728 (N_2) the best heating effect (3.65 °C). Unfortunately, not many works provide in-depth explanations as why certain fluids perform better than the others.

Due to incompressible nature of liquid, it is expected that considerable drops in the TSE would result when a two-phase fluid enters the VT, as observed in the work of Collins and Lovelace[39] on R290; the TSE decreases sharply when the nozzle inlet vapour quality drops below 80%. Takahama and Yokosawa[50] tested with steam and found that the effective energy/temperature separation can only happen when the dryness fraction was larger than around 0.98 at the nozzle outlet.

It is clear that so far only few working fluids have been studied in the VT research, and liquid-phase fluid entering the VT would impair the VT performance. Detailed research on the influence of fluid properties on the TSE is rather scarce.

2.1.4 Remarks

The published results reveal that the temperature separation performance of a VT is strongly influenced by the chamber inlet velocity which is a function of the VT inlet pressure. Until a sonic condition is reached at the nozzle exit, a higher inlet pressure generally leads to a higher chamber inlet velocity, thus generating a stronger rotation and a larger TSE.

Tangential convergent nozzles appear to generate the strongest rotation, and there appears to be an optimal nozzle number that would give rise to a maximum rotation depending on the experimental conditions.

The setting/selection of certain parameters, such as VT inlet temperature and aspect ratio of the VT, to achieve the desirable TSE depends on the design of the VTs, fluid choices and the operating condition. The influence of the VT inlet temperature on TSE is related to the VT isentropic efficiency which is in turn affected by the choice of working fluids and operating conditions.

Though most of the VT research is based on using air, it is expected that certain observations made could be also applicable to other working fluids, especially for refrigerants at superheated state. Depending on the fluids, the inlet quality of the fluid at the nozzle exit should be above a certain value, to achieve a noticeable temperature separation.

Some existing refrigerants have been shown to produce better TSE than air and N_2. However, it is practically not possible to experimentally assess too many different combinations of fluid choices, VT designs and working conditions. To develop an approach that could be used to narrow down the fluid choices based on different VT parameters would therefore be desirable.

2.2 Understanding the temperature separation process in VT

2.2.1 General explanation and understanding of the TSE

An agreement on the exact principles/mechanism of the temperature separating process has not been universally reached, but several explanations have been put forward by researchers[4, 8, 51-60]. Hilsch[4] presumed that the centrifugal force and the internal friction produce a low pressure region at the axis of the VT, and the expansion of the fluid near the wall to the central of the tube leads to a temperature drop. At the same time, the inward expanding fluid transfers its kinetic energy to the peripheral fluid by some kind of internal friction, thus increasing its temperature.

Kassner and Knoernschild[8] analysed the friction laws and the energy transfer in a circular flow, and suggested that the temperature separation is caused by a conversion from an irrotational flow to a rotational flow in the VT. When the fluid enters the VT chamber, it rotates as an irrotational flow. For a viscous fluid, the shear force works on two annular layers, thus reducing the velocity difference between them and converting the flow in to rotational flow. This process results in a kinetic energy transfer from the inner rotating layers to outer layers by friction. At the same time, the

pressure difference between the peripheral and the central layers leads to a temperature drop towards the centre. In addition, the pressure differential between the hot end and the cold end along the axis leads to an expansion of the fluid and a drop in fluid temperature towards the cold orifice along the axial direction.

Deissler and Perlmutter[61] derived the energy balance in the VT and believed that the inner fluid does shear work on the outer fluid when it spirals inwards, and this work produces most of the energy/temperature separation. This shear work consists of three energy terms (turbulent dissipation, kinetic energy and potential/pressure energy), and the turbulent dissipation produces most of the heating for the outer fluid, while the cooling is generated mainly by the negative kinetic and potential/pressure energy terms[61].

Kurosaka[62] put forward an analytical explanation based on acoustic theories, stating that the streaming coming from the vortex whistle (a pure-tone noise in swirling flow) forces the Rankine vortex (an initial swirl in the VT) to become a forced vortex, and this transformation, to a substantial degree, leads to the temperature separation, and he also experimentally verified it by examining the influence of the intensity of the vortex whistle at a tuned frequency on the TSE[62].

Polihronov and Straatman[63] studied the thermodynamics of the flow rotation in a rotating reference frame (considering the Coriolis force and centrifugal force) instead of an inertial frame of reference. They concluded the cooling effect is a result of an adiabatic expansion process, during which the fluid overcomes the centrifugal force and does work on its surroundings by keeping the frame rotating when it spirals towards the centre.

Xue et al[64] used an experimental visualization method to investigate the TSE in VT. A low velocity water flow is supplied to an acrylic VT which is immersed in a water tank. Air bubbles, small plastic particles or hydrogen bubbles are used to visualize the flow streamlines and calculate the water velocities. They observed that the expanded water from the nozzle flows through the vortex chamber out of the cold end without reaching the hot end, and the rebounced fluid from the hot throttle turns back at several axial locations (setting up multi-circulation) to the periphery of the VT and moves towards the hot exit. Then, they concluded that the cooling effect is the result of the expansion from the nozzle, and the heating effect is mainly due to viscous friction in

the multi-circulation.

Lewins and Bejan[65] used a VT heat exchanger theory (in which the fluid is assumed to have a constant specific heat capacity) to understand the flow process and to correlate the TSE with the VT length, fluid specific heat, thermal conductivity and the mass flow rate. As shown in Figure 2.3, the VT is regarded as a heat exchanger, in which the hot and the cold stream flow in the opposite directions, and the Number of Transfer Units (NTU) method[66] is used to analyse the heat transfer rate between them. Their approach is applied by Cao[28] to show the relation between the TSE with the VT length, the fluid thermal diffusivity and the volume flow rate. Cao validated his work by comparing his results with the experimental data from Hilsch[4] (Figure 2.4). The discrepancies arose due to the fact that the conditions used in the experiments were slightly different to that in the calculation; a constant pressure gas was fed into the VT in experiment, and thus the inlet volume flow rate would vary slightly at different μ_c. However, in the calculation, a fixed inlet volume flow rate was employed.

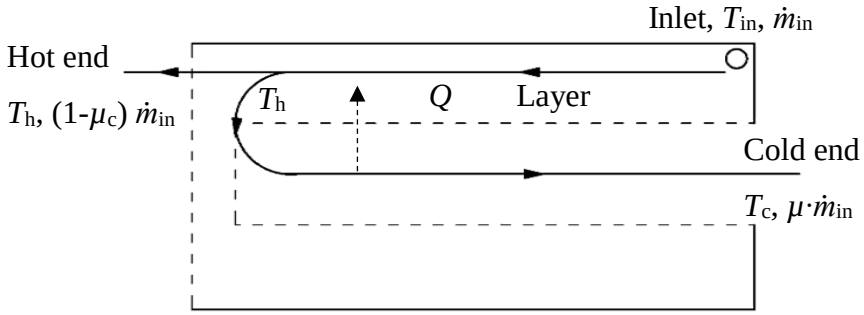

Figure 2.3 Schematic diagram of the VT counter flow heat exchanger[28]

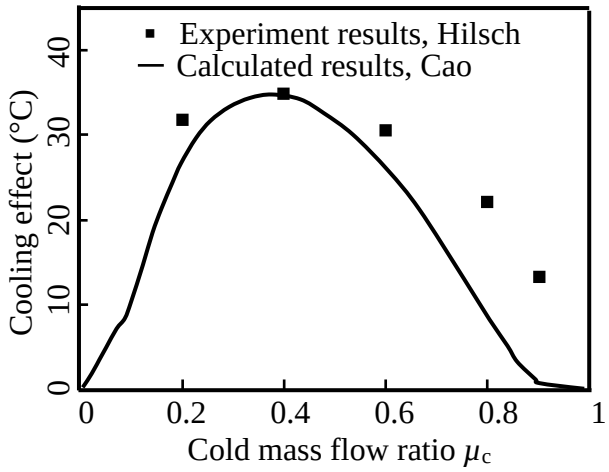

Figure 2.4 Comparison of the experimental[4] and calculated results[28]

Ahlborn and Gordon[54] attempted to use the concept of a classic refrigeration cycle to understand the energy transfer process in the VT. As shown in Figure 2.5, the flow

undergoes through four typical processes of a refrigeration cycle: 1) the condensing process 2-3 in which the secondary flow is cooled by the expanded fluid from the nozzle (the authors believe that the fluid at the nozzle outlet has the lowest temperature within the VT); 2) the cooled fluid then undergoes an expansion process 3-4 in which the pressure drops from the peripheral part (high pressure region) to the central part (low pressure region) of the VT; 3) the evaporating process 4-1 in which the expanded fluid absorb heat along the axis of the VT moving toward the cold end; 4) the compression process 1-2, the heated fluid moves back from the inner part to the peripheral high pressure regions.

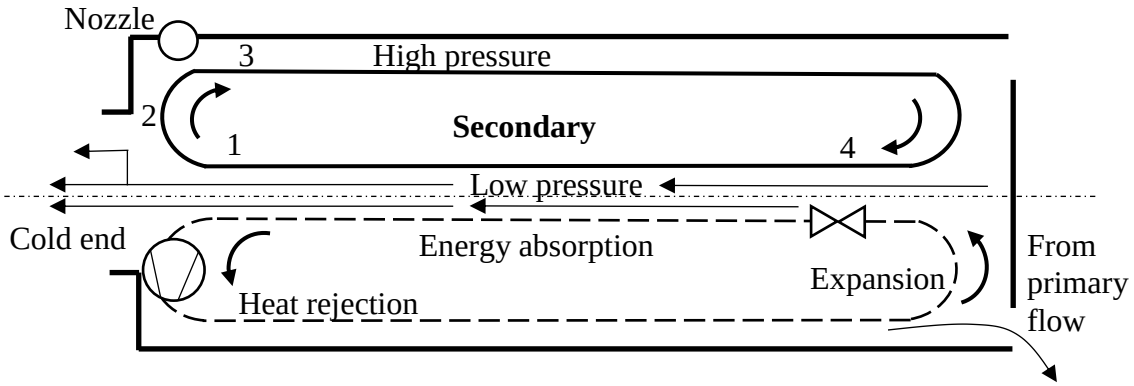

Figure 2.5 Schematic of the classic refrigeration cycle in the VT[54]

2.2.2 Remarks

Various theories have been suggested by researchers attempting to explain or to gain a better understanding the temperature separation mechanism, and among them, transfer of the kinetic energy caused by fluid friction or shear stress is probably the most widely adopted one. When the fluid enters the VT chamber, it experiences a change from a free vortex to a forced vortex flow which can be regarded respectively as a change from an irrotational flow to a rotational flow. For viscous fluid, the shear forces in the irrotational flow slow down the rotating speed and generate viscous friction.

Specific heat capacity has been taken as constant by researcher when applying the heat exchanger theory to correlate the TSE with the VT length and operating conditions. However, for many existing refrigerants, the specific heat capacity should not be taken as a constant as it varies noticeably under different conditions, and the author is not convinced that the current VT heat exchanger theory is accurate enough to be applicable to common refrigerants.

2.3 Computational fluid dynamics for analysing flow behaviour in VT

2.3.1 Previous CFD research in VT

Computational fluid dynamics (CFD) has enabled researchers to obtain detailed flow velocity and temperature distributions within the VT[67-71]. A typical 2-D or 3-D CFD numerical simulation process includes geometry definition, meshing construction, turbulence model selection, experimental validation and results presentation/analysis.

Probably to save time, VT CFD researchers often use published geometries and experimental data for validation purposes. The key geometric parameters of Bruun's[72] VT (as shown in Figure 2.6) and his experimental data (p_{in} = 0.2 MPa, T_{in} = 21 °C and μ_c = 0.23) have been used by various researchers in their simulations[73, 74] for validation purposes, as he had acquired a very comprehensive range of data on air velocity and pressure distributions, and total temperature at 14 cross sections of the VT.

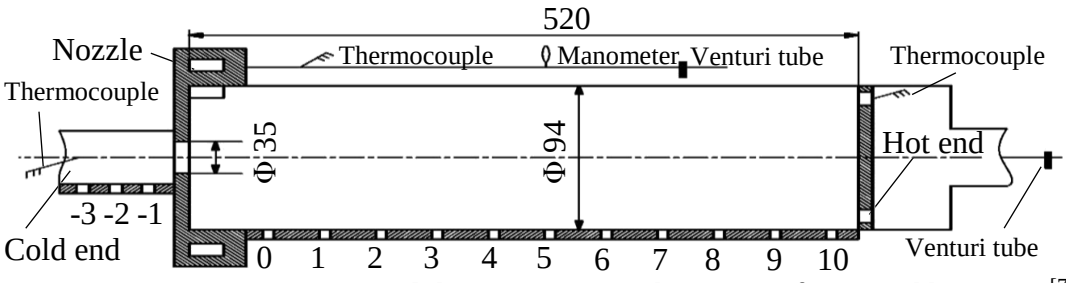

Figure 2.6 Dimensions (mm) and the measurement locations of VT used by Bruun[72]

Frohlingsdorf and Unger[73], and Karimi-Esfahani et al[74] used respectively the CFX and Fluent codes to simulate the flow. They developed a 2-D axisymmetric geometry and set the nozzle arrangement as a circumferential inlet. Frohlingsdorf and Unger[73] defined the inlet flow angle, as shown in Figure 2.7, whereas Karimi-Esfahani et al[74] did not provide any details of the entry flow angle but only gave the dimensions, as shown in Figure 2.8.

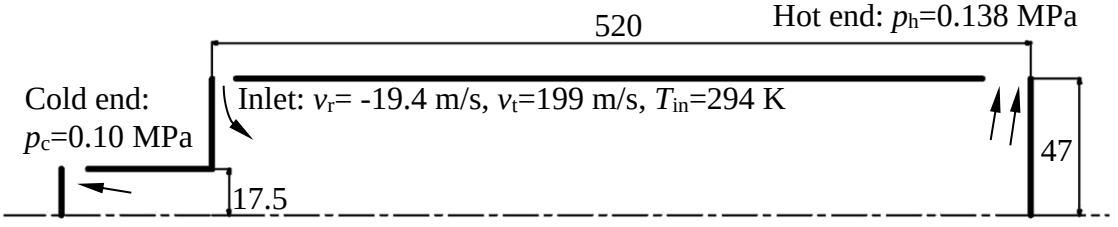

Figure 2.7 Simplified geometry (mm) and boundary conditions used by Frohlingsdorf and Unger[73]

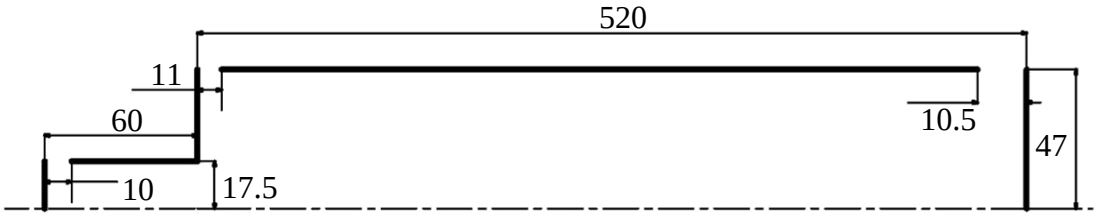

Figure 2.8 Dimensions (mm) used by Karimi-Esfahani et al[74]

Frohlingsdorf and Unger[73] believed that in the rotation, the friction forces cause the outward transfer of mechanical energy, which is partially compensated by the inward heat transfer by diffusion. When they set the turbulence Prandtl number (Pr_t) at 9.0, the CFD results can better match with experimental results. Karimi-Esfahani et al[74] found that a swirl factor of 0.075 is quite suitable for the highly swirling flow, and then used this value in the *Re-Normalisation Group* (*RNG) k-ε* turbulence model in his initial Fluent simulations. In both studies, the turbulent viscosity in the *k-ε* turbulence model was replaced by a correlation, accounting for the highly swirling nature of flow, suggested by Keyes[75], enabling them to get a better match with Bruun's[72] data.

The boundary conditions (e.g. p_{in}, T_{in}, p_h and p_c) used by CFD researchers are often varied, but some published literatures do not provide any details at all, making it difficult to compare results. Frohlingsdorf and Unger[73] and Karimi-Esfahani et al[74] chose to vary the hot end pressures p_h when the cold end pressure p_c was kept constant while some others[58, 76] change both p_h and p_c in their simulations in order to achieve the required cold mass flow ratios. Frohlingsdorf and Unger[73] analysed the energetic processes in the VT and identified a circulating secondary flow which receives the energy from the cold air and transfers outward to the hot air; Karimi-Esfahani et al[74] predicted the optimal VT dimensions (Φ_{co} / Φ_{cham} = 0.5) and operating conditions (a large p_{in} and a small μ_c) for generating the largest cooling effect.

The experimental results of Aljuwayhel et al[77] and Skye et al[78] were used by themselves[77, 78] and other researchers[79, 80] for validating their CFD works. Aljuwayhel et al[77] constructed a VT and provided the key dimensions (L_{VT} = 100 mm, Φ_{cham} = 19 mm, Φ_{ht} = 19 mm and Φ_{co} = 6 mm, radial annular hot exist, and the μ_c is adjusted by controlling the hot end throttle/pressure) needed for their CFD works. On the other hand, Skye et al[78] used a commercial VT (model: Exair 708 slpm VT), and measured all the dimensions of the VT (L_{VT} = 144 mm, H_{noz} = 0.97 mm, W_{noz} = 1.41mm, $A_{noz,in}$ = 8.2 mm^2, Φ_c = 6.2 mm, Φ_h = 11.0 mm) except that the flow area (a function of

the throttle position) at the hot end was not given (Figure 2.9). Unlike Bruun's[72], only the data (e.g. pressure and temperature) at the VT inlet and outlets were measured in their research.

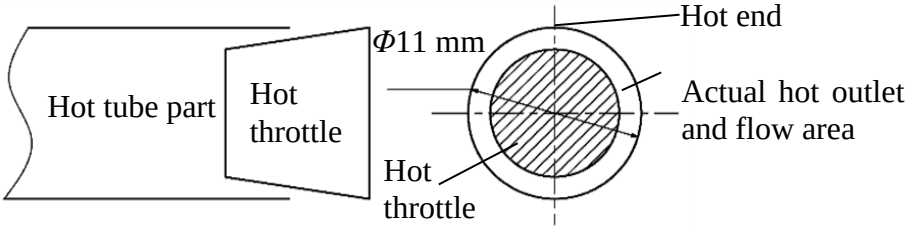

Figure 2.9 Hot end of the VT[78]

Farouk and Farouk[80] performed a CFD simulation based on the measurements from Skye et al[78]. As shown in Figure 2.10 and Figure 2.11, both Farouk and Farouk[80] and Aljuwayhel et al[77] developed a 2-D model with similar geometric parameters; the former used radial annular and the latter used both an axial and a radial configurations. Aljuwayhel et al[77] found that the two nozzle entry configurations (axial and radial annular) gave very similar results and thus their paper mainly focussed on the axial entry; in addition, they claimed that the axial entry provide a better numerical stability compared with the radial entry.

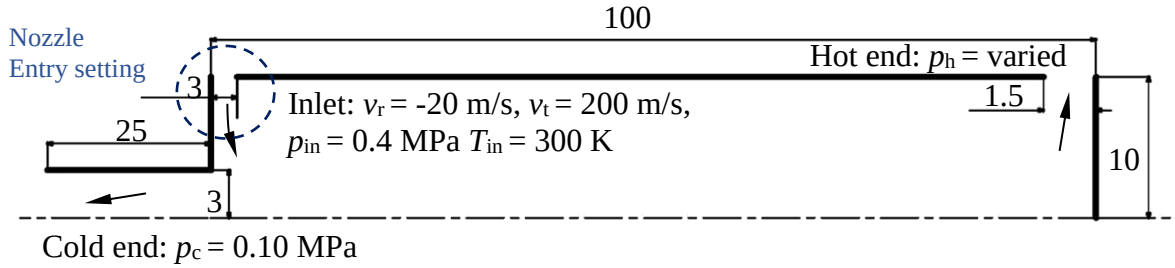

Figure 2.10 Geometry (mm) and boundary conditions used by Farouk and Farouk[80]

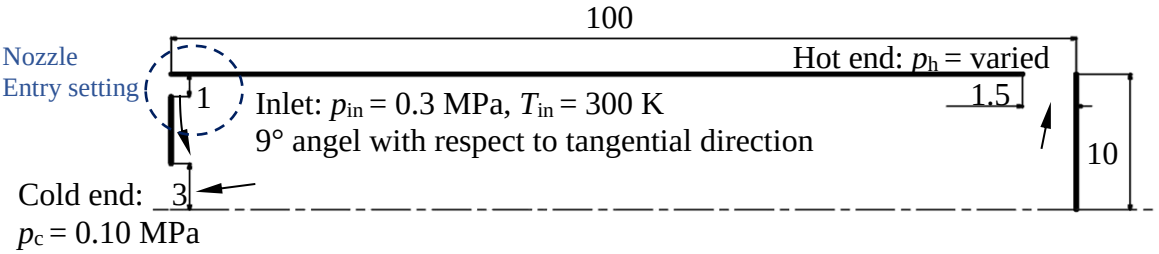

Figure 2.11 Geometry (mm) and boundary conditions used by Aljuwayhel et al[77]

The *Standard k-ε* and the *RNG k-ε* turbulence models were used in Fluent by Aljuwayhel et al[77], and the results showed that the *standard k-ε* model could give more accurate results than the *RNG k-ε* model. The *large eddy simulation* (*LES*) was used in the CFD-ACE+ code by Farouk and Farouk[80], and the results proved the *LES*

can also generate good agreement with the experimental results.

Similar to Frohlingsdorf and Unger[73] and Karimi-Esfahani et al[74], both Aljuwayhel et al[77] and Farouk and Farouk[80] attempted to vary the p_h (e.g. p_h from 60 kPa to 115 kPa in Farouk and Farouk[80]) to control the μ_c, while the p_c was kept constant.

Aljuwayhel et al[77] used their validated VT model to study the flow behaviour inside the VT and examine the influence of the VT dimensions (L_{VT} and Φ_{cham}) on the TSE. They concluded that the TSE will increase when the L_{VT} increases to a critical length, after that any further increase in L_{VT} will not lead to a larger TSE, and the TSE decreases when the Φ_{cham} increases as the angular velocity of the rotation flow decreases.

The experimental data of Behera et al's[81] were used by themselves to compare with their CFD results to identify the optimal VT geometric parameters[81], and were also used by other researchers[82] to validate their CFD results. In Behera et al's experiment, the VT had 6 convergent nozzles ($A_{noz,in}/A_{cham}$=0.07), the value of Φ_{co} varied from 5 to 7.5 mm, the ratio of L_{VT} to Φ_{cham} changed from 10 to 35 while the Φ_{cham} was fixed at 12 mm, and the cold and hot end temperatures were measured.

Behera et al's used the Star-CD CFD code to perform a 3-D simulation, employing a *RNG k-ε* turbulence model. As shown in Figure 2.12, the hot end was modelled as a throttle with a conical trapezium shape, same as that used in their experiment, whereas mainly annular axial or radial geometries were adopted by other modellers[68, 69, 72-74, 77, 78, 80, 82]. The simulation and the experimental results were found to match well at 300 K and 0.54 MPa compressed air.

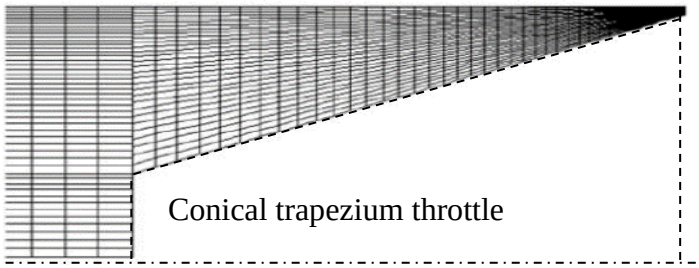

Figure 2.12 Cut- away view of the hot end of a 3-D VT model[54]

Based on Behera et al's VT dimensions and boundary conditions, Dutta et al[82] developed a 2-D VT model (Φ_{co} = 6 and 7 mm, L_{VT} = 120 and 180 mm, Φ_{cham} = 12 mm, p_c = 0.136 MPa, p_h = 0.15 MPa, as shown in Figure 2.13 using various hot end flow areas, instead of varying the hot end pressure seen in other work[73, 74, 77, 78, 80], as a means

to control the μ_c. Four turbulence models: *standard k-ε*, *RNG k-ε*, *standard k-ω*, and *SST k-ω* were used in Fluent. The results showed the *standard k-ε* turbulence model has a better agreement with T_c and T_h obtained from the experiments, and the predicted results from the *standard k-ω* and *SST k-ω* models are also quite close to the experimental results. However, the turbulent viscosity calculated by the *RNG k-ε* model is much smaller than that from other models, thus resulting in a reduction of the total temperature of the peripheral fluid.

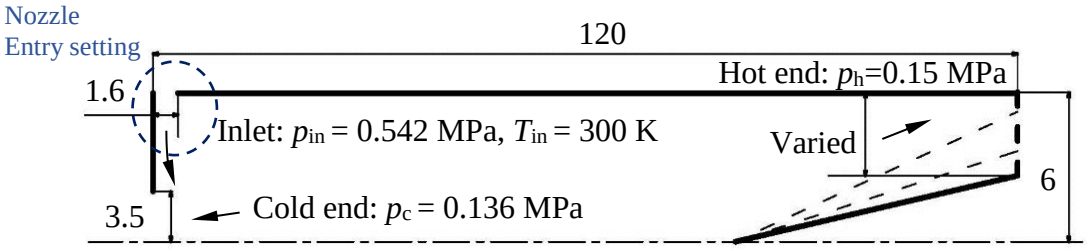

Figure 2.13 Geometry (mm) and boundary conditions used by Dutta et al[82]

Dincer et al[83] experimentally investigated the influence of the throttle position and its taper angle on the TSE. The L_{VT}, the Φ_{cham} and the A_c were kept constant at 135 mm, 9 mm and 19.6 mm^2, respectively. The straight nozzle (2×2 mm^2) numbers were varied from 2 to 6, the hot end area changed from 13.3 to 43.9 mm^2, the taper angle increased from 30° to 180° and the throttle moved from the hot end towards the cold end by 1, 2 or 3 mm. The compressed air was supplied at 200 to 420 kPa. Different to previous experimental researches, only the total temperature separation effect was presented.

Based on Dincer et al's data[83], Baghdad et al[84], compared the *standard k-ε*, *standard k-ω*, *SST k-ω* and the *Reynolds-Stress Model* (*RSM*) models in Fluent in his simulations (the geometry and boundary conditions are shown in Figure 2.14), and results showed that all of the turbulence models could in general predict the fluid motions of the VT, though the RSM produced the best agreement with the experiments of Dincer et al's.

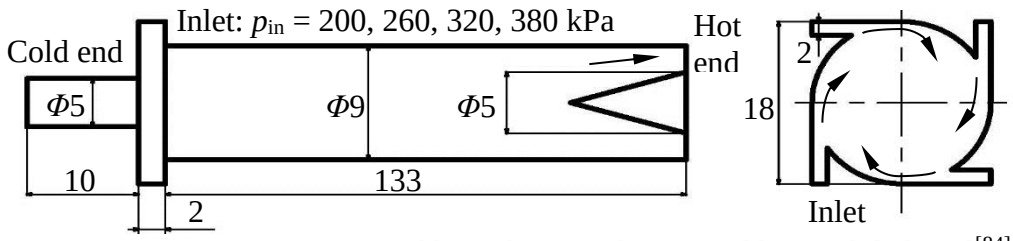

Figure 2.14 Geometry (mm) and boundary condition used by Baghdad et al[84]

2.3.2 Remarks

Regarding the VT structure, the main difference between various experimental research appeared to be the geometry of the hot throttle. Compared to the axial or radial slot (by Bruun's[72] and Aljuwayhel et al[77]), a tampered throttle (by Dincer et al[83], Skye et al[78] and Behera et al's[81]) introduces additional complexity in performing CFD simulation, as the throttle position represents an additional parameter to adjust the μ_c.

Although comprehensive temperature/pressure measurements were made by Bruun[72] in his VT, the accuracy of their results is questionable as an intrusive measurement technique was used. On the contrary, it is expected that the temperatures/pressures measured at the VT inlet, cold and hot end by Aljuwayhel et al[77], Dincer et al[83], Skye et al[78] and Behera et al's[81] are accurate.

Fluent was the most popular CFD package choice for simulation work. The *standard k-ε*, the *RNG k-ε*, the *standard k-ω* and the *SST k-ω* turbulence models all appeared to be able to provide good accuracy. Varying the hot end pressure was a popular way to adjust the cold mass flow ratio.

For modelling and analysing the flow filed and predicting the TSE, either a 2-D or a 3-D geometry can be used to provide a good match with experimental results. However, each individual 3-D model corresponds to a specific VT and cannot be used for general purpose in studying other VTs with, say, different nozzle numbers or hot end throttle design. On the other hand, most of the 2-D models defined the nozzle, the hot end and the cold end as annular openings, thus ignoring the influence of nozzle number, hot end throttle position, making them more applicable for general studies.

In terms of the modelling the VT inlet conditions, for a 2-D model, the fluid status (such as velocity magnitude and total temperature) at the nozzle outlet (i.e. the chamber inlet) must be pre-defined, but the data are usually difficult to be acquired accurately from experiments. On the other hand, for 3-D models, the fluid data at the nozzle inlet needs to be defined, and these (e.g. mass flow rate and temperature) could also be easily and accurately measured.

2.4 Incorporating VTs in thermal systems for enhancing the overall energy efficiency

When connected to a high pressure source, an open VT system can be conveniently setup to directly produce cooling[2, 85-89] or heating[3, 90-93] effect.

For a given pressure drop across a VT, the associated temperature drop is larger than that of the J-T isenthalpic temperature drop[24, 25] experienced in a typical throttling device. Therefore, employing a VT in, say a closed compressor cooling system has an additional benefit of potentially improving the system efficiency[26]. On the other hand, the heating effect of a VT can potentially be used to upgrade relatively low grade heat to a more useable temperature, as seen in [94].

2.4.1 Application of VT in closed VT systems

Unlike for open systems[2, 3, 85-93, 95], only limited published literature regarding closed VT systems[26, 94, 96-99] could be found. Some proposed ideas from various researchers are given below.

Figure 2.15 shows a compressor VT cooling cycle[26], in which the VT is applied as a throttling device. The high temperature and pressure fluid from the compressor is cooled both in the cooler 1 and recuperative heat exchanger, and then it enters the VT still as a superheated vapour. The cold stream from the VT produces cooling/ refrigeration effect in the heat exchanger. A semi-empirical model is established to predict the VT cold and hot end temperature; it is based on the conservation of angular momentum and energy, and the conventional heat exchanger theories.

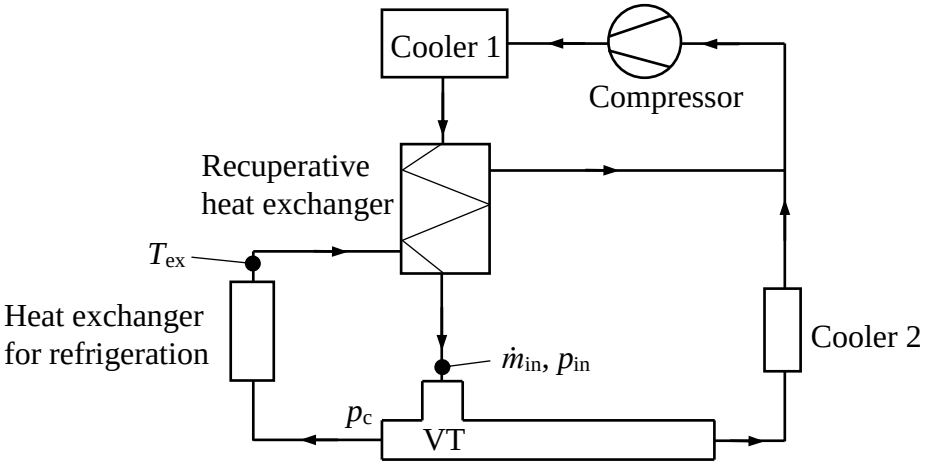

Figure 2.15 A compressor VT cooling cycle[26]

The cooling capacity Q_c at different μ_c is analysed and presented in Figure 2.16. Referred by the authors as a J-T cycle when μ_c is set to 1 (this is equivalent to having an ordinary throttle instead of a VT), all fluid flows out of the VT cold end into the heat exchanger. The calculation results show that there is an optimal μ_c (≈ 0.53) to produce the largest Q_c, and the system with the VT (at μ_c < 1) always has larger Q_c than that of J-T cycle. However, the analysis does not evaluate the system efficiency and it is unclear whether the semi-empirical model could be applied to assess other working fluids.

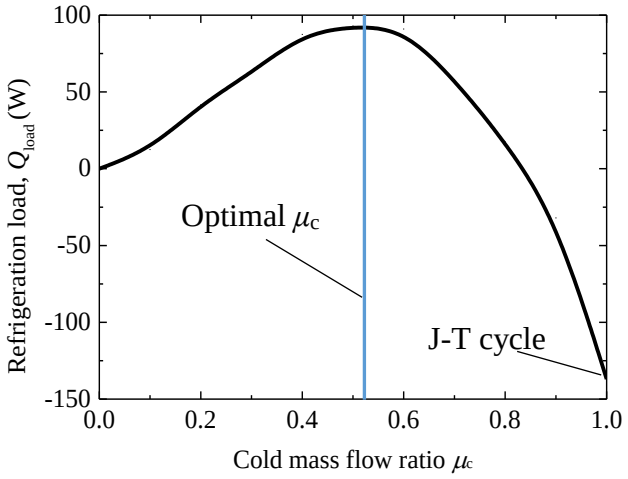

Figure 2.16 Refrigeration capacity at different μ_c (air, $T_{cooler1}$ = 300 K, $\dot{m}_{in}$ = 10 g/s, T_{ex} = 250 K, p_{in}/p_c=5, total conductance for the heat exchanger is 10 W/K) [26]

Figure 2.17 shows a VT-ejector refrigeration system, which can provide two different evaporating temperatures (at Eva1 and Eva2), proposed by Wang et al[96]. A VT is used as a throttling device which is expected to generate a higher liquid quality fluid entering the evaporator. In this closed system, the high-pressure CO_2 from the compressor 2 enters the gas cooler, and part of the cooled gas enters the VT, while the rest enters the ejector. The low-pressure cold gas and liquid streams from the VT merge and produce refrigeration effect in evaporator 1. The evaporated gas from evaporator 1 mixes with the gas from the cooler following the VT, and induced into the ejector by the high-pressure CO_2 from gas cooler. The two phase CO_2 at the intermediate pressure enters the gas-liquid separator.

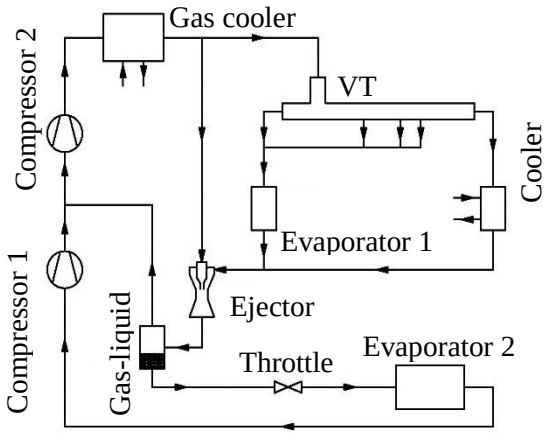

Figure 2.17 Flow chart of the VT-ejector refrigeration system[96]

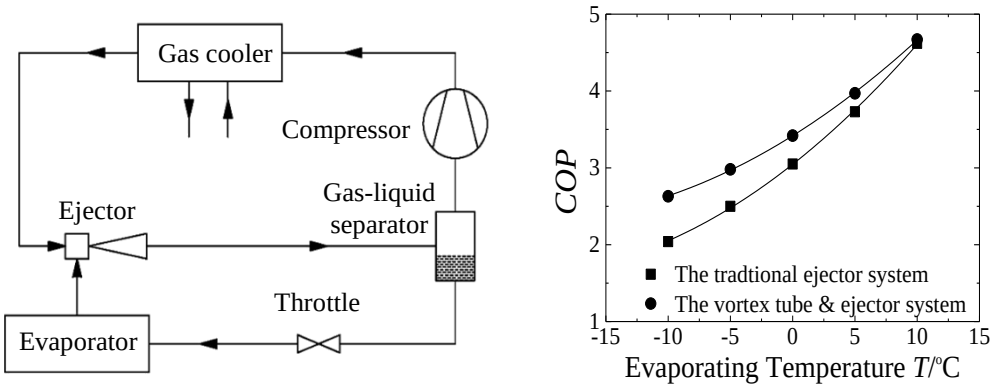

a b

Figure 2.18 a. Schematic diagram of the traditional ejector system; b. The COP of a traditional ejector system and of a VT-ejector refrigeration system[96]

Compared to a basic ejector system shown in Figure 2.18a, the energy and mass balance calculations[96] show that when all the evaporators are controlled to have the same temperature (from -10 to 10 °C, $\mu_c = 0.6$), the *COP* of the VT system (Figure 2.18b) is always higher than the basic system. However, this gain diminishes at higher evaporating temperature, as a smaller pressure ratio is less favourable for the operation of the VT. The energy balance calculation is based on the assumption that the VT is capable of providing the required cooling temperature at the defined inlet and outlet pressures; however, there is no evidence that the VT can indeed achieve this.

Figure 2.19a and b present respectively a close transcritical CO_2 VT system proposed by Maurer[100] and the corresponding *p-h* diagram used in the analysis of Sarkar[99]. In the system, the VT is used as an expansion/throttling device which could potentially reduce the entry vapour quality to the evaporator when compared to a conventional expansion valve, thus improving the specific refrigerating effect. The system was analysed by Sarkar[99] based on the first and second laws of thermodynamics, and

compared the two systems, the VT system has a higher specific refrigerating effect, i.e. (h_7-h_3) is increased to (h_7-h_6), and a better *COP*. Once again, the analysis is based on the assumption that the VT will perform at the specified system pressure, as intended.

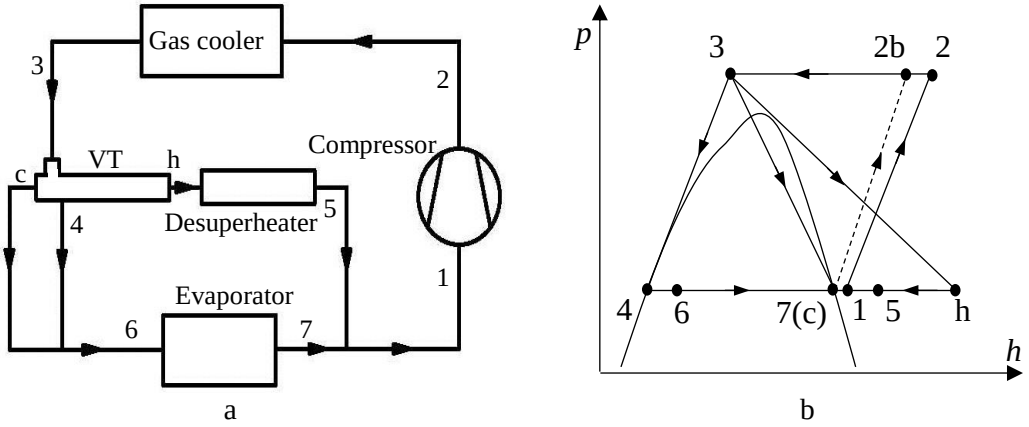

Figure 2.19 Schematic diagram of the closed transcritical CO_2 VT system. Maurer model[100] (a), *p-h* diagram[99] (c and 7 are both taken as saturated vapour) (b)

Figure 2.20a presents a VT auto-cascade refrigeration system. The use of a VT as a temperature separation device enables an additional cooler (cooler 2) to be incorporated so that more heat can be removed from the refrigerant before it enters the throttle valve 2[98]. Figure 2.21 shows the corresponding flow processes on a *p-h* diagram for the low boiling point fluid, and compared to the traditional auto-cascade system shown in Figure 2.20b, the VT system can reject additional quantity of heat (h_h - $h_{3'}$), thus increasing the cooling capacity from (h_7-h_6) to (h_7-$h_{6'}$).

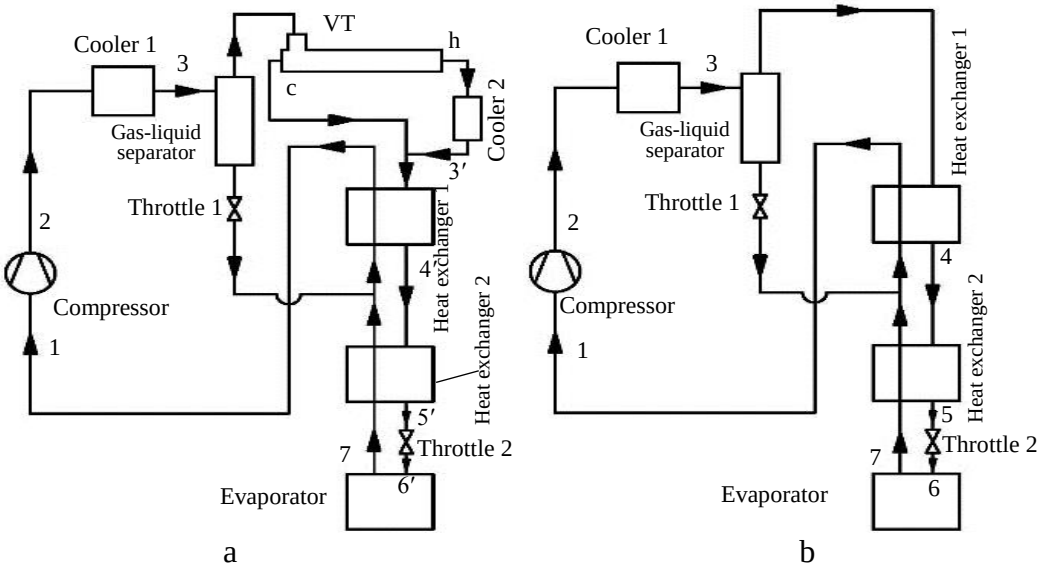

Figure 2.20 Schematic diagram of the auto-cascade refrigeration system: with VT (a), without VT[98] (b)

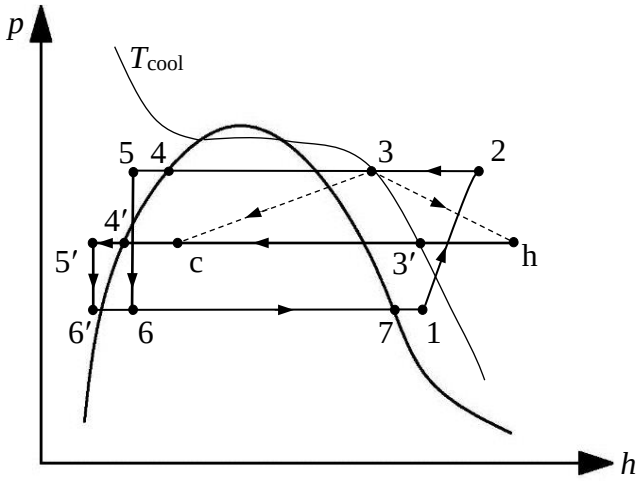

Figure 2.21 Flow processes for the low boiling point refrigerant in the two systems (T_{cool} is the temperature for fluid at the coolers' exist)

In their performance analysis[98], in addition to the energy balance, heat exchanger theory[28] is applied to predict the VT cold and hot fluid temperature. The calculation shows that this system has a higher *COP* (0.59) than the traditional system (0.37) under the same conditions (R600a : R23 (by mole) = 1 : 4, T_{cool} = 30 °C, T_e = -60 °C, μ_c = 0.45). However, the heat exchanger theory[28] for the VT is derived based on the constant specific heat fluid; it has not been validated that it can be applied for correlating the TSE of refrigerant with the VT operating conditions.

Figure 2.22 displays a liquid pump VT heating system driven by waste heat[94], in which the VT is used as a temperature separation device to increase the fluid temperature coming from the heat source (Q_1) to a higher level. The hot stream from the VT provides the heating function at a temperature higher in the heat exchanger 2, than the original heat resource temperature. The calculation results (based on the energy balance and heat exchange theory[28]) show that, when the heat resource temperature is 85 °C ($\dot{m}_{in}$ = 750 g/s, R245ca), this VT (p_{in} = 0.3 MPa, p_c = 0.1 MPa) could provide respectively 31.69 kW (μ_c = 0.79, ΔT_h = 35 °C) and 49.34 kW (μ_c = 0.67, ΔT_h = 30 °C) heating capacity[94] when the exist fluid temperature of Heat exchanger 2 is set 25 °C.

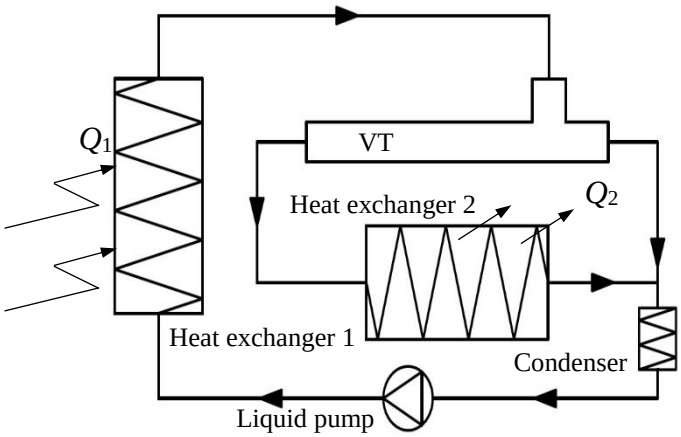

Figure 2.22 Schematic diagram of the closed liquid-pump heat driven VT system[94]

2.4.2 Remarks

VTs are mainly used for either direct cooling or heating in open systems in which compressed air and N_2 are most commonly used as working fluids. The integration of the VTs into closed thermal systems is still in its infant stage. The role of the VT in closed systems is primarily to use its TSE to facilitate the internal transfer or external exchange of energy to improve the overall thermal efficiency of the systems.

It has also been proposed in some configurations that VT could be used as an expansion/throttling device, in which production of cold vapour/liquid could be achieved and used for direct cooling. In some cases, the VTs are coupled with other thermal devices to expand the functionalities and capabilities of the existing systems. However, the literature reflects that overall only very few VT systems have been proposed in refrigeration and heat pump applications.

Although the basic energy balance or thermodynamic analysis has shown some systems employing the VT could potentially have a better efficiency under certain working conditions, no methodologies have been established to verify whether the VT could indeed generate the required cooling or heating effect under the specified conditions. Research efforts devoted to practical implementation and full operational analysis of closed VT systems are still rather limited.

The development of closed VT systems offers the possibility of using a wider range of working fluids, however very few fluids have been examined and trialled. It also appears that no systematic screening, evaluation and optimization of refrigerant choices, in relation to specific closed system configurations and operating conditions, as well as to individual VT characteristics has been considered.

2.5 Key research questions, objectives and aims

2.5.1 Key research questions

Some key questions can be asked based on the literature review, and the associated observations could help to identify research gaps and to formulate research strategies.

1. The influence of certain parameters, such as inlet fluid temperature and cold mass flow ratio, on the TSE have been studied. Different or even opposite trends were observed due to the use of different VT constructions under different conditions. What could be learned from these trends and for a given VT, and how various parameters could be controlled/adjusted to achieve the required temperature separation in relation to working fluid choices?

2. Convergent nozzles with a tangential entry angle have been observed to deliver good cooling or heating results, while the optimal nozzle shape and nozzle numbers vary with working conditions. Would it be possible to define a VT geometry to reduce its performance sensitivities towards nozzle shape and number over a wide range of conditions, so that the results could be generalised and become applicable for other VT designs?

3. The observations on the TSE and flow process in VTs are made mainly based on air and N_2. Some of these observations may be applied to some saturated or superheated refrigerants, thus helping us to understand their flow behaviour in VT. Being a real fluid, refrigerants are expected to exhibit certain unique VT characteristics. Would it be possible to identify both the similarities and differences between air and refrigerants in their VT behaviour, and what can we learn from this behaviour?

4. Many refrigerants could be potentially used in closed VT systems, but only a few have been studied by researchers. It is not practically possible to experimentally evaluate all the available refrigerants, nor is possible to perform much theoretical analysis of the refrigerant behaviour within VT due to lack of thorough theories/ understanding of the associated heat and mass transfer mechanisms. Would it be possible therefore to develop a reliable, relatively simple and cost effective refrigerants screening methodology for the VT applications?

5. The current VT system analysis is mainly based on the energy balance and heat exchanger theory which correlates well the TSE and operating condition for air or

nitrogen, but it is not clear if heat exchanger theory is applicable to refrigerants for VT analysis. Computational Fluid Dynamics (CFD) simulations are becoming popular in recent years for analysing/predicting the TSE in open system VTs. Would it be practically possible to use the CFD tool for the closed system environments and to couple the CFD simulations with any thermal calculation to analyse system operations and performance?

2.5.2 Research objectives and aims

From the above, it can be seen that the study of refrigerant applications in VT is limited, the method on how to select an appropriate fluid has not been established, and the analysis of how to practically integrate a VT within a thermal system is not available. Therefore, three closely linked objectives of this research are set as follows:

- To create an accurate VT CFD model for studying the influence of various parameters on the VT thermal and flow behaviour, and for predicting the TSE of different refrigerants under specified working conditions.

- To develop a refrigerant screening methodology for evaluating the suitability of various refrigerants, to achieve the desired VT operation and performance.

- To establish a procedure for examining the matching of refrigerant properties, VT design and the closed system configuration, in order to assess whether a chosen refrigerant could perform satisfactorily in practice in a closed system or if the VT needs to be redesigned.

Fulfilling the objectives would enable us to answer fully Questions 3 - 5. Due to limited time, Questions 1 and 2 will only partially be touched upon.

2.6 Main research tasks (outline)

1. Establishing an accurate VT numerical simulation model. The commercial CFD code Ansys Fluent is employed as the tool for this part of the work, involving the following tasks:

- Deciding upon appropriate VT geometries, creating good quality meshing, selecting suitable turbulence models and validating the CFD results.

- Understanding the application of various boundary conditions, analysing the internal flow process and the associated influencing factors, based on initially using air, R134a and R600 as the working fluid.

2. For individual selected refrigerants, their TSEs, the pressure drops and velocity distributions in relation to VT inlet temperature and pressure are to be fully analysed. The established CFD model together with the gas dynamics calculation (to be explained later, and also see Appendix 8.1) will be used to carry the following tasks.

- Preliminary screening of existing refrigerants for their potential suitability in either cooling or heating purpose based on their *T-s* profile. Identifying suitable fluid working conditions by analysing the flow through the nozzle using the gas dynamics theories, to further narrow down the fluid choices for VT applications.
- Simulating the TSE for the "chosen" refrigerants under the defined working conditions by CFD, and relating the TSE ranking with their physical-thermal properties, and fully evaluating their temperature and pressure variations within the VTs.

3. Matching the VT working conditions of different refrigerants with the system operating condition, involving the following.

- Defining the closed VT heating/cooling system configurations and relevant working conditions, identifying potential refrigerants applicable for the defined systems based on (2) above.
- Identifying the matching of the refrigerant choice and the required cooling/heating temperature under the system operating conditions for a given VT. This is followed by detailed CFD simulation to achieve any necessary re-dimensioning of the VT to match with the system requirements, or to assess the refrigerant performance.

3 Research Methodology

This chapter provides execution details of the tasks outlined in Section 2.6, and the associated procedures; all the corresponding results are presented in Chapters 4 to 6.

3.1 Setting up a VT simulation model

Generally, the CFD modelling process includes defining the appropriate geometry, choosing the "right" meshing number/density and selecting suitable turbulence models.

3.1.1 Defining an appropriate VT geometry (flow configuration and dimensions)

The chosen geometry is mainly based on the primary VT dimensions of Aljuwayhel et al[77], as they provide a comprehensive set of measured data suitable for validation, and at the same time their hot throttle is set up as an annular exit thus allowing the cold mass flow ratio be adjusted easily by changing the pressure. As in their work, a 2-D model is used with the primary dimensions given in Figure 3.1.

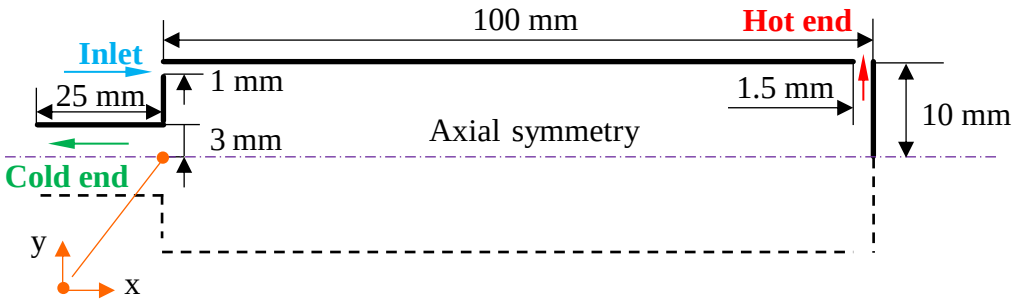

Figure 3.1 VT geometry and dimensions used in this project

Though a 3-D model which can define precisely specific VT structure/design, in terms of nozzle and hot end geometries, could be used, a 2-D model is employed to allow greater flexibility to make changes, such as nozzle exit flow direction, in the current research. This decision is supported by the observations that the TSE generated by 2-D model simulations have been found to match well with experimental results[101-104].

The axisymmetric swirl option (in the Ansys Fluent solver) is chosen to simulate the 3-D rotating flow, and under this option, the 2-D model is taken as a slice in the x-y plane, as shown in Figure 3.2.

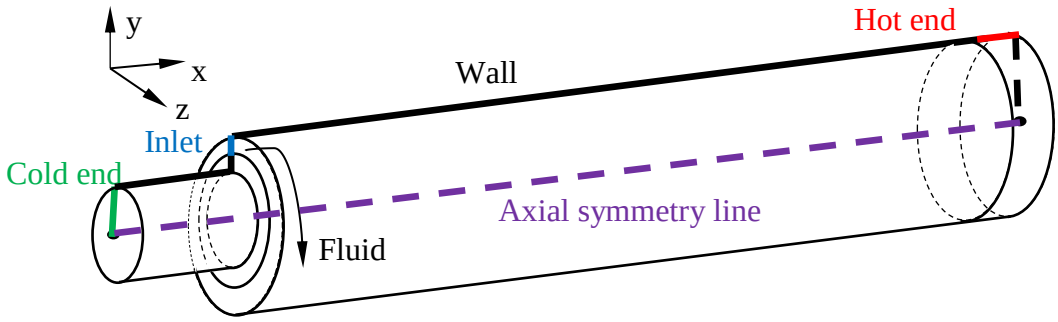

Figure 3.2 Isometric view of the VT model

The inlet geometry:

- As allowed in the axisymmetric 2-D model, an axial annular inlet is adopted to ensure that the required rotational flow and the inlet flow angle can be obtained/changed by specifying the axial, radial and tangential velocity components; this is equivalent to having the capability of designing the VT with different nozzle numbers, sizes, shapes and entry angles. It has also been reported that an axial annular inlet could improve the numerical stability, leading to relatively a quicker convergence, in the numerical simulation[77].

The cold end geometry:

- The length of the cold end is set at 25 mm which is different to that of Aljuwayhel et al[77] who set it at 0 mm for their CFD model. The 25 mm extension is needed in order to match the current model with their experimental set up in which a short length was added to allow temperature measurements. A similar extension was observed in Shamsoddini and Khorasani's[105] CFD work which has a similar geomety to Aljuwayhel et al's VT.

The hot end geometry:

- A radial annular outlet is employed, same as that of Aljuwayhel et al, though an axial one could be chosen too; the literature review reveals that there is not much difference in terms of CFD results between radial and axial annular outlets.

3.1.2 Selection of suitable meshing elements number and turbulence models

1) Definition of the terms used for assessing the VT performance

Several basic VT parameters are used to define the VT performance, as similarly used by other researches[1, 76, 106-108].

In VT research, instead of using static temperature, total temperature[1] is often chosen for defining the cooling effect, the heating effect or the total temperature difference, as high speed flow is involved.

The cooling effect ΔT_c is defined as the difference between the inlet fluid total temperature T_{in} and the cold end fluid total temperature T_c, i.e.

$$\Delta T_c = T_{in} - T_c \tag{3.1}$$

The heating effect ΔT_h is defined as the total temperature difference of the hot end fluid T_h and the inlet fluid T_{in}, i.e.

$$\Delta T_h = T_h - T_{in} \tag{3.2}$$

The total temperature separation effect ΔT_{hc} is defined as the total temperature difference of the hot end fluid T_h and the cold end fluid T_c, also equivalent to the sum of ΔT_h and ΔT_c, i.e.

$$\Delta T_{hc} = T_h - T_c \text{ or } \Delta T_h + \Delta T_c \tag{3.3}$$

The cold mass flow ratio μ_c is defined as the cold mass flow rate $\dot{m}_c$ divided by the inlet fluid mass flow rate $\dot{m}_{in}$.

$$\mu_c = \frac{\dot{m}_c}{\dot{m}_{in}} \tag{3.4}$$

2) The solver factors and boundary conditions

The solver factors and the boundary conditions of the Fluent simulation are given below.

The solver factors:

- The preliminary iteration using the first order upwind method[109] is employed to obtain the initial approximated results quickly, based on the default under-relax factors. The convergent target for continuity is set at 0.0001, and for the others, including x-velocity, y-velocity, swirl and energy are set at 0.00001.

- The primary iteration employing the second order upwind method[109] is used to obtain the final results. Lower than the default values of under-relax factors are then used to achieve a smaller convergent target.

The boundary conditions are set to match the experimental setup of Aljuwayhel et al's[77]:

- Inlet air mass flow rate 3.9 and 4.1 g/s and inlet total temperature 295 K
- Cold end at 1atm static pressure (absolute)
- Hot end static pressure: varied
- Cold mass flow ratio μ_c: 0.2 is used for meshing elements number investigation; 0.1 and 0.2 for turbulence model selection

3) Choosing the "right" meshing element number

The number of the meshing elements influences the simulation accuracy and time. The simulated VT parameters were compared when using different meshing elements numbers. The number was increased from 30 000 to 160 000 at an increment of 20 000.

4) Selection of suitable turbulence models

Various turbulence models have been compared and chosen by previous VT researchers[68, 77, 78, 80, 81, 84, 110-112]. The 5 turbulence models (*standard k-ε* model, *RNG k-ε* model with swirl option[7], *RNG k-ε* model without swirl option, *SST k-ω* model and *standard k-ω* turbulence model) are compared to assess their suitability for the current study. The results from different turbulence models (presented in Section 4.1.2) are compared to the experimental results of Aljuwayhel et al[77], and based on the comparison, the *standard k-ε* turbulence model is chosen for this study.

3.1.3 Qualitative comparison of the TSE predictions with other studies

In addition to air, CFD simulations are also carried for N_2, O_2, CO_2 and R134a, and the results are compared with those of others' experimental and numerical studies[19, 114, 115]. This is to assess if the established model can also be used for other fluids.

[7] Effects of swirl/rotation in *RNG* model of ANSYS Fluent can be represented by modifying the turbulent viscosity $\mu_t = \mu_{t0} f(\alpha_s, \Omega, k/\varepsilon)$[113]. μ_{t0} is turbulent viscosity calculated without swirl modification, and Ω is a characteristic swirl number evaluated within ANSYS Fluent. α_s is a swirl constant that assumes different values based on the flow: swirl-dominated or only mildly swirling, and set to 0.07 for mildly swirling flows (the default in ANSYS Fluent) while higher values are set for strong swirling flows.

The comparisons are mainly qualitative as exact matches of VT structures and working conditions with that of the published work cannot be achieved. To assess if the established model can predict reliably the trends, the comparison looks at the TSE and the velocity distributions within the VT, and in the case of R134a also the temperatures along the length of VT outside wall. CO_2 is included as it is identified as a possible candidate fluid for future applications in closed VT systems[100, 116], and R134a is a popular refrigerant in current refrigeration systems and suitable for use in developing the system integration procedure.

The predicted TSE trends of air, N_2 and O_2 are compared to the experimental results[19]. The boundary conditions are set as below.

- Inlet: 0.4 MPa, 295 K inlet total temperature
- The cold mass flow ratio from 0.1 to 0.9 (as adjusted by varying both the hot end and the cold end static pressure)

In addition, the simulated velocity distributions are qualitatively compared with the CFD results of Khazaei et al[114] who employed air, N_2, O_2 and CO_2; the tangential velocities in the y-z plane at x = 40 mm from the cold orifice are compared, based on the same x/Φ_{cham} ratio (= 2) as used Khazaei et al[114]. The boundary conditions are set as below.

- Inlet: 218.4 g/s, 297 K inlet total temperature
- Cold end: closed (as in [114])
- Hot end: 1 atm. static pressure (absolute)

For the VT wall temperatures, the experimental data for R134a[115] is obtained from a research collaborator (Refrigeration group, Institute of Refrigeration and Cryogenics, Zhejiang University, China). In the experiment, the VT has 6 straight tangential nozzles (0.95 × 0.2 mm) and the length of the hot tube and the cold end are 85 mm and 20 mm, respectively, while the diameters of the hot tube and the cold end are 6 mm and 3.5 mm, respectively. The VT inlet temperature is around 20 °C and the inlet pressure is controlled at 0.3 MPa. The mass flow rates at the VT inlet and the cold end are measured too. The CFD results of the flow temperatures at 0.001mm from the wall along the VT length are approximated as the wall temperatures. The boundary conditions are set as follow.

- Inlet: 0.3 MPa, 293.15 K inlet total temperature
- The cold mass flow ratio μ_c from 0.25 to 0.57 (as adjusted by varying both the hot end and the cold end static pressure)

Wall temperatures at 4 locations (Figure 3.3) are compared; they are chosen in order to keep the same ratios of the distance x_i (i = 1, 2, 3, 4) to the VT length L_{VT}, between the CFD and the experimental work.

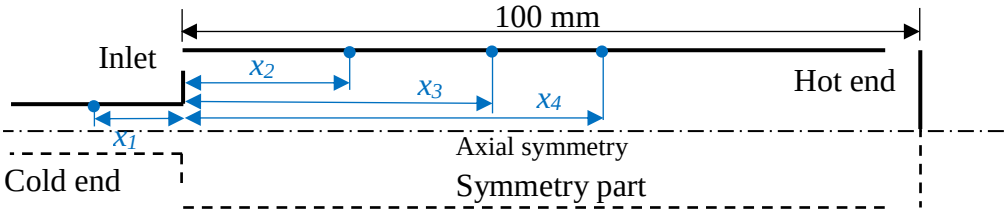

Figure 3.3 Schematic diagram showing the 4 compared positions
x_1 = -19 mm (-16 mm), x_2 = 21 mm (18 mm), x_3 = 40 mm (34 mm), x_4 = 59 mm (50 mm), L_{VT} = 100 mm (85 mm), the values in blankets represent the locations in the experiment

3.1.4 Influence of operating conditions on TSE

The influences of four operating conditions (the cold mass ratio μ_c, the inlet pressure p_{in}, the inlet mass flow rate $\dot{m}_{in}$ and the inlet temperature T_{in}) on the cooling and heating effect, the VT pressure drop, the temperature distributions and the velocity profiles are examined. Air, R134a and R600 (a natural fluid) are used as the working fluids, and R600 is included as it, being an environmental friendly refrigerant, has a great potential in the VT refrigeration applications.

For this part of the CFD work, the total pressure and total temperature are set as the boundary conditions in the Fluent solver; they are specified at the VT chamber inlet (i.e. the nozzle outlet), since it is not necessary to define the nozzle geometries in the 2-D model. In addition, this would allow relating the pressure and temperature directly to the nozzle inlet conditions since based on the isentropic flow assumption, the chamber inlet total pressure and temperature are in fact equal to the VT inlet ones which in terms have approximately the same values at the static pressure and temperature. Thus, the practical relevance is that assessing the effects of variations of chamber inlet total pressures and temperatures can be regarded as the same as looking at how system operating conditions influence the VT performance during system integration.

Unless otherwise stated, all the cold mass flow ratios are set between 0.1 to 0.9, by

adjusting the hot end static pressures p_h and cold end static pressures p_c.

1) Effect of the cold mass flow ratio μ_c

The boundary conditions:

- Inlet: 4.1 g/s inlet mass flow rate, 295 K (≈ 22 °C) inlet total temperature
- cold end: 1 atm. static pressure (absolute)

The following parameters are analysed: the cooling and heating effect, the temperature distribution, the chamber inlet velocities, the fluid streamlines, the velocity profiles and the pressure drop across the VT inlet and the cold/hot end.

2) Effect of the inlet pressure p_{in}

The boundary conditions:

- Inlet: 150 kPa - 300 kPa inlet total pressures, 295 K inlet total temperature

The following parameters are analysed: the cooling and heating effect, the temperature distribution, the pressure drops and the velocity profiles.

3) The effect of the inlet mass flow rate $\dot{m}_{in}$

The boundary conditions:

- Inlet: 4.1 g/s to 16.4 g/s inlet mass flow rates, 295 K inlet total temperature

The following parameters are analysed: the cooling and heating effects, the chamber inlet velocities and the pressure drops.

4) The effect of the inlet temperature T_{in}

The boundary conditions:

- Inlet: 4.1 g/s inlet mass flow rate, 280 K (≈ 7 °C) to 315 K (≈ 42 °C) inlet total temperatures
- Cold end: 1 atm. static pressure (absolute)
- The cold mass flow ratio: 0.3 for cooling, 0.7 for heating (as adjusted by varying the hot end static pressure)

The following parameters are analysed: the cooling and heating effects, and the chamber inlet velocities and the pressure drops.

3.2 Development of the refrigerant screening method for VT applications

Air and N_2 are commonly used in open VT systems and they have quite low critical temperatures, -140.3 °C and -147.0 °C respectively. Therefore, they are usually in a superheated state under the conditions that are likely to be encountered within a VT and have little chances to be liquefied when undergoing a temperature reduction process inside the VT. However, when considering the use of common refrigerants which typically have much higher critical temperatures, e.g. R134a: 101.06 °C, R600: 151.98 °C, they will have a chance of liquification inside the nozzle or inside the VT main body, depending on the operation conditions. As previously mentioned, liquid formation within the nozzle must be avoided as it would impair the VT performance as a temperature separation device[39, 50]. Therefore, an approach is proposed by the author to systematically assess the individual refrigerant whether liquification would occur in the nozzle and whether the refrigerant is likely to perform well for the intended heating or cooling purposes; 3 steps are involved, as presented in Sections 3.2.1 to 3.2.3.

3.2.1 Initial grouping refrigerants based on their *T*-*s* diagrams

Refrigerants are initially grouped to show the possible VT entry regions that could produce liquification in the nozzle or/and VT main body, and for their potential VT applications in cooling and heating. This grouping is then used to assist in establishing the approach to identify VT entry state, as described in Section 3.2.2.

The Step 1 involves examining the *T*-*s* diagram (or the saturated vapour entropy data as a function of temperature) of each individual refrigerant. Based on their *T*-*s* diagram, the refrigerants can be broadly divided into two groups.

One group is for the refrigerants that behave in such a way that the refrigerant could have more than 1 saturated temperature for a given entropy on the right hand side of the critical point. This corresponds to their *T*-*s* diagrams having both positive and negative gradients on the saturated vapour line, as shown in Figure 3.4a. On the other hand, when the line always has negative gradients, as shown in Figure 3.4b, they belong to the second group. In other words, for the second group, their saturated vapor entropy is increasing with decreasing temperature on the right hand side of the critical point. The refrigerants in the second group are likely to encounter liquification as they have a higher chance of entering the 2-phase zone during the temperature reduction

process within the VT. R134a is an example in this group. It is more likely that in the first group they stay in the superheated region, e.g. R600a.

In this study, various refrigerants in individual groups will be analysed thoroughly, including R227ea, R236fa, R245ca, R245fa, R218, R600 (natural fluid) and R600a (natural fluid) in Group 1, and R125, R134a, R143a, R152a, R290 (natural fluid), R32, R41, R717 (natural fluid) for Group 2.

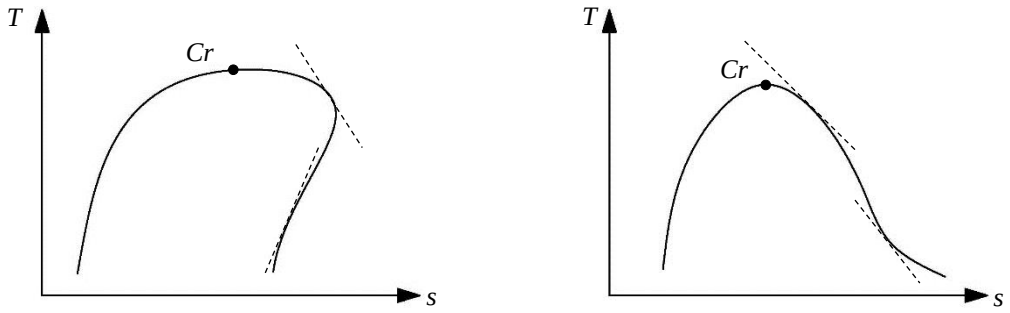

Figure 3.4 Sketch of refrigerants in two groups: Group 1 (a); Group 2 (b)

In order to identify what regions (on the *T-s* diagram) might be considered as suitable for the VT entry state, the diagram is divided into 3 regions, A, B & C, Figure 3.5a (for Group 1) and Figure 3.5b (for Group 2). Region A represents sub-cooled liquid; this region has little relevance for VT operation. B is the two-phase region, consisting of a mixture of saturated liquid and saturated vapour. C is the superheated region. As seen in Figure 3.5a, there is an inflection point *P*[8]. In addition, the saturated liquid and vapour lines themselves can also be treated as two individual sub-regions. For Group 1, Region C can be sub-divided into three areas, I, II and III. Sub-area I is bounded by the saturated vapour line, the vertical line passing through *P* and the critical pressure line (constant *Cr* pressure line). Sub-area II is on the right side of the vertical line passing through *P*. Sub-area III is below point *P*, and between the saturated vapour line and the vertical line passing through *P*.

[8] At this point, the rate of change of entropy with respect to the change in temperature (i.e. *dT/ds*) is equal to infinity

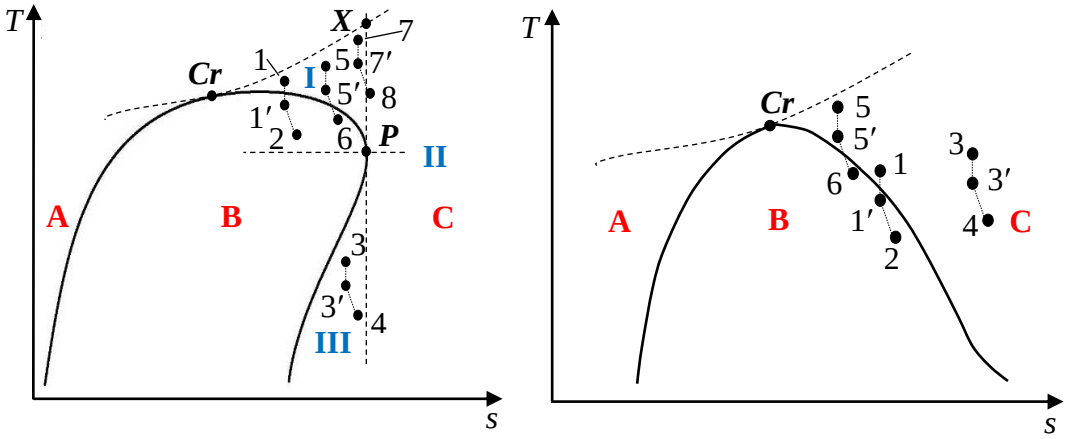

Figure 3.5 Regions in two groups and some possible flow processes from the VT nozzle entry to the cold end: (a) Group 1 and (b) Group 2 (Points 1, 3, 5 and 7 are the possible VT nozzle entry positions; Points 1′, 3′, 5′ and 7′ are respectively the possible VT nozzle outlet positions; Points 2, 4, 6 and 8 are respectively the fluid state at the cold end

In Group 1, when the refrigerant, at a state either on or close to the saturated vapour line, enters the nozzle from the Sub-area I (e.g. Point 1 and 5, Figure 3.5a), liquid formation may occur as the flow enters into region B (e.g. 1 to 2, and 5 to 6, Figure 3.5a). However, when the entry point is located in the Sub-areas II & III, then liquid formation within either the nozzle or in the VT main body is rather unlikely (e.g. 3 to 4, Figure 3.5a). It is useful to note that in certain locations within Sub-area I, though liquification inside the nozzle can be avoided (5 to 5′), it is still possible for it to occur in the cold end (5′ to 6).

On the other hand, for Group 2, the entry state to the nozzle could be at, say, location 1, 3 or 5, as shown in Figure 3.5b. Points 1 and 5 could be considered either on or close to the saturation line. Once again, the refrigerant could enter the 2-phase region, B, during its transit through the nozzle (1 - 1′, Figure 3.5b) or the main VT body towards the cold end (5′- 6, Figure 3.5b). However, if the entry point is moved further away from the saturation line into the superheated region C, such as location 3, then the VT should be able to operate without the presence of liquid either in the nozzle or in the VT main body.

Based on the above discussion, it can be concluded that:

- to purposely achieve a two-phase fluid at the cold exit for cooling purpose, as exemplified in Figure 2.19, for Group 1 refrigerants, the entry point must be located in the area I of region C and at the same time must avoid liquid

formation within the nozzle. For Group 2 refrigerants, the entry point should be close to the saturated vapour line in the region C, and also must ensure no liquid forms inside the nozzle.

- to ensure only vapour phase at the cold exit, as exemplified in Figure 2.22, for Group 1 refrigerants, the entry point should locate in the Sub-areas II & III of region C where liquid formation is not possible. When the entry point situates in the Sub-area I of C, liquid formation must be prevented inside both the nozzle and the VT main body (e.g. 7 to 8, Figure 3.5a) by adding a suitable degree of superheat. For Group 2 refrigerants, the entry point should be far away from the saturated vapour line to eliminate any possibilities of liquification in the VT.

Therefore, author is proposing that the refrigerant state point at the nozzle entry could be used as an initial selection criterion for their applications in VT.

3.2.2 Identifying appropriate refrigerants entry state points into the nozzle

In theory, if the entry point into a VT is moved far enough into the superheated region, no liquid formation is possible regardless which group the refrigerant belongs to. However, when integrating a VT into a system, the choices of entry state become much more restrictive, and they could potentially be near to the saturated temperatures/ pressures. Hence, it is essential to identify and quantify appropriate ranges of refrigerant entry state points. The Step 2 involves establishing the suitable refrigerants entry states, using strategies developed by the author based on the unique features of the two refrigerant groups as discussed above.

For Group 1 (shown in Figure 3.6), the procedures are as follows:

1) To note the critical point *Cr* (T_{cr} and p_{cr}), and the corresponding entropy s_{cr}. The critical point can be obtained from refrigerants property database (e.g. the software Refprop[117]) for a specific refrigerant.

2) To determine the inflection point *P* (T_p and p_p), and the corresponding entropy s_p. The inflection point *P* has the largest entropy on the saturated vapour line and can be located when decreasing the saturated temperature from the critical point T_{cr} to identify the turning point (the maximum point s_p) of the entropy.

3) To locate the interception point *X* (the intersection of the vertical line passing through *P* and the critical pressure line) ($s_x = s_p$ and $p_x = p_{cr}$). This enables the corresponding temperature T_x to be determined, which represents the maximum temperature allowed for Sub-area I operation.

4) To identify the superheated vapour state points between s_{cr} and s_p (in Sub-area I), which will result in no liquid formation within the nozzle. For any point located on the saturated vapour line, say point *O*, between inflection point *P* and the critical point, a certain degree of superheat (ΔT_{sh}) can be added to move the point into the superheated vapour Sub-area I along a constant pressure line. ΔT_{sh} must be less than a $\Delta T_{sh,max}$, above which the refrigerant enters the nozzle from the Sub-area II, and must be larger than a $\Delta T_{sh,min}$, below which liquid formation would occur in nozzle.

$\Delta T_{sh,max}$ is the temperature difference between point *M* and point *O*, while *M* is the interception point of the vertical line through *P* and the constant pressure line at *O*. $\Delta T_{sh,min}$ is determined by employing the gas dynamics calculations[9][118] based on a specified inlet gas velocity to the nozzle and the sonic condition (Mach number = 1, maximum speed for convergent nozzle) at nozzle exist, through gradually increasing the degree of superheat by a small increment (e.g. 0.1 °C at a time) along the constant pressure line until T_n is reached, where $T_n - T_o = \Delta T_{sh,min}$. The procedure is then repeated with another temperature on the saturated line between *Cr* and *P*, at say, a 5 °C interval. In Figure 3.6, point *F* represents the $\Delta T_{sh,min}$ corresponding to $T_{sat} = T_{cr}$, and *U* is taken as the lowest state point used to define the suitable region in terms of its saturation temperature. Having established the $\Delta T_{sh,min}$ and $\Delta T_{sh,max}$ for all the saturation points between *Cr* and *P*, a closed sub-area of I (denoted as Sub-area IV) can be created for individual refrigerant, in which only superheated vapour exits the nozzle to drive the VT.

The area on the right of the line FP (blue dotted line, Figure 3.6) and below the critical pressure line is considered suitable as the entry state for the VT, as well as all the state points on the right of the saturation vapour line below *P*. That is to say the line FU represents the boundary of the region, which the entry state points on its right are suitable to ensure dry nozzle operation. In the research, line FU is called the boundary line for Group 1 refrigerants.

[9] Procedure of gas dynamics calculations is presented in Appendix 8.1

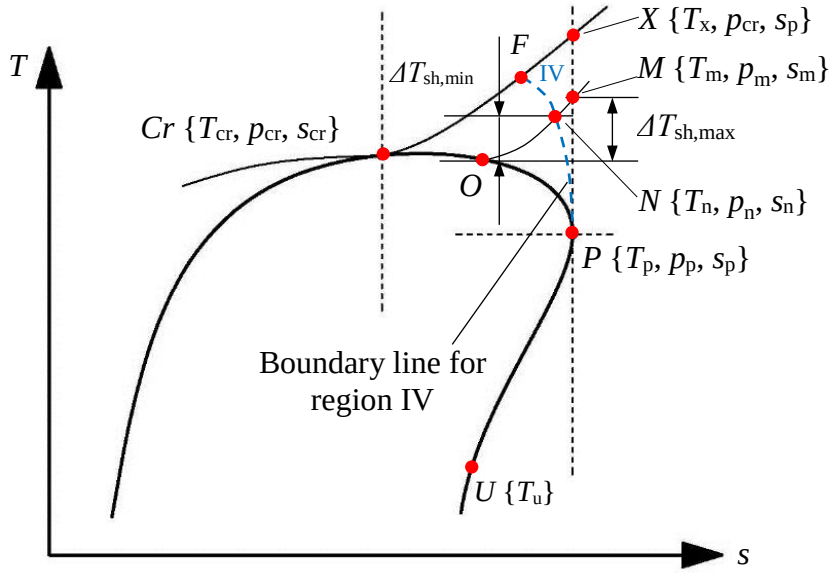

Figure 3.6 Key points (●) used for establishing the suitable VT entry regions for Group 1 refrigerants (It is to note that for a given refrigerant, the position of the FP line will shift according to the entry velocity)

Using refrigerant R600a to illustrate:

i. Noting the critical point *Cr*: T_{cr} = 134.66 °C, p_{cr} = 3.63 MPa, s_{cr} = 2.23 kJ/kg·K

ii. Determining the inflection point *P*: T_p = 107.79 °C, p_p = 2.29 MPa, s_p = 2.38 kJ/kg·K

iii. Deciding T_x = 137.34 °C ($p_x = p_{cr}$ = 3.63 MPa, $s_x = s_p$ = 2.38 kJ/kg·K)

iv. Identifying the $\Delta T_{sh,min}$ and the $\Delta T_{sh,max}$ (Table 3.1). The $\Delta T_{sh,min}$ is calculated based on 5 ~ 20 m/s VT inlet velocities.

Table 3.1 Identified superheated $\Delta T_{sh,min}$ and $\Delta T_{sh,max}$ corresponding to individual saturated temperatures for R600a

T_{sat}	p_{sat} (p_m)	T_m	$\Delta T_{sh,min}$	$\Delta T_{sh,max}$
°C	MPa	°C	°C	°C
134.66 (*Cr*)	3.63 (*Cr*)			
134	3.59	136.57	2.57	2.57
130	3.36	131.93	1.93	1.93
126	3.14	127.34	1.34	1.34
122	2.94	122.83	0.83	0.83
118	2.74	118.43	0.43	0.43
114	2.56	114.16	0.16	0.16
110	2.38	110.02	0.02	0.02
107.79 (*P*)	2.29	107.79	0.00	0.00

T_u is set at 20 °C (taken as the lower end of a typical condensing temperature range). The suitable region for the VT entry states to ensure dry nozzle operation for R600a is depicted in Figure 3.7.

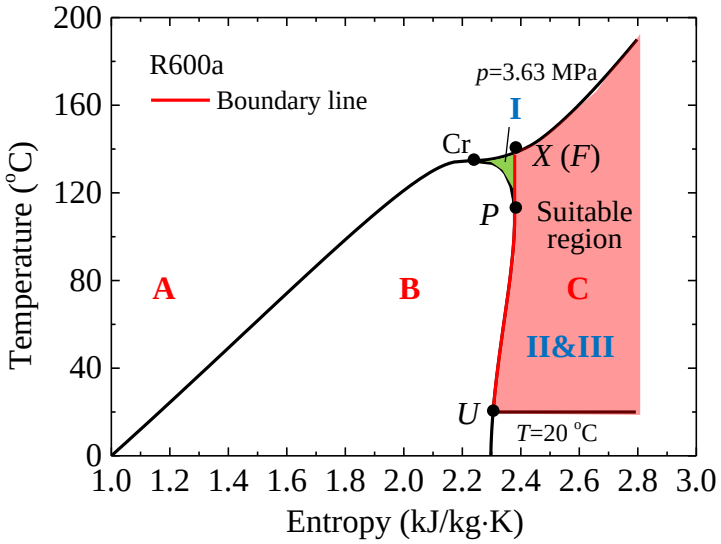

Figure 3.7 Suitable region for R600a based on Table 3.1

As shown in Table 3.1, for R600a, the $\Delta T_{sh,max}$ and the $\Delta T_{sh,min}$ are actually same, indicating the line FP coincide with line XP and the Sub-area IV in fact does not exist, meaning that if R600a enters the VT nozzle from this area at a velocity in the range of 5 ~ 20 m/s, there will be liquid formation within the nozzle. This is supported by the gas dynamics calculation which shows a more than 100 °C isentropic temperature drop will be encountered through the nozzle; this is larger than the maximum temperature drop in this area ($T_x - T_p$ = 31 °C), implying that R600a must be passing through the two phase zone when it flows inside the nozzle.

For Group 2 (Figure 3.8), the procedures are as follow:

1) As for Group 1, the critical point *Cr* (T_{cr} and p_{cr}) and the corresponding entropy s_c are noted.

2) To determine the boundary line FDS, as in Step 4 for Group 1 refrigerants, for any points on the saturated vapour line below the critical point *Cr*, say point *O*, gas dynamics calculations are used to determine the $\Delta T_{sh,min}$. DS is the state point corresponds to adding a $\Delta T_{sh,min}$ to T_u. This procedure is repeated for other saturated temperatures between T_{cr} and T_u (= 20 °C). As before, the state points for different $\Delta T_{sh,min}$ are then joined together to form the boundary line FDS. Other boundary lines

could be obtained for different entry velocities. The right hand side of the boundary line is considered to be suitable for "dry" nozzle operation.

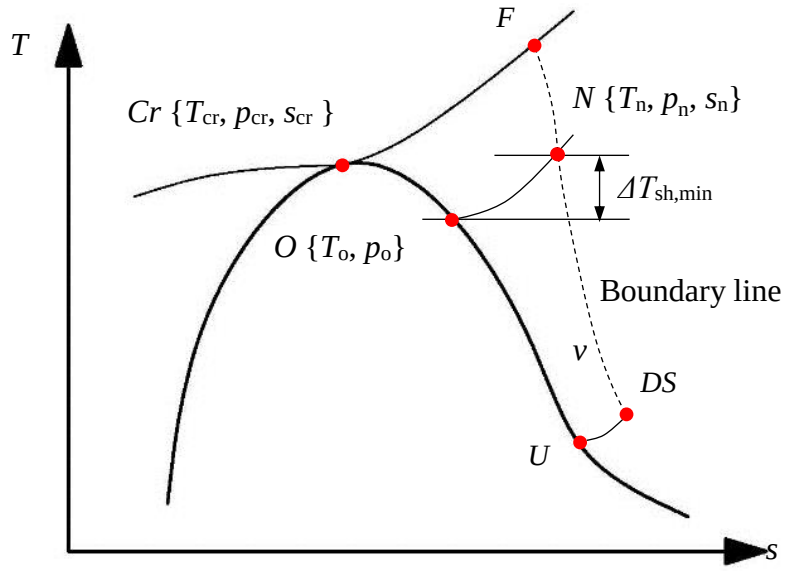

Figure 3.8 Key points (●) used for establishing the suitable VT entry regions (or the boundary line) for Group 2 refrigerants at a given VT inlet velocity v

R134a with an entry velocity of 10 m/s at the nozzle inlet is used to illustrate the procedure.

i. Noting the critical point *Cr*: T_{cr} = 101.06 °C, p_{cr} = 4.06 MPa, s_{cr} = 1.55 kJ/kg·K

ii. Establishing the boundary line FDS: the selected saturated point *O* decreases from 100 °C (chosen as it is just below the *Cr*) to 20 °C at a decrement of 5 °C. The degree of superheat added to the point *O* is increased at a 0.1 °C increment. Employing the gas dynamics calculations, the nozzle outlet states, L for liquid and V for vapour, are shown in Table 3.2, and the corresponding boundary line is presented in Figure 3.9. For instance, at T_{sat} = 90 °C and $\Delta T_{sh,min}$ = 7.2 °C, the nozzle exist state is still liquid until $\Delta T_{sh,min}$ reaches 8.2 °C. When T_{sat} is lowered, the required $\Delta T_{sh,min}$ generally decreases. Though it is observed that at T_{sat} below 25 °C, the required $\Delta T_{sh,min}$ starts to increase again. This is related to the gradient of the saturated line and this observation can also be made for a few other refrigerants. This observation is technically insignificant as its influence of the actual positions of the state points on the boundary line is minimal.

Table 3.2 States of R134a at the nozzle outlet for different inlet conditions (V-Vapour, L-Liquid)

T_{sat} °C	p_{sat} MPa	$\Delta T_{sh,min}$ °C											
		3.1	3.2	3.4	3.6	4.0	4.4	4.9	5.6	6.3	7.2	8.2	9.3	10.4
100	3.97	--	--	--	--	--	--	--	--	--	--	--	L	V
95	3.59	--	--	--	--	--	--	--	--	--	--	L	V	--
90	3.24	--	--	--	--	--	--	--	--	--	L	V	--	--
85	2.93	--	--	--	--	--	--	--	--	L	V	--	--	--
80	2.63	--	--	--	--	--	--	--	L	V	--	--	--	--
75	2.36	--	--	--	--	--	--	L	V	--	--	--	--	--
70	2.12	--	--	--	--	--	L	V	--	--	--	--	--	--
65	1.89	--	--	--	--	L	V	--	--	--	--	--	--	--
60	1.68	--	--	--	L	V	--	--	--	--	--	--	--	--
55	1.49	--	--	L	V	--	--	--	--	--	--	--	--	--
50	1.32	--	L	V	--	--	--	--	--	--	--	--	--	--
45	1.16	L	V	--	--	--	--	--	--	--	--	--	--	--
40	1.02	V	--	--	--	--	--	--	--	--	--	--	--	--
35	0.89	V	--	--	--	--	--	--	--	--	--	--	--	--
30	0.77	V	--	--	--	--	--	--	--	--	--	--	--	--
25	0.67	V	--	--	--	--	--	--	--	--	--	--	--	--
20	0.57	L	V	--	--	--	--	--	--	--	--	--	--	--

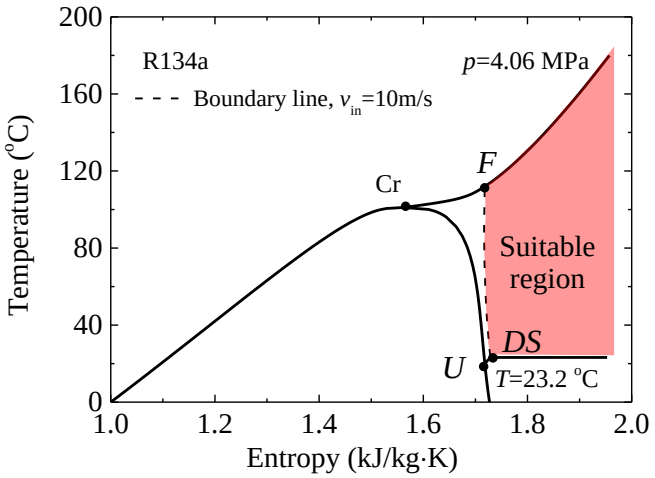

Figure 3.9 Suitable region at a nozzle inlet velocity of 10m/s for R134a based on Table 3.2

With the procedures established for identifying the suitable nozzle entry region (or the position of the boundary), one can now determine if a given state point is able to achieve a dry nozzle operation. The process is summarised in Figure 3.10 which also highlights the key differences in terms of the application of the procedures between Group 1 and Group 2 refrigerants.

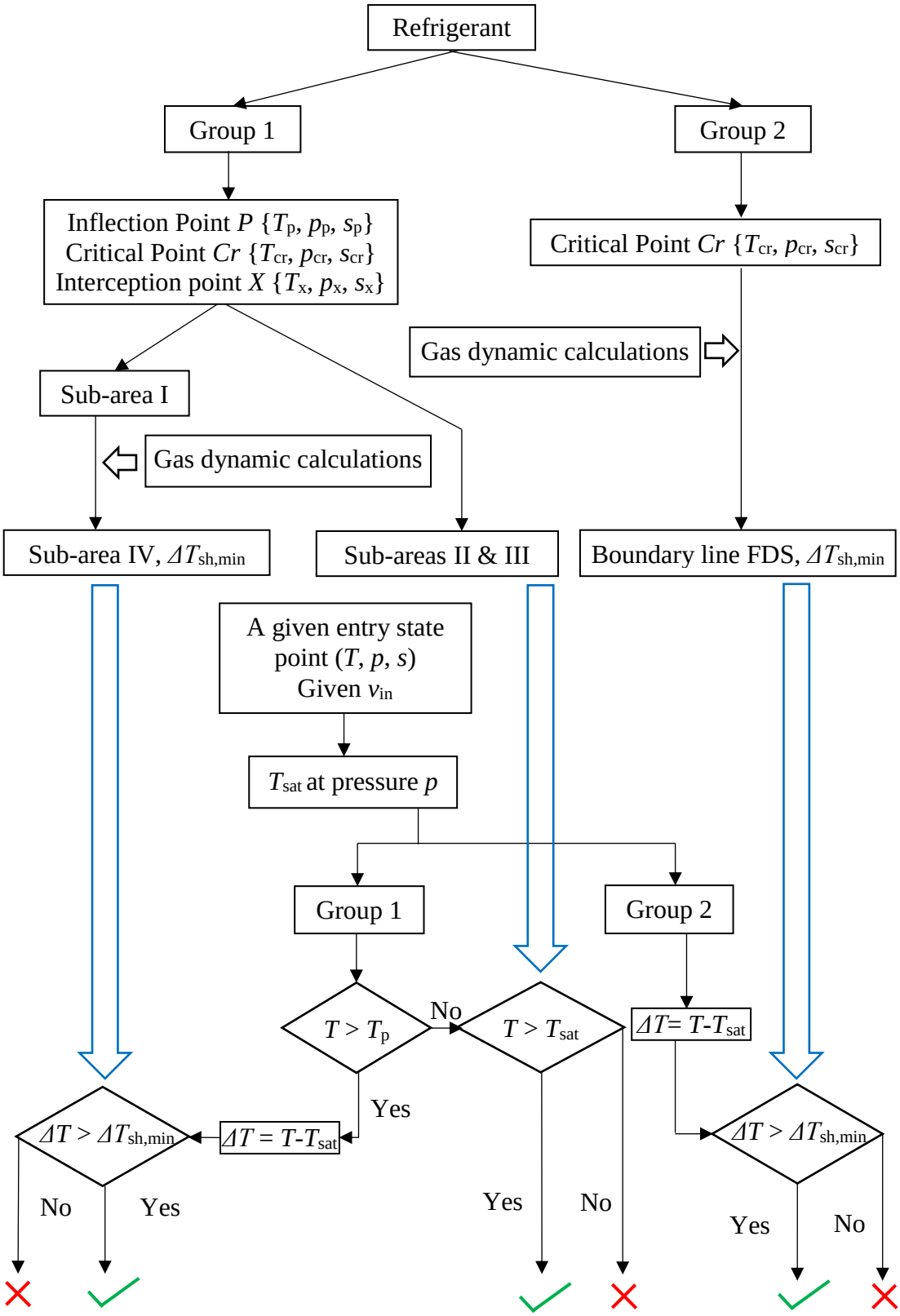

Figure 3.10 Procedure logic for determining if liquid formation is to occur in the VT nozzle (A cross represents the chosen entry state point is not able to achieve a dry nozzle operation)

3.2.3 Further sub-grouping of the refrigerants and examining their thermal behaviour in VT

The Steps presented in Sections 3.2.1 and 3.2.2 are mainly to establish the suitable superheated region for the entering T_{in} and p_{in} on the *T-s* diagram of individual refrigerants to ensure "dry" operation within the nozzle. Qualitatively, for each refrigerant, the region is essentially bounded by (i) the constant critical pressure line, (ii) the established boundary line and (iii) a defined temperature line depending on the applications (e.g. a temperature at the low end of the cooler temperature range). However, quantitatively the actual temperature and pressure values associated with this region vary among refrigerants. Therefore, in order to compare the refrigerant choices for their VT performance, they need to be first grouped under the same pressure and temperature conditions and assessed accordingly. This section presents a simple grouping procedure, involving two simple steps.

1) Transferring the working region from the *T-s* diagram to the *T-p* diagram

In practice, to match the VT characteristics with system operation, temperature and pressure are usually the chosen parameters for setting up the VT entry conditions during system integration. It is thus logical to transpose the superheated region from a *T-s* diagram onto a *T-p* diagram, as sketched in Figure 3.11. The vertical green dash line corresponds to the constant critical pressure line and the blue horizontal dash line represents the defined start temperature line, labelled as T_{ds} (for Group 1, $T_{ds} = T_u$). Figure 3.12a and b show the actual position of the suitable superheated regions for R600a and R134a on the *T-p* diagram, respectively, which are used in the previous illustration on the *T-s* diagrams in respectively Figure 3.7 and Figure 3.9.

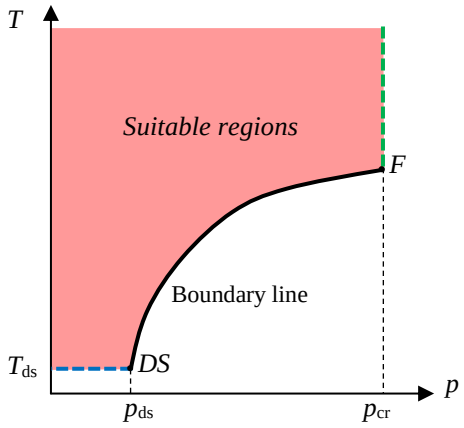

Figure 3.11 Suitable enrty state regions based on a *T-p* diagram

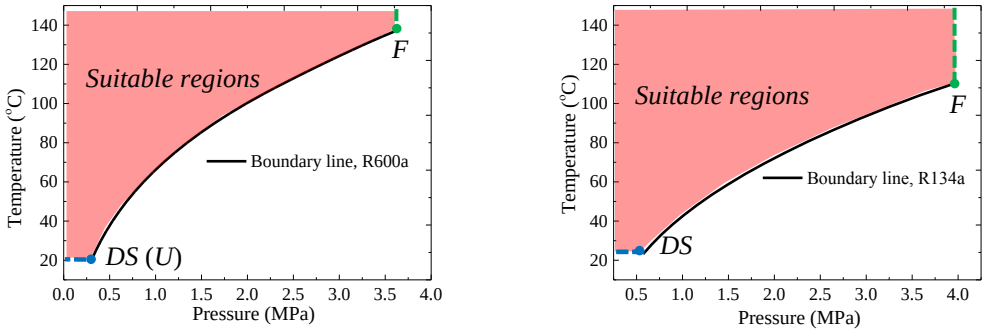

a b

Figure 3.12 Suitable regions based on the *T-p* diagram for R600a (a), R134a (b)

2) Sub-grouping of refrigerants according to the working pressures and temperatures

The refrigerant choices are then put on the same *T-p* diagram, and the grouping is mainly based on the chosen design pressure and temperature. To illustrate, 6 fictitious refrigerants ($Ref_{1,\ldots,6}$) are put on a *T-p* diagram in Figure 3.13. Taking a design temperature of T_a and pressure of p_{a1}, this state point falls in the over-lapping region of all the 6 refrigerants and they can therefore be grouped together for further evaluations; on the other hand, for the same temperature but at a different pressure of say p_{a2}, only Ref_4, Ref_5 and Ref_6 are grouped together and they will be evaluated between p_5 and p_7. At a different design value of T_b and p_{b1}, the group then consists of Ref_1, Ref_2, Ref_3, and Ref_5. For another unique combination of T_b and p_{b2}, only Ref_5 is involved so no comparison under similar conditions is possible. The grouping examples are summarised in Table 3.3 which also show that depending on the conditions, the numbers of refrigerants in individual groups vary.

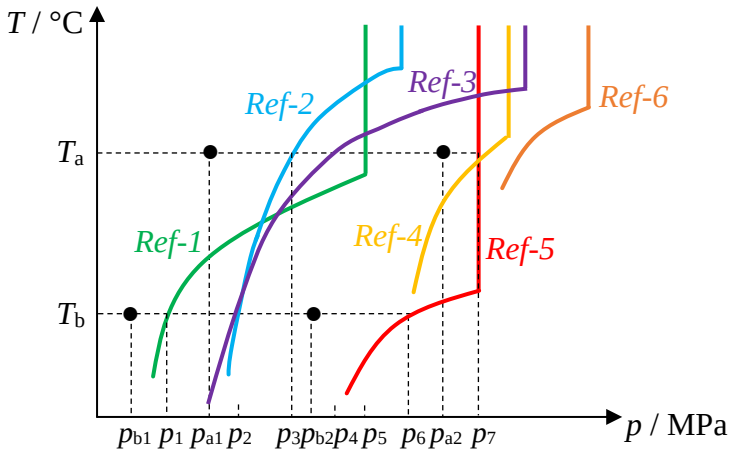

Figure 3.13 Boundary lines of six fictitious refrigerants on the *T-p* diagram (*Ref* - refrigerant)

Table 3.3 Possible sub-grouping of six fictitious refrigerants, for their evaluation under different working conditions

Sub-groups	T_{in}	p_{in}	Refrigerants
***	T_a	$< p_3$	*Ref-1, Ref-2, Ref-3, Ref-4, Ref-5, Ref-6*
	T_a	p_5~p_7	*Ref-4, Ref-5, Ref-6*
	T_b	$< p_1$	*Ref-1, Ref-2, Ref-3, Ref-5*
	T_b	p_2~p_6	*Ref-5*

Once the refrigerants have been selected for a group according to the design conditions, they can be systematically subject to a parametric evaluation/comparison of their TSE, using the defined 2-D VT model in Section 3.1.1 and following the procedures as presented in Section 3.1.4. In the evaluation, two temperature ranges are of particular practical relevance, i.e. 30 to 40 °C and 60 to 75 °C; the refrigerants evaluated in the former could be considered for either cooling or heating applications whereas the latter is mainly for consideration in heating applications.

The thermal properties of refrigerants will also be examined to correlate their influence on the cooling/heating effect. Properties to be analysed include the thermal diffusivity, the kinematic viscosity, the density, the J-T coefficient and the isentropic expansion exponent (results to be present and discussed in Chapter 5).

3.3 Coupling the VT working requirements of different refrigerants with the system operating conditions

3.3.1 Specifying thermal systems

It must first be emphasised that it is not the objective of this research to create new closed VT systems or to improve the efficiency of any thermal systems by considering to incorporate a VT in them. Instead two published systems are used to illustrate the application and effectiveness of the proposed coupling procedures (present in next section). A simplified compressor system for cooling from Nellis and Klein[26] and a liquid pump system[94] for heating are chosen, as shown respectively in Figure 3.14 and Figure 3.16.

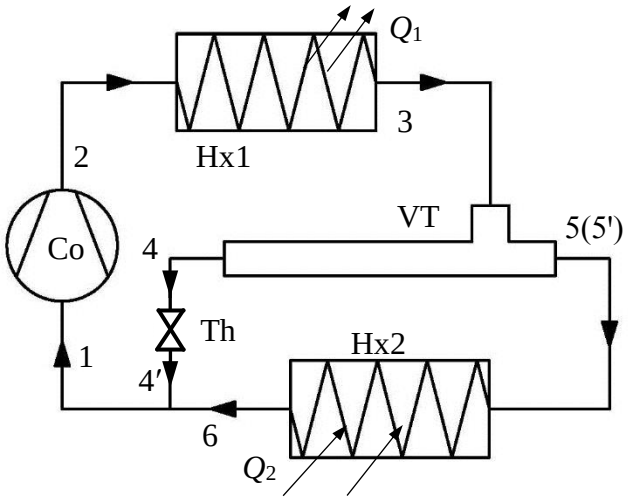

Figure 3.14 Schematic diagram of a closed VT compressor cooling system (Co-Compressor; Hx1, Hx2- Heat exchanger; Th-Throttle, VT- Vortex tube)[26]

In the closed compressor system, the compressor raises both the pressure and temperature of the refrigerant vapour, from point 1, and the heat energy is then rejected from the hot vapour in the heat exchanger 1 to, say, the environment (point 2 to 3). The high pressure vapour, from point 3, throttles to cold vapour stream 5 (5′ refers to liquid phase exit), providing the required cooling duty in the heat exchanger 2, and reaches the point 6; it then mixes with the hot stream (4′) and the cycle repeats at the compressor intake. A throttle Th is placed after the hot end as the hot end pressure always has a higher pressure than the cold end.

For this closed compressor system, several cycle positions on the *T-s* diagram are possible (Figure 3.15) depending on the refrigerant choices and system operating conditions, and 4 different scenarios, two for Group 1 refrigerants (one of which can be further divided into 3 sub-scenarios) and two for Group 2 refrigerants.

As shown in Figure 3.15, for Group 1 refrigerants, there are three sub-scenarios (a1 - a3) representing respectively when refrigerant is cooled in the heat exchanger (Hx1) to enter the VT as, (a1) saturated vapour below the inflection point *P*, (a2) superheated vapour in regions II or III, or (a3) in Sub-area IV. All these three sub-scenarios have no liquid formation at the cold end. For the second scenario (b) for Group 1 refrigerants, the refrigerant enters the VT as superheated vapour in Sub-area IV, then exits the cold end as a two-phase mixture of saturated liquid (5′) and saturated vapour (5). For Group 2 refrigerants, scenario (c) represents the situation that liquid formation occurs at the cold end (5′), whereas the entry point 3 could be located in such a way that the VT is running "dry" as shown in (d).

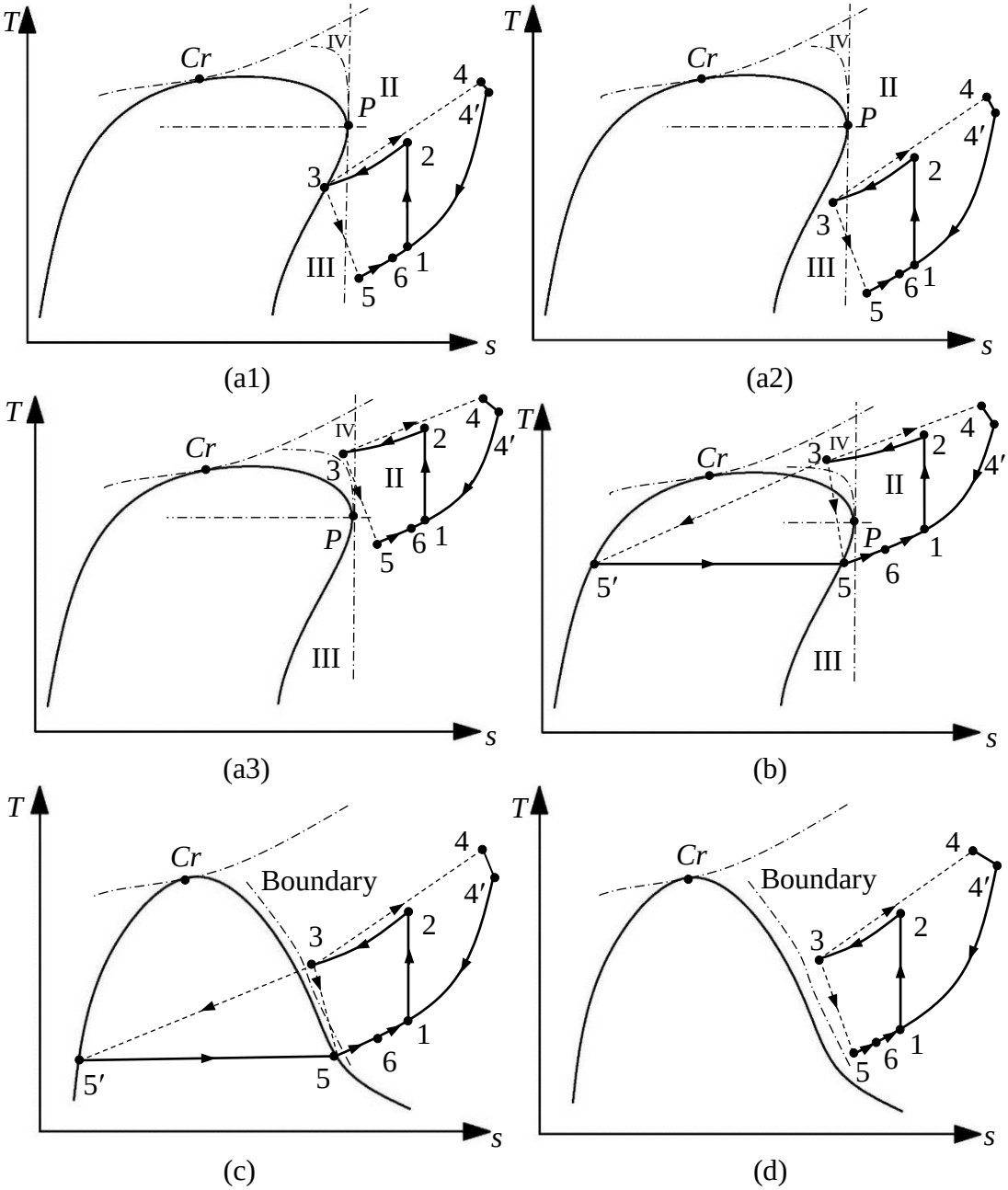

Figure 3.15 Possible cycle positions of the VT compressor cooling system. The numbers correspond to the state points in Figure 3.14

For the liquid pump VT heating system (Figure 3.16), a low pressure liquid (point 1) is pumped into the boiler where it receives waste heat. The high pressure vapour enters the VT (point 4) and the hot stream (point 5) provides the heating function in the heat exchanger, and it then passes the expansion valve and mixes with the cold stream (point 6) before entering the condenser.

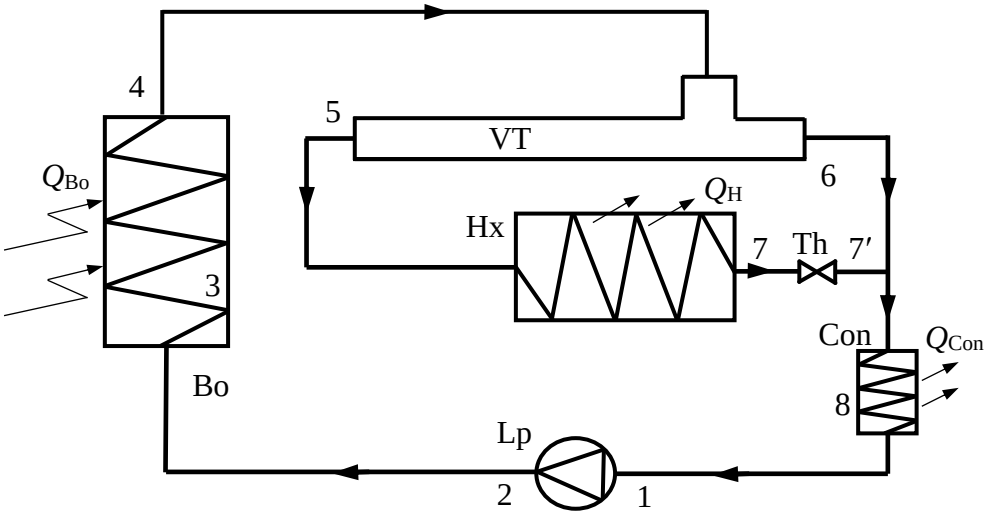

Figure 3.16 Schematic diagram of the closed liquid-pump VT heating system[94] (Lp-Liquid pump, Bo-Boiler, Con-Condenser, Hx-Heat exchanger, Th-Throttle, VT-Vortex tube)

All the possible cycle scenarios, two for Group 1 refrigerants (again one of the scenarios could be sub-divided into 3 sub-scenarios, a1, a2 and a3) and two for Group 2 refrigerants, need to be identified to aid the development of the coupling method. As shown in Figure 3.17, for Group 1, the refrigerant enters the VT (point 4), either as a saturated (a1) or superheated vapour (a2 and a3); in scenario (b), the superheated vapour in Sub-area I enters the VT, accompanied by the liquification at the cold end. For Group 2 refrigerants, scenarios (c) and (d) represent respectively the situation with and without liquid formation within the VT.

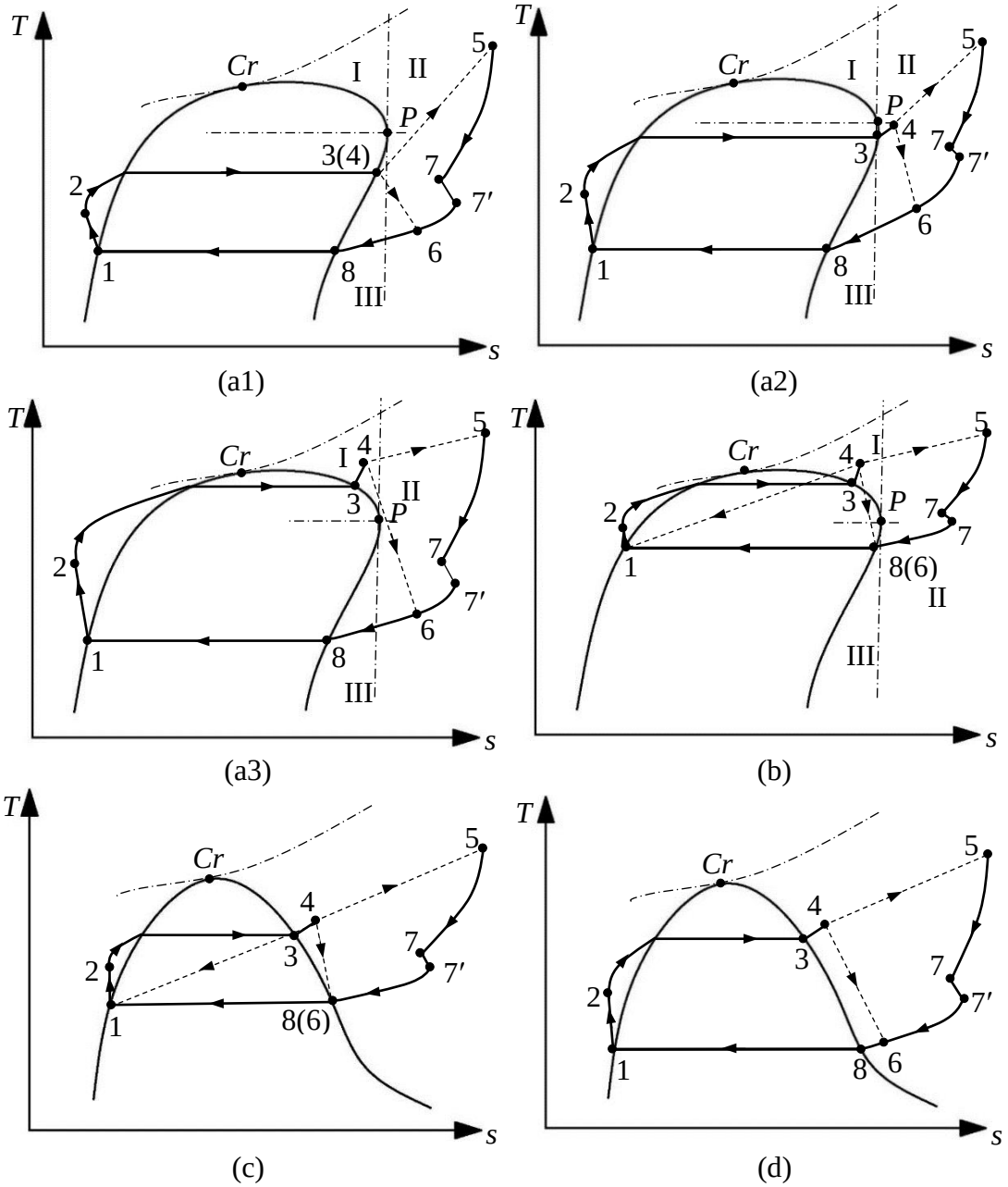

Figure 3.17 Possible cycle positions in the VT liquid pump heating system. The numbers correspond to the state points in Figure 3.16

A unique feature of this heating system must be pointed out, i.e. both the VT cold end pressure and nozzle inlet pressure must be defined, implying that the entry point to the nozzle could be on either side of the boundary line; in other words the boundary concept needs not be applied here, hence the line is not shown at all. However, for other heating systems, it may be necessary to apply the boundary line concept when the VT inlet pressure is initially unknown.

For illustration purpose, both systems are specified to operate under typical refrigeration or heating conditions. In the cooling system, the exit temperature of Hx2

(T_6) is specified at between -5 °C and 15 °C, and the Hx1 outlet temperature (T_3) is specified at between 20 °C and 40 °C. In the heating system, the heat exchanger exit (T_7) is specified at between 80 °C and 100 °C, the condensing temperature (T_8) is controlled at between 20 °C and 30 °C, and boiler outlet/VT inlet temperature (T_4) is specified at between 60 °C and 80 °C. The system operating pressures are governed by the choice of the refrigerant and the system operating temperatures, as will be discussed next.

3.3.2 Coupling of the specified closed systems with refrigerants for a given VT

For a VT, the cooling or heating effect is strongly dependent of its inlet and outlet pressures which must be matched with the system operation requirement for a given refrigerant. Therefore, the coupling of a VT with a system essentially aims at identifying the suitable pressures at certain defined temperature ranges; the coupling process also involve re-dimensioning of VT, if needed, to deliver the specified cooling or heating effect. Optimization can be achieved by switching refrigerants if necessary.

Out of the six scenarios and sub-scenarios for each of the two systems, only three for each them (Figure 3.15a1, a3 and d, and Figure 3.17a1, a3 and d) need to be considered, as the coupling procedures can be adapted and outcome applied to the other three. They are re-drawn respectively in Figure 3.18i, ii, and iii, and Figure 3.20i, ii and iii, showing the key state points of the two systems on the *T-s* diagram, particularly showing the application of the boundary line for the cooling system.

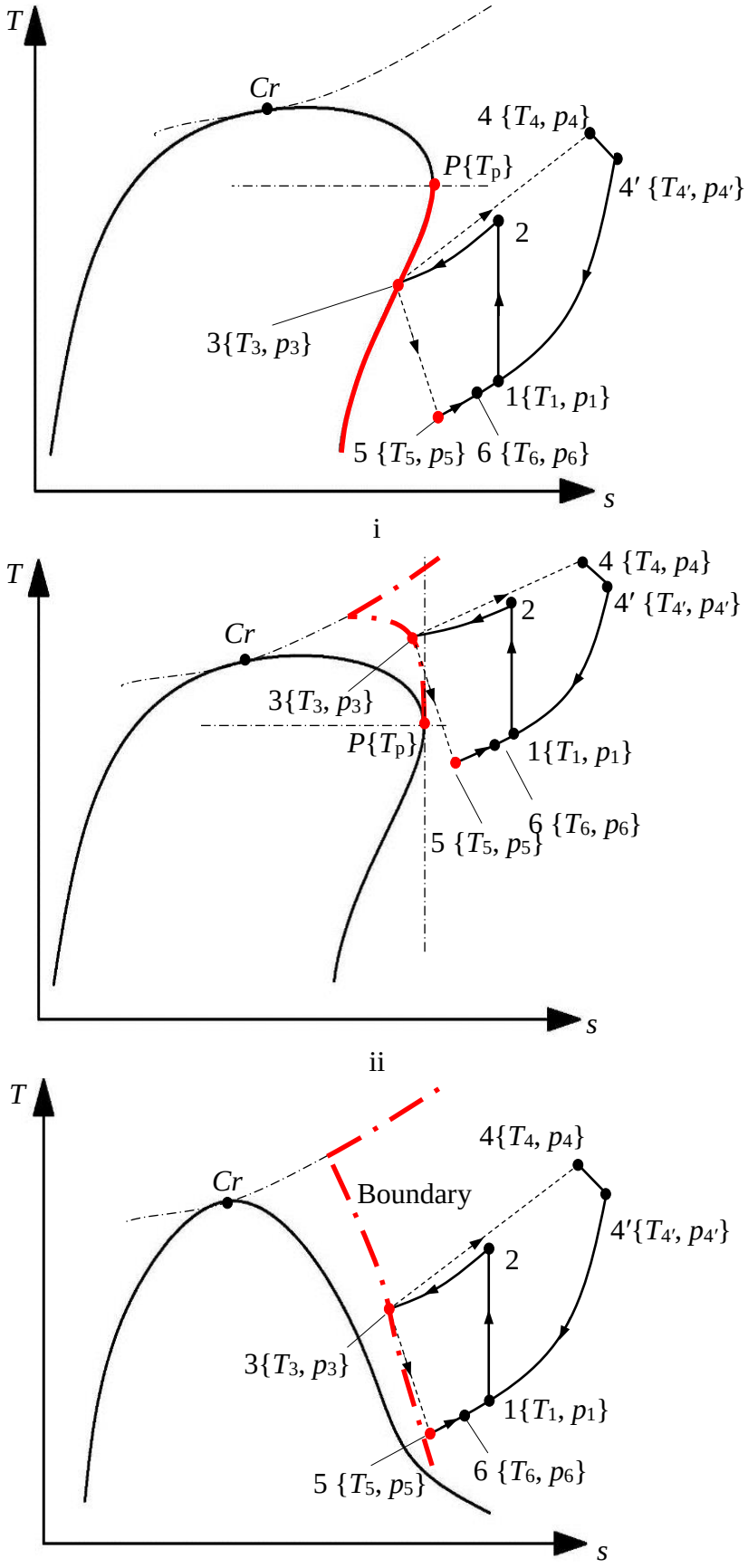

Figure 3.18 Key state points (●) and the boundary lines used in the coupling process for the defined cooling system

The Cooling System

Preliminary observations based on the CFD results show that, for a given refrigerant and a VT inlet temperature, a higher chamber inlet velocity would lead to a larger cooling effect. Therefore, a key assumption is made prior to start of the procedures, i.e. the refrigerant velocity at the VT nozzle outlet is assumed to be at the sonic speed or choked, which is the maximum speed possible for a convergent nozzle. Also it should be noted that for the cooling system, the VT inlet and outlet pressures are initially unknown. The proposed coupling procedures are as follows:

1. Locate the VT inlet state (T_3, p_3) on the *T-s* diagram

As noticed from the preliminary CFD runs, at a constant pressure, a higher VT inlet temperature (within the range of 20 to 40 °C) would lead to only little changes in cooling effect. On the other hand, a higher VT inlet pressure would generate a bigger cooling effect when the inlet temperature is kept constant. Accordingly, for any chosen temperature T_3 in the range of 20 to 40 °C, the corresponding pressure p_3 can only be chosen at a point either on the boundary line or close to the critical pressure line[10].

For a Group 1 refrigerant, if T_3 is smaller than the T_p, as represented in Figure 3.18i, p_3 is taken as the saturated pressure at T_3. On the other hand, if T_3 is larger than the T_p, as seen in Figure 3.18ii, p_3 is taken as the pressure of the point either on the boundary line or close to the critical pressure line. Figure 3.18iii presents the situation for a Group 2 refrigerant, and p_3 is the pressure of the point either on the boundary line or again close to the critical pressure line.

2. Calculate the total temperature and total pressure of the refrigerant at the VT inlet

The total temperature $T_{3\text{-total}}$ and pressure $p_{3\text{-total}}$, as required in the CFD simulation, can be determined by employing basic gas dynamics calculations, using the static temperature (T_3), pressure (p_3) and a specified refrigerant velocity at the nozzle inlet.

3. Obtain the required VT cold end temperature T_c

The VT cold end temperature T_c (obtained by the CFD simulation) is to match with the required Hx2 exit temperature T_6 (*Note*: the specified design Hx2 exit temperature T_6 is previously set between -5 to 15 °C). If T_c is lower than T_6, the coupling is

[10] The position on these lines has the largest pressure at a constant temperature

considered successful, otherwise the chosen VT must be changed and/or an alternative refrigerant should be considered. The details of changing the VT dimensions and switching the refrigerants are introduced in Chapter 6 based on the understanding of the influence of fluid properties and of the development of velocity fields in the VT.

To show the method clearly, the full procedure is summarised in Figure 3.19.

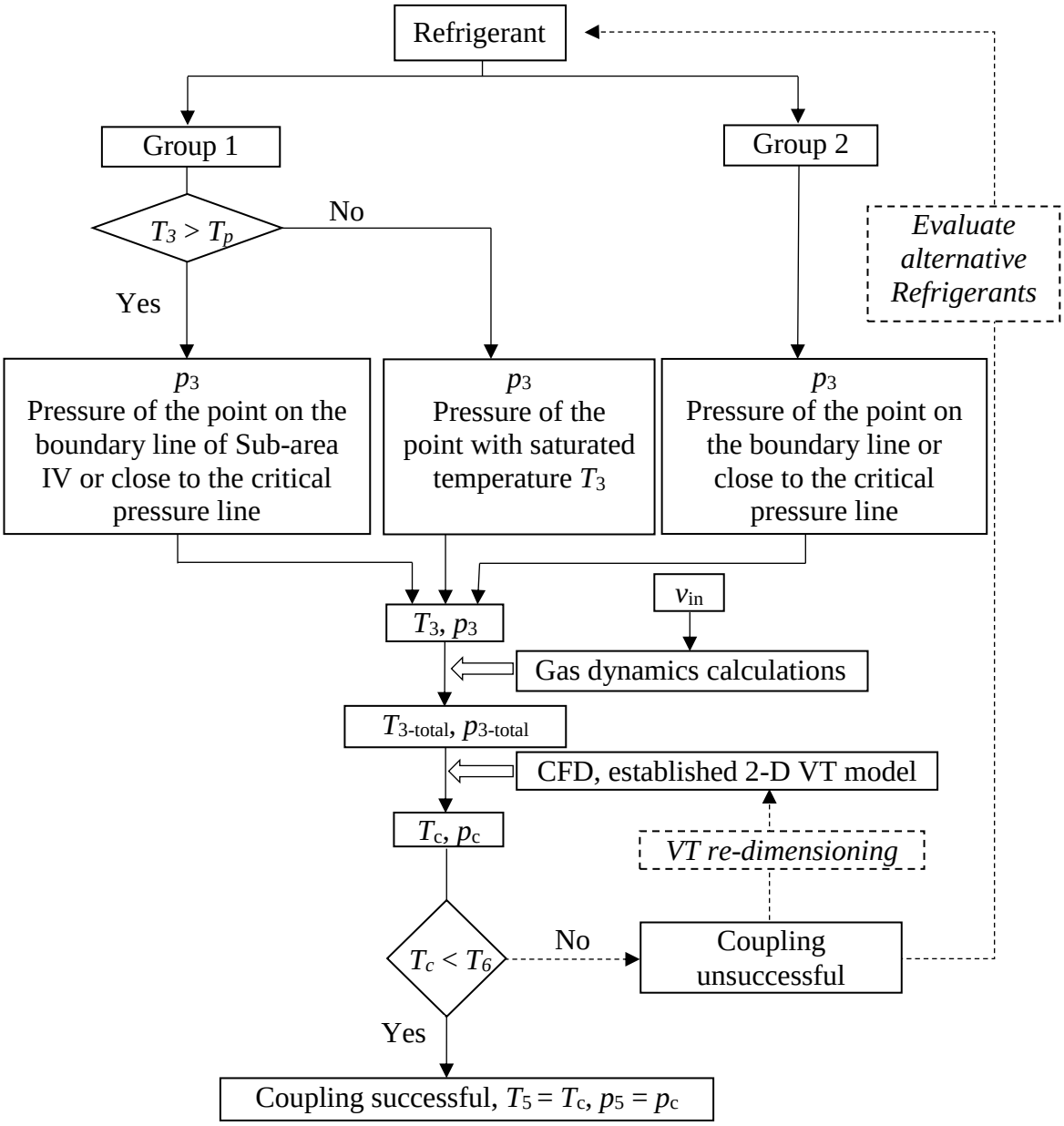

Figure 3.19 Procedure of coupling the cooling system with the refrigerant for a given VT

The Heating System

In the liquid-pump VT heating system, (Figure 3.16), the VT cold end pressure is governed by the condensing temperature and the VT inlet conditions are controlled by the varying heat input to (or temperature of) the boiler.

Preliminary CFD results show that the heating effect would be the largest when the inlet pressure reaches certain values, above which further increases of pressure will lead to a larger temperature drop between the VT inlet and hot end, resulting in a smaller heating effect. In addition, at a constant VT inlet pressure, a larger degree of vapour superheat always leads to a bigger heating effect. Therefore, the key is to determine the combination of VT inlet pressure and its corresponding degree of vapour superheat which will deliver the largest heating effect and whether this meets the design heating requirement. The procedures to identify this combination are presented in Figure 3.20 and described as follows.

1. Identify the VT inlet pressure value (p_4) and its corresponding degree of super heat (ΔT_{sh}) for a specified VT inlet temperature within the range of T_4 (= 60 °C ~ 80 °C).

For a specified T_4, the pressure p_4 is known if the degree of the superheat, ΔT_{sh} (= T_4 – T_3), is specified too, where T_3 is the saturated temperature at p_3 which has in fact the same value as p_4. For either a Group 1 or Group 2 refrigerant, the degree of superheat ($\Delta T_{sh,i}$) can be systematically and decrementally adjusted, giving $T_{3,i} = T_4 - \Delta T_{sh,i}$ (i = 1, 2⋯n), as shown in Figure 3.21 and $\Delta T_{sh,i}$ should be no larger than $T_4 - T_8$.

2. Calculate the total temperature and pressure of the refrigerant at the VT inlet, procedures similar to Step 2 in the cooling system are implemented.

3. Obtain the required VT hot end temperature $T_{h,\,i-1}$.

The $T_{h,i-1}$ (obtained by the CFD simulation) is to match with the required Hx exit temperature (T_7) (*Note*: the desired heating temperature range is 80 ~ 100 °C). If $T_{h,i}$ is smaller than $T_{h,i-1}$, $T_{h,i-1}$ is taken as the largest possible heating temperature. The $T_{h,i-1}$ is checked against the required Hx exit temperature (T_7), and if $T_{h,i-1} > T_7$, the coupling is considered successful, otherwise changes in the VT dimensions and alternative refrigerants should be considered. The full algorithm is summarised in Figure 3.21.

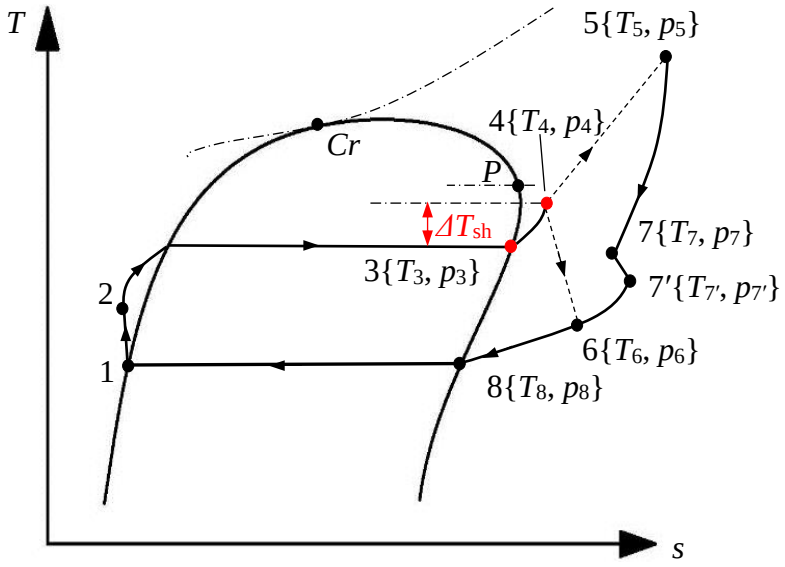

i

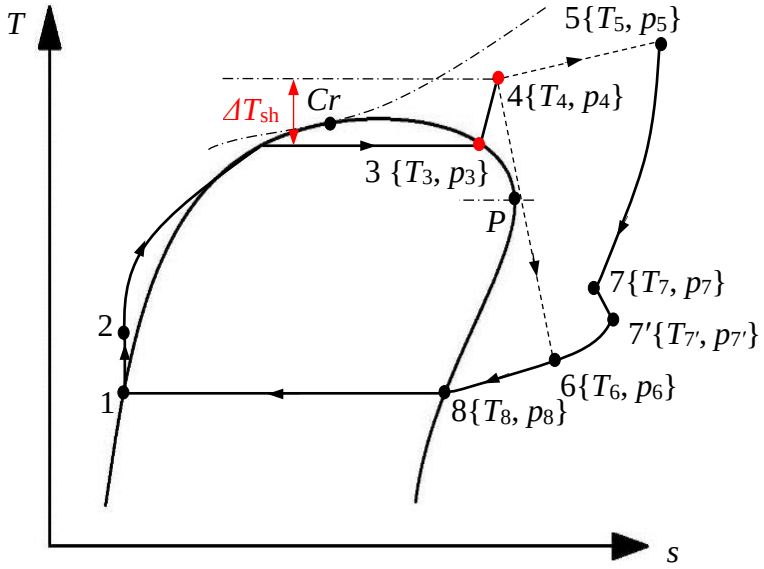

ii

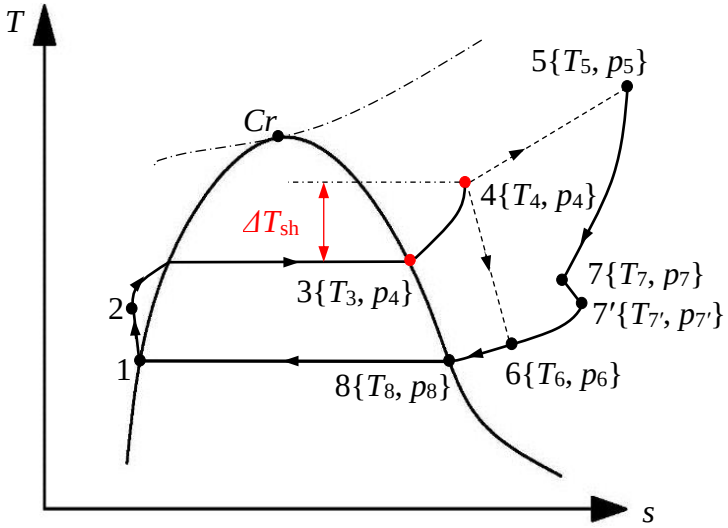

iii

Figure 3.20 Key state points (●) used in the coupling process for the specified heating system

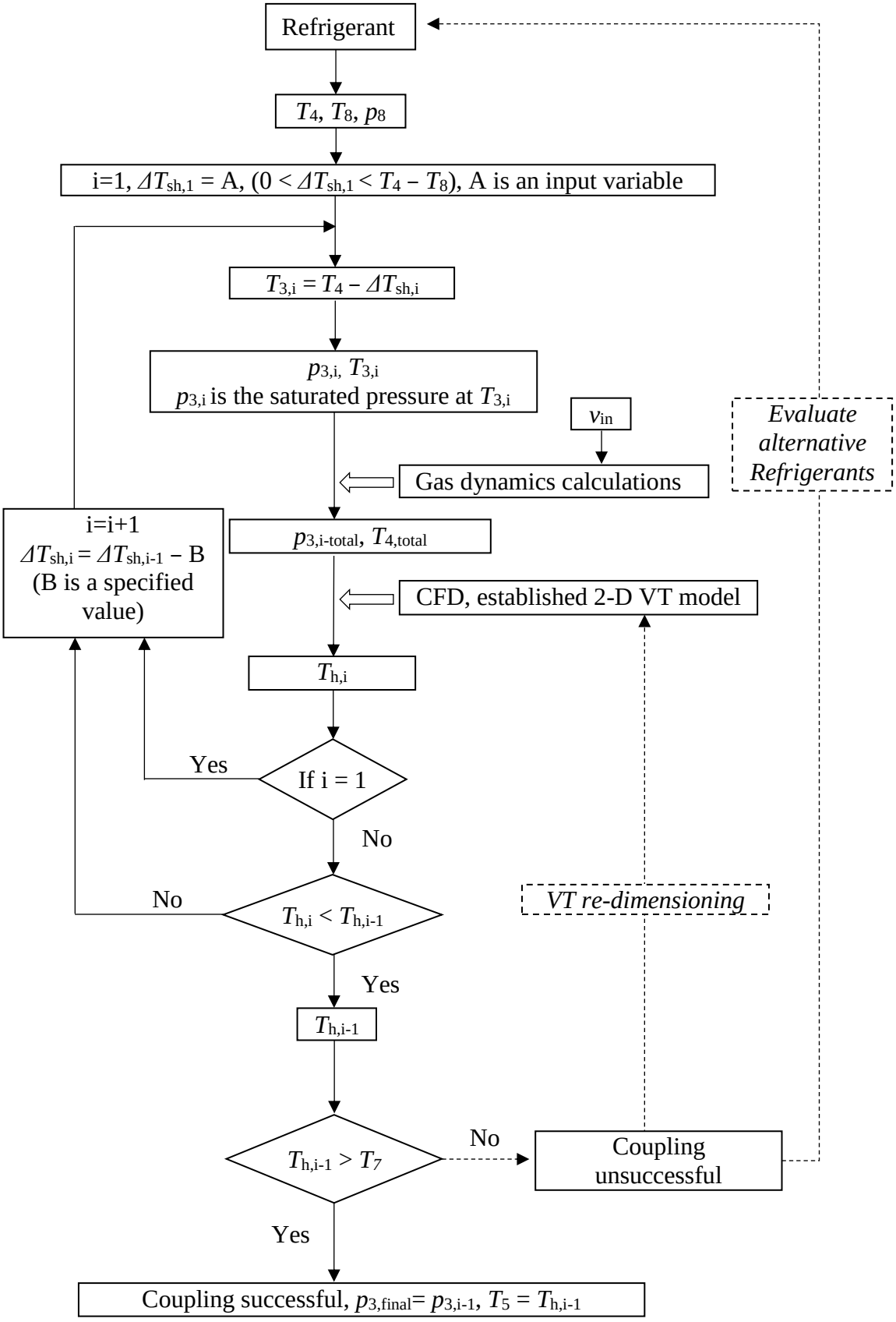

Figure 3.21 Procedure of coupling the heating system with the refrigerant for a given VT

It should be noted that the current proposed/developed VT closed system integration procedure is based on two specified VT systems. For both of them, the VT inlet temperature is a known value as it can be defined, though inlet pressure is usually unknown. The VT cold end outlet pressure can be controlled in the heating system while is unknown in the cooling system.

In other systems, two other situations are possible. First is when the cold end pressure is unknown in a heating system, and second the cold end pressure can be controlled to a required value for cooling system. The proposed procedure can be easily adapted for these two possibilities, with the same aim of identifying the VT inlet pressure (p_{in}) at the specified inlet temperature (T_{in}) to meet the design cooling/heating requirement.

For the adaptation, certain steps are revised as follow.

For an unknown VT cold end outlet pressure in a heating system, the VT entry point should be on the right side of the boundary line, with reasons previously explained. The range of $\Delta T_{sh,1}$ (Figure 3.21) should be changed to be larger than $\Delta T_{sh,min}$ (Figure 3.8) but less than T_{in}, while other steps (Figure 3.21) remain unchanged.

For a known VT cold end outlet pressure of a cooling system, a VT inlet pressure p_{in} is initially picked up at the position on the boundary line at T_{in}. If the CFD prediction of T_c is either equal to or smaller than the design cooling temperature, then p_{in} should be progressively decreased to obtain the largest system performance, such as coefficient of performance (*COP*). If not, the p_{in} is raised gradually to see whether T_c can attain the design temperature but at the same time to ensure that no liquification inside the nozzle occurs.

Following the successful integration of the system, optimization of the working conditions could be carried out by comparing *COP* and capacity values for different combinations of the required cooling/heating and VT inlet temperatures. This exercise can be repeated for different refrigerants and/or VT designs to achieve the optimum performance.

This chapter outlined the steps for establishing the VT CFD model and also a unique refrigerant screening methodology. This was followed by presenting a systematic coupling procedure for integrating a VT into thermal systems, comprising optimal matching of the VT geometry with the refrigerant choice and the operating conditions.

In the next chapter, the details of establishing the VT CFD model, including geometry definition, analysis on the appropriate choice of meshing element numbers, turbulence models consideration and model validation, are presented. This is followed by a preliminary examination of the influence of different VT operating conditions on the TSE for three chosen fluids (air, R134a and R600).

4 Establishment of the VT simulation model and preliminary CFD runs

In the process of setting up the CFD model of the VT, the results are initially analysed to assess the influence of the meshing element number on the accuracy/stability of the numerical simulations and to aid the selection of the appropriate turbulence models. The model is validated by comparing the CFD results with other experimental and/or numerical results.

Using the established VT model, the cold mass flow ratio μ_c is adjusted to determine whether the VT is to be primarily used as a heating or a cooling device, and the influence of the inlet conditions, such as mass flow rates $\dot{m}_{in}$ and inlet temperatures T_{in}, on the TSE are investigated. Air, refrigerants R134a and R600 are chosen as the working fluids to be examined.

4.1 Establishment of VT simulation models

All results generated are based on the VT geometry defined in Section 3.1.1. An axisymmetric swirl option is chosen for the 2-D model to simulate the rotating flow in the VT.

4.1.1 Meshing elements number consideration

Eight mesh densities using the quadrilateral pattern are tested under the same conditions, and the results (ΔT_c, ΔT_h, $p_{cham,in(total)}$, $p_{cham,in(sta)}$) using five turbulence models (the *k-ε standard*, the *k-ε RNG*, the *k-ε RNG (swirl)*, the *k-ω standard,* the *SST k-ω*) are presented respectively in Table 4.1 to Table 4.5. A sample mesh is shown in Figure 4.1.

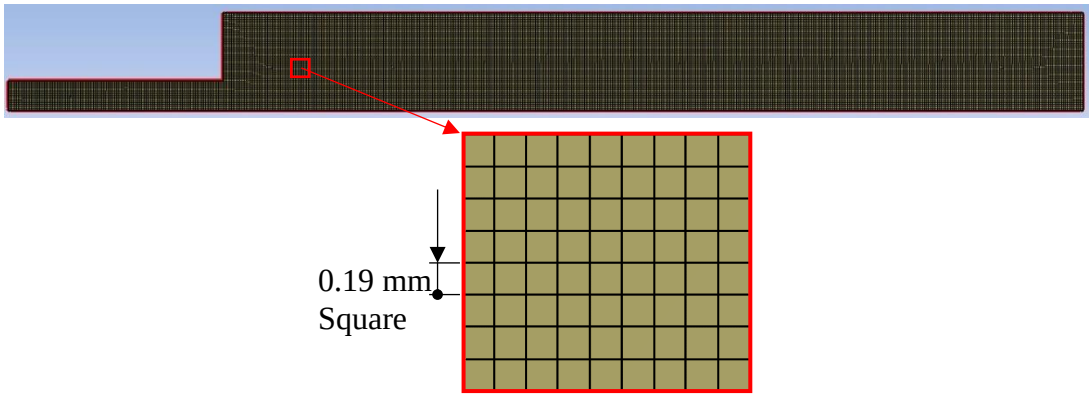

Figure 4.1 Mesh of the geometry with 29990 meshing elements

When the number of meshing elements is increased from 30,000 to 160,000 with an approximate increment of 20,000, it can be generally noted that the incremental changes (Δ) of the cooling effect (ΔT_c) and heating effect (ΔT_h) for all five models keep decreasing to well below 0.1 °C, and to below 0.1 kPa for both the chamber inlet total ($p_{cham,in(total)}$) and static ($p_{cham,in(sta)}$) pressures (Table 4.1 to Table 4.5). The convergence can also been seen in Figure 4.2 and Figure 4.3.

Table 4.1 Variations of CFD simulated chamber inlet pressure, cooling and heating effect with meshing numbers for the *k-ε standard* turbulence model

Element number	ΔT_c °C	Δ °C	ΔT_h °C	Δ °C	$p_{cham,in(total)}$ kPa	Δ kPa	$p_{cham,in(sta)}$ kPa	Δ kPa
29990	8.51	+0.44	2.12	+0.10	42.14	+0.43	13.38	+0.53
48029	8.95	+0.21	2.22	+0.10	42.57	+0.24	13.91	+0.34
68800	9.16	+0.12	2.32	+0.03	42.81	+0.12	14.25	+0.16
88894	9.28	+0.06	2.35	+0.02	42.93	+0.08	14.41	+0.10
107500	9.34	+0.05	2.37	+0.01	43.01	+0.05	14.51	+0.07
127459	9.39	+0.04	2.38	+0.01	43.06	+0.04	14.58	+0.05
149176	9.43	+0.03	2.39	+0.00	43.10	+0.03	14.63	+0.03
162328	9.46		2.39		43.13		14.66	

Table 4.2 Variations of CFD simulated chamber inlet pressure, cooling and heating effect with meshing numbers for the *k-ε RNG* turbulence model

Element number	ΔT_c °C	Δ °C	ΔT_h °C	Δ °C	$p_{cham,in(total)}$ kPa	Δ kPa	$p_{cham,in(sta)}$ kPa	Δ kPa
29990	4.52	+0.28	1.16	+0.07	42.25	+0.35	13.51	+0.44
48029	4.80	+0.19	1.23	+0.10	42.60	+0.21	13.95	+0.29
68800	4.99	+0.07	1.33	+0.03	42.81	+0.10	14.24	+0.13
88894	5.06	+0.05	1.36	+0.01	42.91	+0.05	14.37	+0.08
107500	5.11	+0.03	1.37	+0.01	42.96	+0.04	14.45	+0.05
127459	5.14	+0.02	1.38	+0.01	43.00	+0.03	14.50	+0.04
149176	5.16	+0.02	1.39	+0.00	43.03	+0.02	14.54	+0.01
162328	5.18		1.39		43.05		14.55	

Table 4.3 Variations of CFD simulated chamber inlet pressure, cooling and heating effect with meshing numbers for the *k-ε RNG (swirl)* turbulence model

Element number	ΔT_c °C	Δ °C	ΔT_h °C	Δ °C	$p_{cham,in(total)}$ kPa	Δ kPa	$p_{cham,in(sta)}$ kPa	Δ kPa
29990	3.68	+0.12	0.95	+0.05	42.58	+0.54	13.97	+0.69
48029	3.80	+0.15	1.00	+0.07	43.12	+0.15	14.66	+0.22
68800	3.95	+0.07	1.07	+0.03	43.27	+0.11	14.88	+0.13
88894	4.02	+0.04	1.10	+0.02	43.38	+0.08	15.01	+0.10
107500	4.06	+0.02	1.12	+0.02	43.46	+0.04	15.11	+0.06
127459	4.08	+0.02	1.14	+0.00	43.50	+0.04	15.17	+0.03
149176	4.10	+0.02	1.14	+0.00	43.54	+0.03	15.20	+0.03
162328	4.12		1.14		43.57		15.23	

Table 4.4 Variations of CFD simulated chamber inlet pressure, cooling and heating effect with meshing numbers for the *k-ω standard* turbulence model

Element number	ΔT_c °C	Δ °C	ΔT_h °C	Δ °C	$p_{cham,in(total)}$ kPa	Δ kPa	$p_{cham,in(sta)}$ kPa	Δ kPa
29990	6.33	+0.31	1.53	+0.14	13.08	+0.62	41.88	+0.50
48029	6.64	+0.21	1.67	+0.09	13.70	+0.32	42.38	+0.22
68800	6.85	+0.09	1.76	+0.02	14.02	+0.18	42.60	+0.15
88894	6.94	+0.06	1.78	+0.02	14.20	+0.06	42.75	+0.06
107500	7.00	+0.05	1.80	+0.00	14.26	+0.05	42.81	+0.01
127459	7.05	+0.02	1.80	+0.01	14.31	+0.03	42.82	+0.02
149176	7.07	+0.01	1.81	+0.00	14.34	+0.04	42.84	+0.05
162328	7.08		1.81		14.38		42.89	

Table 4.5 Variations of CFD simulated chamber inlet pressure, cooling and heating effect with meshing numbers for the *k-ω SST* turbulence model

Element number	ΔT_c °C	Δ °C	ΔT_h °C	Δ °C	$p_{cham,in(total)}$ kPa	Δ kPa	$p_{cham,in(sta)}$ kPa	Δ kPa
29990	8.46	+0.16	2.04	+0.15	43.69	+0.40	15.44	+0.50
48029	8.62	+0.13	2.19	+0.03	44.09	-0.21	15.94	-0.26
68800	8.75	+0.08	2.22	+0.01	43.88	-0.03	15.68	-0.04
88894	8.83	+0.03	2.23	+0.01	43.85	-0.03	15.64	-0.04
107500	8.86	+0.02	2.24	+0.01	43.82	-0.04	15.60	-0.05
127459	8.88	+0.01	2.25	+0.02	43.78	-0.04	15.55	-0.04
149176	8.89	+0.02	2.27	-0.02	43.74	-0.01	15.51	-0.03
162328	8.91		2.25		43.73		15.48	

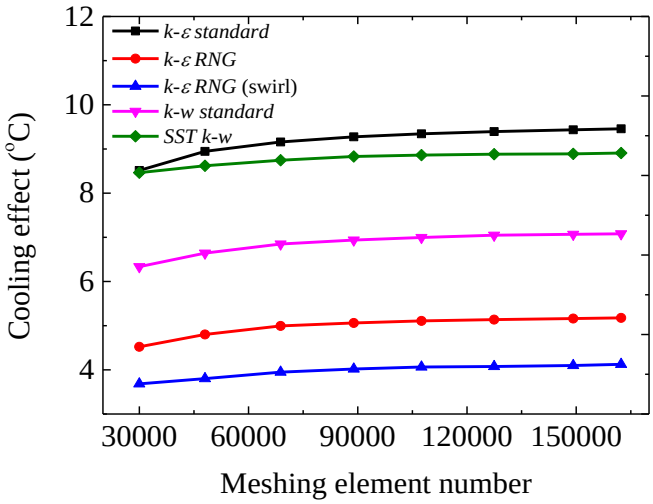

Figure 4.2 Cooling effect change with various meshing element numbers for different turbulence models (μ_c = 0.2, $\dot{m}_{in}$ = 3.9 g/s, p_c = 0.10 MPa, air)

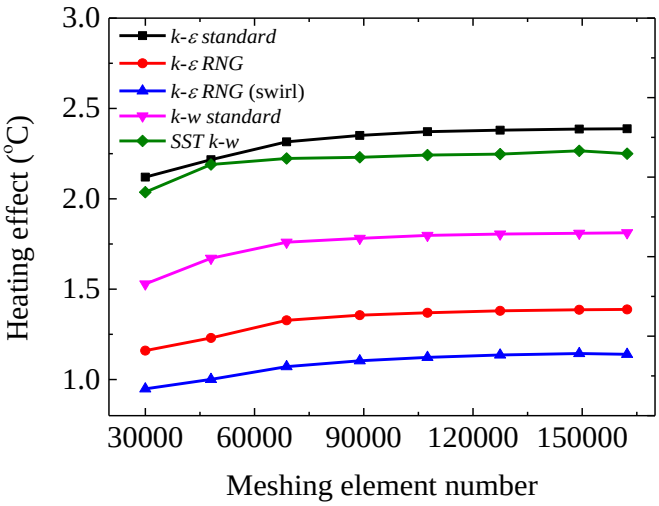

Figure 4.3 Heating effect change with various meshing element numbers for different turbulence models (μ_c=0.2, $\dot{m}_{in}$=3.9 g/s, p_c = 0.10 MPa, air)

It is therefore decided to use around 90 000 meshing elements which represents a good compromise between accuracy and computer run time, and there seems to be no noticeable benefits in using any higher meshing numbers. For the data listed in Table 4.1 to Table 4.5, an increase from 90 000 to 110 000 is found to almost double the run time for air but with only around 0.1 °C change in the cooling and heating effect for most turbulence models (for R134a and R600, 10 hours for 90000, and 19 hours for 110000 when using *k-ε standard* turbulence model). This decision is also supported by examining the simulated pressures at the chamber inlet, where their incremental changes for all turbulence models drop to below 0.1 kPa. However, it must be pointed out that the meshing element number may need to be revised when the VT geometry

is adjusted during the coupling process in Section 6.2.3.

4.1.2 Selection of suitable turbulence models

Based on the discussion in Section 2.3 and the procedure described in Section 3.1.2, five commonly used turbulence models (the *standard k-ε* model, the *RNG k-ε* model with swirl option, the *RNG k-ε* model without swirl option, the *standard k-ω* model, the *SST k-ω* model) are tested under the same conditions using the 90000 meshing elements, and the results are shown respectively in Table 4.6 and Table 4.7 for two cold mass flow ratios, as used in the experiments of Aljuwayhel et al[77].

Table 4.6 Comparison of simulated results by different turbulence models and experiment results (μ_c = 0.2, air)

Selected model	$\dot{m}_{in}$ kg/s	ΔT_c °C	ΔT_h °C	$p_{h,sta}$ kPa
Experiment[77]	3.9±0.1	9.4±0.2	2.0±0.2	116±0.34
k-ε standard	3.9	9.3	2.3	110.91
k-ε RNG	3.9	5.1	1.4	112.66
k-ε RNG (swirl)	3.9	4.1	1.1	113.75
k-ω SST	3.9	8.8	2.3	113.58
k-ω standard	3.9	4.1	1.1	113.75

Table 4.7 Comparison of simulated results by different turbulence models and experiment results (μ_c = 0.1, air)

Selected model	$\dot{m}_{in}$ kg/s	ΔT_c °C	ΔT_h °C	$p_{h,sta}$ kPa
Experiment[77]	4.0±0.1	11±0.2	1.2±0.2	113.3±0.34
k-ε standard	4.0	10.9	1.3	109.48
k-ε RNG	4.0	7.2	0.9	110.83
k-ε RNG (swirl)	4.0	5.9	0.8	111.70
k-ω SST	4.0	10.7	1.3	111.75
k-ω standard	4.0	8.6	1.1	110.21

It can be shown that the *standard k-ε* model and the *SST k-ω* model can better match with the experimental results. Between these two, however, the pc run time for the *standard k-ε* model is three times less than that of the *SST k-ω* model (e.g. at μ_c = 0.2, 1.5 hour for the *standard k-ε* model and 5 hours are needed for the latter). Hence the *standard k-ε* model (governing equations are shown in Appendix 8.2) is chosen for this study.

4.1.3 Qualitative comparison of the predicted TSE with other studies'

The current 2-D VT model (90000 meshing elements, *standard k-ε* model) is then used for a number of selected fluids which have been employed in other VT computational and/or experimental studies. Though the same run conditions as in the other studies are used, only qualitative comparison of the results can be made as the individual VT geometries are different.

1) TSE trends for air, N_2 and O_2

As in the experiments of Aydin and Baki[19], the VT chamber inlet is kept at 0.4 MPa total pressure. The VT inlet total temperature is set at 295 K in the simulation and the hot end and cold end pressures are varied to adjust the cold mass flow ratio μ_c from 0.1 to 0.9. The predicted cooling effects of air, N_2 and O_2 are presented in Figure 4.4, together with the measurements from Aydin and Baki[19].

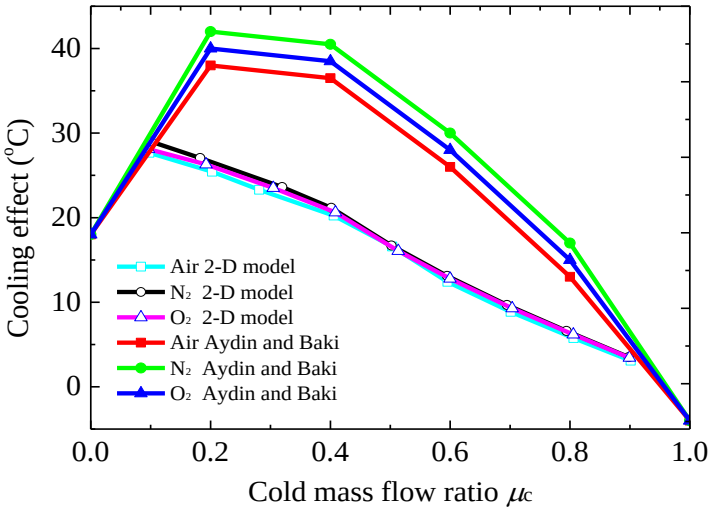

Figure 4.4 Cooling effects of air, N_2 and O_2 predicted by defined 2-D VT model and in experiment

Among the three fluids, Aydin and Baki[19] observed that N_2 produces the largest cooling effect while air always generates the smallest, though their differences are considered small, and these trends are correctly predicted by the current model. Due to different geometries, the current model produces a weaker overall cooling effect that also peaks at a lower μ_c. Aydin and Baki[19] believed that N_2 has the smallest molecular weight, thus generating the highest cooling effect. One would therefore expect O_2 to produce a smaller cooling effect than air as it is heavier than air, which is different to the results. This suggests that other thermal-physical properties also play

a role in determining the TSE. The influences of these properties on the TSE will be analysed and discussed in a later chapter.

2) Velocity profiles inside the VT for air, N_2, O_2 and CO_2

As in the CFD work of Khazaei et al[114], a "wall" boundary condition is set up for the cold end in the current VT model (i.e. a physically closed cold end), ensuring no fluid exiting this end. As in [114], the inlet mass flow is kept constant at 218.4 g/s and the inlet total temperature at 297 K for these four fluids. The tangential velocities at the cross section 40 mm away from the VT inlet are depicted in Figure 4.5 and numerically given in Table 4.8, and the cross section velocities at the same distance-to-diameter ratio from [114] are also plotted for comparison.

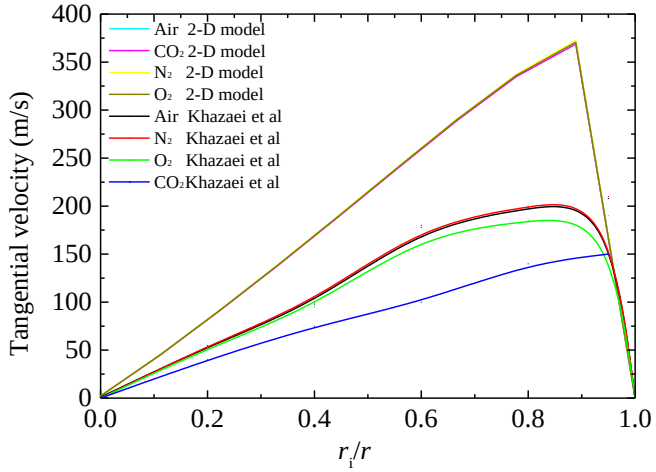

Figure 4.5 Predicted tangential velocities of air, N_2, O_2 and CO_2 at the cross section $x/\Phi_{cham} = 2$ and in [114]

Table 4.8 Tangential velocities for air, N_2, O_2 and CO_2 prodcued by the current 2-D VT model

r_i/r	Tangential velocity m/s						
	CO_2		O_2		air		N_2
0.00	2.20	<	2.210	<	2.215	<	2.218
0.11	44.69	<	44.85	<	44.94	<	45.00
0.22	90.75	<	91.08	<	91.27	<	91.37
0.33	138.74	<	139.21	<	139.47	<	139.60
0.44	188.56	<	189.17	<	189.49	<	189.60
0.56	239.26	<	240.02	<	240.42	<	240.50
0.67	289.07	<	290.06	<	290.55	<	290.59
0.78	334.92	<	336.16	<	336.77	<	336.96
0.89	368.65	<	370.52	<	371.58	<	372.44

As shown in Figure 4.5, in [114] the N_2 has the largest tangential velocities followed by air, O_2 and CO_2; qualitatively, this order is also matched well by the current model, as seen in Table 4.8, though much smaller differences between the fluids are predicted by the latter. The order is believed to be associated with the density differences of these fluids; CO_2 has the largest density whereas N_2 has the smallest value. However, the current model predicts much larger velocities when compared to those of [114].

In [114], CO_2 has much smaller velocities than that of the other fluids, whereas the tangential velocities produced by the current model are of very similar magnitudes for all four fluids. These are probably due to respectively the fact that the current VT is much shorter in length and smaller in diameter (i.e. a smaller rotating distance, and less friction) than that used in [114], thus leading to smaller velocity reduction within the rotating flows.

3) Temperatures along the VT wall when using R134a

The VT chamber inlet total pressure is set at 0.3 MPa and total temperature at 293.15K, as in the experimental work (L_{VT} = 105 mm) in the Institute of refrigeration and cryogenics, Zhejiang university[115] (the experimental apparatus is described in [119]), using R134a as the working fluid. The hot end and the cold end pressures are varied to achieve various cold mass flow ratios (0.25 - 0.57). The total temperature difference (T_w - T_{in}) at specified positions are presented in Figure 4.6.

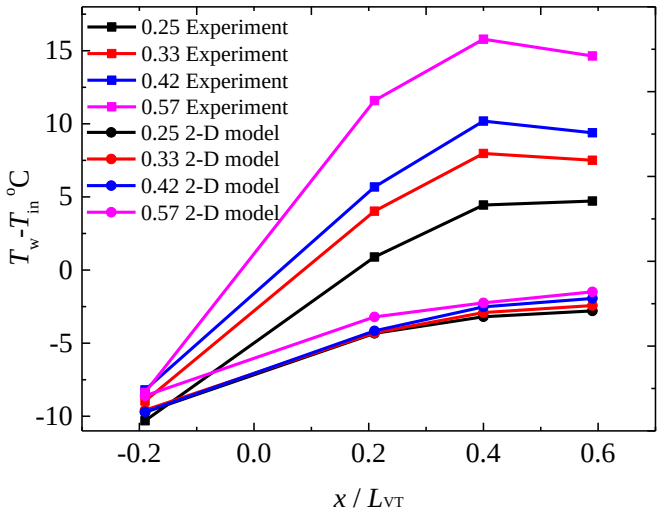

Figure 4.6 Total temperatures along the VT wall predicted by the current 2-D VT model and the experiments[115].

It can be noticed that, qualitatively, the predicted trends match well with the experimental results, i.e. at the same relative location (x/L_{VT}), the total temperature difference (T_w - T_{in}) generally increases with increasing the μ_c. For a given μ_c, the simulated total temperature difference keeps increasing towards the hot end, whereas a slight drop is observed in the experiment. This difference is due to the fitting of a vortex interruption/stopper device[11] inside the VT in the experiment, which throttles the flow and causes a temperature drop in the fluid.

In conclusion, based on quantitative and qualitative validations, it is believed the established VT model is able to predict the results reliably and accurately.

4.1.4 Understanding the development of the flow and thermal processes in the VT

As previously discussed in Chapter 2.2, the TSE is mainly regarded as the combined effect of the adiabatic expansion and the internal friction; the former accounts primarily for the cooling effect and the latter for the heating effect at the opposite end of the VT. Three main stages which lead to the temperature separation can be identified based on the published works[120-123], involving the flow through the nozzle, the primary flow towards the hot end and the secondary flow towards the cold end, as shown in Figure 1.1. Using the current CFD model, some preliminary results are obtained that allow us to gain an appreciation in the associated thermal processes.

1) The flow through the nozzle

A convergent nozzle is always employed in VT. The fluid undergoes an isentropic expansion[118] when passing through this kind of nozzle, resulting in a considerable temperature drop[118]. As shown in Figure 4.7, the fluid static (actual) temperature at the nozzle outlet (or chamber inlet) area is around 245 K; with a nozzle inlet temperature set at 295 K (not shown), this represents a drop of around 50 K through the nozzle.

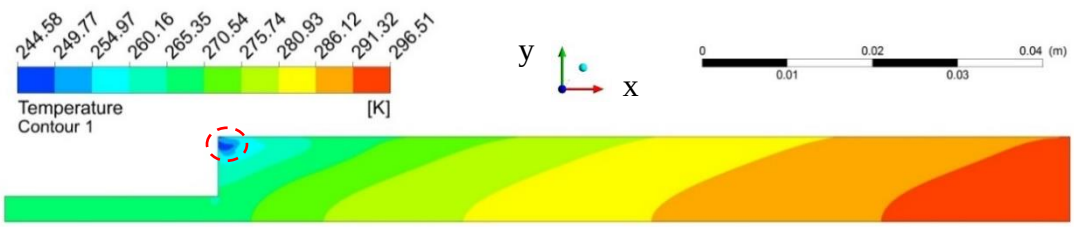

Figure 4.7 Static temperature distribution of the VT (air, μ_c = 0.3, T_{in} = 295K, p_{in} = 0.17 MPa, p_c = 0.10 MPa)

[11] The interruption/stopper is applied to stop the flow from rotating before exiting the hot end[17]

2) The primary flow towards the hot end

Along the axial direction of the vortex chamber and the hot tube, the fluid expands and moves, from higher pressures at inlet towards a lower pressure at the hot end (as shown in Figure 4.8). At any cross-section along the hot tube, the primary flow can be seen as consisting of two movements, an outward and an inward movement, as shown in Figure 4.9 and Figure 4.10 (also shown in [81]). In the former the flow rotates around the axis and leaves at the hot end, and in the latter, the flow spirals inwardly towards the throttle. Part of this inward movement in fact turns around towards the cold end before even reaching the throttle and the rest gets rebounded by the throttle.

Figure 4.10 presents the combined tangential and radial velocity vectors at cross-sections along 4 axial locations as indicated in Figure 4.9, and Figure 4.11a-c presents respectively the tangential, axial and radial velocity components at the same locations. As seen, the rotational strengths gradually decrease as the flow moves from positions 1 to 4. The radial velocity components are much weaker than the tangential ones, especially in the middle part of the hot tube; small positive radial velocities at location 4 indicate the flow are moving away from the axis existing the hot end, whereas negative radial velocities at location 1 suggest the flow is moving towards the axis joining the secondary flow.

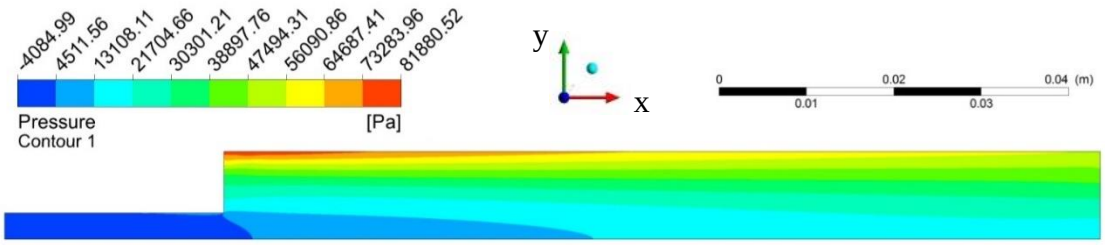

Figure 4.8 Static pressure (gauge) distribution in the VT (air, $\mu_c = 0.3$, $T_{in} = 295$K, $p_{in} = 0.17$ MPa, $p_c = 0.101$ MPa)

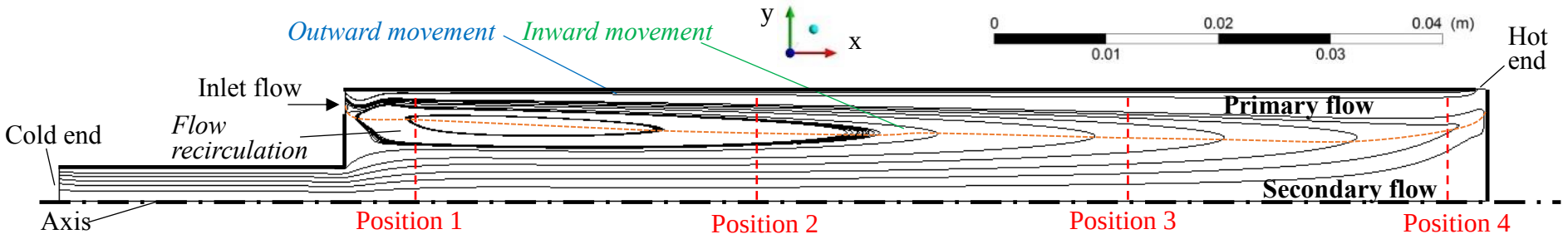

Figure 4.9 Streamlines generated from CFD simulation, (air, $\mu_c = 0.3$, $T_{in} = 295K$, $p_{in} = 0.17$ MPa, $p_c = 0.101$ MPa), the dotted line shows the boundary between the primary and the secondary flows

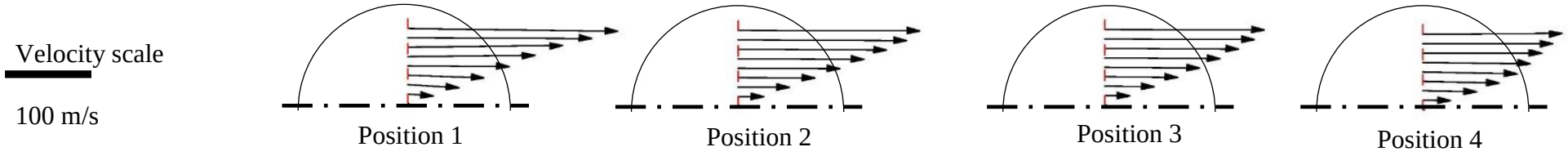

Figure 4.10 Combined tangential and radial velocity vectors at four positions corresponding to that shown in Figure 4.9

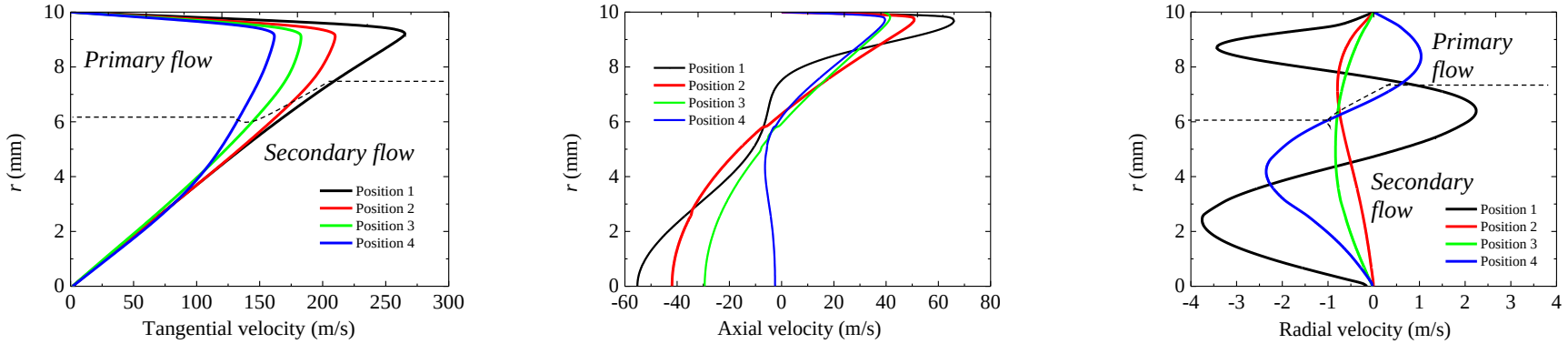

Figure 4.11 Tangential (a), axial (b), radial (c) velocities of 4 positions corresponding to Figure 4.9

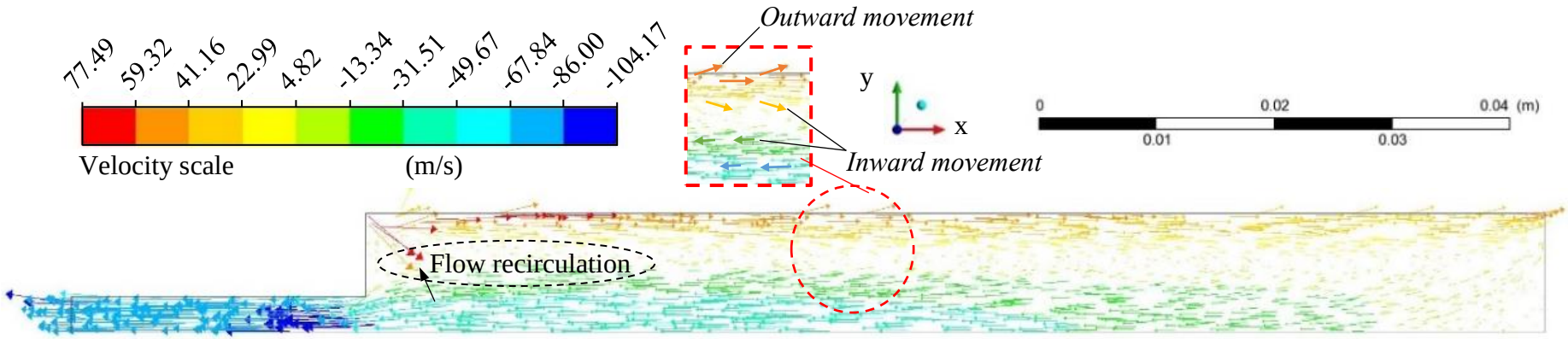

Figure 4.12 Flow vector (x-y plane) within the VT (air, $\mu_c = 0.3$, $T_{in} = 295K$, $p_{in} = 0.17$ MPa, $p_c = 0.101$ MPa)

As illustrated in Figure 4.13, when considering the two adjacent fluid elements 1 and 2 in a y-z plane, entering the VT chamber, say, belonging respectively to an outward movement and an inward movement. The inertia force attempts to maintain their angular momentum when entering the rotating flow. At the same time, the shear force between these two elements slow down their rotating speed, as indicated by the decreasing tangential velocities in the radial direction, as presented in Figure 4.11a. Therefore, there must be a transfer of kinetic energy to the internal energy by some kind of internal friction, leading to a temperature rise of these fluid elements in the primary flow towards the hot end, as shown in Figure 4.7.

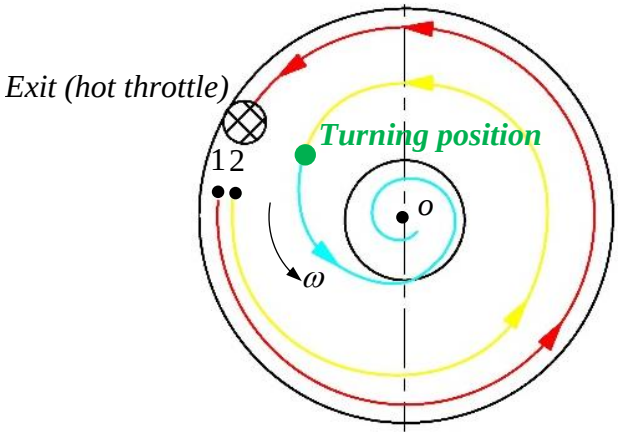

Figure 4.13 Sketch of the flow process within the VT (red and yellow line representing the primary flow, blue line the secondary flow)

In experimental research for VT, the total temperatures instead of static temperatures were often measured[1] and presented, and the TSE is also defined based on the difference of the total temperature[72]. Figure 4.14 presents the CFD results of the total temperature.

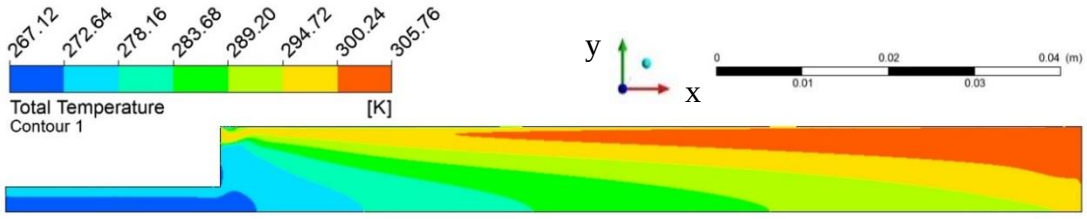

Figure 4.14 Total temperature distribution of the VT (air, μ_c = 0.3, T_{in} = 295K, p_{in} = 0.17 MPa, p_c = 0.101 MPa)

Before reaching the hot throttle, in the radial direction, element 2 (as illustrated in Figure 4.13 and represented by the inward movement in Figure 4.12) moves inwards and undergoes an adiabatic expansion due to the pressure differential, as seen in Figure 4.8, between the peripheral and the central parts of the VT. This is similar to the

angular propulsion process for a rotating flow[63], in which the element both rotates around and moves toward the rotating centre. Within the rotating frame of the primary flow, element 2 which has the same angular velocity as the frame, will overcome the Coriolis force and the centrifugal force to move inward[63]. On its journey to the hot throttle, work must have been done by element, transferring its internal energy and the rotational (kinetic) energy to the rotational (kinetic) energy of the rotating frame. As a result, the total temperature of this fluid element drops[63]. This increased rotational energy of the frame is transferred to the outer part of the primary flow by friction from shear force, resulting in an increase of total temperature towards the wall, as seem in Figure 4.14.

3) The secondary flow towards the cold end

Near the hot end, the turning around of the inner layers of the primary flow become the secondary flow moving towards the cold end (Figure 4.11b) due to pressure differential, while still maintaining the same rotating direction, as shown in Figure 4.11a. However, despite a pressure drop between the chamber inlet and the cold end, there is no direct flow between these two locations, though the experimental work by Xue et. al[123] using water shows a direct flow is possible.

As shown in Figure 4.11b, the axial velocities keep increasing when the secondary flow moves towards the cold end, suggesting there may be further transfer of internal energy to the kinetic energy, leading to a temperature decrease of the secondary flow from the hot to cold end, as shown in Figure 4.7. When the secondary flow approaches the cold orifice, the outer part of the secondary flow recirculates and mixes with the primary flow (as shown in Figure 4.9 and Figure 4.12) due to the centrifugal force. This could further convey the energy to the primary flow[73].

In summary, the cooling effect appears mainly due to the expansion through the nozzle, and the adiabatic expansion in the spiral motion (angular propulsion effect) in the primary and secondary flows. The heating effect mainly comes from the internal friction due to shear friction.

4.2 Influence of boundary conditions on VT temperature separation effect

In this part, the effects of the boundary conditions on the TSE are preliminary examined, using the current 2-D VT model for comparing air, R134a and R600. Important boundary parameters including the cold mass flow ratio μ_c, the inlet pressure p_{in} and temperature T_{in}, and the inlet mass flow rate $\dot{m}_{in}$ are varied.

4.2.1 Influence of cold mass flow ratio μ_c on TSE

For a fixed inlet mass flow rate $\dot{m}_{in}$ of 4.1 g/s, the μ_c is adjusted from 0.1 to 0.9 by varying the hot end pressure p_h while the cold end pressure p_c is kept constant; this would also mean that at the same time the VT inlet pressure is also changing.

Figure 4.15 presents the cooling and heating effect for the three chosen fluids. It is clear that, for all of them, the decrease of the μ_c leads to an increase of the cooling effect, and the heating effect increases with increasing the μ_c. The observations suggest that the VT can be controlled to either primarily function as a cooling or heating device depending on the setting of the μ_c. The results are similar to those observed by other researchers[4, 19]. At a given μ_c, air has a much stronger cooling/ heating effect which are also more sensitive to the changes in μ_c, when compared to R134a and R600. For the cooling effect, R600 performs marginally better than R134a, though their heating effects are of very similar magnitudes across the μ_c range. The differences in their behaviour are likely to be attributed to various factors, including the fluid thermal properties (e.g. thermal diffusivity) which are analysed and discussed thoroughly in Section 5.2.

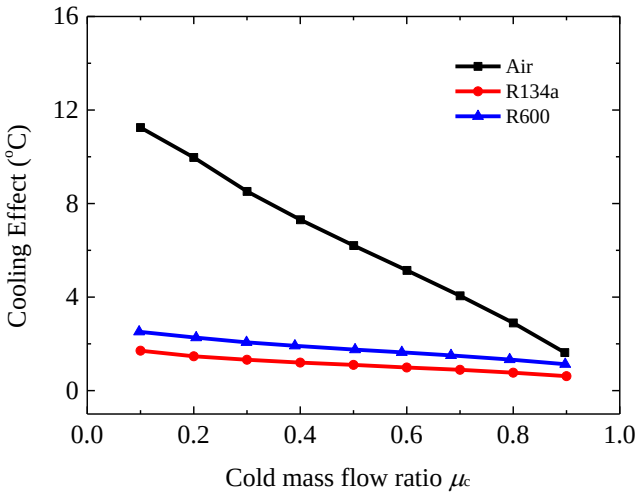

a

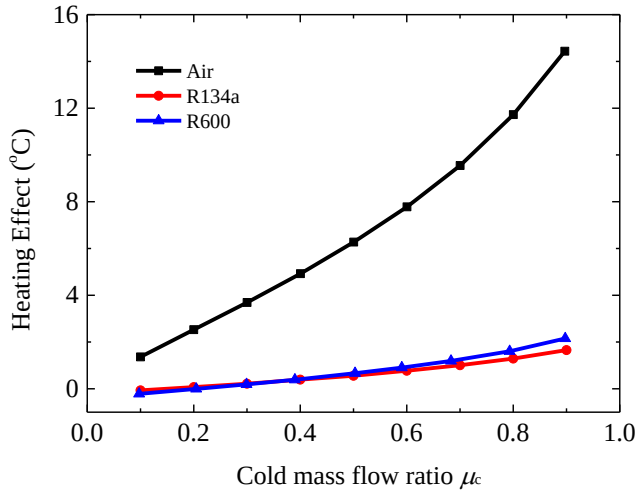

b

Figure 4.15 Variations of cooling effect (a) and heating effect (b) with cold mass flow ratios μ_c for air, R134a and R600

Figure 4.16 presents the chamber inlet velocity $v_{cham,in}$ and the pressure drops between the VT inlet and the cold end $\Delta p_{in\text{-}c}$ and hot end $\Delta p_{in\text{-}h}$. It can be seen that, for a specified fluid, a smaller μ_c would lead to a larger $v_{cham,in}$ due to the changes in the chamber inlet pressure, which in turn is expected to generate a stronger rotation, a higher momentum transfer and thus deliver a larger cooling effect[41]. However, when the μ_c is decreased, the pressure drop $\Delta p_{in\text{-}c}$ also decreases (Figure 4.17a), which should lead to a smaller temperature drop from the expansion of the fluid towards the cold end. An increase in the cooling effect at smaller $\Delta p_{in\text{-}c}$, as seen in Figure 4.15a, suggests the influence of the $v_{cham,in}$ on the cooling effect is stronger than the expansion process.

The chamber inlet velocity $v_{cham,in}$ decreases at higher μ_c (Figure 4.16), this could lead to a weaker rotation and smaller increases. At the same time, at the higher μ_c, a smaller temperature drop from the expansion process can be expected as a lower pressure drop $\Delta p_{in\text{-}h}$ is observed in Figure 4.17b, resulting in the combined heating effect seen in Figure 4.15b.

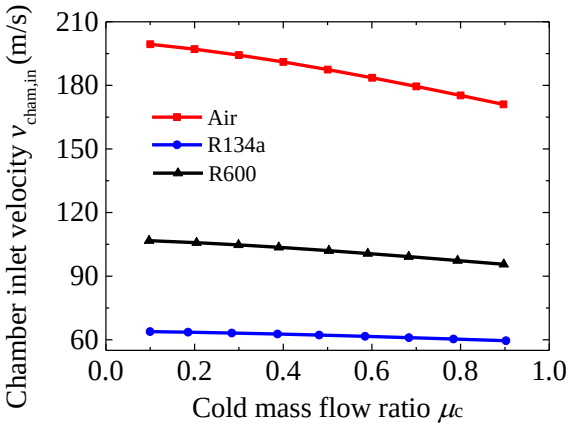

Figure 4.16 Chamber inlet velocities for air, R134a and R600

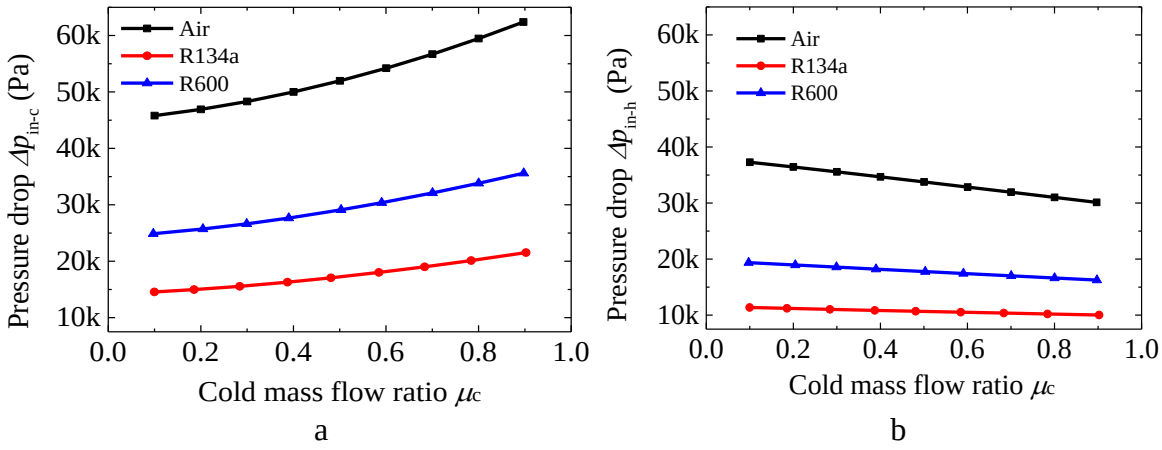

Figure 4.17 Pressure drop between the VT inlet and the cold/hot end for three fluids

Figure 4.18 presents the streamlines for three fluids at three different μ_c. It can be observed that, with the same μ_c, three fluids have almost the same stream lines. This suggests that, for a given VT, the flow pattern is insensitive to the choice of the fluid. For a given fluid, the stream line is quite different when the μ_c is varied. As illustrated by air, one obvious observation is that recalculation area (red dash oval) decreases when μ_c is increased. In other words, at a smaller μ_c, the elements/fluid will encounter a longer rotating distance (friction) before they turn back (from the primary flow to the secondary flow) and much more energy will be transferred outwards from them in the rotation. Thus, the cooling effect is larger at smaller μ_c.

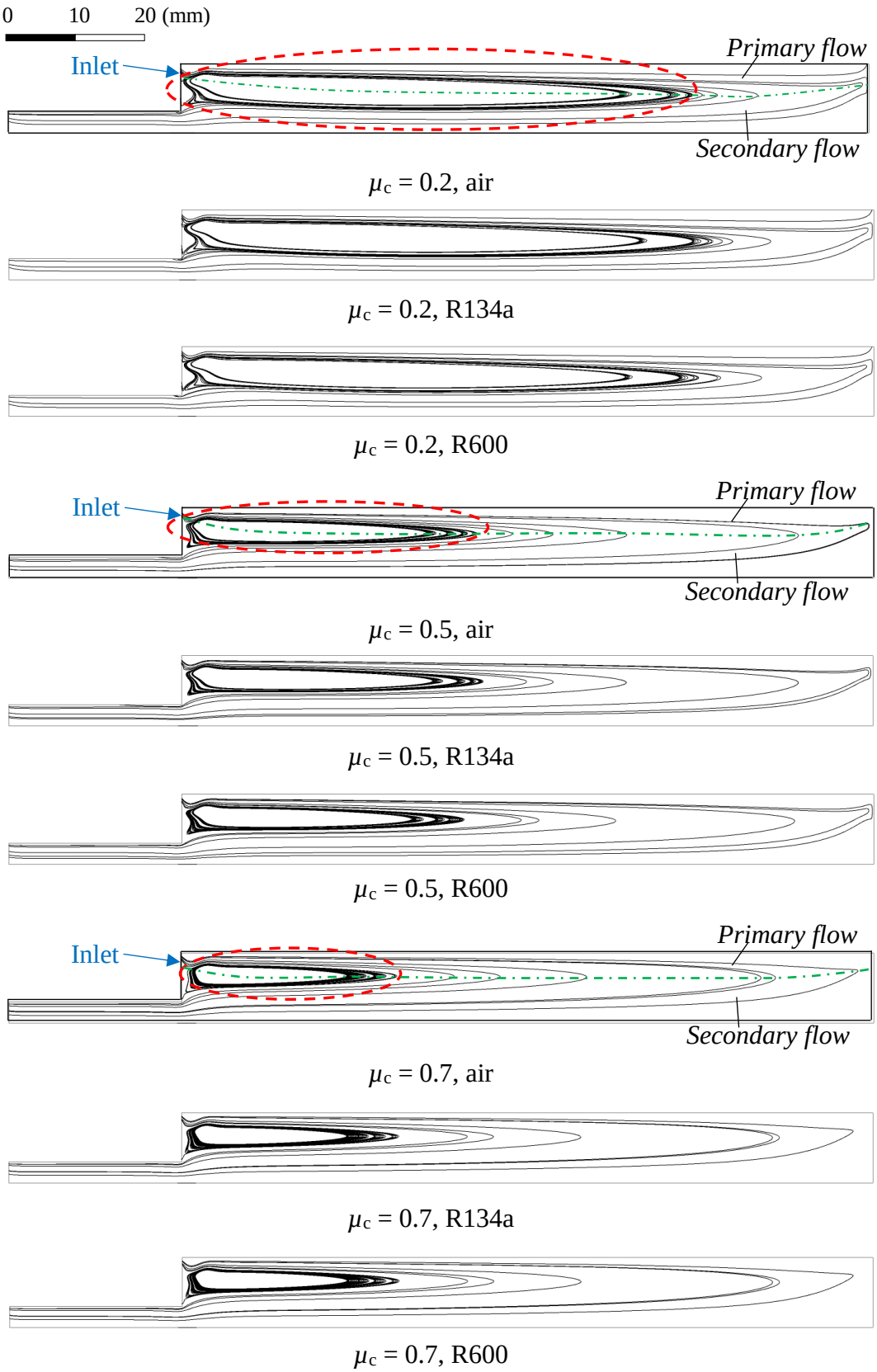

Figure 4.18 Streamlines for three fluid at different cold mass flow ratio μ_c

Figure 4.19 and Figure 4.20 present respectively the tangential shear stress at the cross-section (x = 30 mm) in radial/y and axial/x directions for air and R134a. It can be observed that, qualitatively the trends for the shear stress of air and R134 at various μ_c are rather similar. However, air has a considerable larger magnitudes of shear stress than R134, which suggests air has produced more friction, resulting in a higher temperature drop/increase from the rotation process. For a given fluid and μ_c, the value of τ_{wx} is much smaller than τ_{wy}, suggesting that the tangential shear stress in the radial direction (τ_{wy}) on the TSE has a much stronger influence than that of τ_{wx}.

In addition, in the primary flow, smaller τ_{wy} are found to be associated with larger μ_c, while the situation is reversed in the secondary flow where larger τ_{wy} are found to be associated with larger μ_c. Relative to smaller μ_c, at the larger μ_c the rotation in the secondary flow is stronger suggesting much more energy should be transferring towards the outer layers of the rotating flow. At the same time, in the primary flow the mass flow rate to the hot end decreases, resulting in an overall larger temperature increase for heating, as evident in Figure 4.15b. On the other hand, with a small μ_c, smaller τ_{wy} is created in the secondary flow, and larger τ_{wy} is created in the primary flow which travels a longer rotating distance (when compared to that of a larger μ_c) before part of it turns back (Figure 4.18), and is expected to have more energy transferred outwards in the rotation, thus delivering a larger cooling effect, as evident in Figure 4.15a.

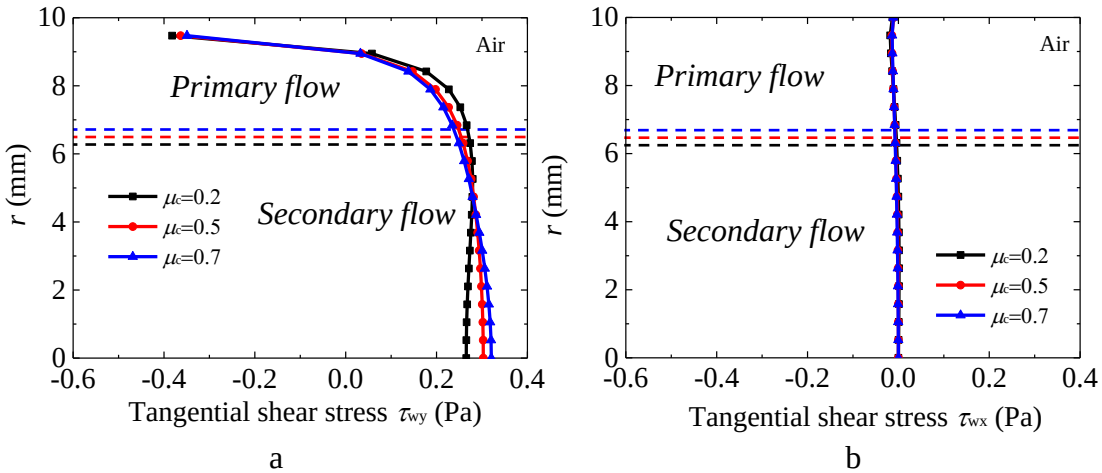

Figure 4.19 Tangential shear stress at the CS (x = 30 mm) in y/radial (a) and x /axial (b) directions for air

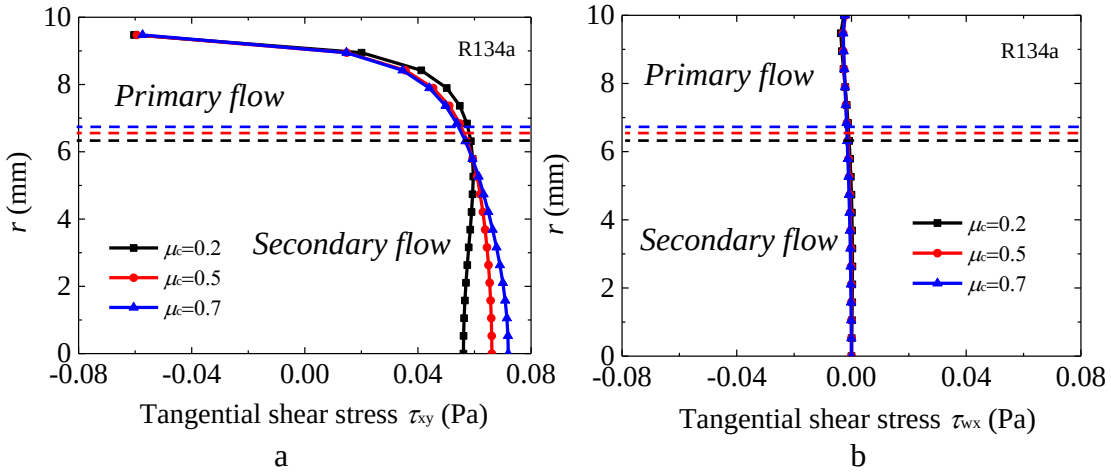

Figure 4.20 Tangential shear stress at the CS (x = 30 mm) in y/radial (a) and x/axial (b) directions for R134a

It can also be noticed that, as shown in Figure 4.15, under the same conditions (μ_c, $\dot{m}_{in}$, T_{in}), R134a and R600 generate much less cooling and heating effect than that of air, most likely due to their smaller chamber inlet velocities (as shown in Figure 4.16), hence weaker rotations. A smaller pressure drop $\Delta p_{in\text{-}c}$ (as shown in Figure 4.17a) for R134a and R600 also contributes to a smaller temperature drop. Though air has a larger pressure drop $\Delta p_{in\text{-}h}$ and the associated temperature drop could potentially cancel out more heating effect when compared to R134a and R600, it can still produce a bigger heating effect than the other two fluids, as shown in Figure 4.15; this suggests the temperature increase from the TSE as influenced by the chamber inlet velocity is significantly larger than the temperature drop caused by the expansion under the specified conditions.

For all range values of μ_c, R600 always has a larger $v_{cham,in}$ and $\Delta p_{in\text{-}c}$ than R134a, and this leads to R600 having a larger cooling effect. However, it also has a larger $\Delta p_{in\text{-}h}$, resulting in a larger cancellation of the heating effect, thus making R600 and R134a have similar values of heating effect.

Figure 4.21 and Figure 4.22 present respectively the velocity components profiles and shear stress for three fluids at the cross-section (x = 30 mm) and μ_c = 0.2. It can be observed that the tangential velocity is always significantly larger than axial and radial velocities. The shear stress τ_{wx} in x direction is much smaller than τ_{wy} in the y (i.e. radial) direction, suggesting once again the friction and energy separation mainly come from the rotation in the radial direction. In addition, air always has largest tangential/axial velocities and shear stresses than R600 and R134a, resulting in a larger temperature change caused by the rotating process.

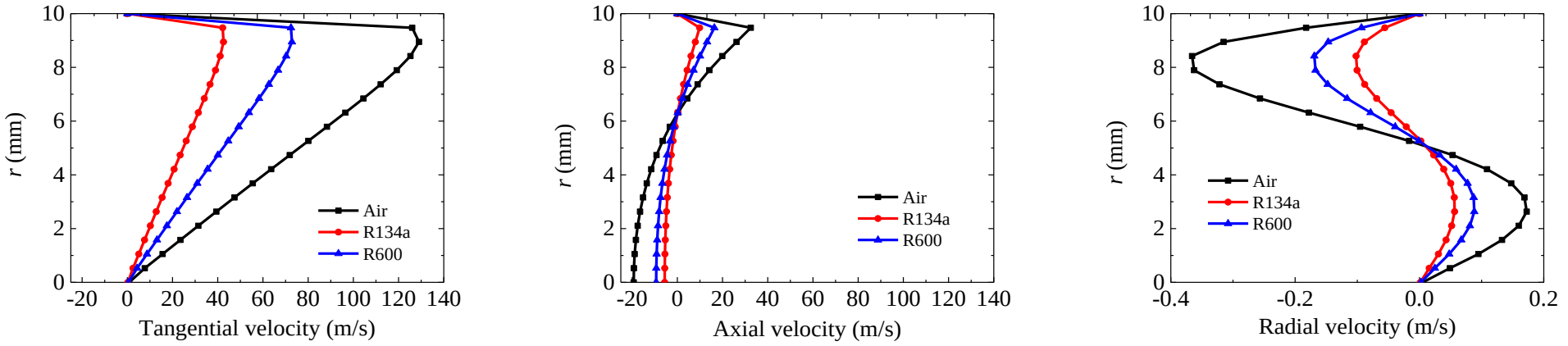

Figure 4.21 Velocity components profile at the cross-section (x = 30 mm, μ_c=0.2) for air, R134a and R600

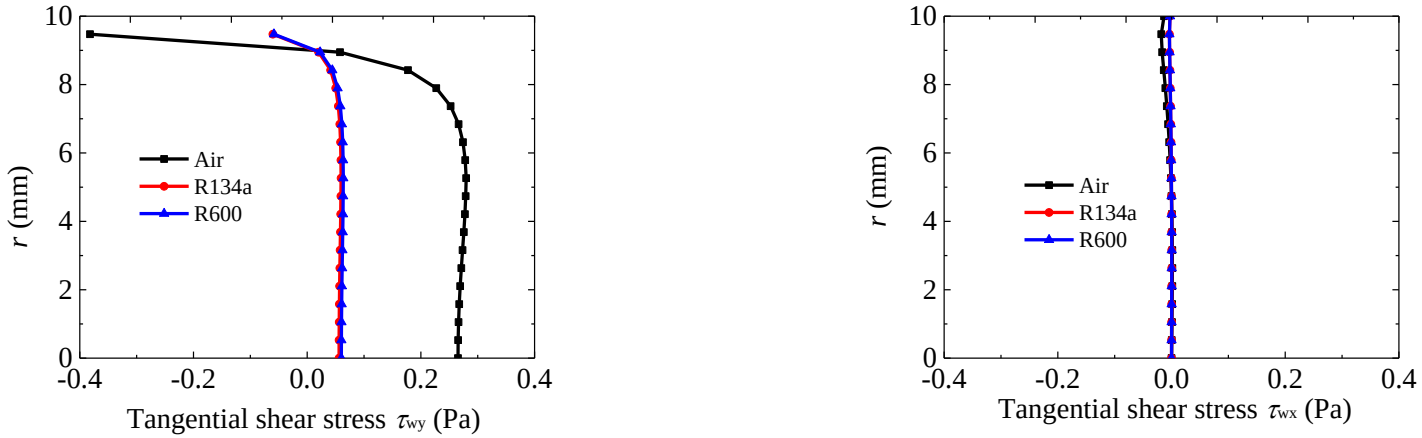

Figure 4.22 Shear stress at the cross-section (x = 30 mm, μ_c = 0.2) for air, R134a and R600 in y/radial (a) and x/axial directions (b)

It can be noted in Figure 4.15b that R600 has a slight negative heating effect when the μ_c drops to below 0.2. It is believed that, under this condition, the temperature drop caused by the adiabatic expansion from the VT inlet to the hot end is larger than the temperature increase from the TSE. This is supported by the estimates (Table 4.9) from EES[124] that, the $\Delta p_{in\text{-}h}$ increases with decreasing μ_c, and at the same time the corresponding isentropic and isenthalpic temperature drops[12] increase.

Table 4.9 Isentropic and isenthalpic temperature drop corresponding to the pressure drop at different cold mass flow ratios for R600

μ_c	Pressure drop through VT inlet and hot end kPa	Isentropic temperature drop K	Isenthalpic temperature drop K
0.1	1.94	4.44	0.51
0.2	1.89	4.30	0.50
0.3	1.86	4.18	0.49
0.4	1.82	4.06	0.48
0.5	1.78	3.92	0.47
0.6	1.74	3.80	0.47
0.7	1.71	3.67	0.45
0.8	1.67	3.52	0.44
0.9	1.63	3.40	0.44

Figure 4.23a-f shows the temperature distributions within the VT at two μ_c (0.1 and 0.9) for air, R134a and R600. In general, the temperature distributions of R134a and R600 are very similar to that of air and to other researchers'[103, 125] too. The temperature decreases along the axis from the hot end towards the cold end, and increases radially outwards across any sections. However, at μ_c = 0.1, local warm spots are noted at the cold end (Figure 4.23a and e for air and R600[13], respectively). These are caused by small flow recirculation as exemplified in the velocity vectors plots of R600 (Figure 4.24), and these are expected to have an impact on the VT performance. At very small μ_c (e.g. 0.01), this flow recirculation would be much larger, as also noted in [94].

[12] It is widely believed that the temperature drop in the VT is larger than the isenthalpic temperature drop, but smaller than the isentropic temerature drop (as friction existis in the roation)

[13] Local warm spot also exists at the cold end for R134a at μ_c = 0.1. It can be observed when the temperature scale include more colours

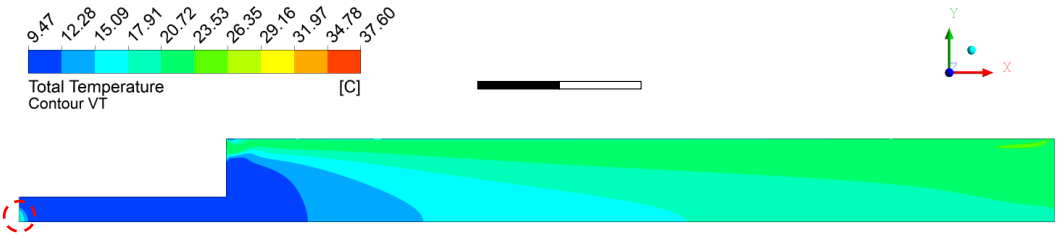

a. μ_c = 0.1, air

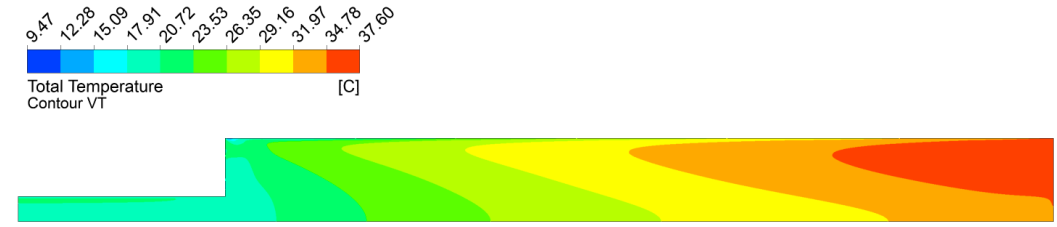

b. μ_c = 0.9, air

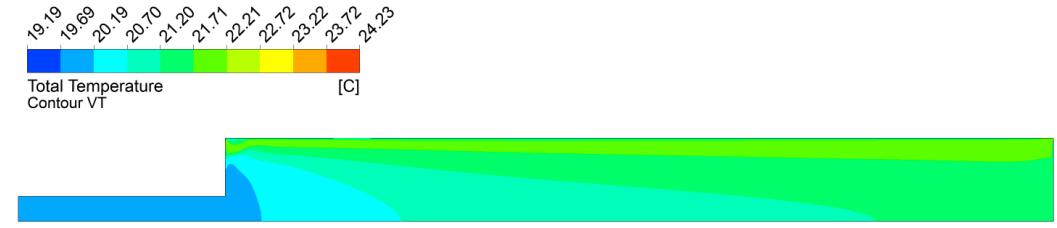

c. μ_c = 0.1, R134a

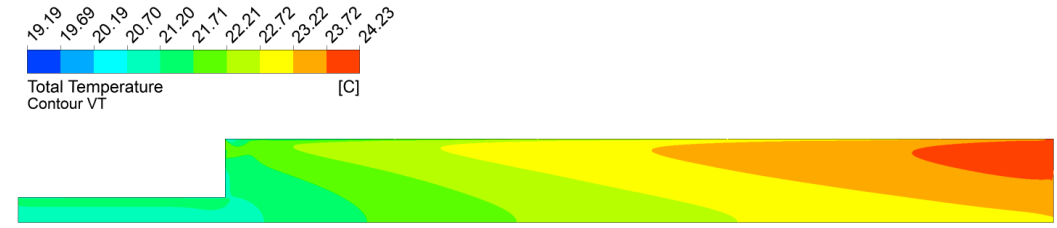

d. μ_c = 0.9, R134a

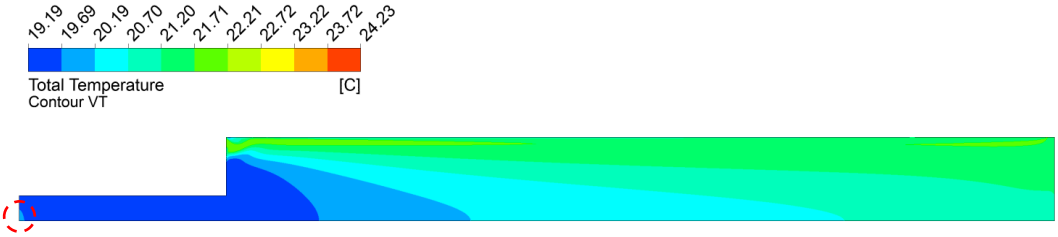

e. μ_c = 0.1, R600

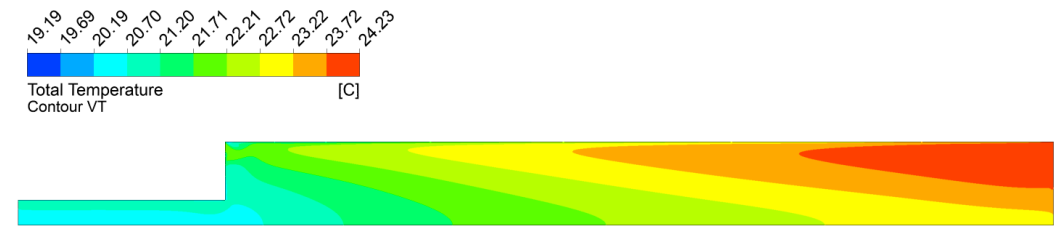

f. μ_c = 0.9, R600

Figure 4.23 Temperature distribution at different cold mass flow ratios

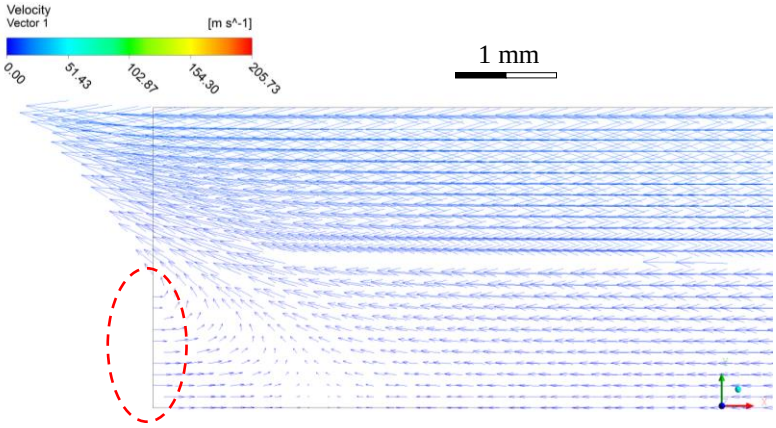

Figure 4.24 Velocity vectors near the cold end at $\mu_c = 0.1$ for R600

4.2.2 Influence of inlet pressure p_{in} on TSE

The chamber inlet total pressure is varied from 150 kPa to 350 kPa at an increment of 50 kPa, while the inlet total temperature is kept constant at 295 K, and both the hot end and the cold pressures are adjusted to control the cold mass flow ratio μ_c between 0.1 and 0.9. The influence of inlet pressure on the TSE is presented in Figure 4.25 for air, R134a and R600. Though all the three fluids share some common trends, individually they have certain distinctive features. At a given inlet pressure, air produces the largest cooling effect while R134a and R600 have similar cooling effects.

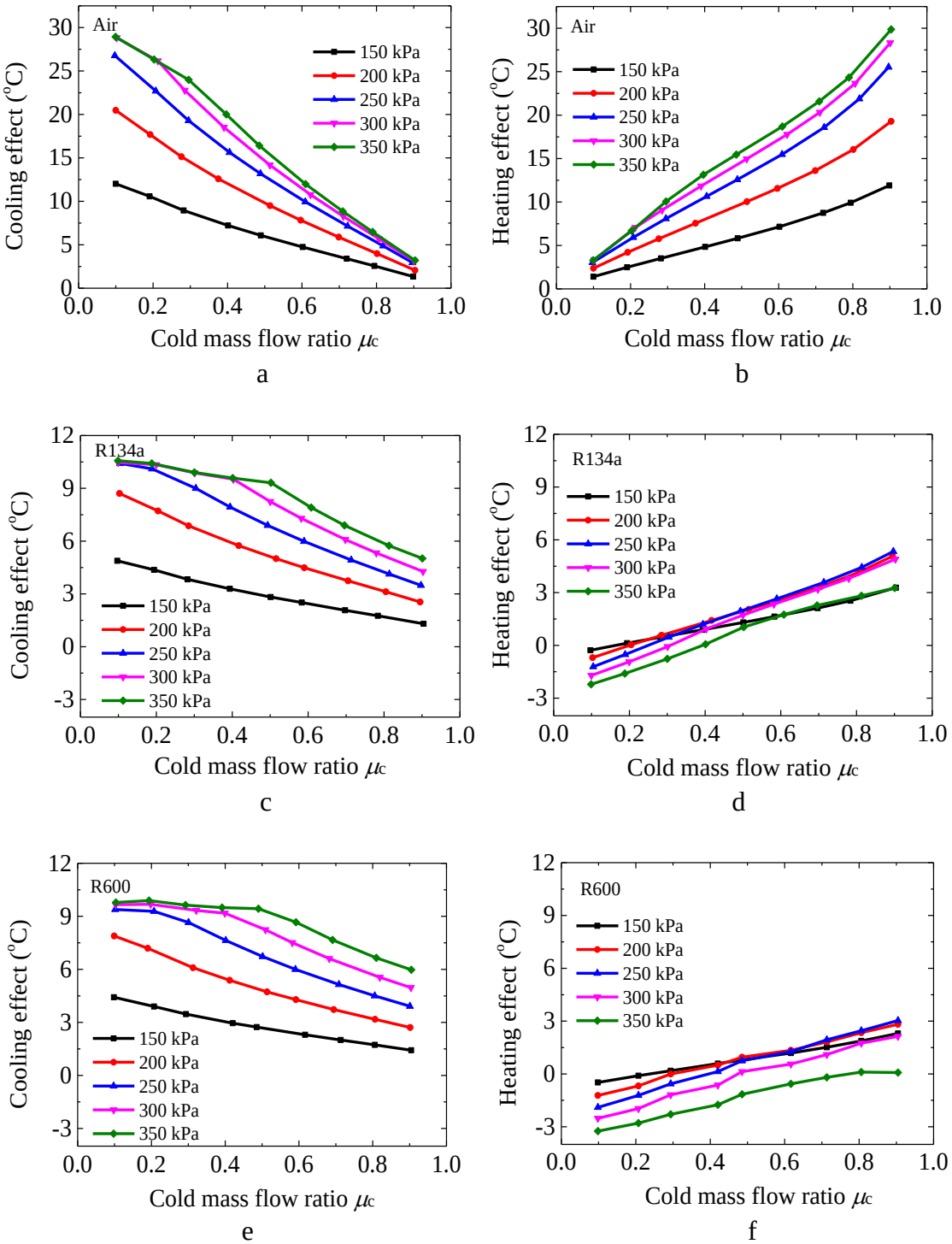

Figure 4.25 TSE under different inlet pressures of air (a) and (b), R134a (c) and (d), R600 (e) and (f), T_{in} = 295 K

1) The cooling effect

At a relatively low inlet pressure, the cooling effect increases with decreasing μ_c, and in general, this trend continues at higher inlet pressures; it is clear that air has a much higher rate of increase with respect to μ_c when compared to R134a and R600. However, as the inlet pressure increases the rate of increase of the cooling effect with respect to decreasing μ_c drops off at a certain μ_c value. For instant, at 300 kPa inlet pressure, the rate drops off at around μ_c equals to 0.2, 0.4 and 0.4 respectively for air, R134a and R600; when the inlet pressure is increased further to 350kPa, the corresponding rate drops off at a higher μ_c value - 0.3, 0.5 and 0.5 respectively.

In addition, for a given μ_c, in general the cooling effect increases with increasing inlet pressure, but the exact pattern would depend on the fluid choice and the μ_c value. For air, it appears that at a high μ_c (= 0.9), the cooling effect only increases by a small margin when the inlet pressure is gradually raised. On the other hand, at a small μ_c (= 0.1), much larger increases in cooling effect can be noted but it will stop increasing when a certain pressure is reached. For R134a and R600, a similar pattern is noted at small μ_c values, but at a high μ_c (= 0.9), the cooling effect is more sensitive to the changes in the inlet pressures when compared to air.

The above behaviour could be related to changes in the VT chamber inlet velocities (Figure 4.26), and the pressure drop between the VT inlet and the cold end $\Delta p_{\text{in-c}}$/hot end $\Delta p_{\text{in-h}}$ (Figure 4.27). All three fluids have the similar pressure drop $\Delta p_{\text{in-c}}$, while air has the largest VT chamber inlet velocities.

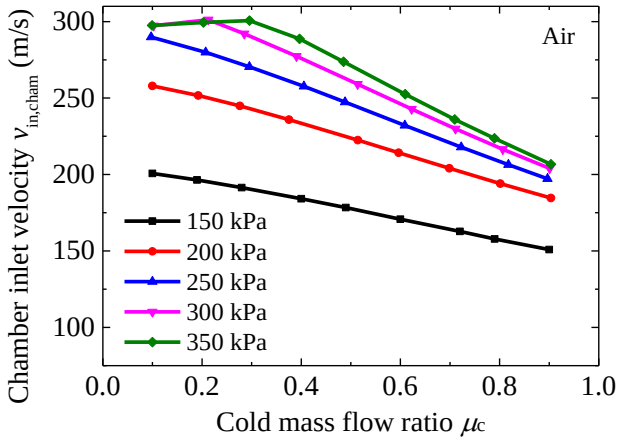

a

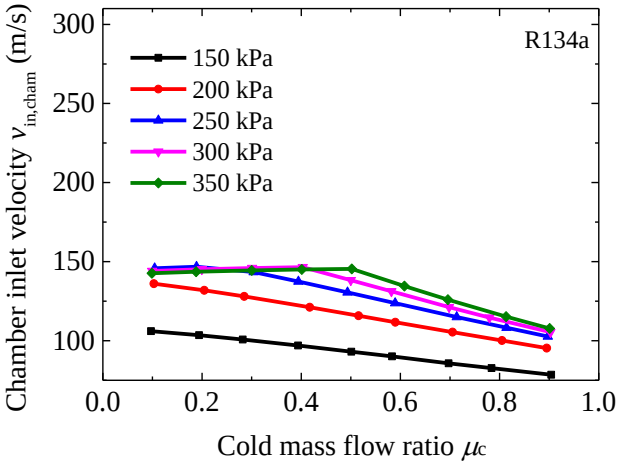

b

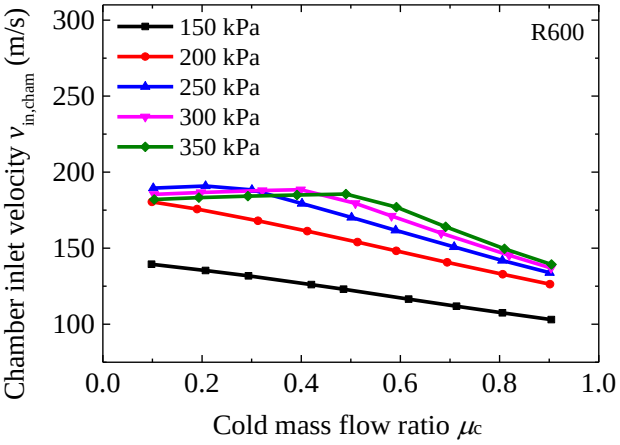

c

Figure 4.26 Inlet velocities of the VT chamber under different inlet pressure: air (a), R134a (b) and R600 (c)

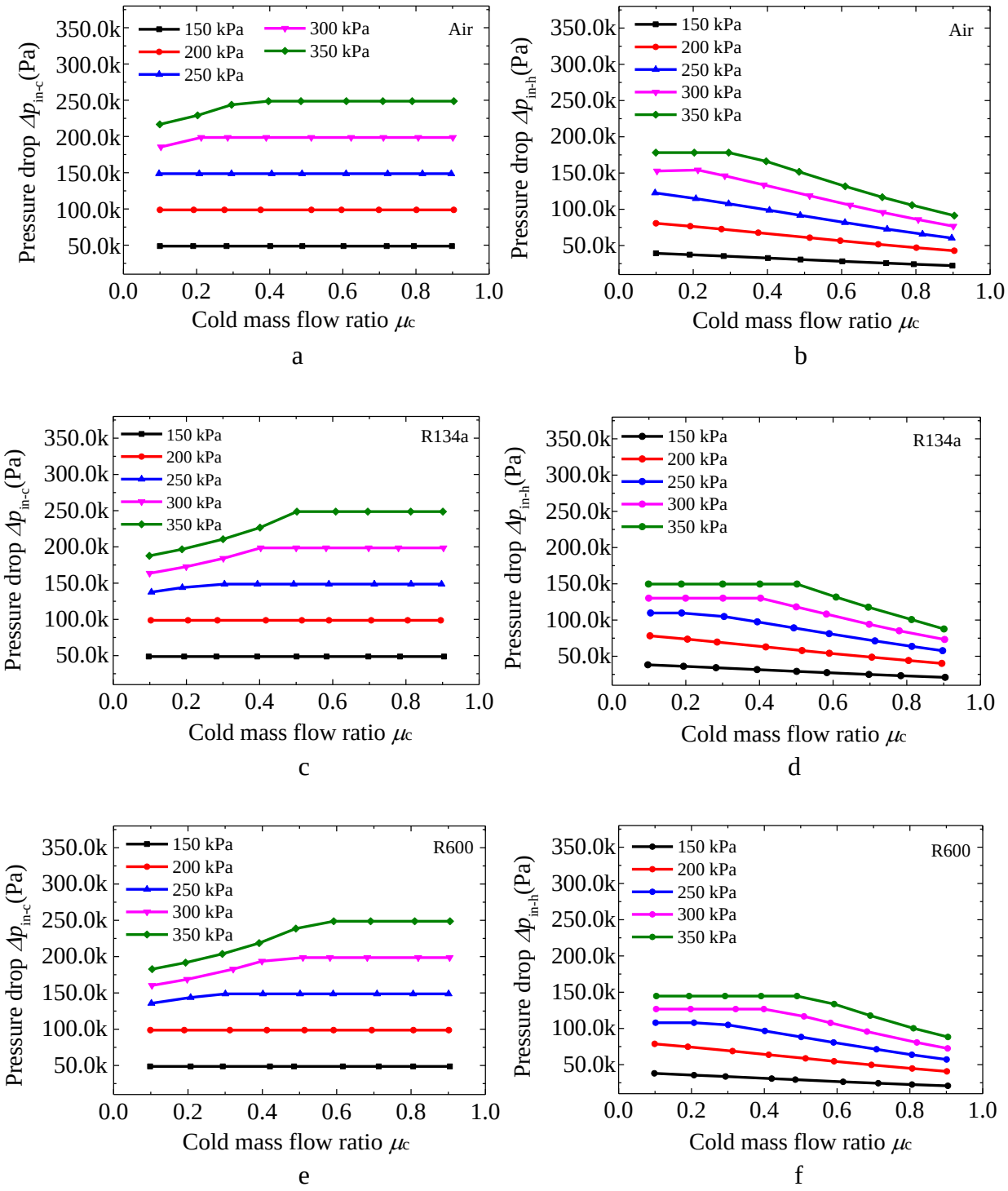

Figure 4.27 Pressure drops through the VT for three fluids, $\Delta p_{in\text{-}c}$ for air (a), R134a (c), R600 (e), and $\Delta p_{in\text{-}h}$ for air (b), R134a (d), R600 (f)

As seen in Figure 4.26, at any μ_c larger than 0.3 for air, or 0.5 for R134a and R600, a higher inlet pressure would lead to a larger chamber inlet velocity, which is expected to generate a stronger rotating flow. Figure 4.27 indicates that a higher inlet pressure always result in a larger $\Delta p_{in\text{-}c}$ which would produce a stronger adiabatic expansion in

the VT. Their combined influence is to create a larger cooling effect when the inlet pressure is raised. However, for the same incremental increase (50kPa) of the inlet pressure, the corresponding incremental gains in the inlet velocities are in fact diminishing (as shown in Figure 4.26), resulting in accordingly smaller gains in the cooling effects as evident in Figure 4.25. The corresponding incremental changes in $\Delta p_{\text{in-c}}$ remain relative constant when the inlet pressure is increased, as shown in Figure 4.27, suggesting the rotating flow, when compared to the expansion process, is the dominant factor governing the TSE.

For smaller μ_c (less than 0.3 for air, and less than 0.5 for R134a and R600), in Figure 4.26, there is also an initial increase of the chamber inlet velocity as well as an increase in $\Delta p_{\text{in-c}}$ when the inlet pressure is raised, as seen in Figure 4.27. However up to a certain value of inlet pressure (300 kPa for air; 250 kPa for R134a and R600), beyond which any further increases of the inlet pressure would bring a small drop of the inlet velocities and a small increase in $\Delta p_{\text{in-c}}$. Therefore, as a net result, the cooling effect only increases initially and remains relatively unchanged at higher inlet pressures.

Figure 4.28 and Figure 4.29 show the shear stresses and the tangential velocities for air and R134a respectively, at the cross-section (x = 30 mm) and at μ_c = 0.2 and 0.7. It can be shown that, at μ_c = 0.2, for air, when the VT inlet pressure is increased to larger than 300 kPa (250 kPa for R134a), both τ_{wy} and tangential velocity starts to decrease. On the other hand, when μ_c = 0.7, for both air and R134a, the τ_{wy} and tangential velocity increase with increasing inlet pressure, though at a reduced rate. For both μ_c = 0.2 and 0.7, the shear stress τ_{wy} in the radial direction is much larger than τ_{wx}.

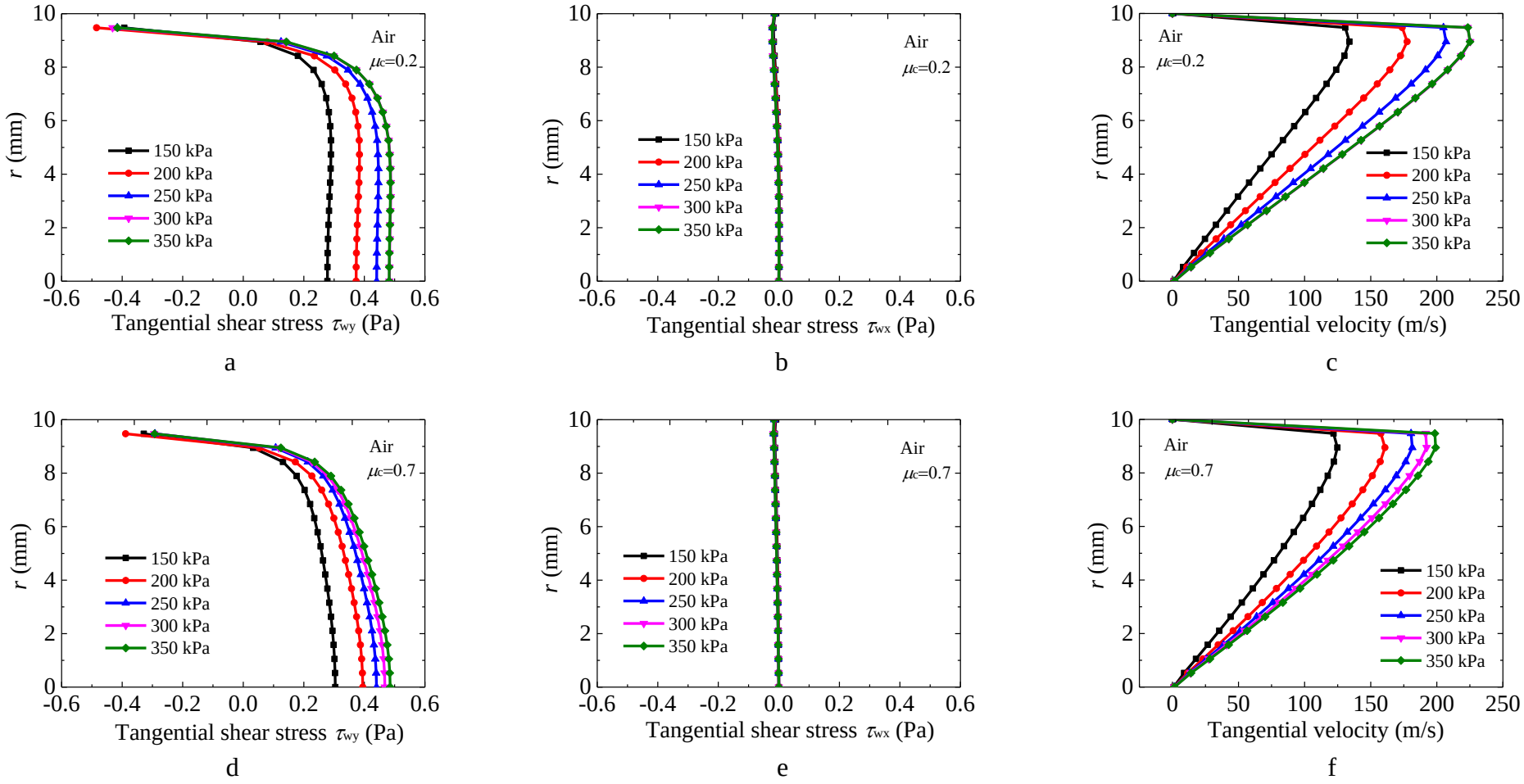

Figure 4.28 Shear stresses and tangential velocities at the cross-section (x = 30 mm) of air at μ_c = 0.2 and 0.7

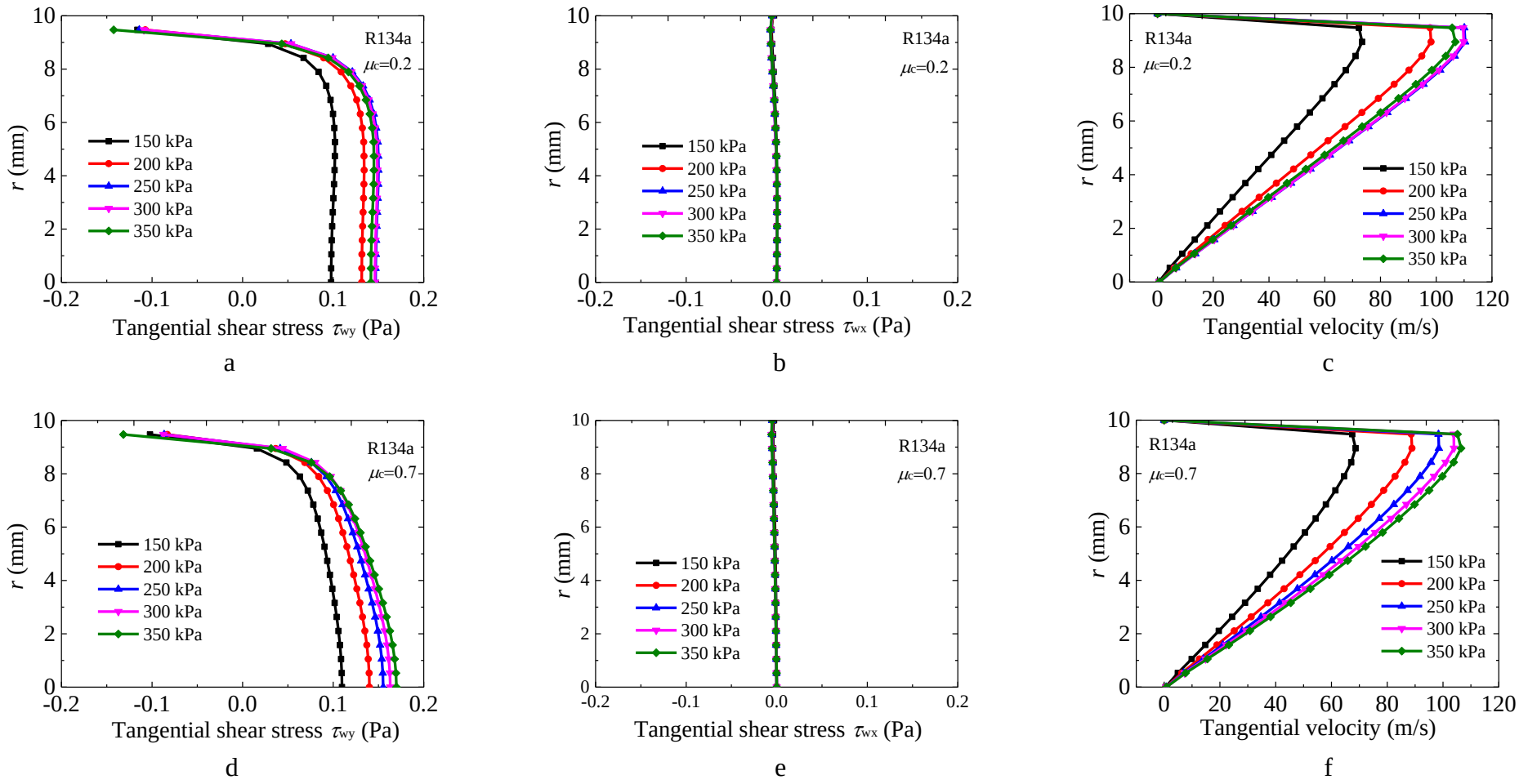

Figure 4.29 Shear stresses and tangential velocities at the cross-section (x = 30 mm) of R134a at μ_c = 0.2 and 0.7

2) The heating effect

As shown in Figure 4.25, in response to increasing the inlet pressure, both R134a and R600 behave rather differently when compared to air, though in general for a given pressure, the heating effect increases with increasing μ_c.

For air, an increase of the inlet pressure produces an increase of the heating effect, though the net gain in the heating effect is progressively getting smaller. As explained previously, this is closely linked to the increasing chamber inlet velocity as presented in Figure 4.26. Although the corresponding pressure drop $\Delta p_{in\text{-}h}$ (shown in Figure 4.27 is also increasing, resulting in a larger temperature drop due to the adiabatic expansion, the influence is not strong enough to cancel out the heating effect.

Quite opposite to air, for R134a and R600, in general with lower values of μ_c (less than around 0.4 ~ 0.5) the heating effect decreases with increasing inlet pressures, leading to little or even negative heating effects, i.e. the hot end temperature is less than the inlet temperature; a similar observation was made in [21]. Though an interesting observation, it has little practical significance when the VT is to be used mainly as a heating device which usually employs higher values of μ_c. It appears that at a low inlet pressure (150 kPa), it has a lower rate of change of heating effect with respect to μ_c, i.e. a smaller gradient, leading to it crossing other pressure lines which have similar gradients, as seen in Figure 4.25d and f. This observation may not have any practical significantly when higher inlet pressures are used, though it would be interesting to understand the cause of this.

Removing the 150 kPa pressure line from consideration, a more recognisable trend emerges, i.e. at higher μ_c values (larger than 0.5), when the inlet pressure is increased, there are not many changes in the heating effect until reaching certain higher pressure value, then one would see a significant drop in the heating effect. As seen for R600, when the inlet pressure is raised to 350 kPa, the heating effect has completely disappeared (i.e. negative heating effect).

The discussion for the above observations is presented below.

As noted in Figure 4.27b, d and f, a higher pressure drop between the VT inlet and the hot end ($\Delta p_{in\text{-}h}$) is obtained at a higher inlet pressure, and all the three fluids have similar trends both qualitatively and quantitatively. Therefore, to understand the causes of the differences in the heating effects between the air and refrigerants seen in

Figure 4.25, two additional CFD simulations were run with the following two boundary conditions.

- The fluid enters the VT chamber in x-direction with zero y and z velocity components – referred as a "Straight" run. The cold end is closed as a "wall" boundary setup in Fluent, i.e. one inlet and one outlet flow configuration and thus no TSE is generated. The associated temperature drop is expected to be purely a result of thermal expansion due to pressure drop.
- The fluid enters the VT chamber with prescribed x, y and z velocity components – referred as a "Rotation" run. The cold end still remains closed as above and thus no TSE.

The two runs are used to calculate the temperature drops (ΔT) between the VT inlet and the hot end caused only by the expansion corresponding to the same $\Delta p_{\text{in-h}}$ presented in Figure 4.27 at μ_c = 0.1 and 0.7 for R134a[14] and air. The results are presented in Table 4.10, in which the Joule-Thomson (J-T) effect (isenthalpic temperature drop[126-128]) corresponding to the same $\Delta p_{\text{in-h}}$ is also included.

Table 4.10a Temperature drop (ΔT) for R134a at the corresponding pressure drop $\Delta p_{\text{in-h}}$ (μ_c = 0.1 and 0.7)

p_{in}	ΔT (K), μ_c = 0.1			ΔT (K), μ_c = 0.7		
kPa	Straight	Rotation	J-T	Straight	Rotation	J-T
150	0.47	0.71	0.87	0.31	0.45	0.57
200	0.94	1.48	1.80	0.61	0.92	1.12
250	1.32	2.11	2.56	0.88	1.34	1.66
300	1.59	2.53	3.08	1.17	1.80	2.23
350	1.86	2.94	3.59	1.48	2.29	2.82

Table 4.10b Temperature drop (ΔT) for air at the corresponding pressure drop $\Delta p_{\text{in-h}}$ (μ_c = 0.1 and 0.7)

p_{in}	ΔT (K), μ_c = 0.1			ΔT (K), μ_c = 0.7		
kPa	Straight	Rotation	J-T	Straight	Rotation	J-T
150	0.0026	0.005	0.09	0.0008	0.001	0.06
200	0.0030	0.008	0.18	0.0001	0.005	0.12
250	0.0017	0.006	0.28	0.0003	0.006	0.17
300	0.0002	0.007	0.36	0.0023	0.007	0.22
350	0.0025	0.009	0.42	0.0017	0.008	0.27

[14] For illustration, R134a is employed in the simulation. Results show R600 has the same trend/behaviour as R134a, thus not presented

It should be noted that, the temperature drop for straight and rotation conditions is based on the total temperature which is typically used in evaluating the VT performance. The J-T effect temperature drop is based on the static temperature. It is chosen to act as an index to evaluate the overall temperature drop.

It can be noted in Table 4.10 that, as air behaves close to ideal gas, there are hardly any temperature drops associated with the expansion process within the entire range of inlet pressures, regardless what boundary conditions are used. Therefore, the heating effect achieved (Figure 4.25b) is mainly a result of TSE.

For the same pressure drop, it appears that the temperature drop due to thermal expansion could achieve a bigger value when rotational flow is involved; this is apparent when the results of "straight" run and "rotation" run are compared. For the same fluid, a higher μ_c always produces smaller temperature drop for R134a, it indicates that a smaller cancelling of the heating effect is expected.

Compared to air, the temperature drops of R134a are always much bigger, suggesting it could potentially cancel out larger part of the TSE, thus resulting in small or even negative heating effects as seen in Figure 4.25. This is particular the case for small μ_c values when inlet pressure exceeds certain values at which the chamber inlet velocity decreases (Figure 4.26) and at the same time the pressure drop $\Delta p_{\text{in-h}}$ (Figure 4.27) keeps increasing. At higher μ_c values, however, when the inlet pressure increases, and since both of the chamber inlet velocities (Figure 4.26) and pressure drop $\Delta p_{\text{in-h}}$ (Figure 4.27) increase, the heating effect could remain relatively unchanged, except when the inlet is raised above certain values then once again low or negative heating effects are possible.

At 150 kPa inlet pressure, it seems that the corresponding chamber inlet velocity is too low to be effective for generating good heating effect. Based on the above, one can preliminary conclude that for R134a and R600, both too low or too high inlet pressures could lead to poor VT heating performance.

It would be useful to know how both the cooling/heating effects and the mass flow rates vary with the inlet pressures, as when incorporating the VT in a system, both would affect the delivered capacities. Figure 4.30 presents the inlet mass flow rate under different inlet pressures for three fluids. The inlet mass flow rate is calculated by Fluent when the VT inlet pressure and temperature are set, but it changes according to the specified cold mass flow ratio. It can be noted that, in general for a

given μ_c, a higher inlet p_{in} corresponds a larger VT $\dot{m}_{in}$, and for a given p_{in} an increase in μ_c leads to a drop of $\dot{m}_{in}$. This has useful practical implication when the *COP* of the system under different μ_c are compared, as the work input to the system may change even when the VT inlet pressure remains unchanged.

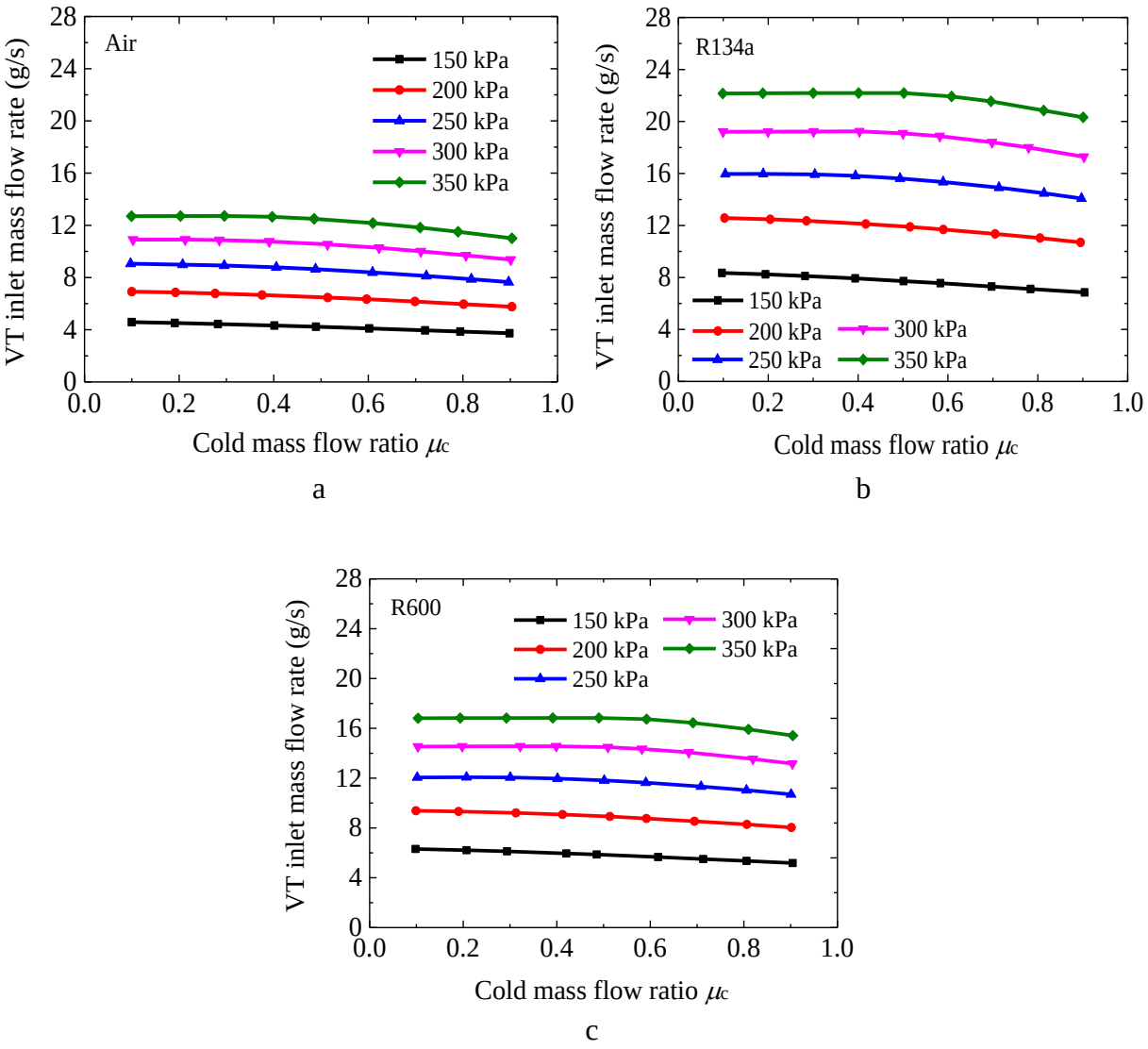

Figure 4.30 VT inlet mass flow rate under different inlet pressure for three fluid: (a) air, (b) R134a, (c) R600

Separate numerical runs with the inlet chamber mass flow rate $\dot{m}_{in}$ varied from 4.1 g/s to 10.25 g/s for air and from 4.1 g/s to 16.4 g/s for R134a and R600 were carried out; the inlet temperature was kept constant at T_{in} = 295K. The same initial flow rate of 4.1g/s was used for all the three fluids, however as R134a and R600 have very small associated velocities, a larger increment of $\dot{m}_{in}$, compared to that of air, was used to ensure there are sufficient increase of velocities to generate noticeable differences in TSE.

The influence of $\dot{m}_{in}$ on the cooling and heating effects are presented in Figure 4.31

for air, R134a and R600. The results match very well with those presented in Figure 4.25, as expected both the variations of inlet pressures and mass flow rates follow the same explanations; this is evident in Figure 4.32 and Figure 4.33 which show respectively the variations of chamber inlet velocities and the variations of pressure drop ($\Delta p_{\text{in-c}}$ and $\Delta p_{\text{in-h}}$) with inlet mass flow rates for all the three fluids.

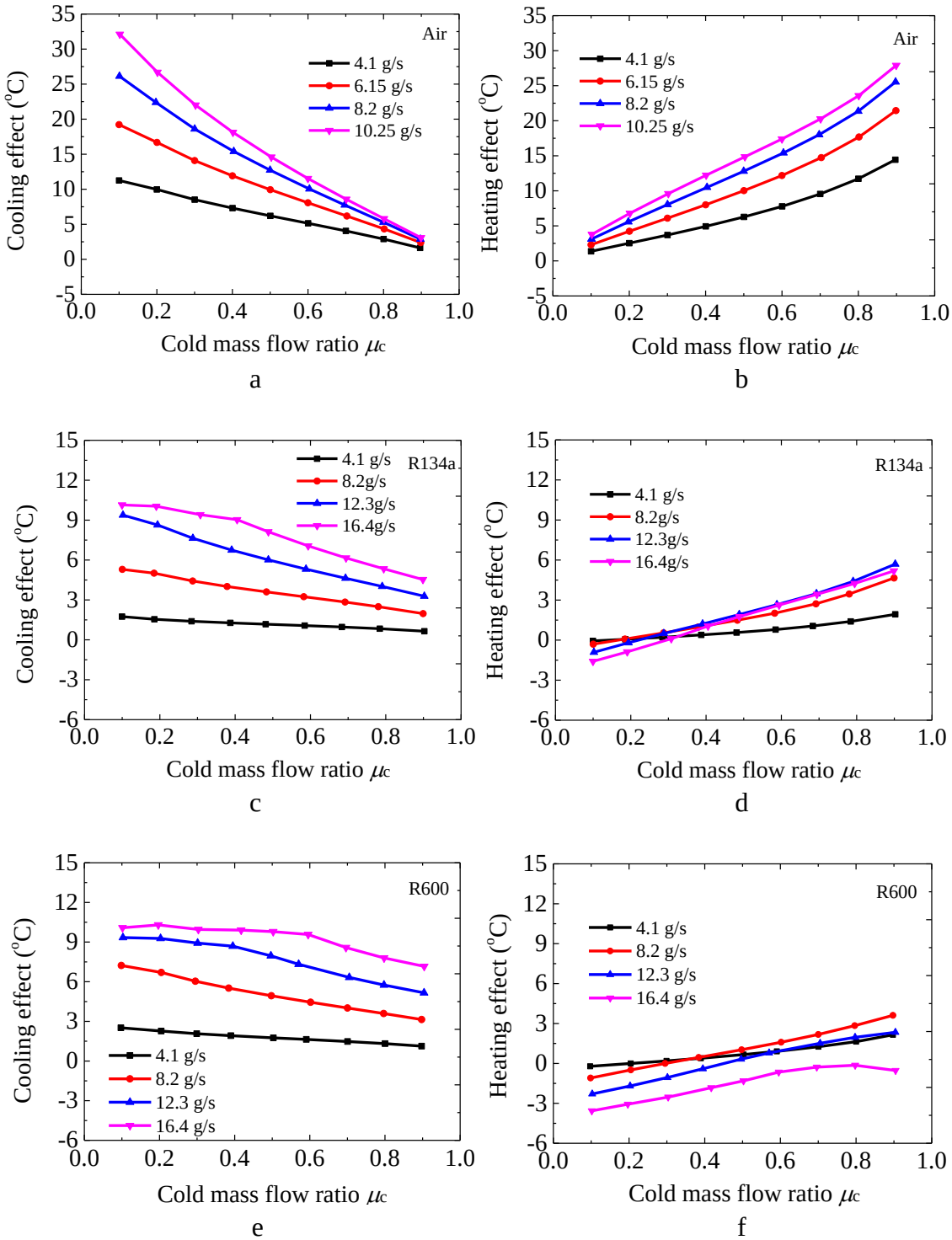

Figure 4.31 TSE under different $\dot{m}_{\text{in}}$ for air (a) and (b), for R134a (c) and (d), for R600 (e) and (f), T_{in} = 295 K

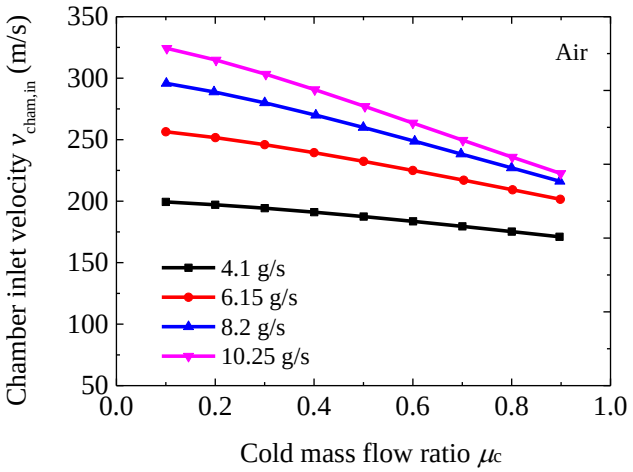

a

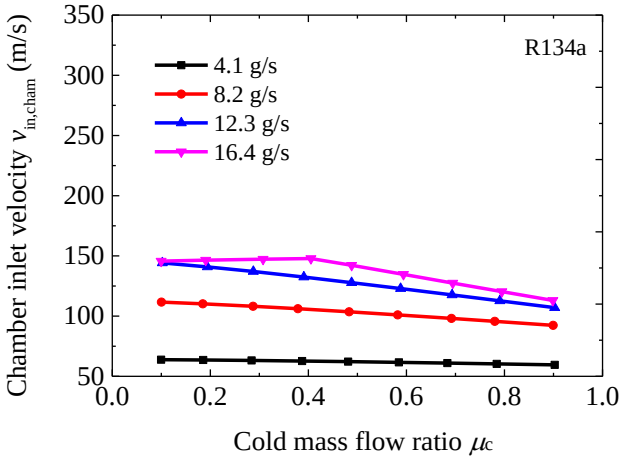

b

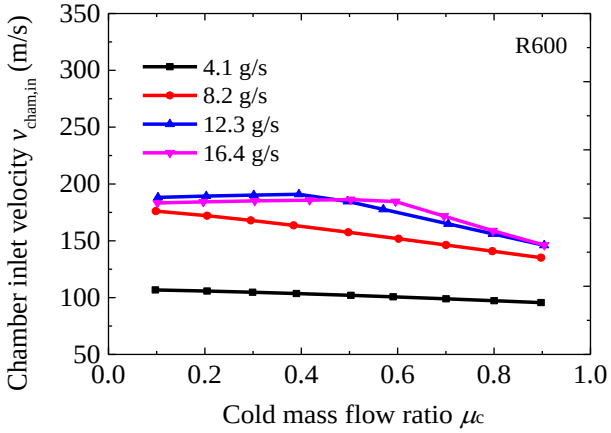

c

Figure 4.32 Chamber inlet velocities under different inlet mass flow rate for air (a), R134a (b) and R600 (c)

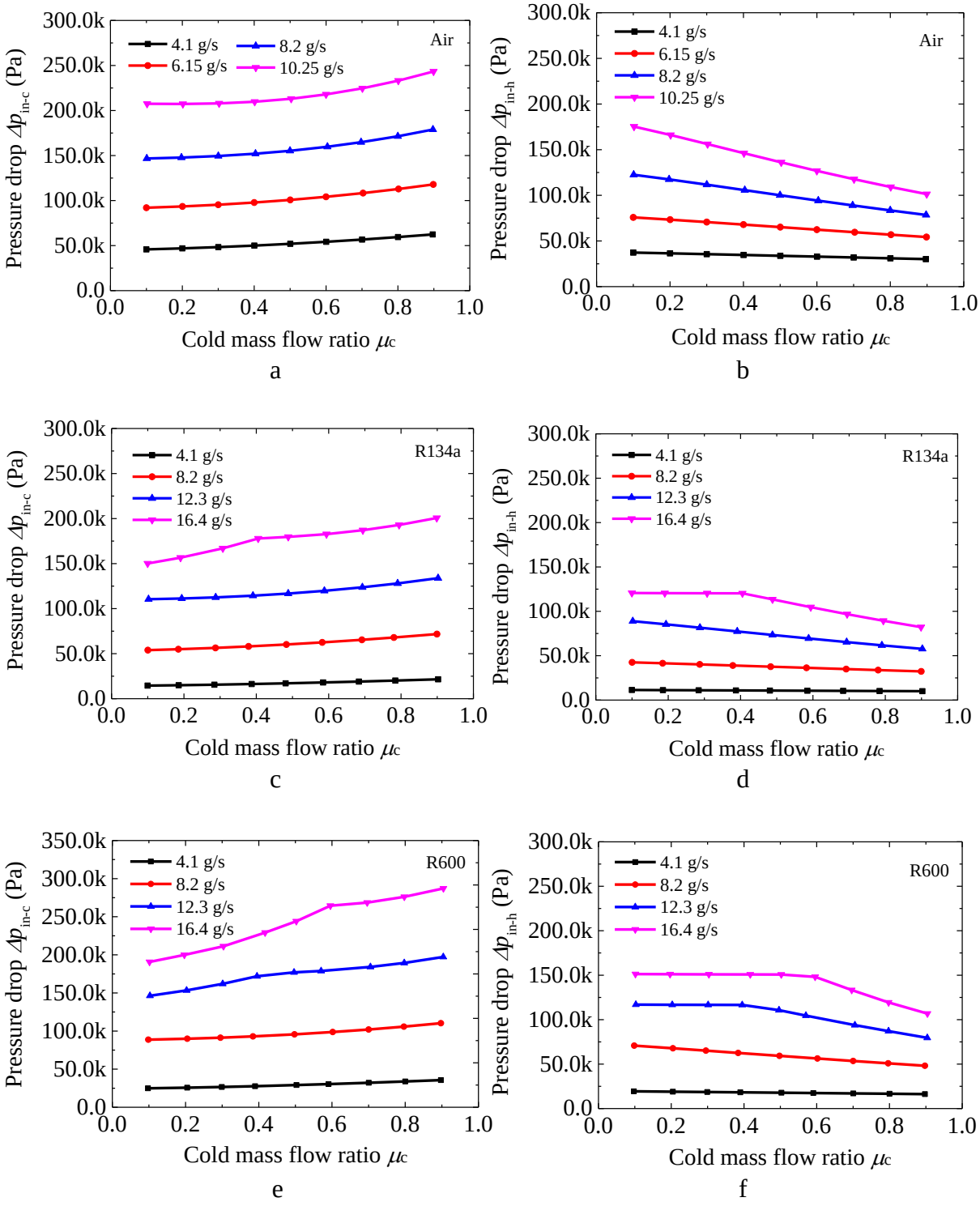

Figure 4.33 Pressure drop through the VT, $\Delta p_{in\text{-}c}$ for air (a), R134a (c), R600 (e), and $\Delta p_{in\text{-}h}$ for air (b), R134a (d), R600 (f)

4.2.3 Influence of inlet temperature T_{in} on TSE

Figure 4.34 shows the cooling effect (at $\mu_c = 0.3$) and the heating effect (at $\mu_c = 0.7$) for air, R134a and R600, over a range of inlet temperatures between 280 K and 315 K.

It can be observed, for all three fluids, an increase of the inlet temperature leads to an increase of the cooling effect, as a larger inlet temperature produces both a higher chamber inlet velocity (Figure 4.35a) and a larger pressure drop $\Delta p_{\text{in-c}}$ (Figure 4.36a), thus respectively generating a stronger rotation in the VT chamber and a stronger expansion process.

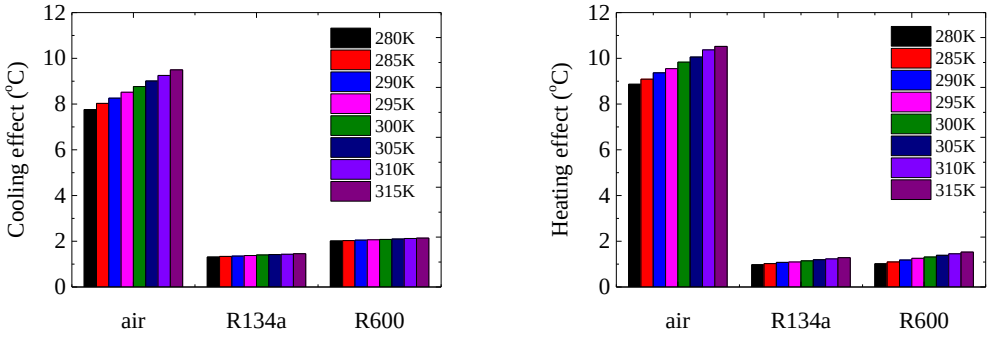

Figure 4.34 TSE at μ_c = 0.3 (a) and μ_c = 0.7 (b) at different T_{in} for air, R134a and R600

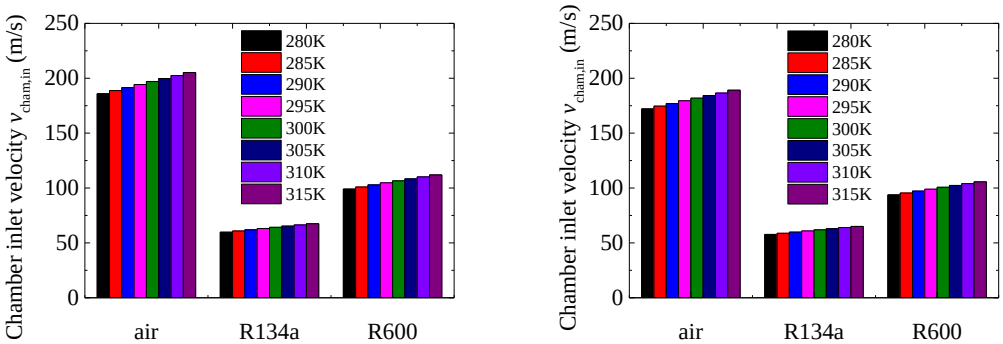

Figure 4.35 Chamber inlet velocities $v_{\text{cham,in}}$ at μ_c = 0.3 (a) and μ_c = 0.7 (b) at different T_{in} for air, R134a and R600

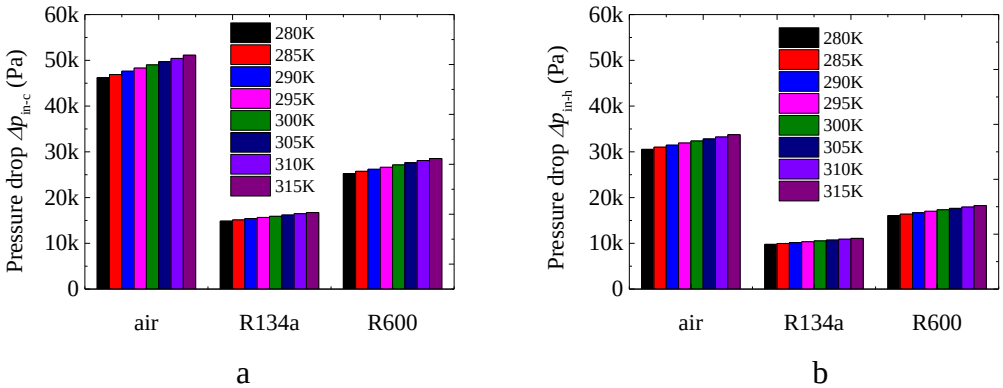

Figure 4.36 Pressure drops through the VT $\Delta p_{\text{in-h}}$ at μ_c = 0.3, $\Delta p_{\text{in-c}}$ (a) and μ_c = 0.7, $\Delta p_{\text{in-h}}$ (b) at different T_{in} for air, R134a and R600

On the other hand, an increase in inlet temperature generally results in an increase in heating effect. Similar to the influence of increasing the inlet pressure or the mass flow

rate on the heating effect, a higher T_{in} generates a higher chamber inlet velocity (Figure 4.35b), leading to a larger TSE; the corresponding increase in pressure drop $\Delta p_{in\text{-}h}$ (Figure 4.36b) does not seem to bring any noticeable temperature cancellation.

Figure 4.37 shows the variations of hot end pressure with T_{in} at μ_c = 0.3 and 0.7. In general, at a higher inlet temperature, the hot end pressure must be adjusted to a higher value to achieve the specified cold mass flow ratio μ_c. This observation has important practical implication when dealing with integrating the VT into a system in which the hot pressure is likely to vary. It is noticed that both the cooling and heating effect as well as the hot end pressure of R134a are rather insensitive to changes in the inlet temperature, when compared to air and R600. This is most likely related to the changes of thermal properties with temperature.

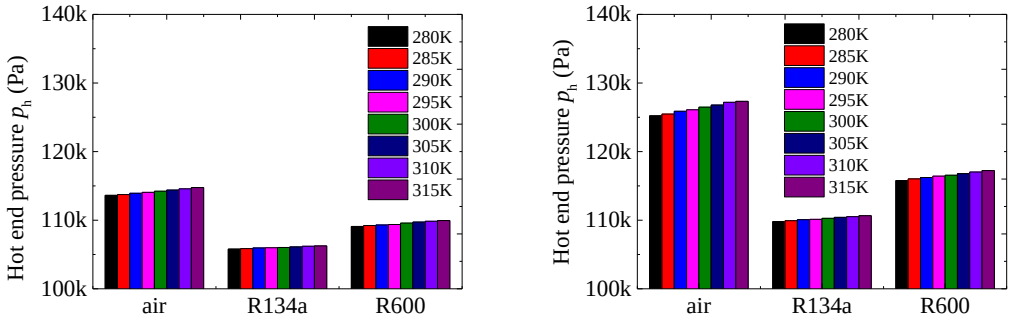

Figure 4.37 Hot end pressure p_h at μ_c = 0.3 (a) and μ_c = 0.7 (b) at different T_{in} for air, R134a and R600

This chapter described in detail the flow domain, the meshing and the k-ε model implement in the study. Both quantitative and qualitative model validations have been attempted. The development of the flow and thermal processes in the VT are analysed. The influence of the boundary conditions on TSE are preliminarily examined, the unique difference between the air and refrigerates (R134a and R600) heating effect for different VT inlet pressures are studied. A temperature cancelling process for the heating effect of refrigerants is explained.

To summarise, the parametric analysis provides a useful insight into how the VT behaves under different boundary conditions, and more importantly enabled the author to understand better the differences on operating characteristics between air and some commonly used refrigerants. This is particularly important when considering putting

a VT into a system and different working fluid choices. In many aspects, qualitatively refrigerants behave similar to air, with a noticeable cooling effect produced at lower μ_c values and heating at high μ_c values. The key summary of these observation is presented below.

The effects of p_{in} or $\dot{m}_{in}$ on heating effect are different between air and refrigerants. As real gases, refrigerants seem to experience a larger temperature reduction caused by the expansion process, thus cancelling out relatively a larger part of the heating effect when compared to air.

Under the same VT inlet condition, R600 and R134a have rather different cooling effects but similar heating effect despite having the similar $\Delta p_{in\text{-}c}$ and $\Delta p_{in\text{-}h}$, suggesting that other than $v_{cham,in}$ and pressure drop influences, additional factors such as thermal-physical properties must be taken into account.

In the next chapter, the details of developing a refrigerant screening methodology will be presented. The boundary line for each chosen refrigerant is constructed, and several sub-groups are formed based on the VT inlet temperature/pressure. The influence of thermal-physical properties on TSE will be comprehensively studied, and the operating conditions' influence on TSE for chosen refrigerants will be thoroughly discussed.

5 Refrigerants screening for VT applications

Chapter 5 presents the systematic screening and evaluation of refrigerants for either cooling or heating applications in VT. The results are obtained by applying the methodology, introduced in Section 3.2, to all the chosen refrigerants, including R227ea, R236fa, R245ca, R245fa, R218, R600 (natural fluid), R600a (natural fluid) within Group 1, and R125, R134a, R143a, R152a, R290 (natural fluid), R32, R41 and R717 (natural fluid) for Group 2.

5.1 Identifying the suitable working regions for two group refrigerants

The procedures developed and described in Section 3.2.2, are applied to establish the suitable VT entry regions on the *T*-*s* diagram for individual refrigerants.

5.1.1 Group 1 refrigerants

Essentially it is to obtain the state values (*T*, *P*, *s*) at *Cr*, *P* and *X* as listed in Table 5.1, and to calculate the $\Delta T_{sh,min}$ and $\Delta T_{sh,max}$ corresponding to the range of T_{sat} between T_p and T_{cr}.

Table 5.1 State values (*T*, *P*, *s*) at *Cr*, *P* and *X* for R227ea, R236fa, R245ca, R245fa, R218 and R600

State points	Group 1 refrigerants					
	R227ea	R236fa	R245ca	R245fa	R218	R600
T_{cr} (°C)	101.75	124.92	174.42	154.01	71.87	151.98
p_{cr} (MPa)	2.93	3.20	3.93	3.65	2.64	3.80
s_{cr} (kJ/kg·K)	1.46	1.57	1.80	1.73	1.33	2.38
T_p (°C)	82.57	97.43	147.71	127.02	55.50	125.23
p_p (MPa)	1.96	1.84	2.45	2.21	1.84	2.43
s_p (kJ/kg·K)	1.51	1.64	1.86	1.80	1.37	2.51
p_x (MPa) (= p_{cr})	2.93	3.20	3.93	3.65	2.64	3.80
s_x (kJ/kg·K) (= s_p)	1.51	1.64	1.86	1.80	1.37	2.51
T_x (°C)	103.83	128.01	177.41	157.05	73.73	154.87

The calculated $\Delta T_{sh,min}$ (based on the specified range of VT inlet velocities, 5 ~ 20 m/s) and $\Delta T_{sh,max}$ for R227ea, are shown as an example, in Table 5.2, and the established suitable VT entry region above 20 °C is depicted in Figure 5.1.

Table 5.2 Identified degrees of superheat corresponding to the T_{sat} between T_p and T_{cr} for R227ea (based on the specified range of VT inlet velocities, 5 ~ 20 m/s)

T_{sat} °C	p_{sat} (p_m) MPa	T_m °C	$\Delta T_{sh,min}$ °C	$\Delta T_{sh,max}$ °C
101.75 (*Cr*)	2.925 (*Cr*)			
100	2.82	101.75	1.75	1.75
98	2.71	99.41	1.41	1.41
96	2.60	97.09	1.09	1.09
94	2.50	94.80	0.80	0.80
92	2.40	92.55	0.55	0.55
90	2.30	90.35	0.35	0.35
88	2.20	88.18	0.18	0.18
86	2.11	86.07	0.07	0.07
84	2.03	84.01	0.01	0.01
82.57 (*P*)	1.96	82.57	0.00	0.00

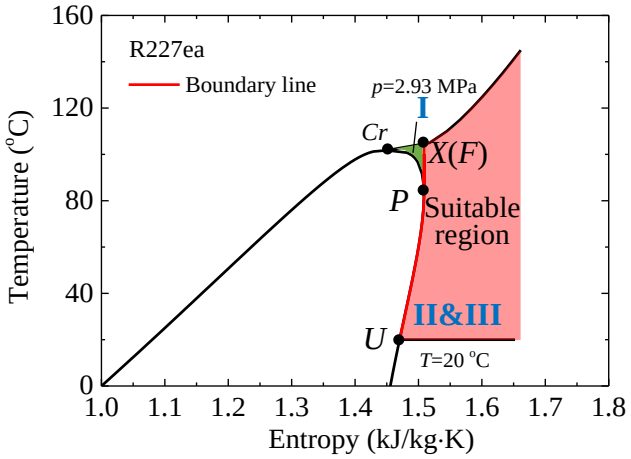

Figure 5.1 Identified suitable VT entry region (pink region) for R227ea

It is important to comment that the $\Delta T_{sh,min}$ and $\Delta T_{sh,max}$ are having the same values; same observations are also made for all the other chosen refrigerants within this group. This indicates that at this specified range of inlet velocities, the Sub-area IV does not exist for these refrigerants and in other words the boundary line becomes vertical when the VT inlet temperature is above T_p. It also means that this part of the boundary line FP overlaps with the line XP. The established suitable regions for individual refrigerants are presented in Figure 5.2, and all the entry state points in these regions are able to deliver gas state at the nozzle outlet.

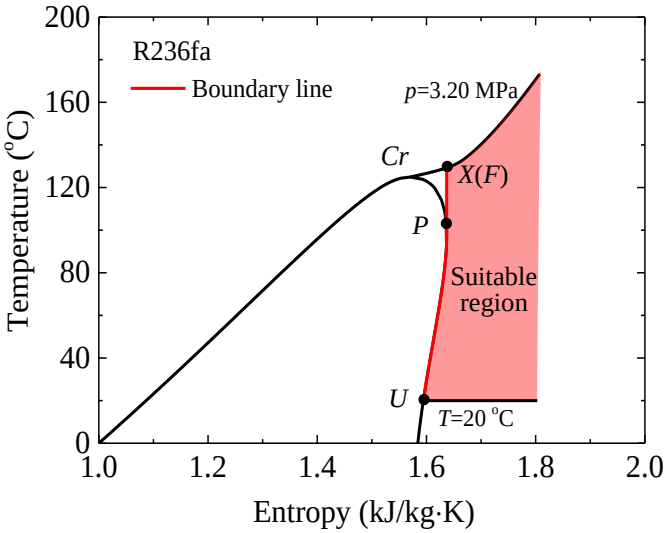
R236fa
Boundary line
p=3.20 MPa
Cr
X(F)
P
Suitable region
U
T=20 °C
Temperature (°C)
Entropy (kJ/kg·K)
0
40
80
120
160
200
1.0
1.2
1.4
1.6
1.8
2.0

a

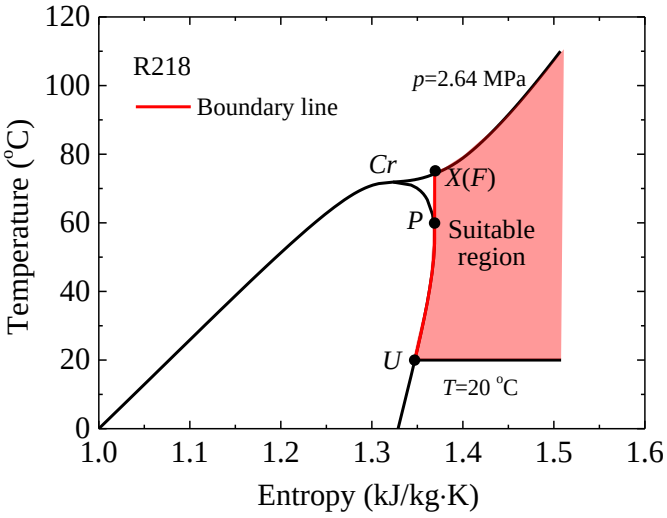
R218
Boundary line
p=2.64 MPa
Cr
X(F)
P
Suitable region
U
T=20 °C
Temperature (°C)
Entropy (kJ/kg·K)
0
20
40
60
80
100
120
1.0
1.1
1.2
1.3
1.4
1.5
1.6

b

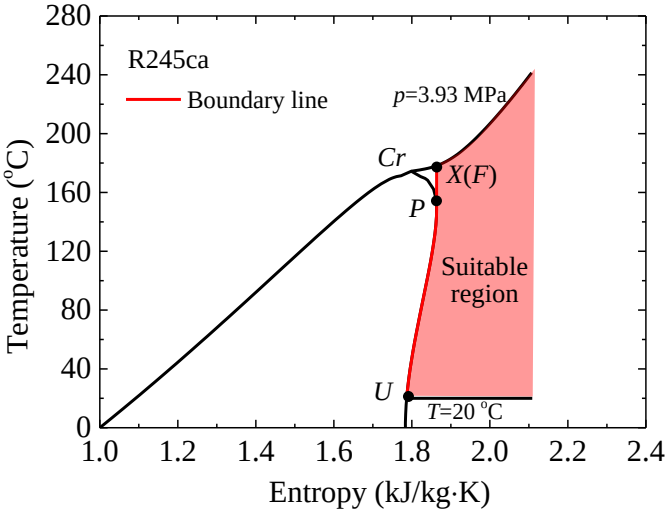
R245ca
Boundary line
p=3.93 MPa
Cr
X(F)
P
Suitable region
U
T=20 °C
Temperature (°C)
Entropy (kJ/kg·K)
0
40
80
120
160
200
240
280
1.0
1.2
1.4
1.6
1.8
2.0
2.2
2.4

c

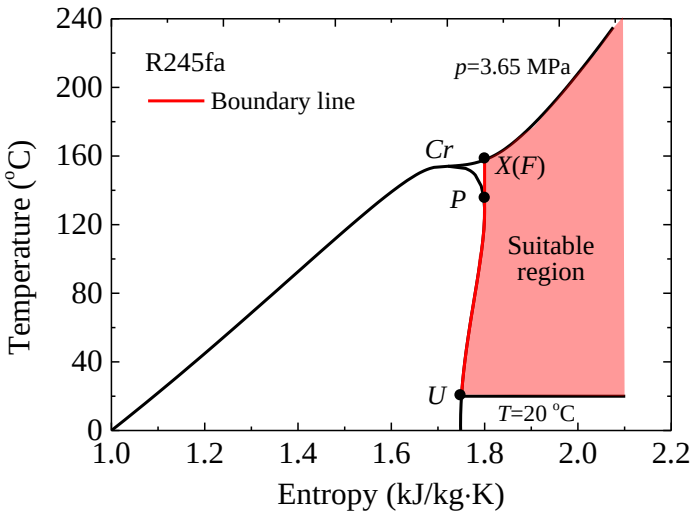

d

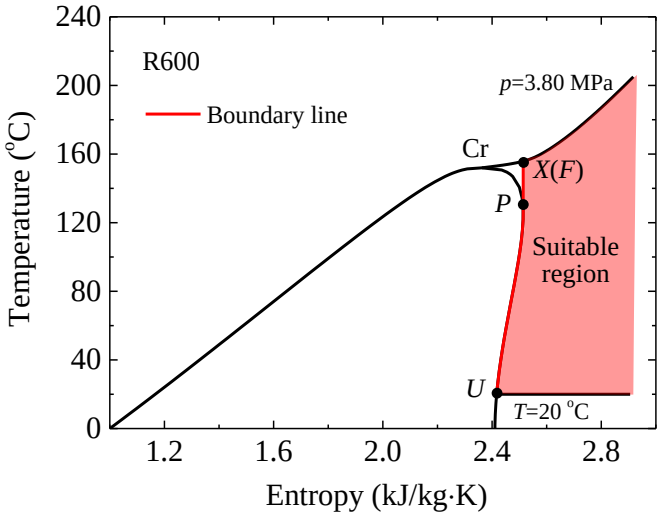

e

Figure 5.2 Established suitable VT entry region for R236fa (a), R218 (b), R245ca (c), R245fa (d) and R600 (e), based on VT inlet velocities 5 ~ 20 m/s

5.1.2 Group 2 refrigerants

The boundary lines of R134a for VT entry velocities at 5, 10, 15, 20, 100 and 200 m/s respectively are constructed and presented in Figure 5.3. It is noted that the positions of the boundary lines for the velocities between 5 to 20 m/s essentially remain unchanged; the same observation can be made for other refrigerants in this group. For a given nozzle inlet temperature and pressure, this should also lead to having very similar nozzle exit temperatures over this range of velocities as evidenced in Table 5.3.

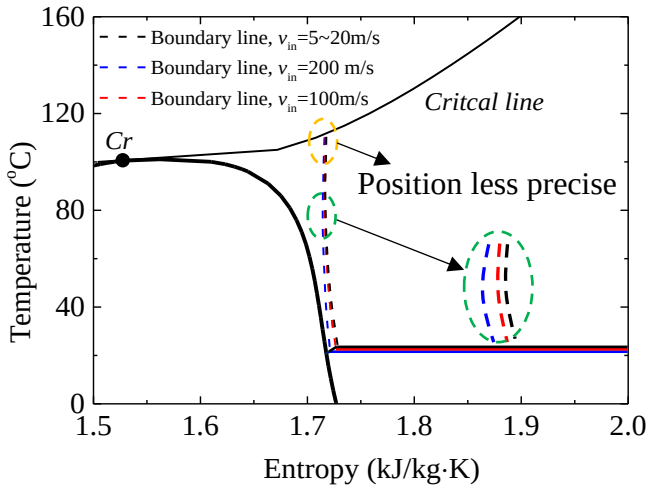

Figure 5.3 Boundary lines for R134a, a Group 2 refrigerant, at different entry velocities (5~20m/s, 100 m/s, 200 m/s)

Table 5.3 Nozzle outlet temperature at different combinations of entry velocity and inlet temperature (i.e. $T_{sat} + \Delta T_{sh}$) for R134a

T_{sat} °C	p_{in} MPa	ΔT_{sh} °C	v_{in} = 5 m/s °C	v_{in} = 10 m/s °C	v_{in} = 15 m/s °C	v_{in} = 20m/s °C
40	1.02	3.1	9.89	9.92	9.97	10.04
35	0.89	3.1	7.03	7.06	7.10	7.04
30	0.77	3.1	3.93	3.96	4.01	3.95
25	0.67	3.1	0.62	0.65	0.71	0.79

However when much larger inlet velocities (e.g. 100 ~ 200 m/s) are involved, the line would shift slightly to the left, as shown in Figure 5.3; this is due to the fact that to achieve the sonic condition at the nozzle exit, a higher inlet velocity would lead to relatively a smaller temperature drop across the nozzle and hence a smaller degree of superheat is needed to avoid liquid formation in the nozzle. It is worth to point out that as the temperature gets closer to the critical line, the position of the boundary line cannot be determined with the same level of precision as the gas behaviour deviates from ideal gas law upon which the gas dynamics theories are derived.

The results for R125 (T_{cr} = 66.02 °C, p_{cr} = 3.62 MPa), R290 (T_{cr} = 96.74 °C, p_{cr} = 4.25 MPa), R143a (T_{cr} = 72.71 °C, p_{cr} = 3.76 MPa), R152a (T_{cr} = 113.26 °C, p_{cr} = 4.52 MPa), R32 (T_{cr} = 78.11 °C, p_{cr} = 5.78 MPa), R41 (T_{cr} = 44.13 °C, p_{cr} = 5.90 MPa) and R717 (T_{cr} = 132.25 °C, p_{cr} = 11.33 MPa) are presented in Figure 5.4. The corresponding data on the degrees of superheat to avoid liquification inside the nozzle, for a 10 m/s nozzle inlet velocity, are presented in Appendix 8.3.

It can be seen in Figure 5.4 that at a higher inlet saturation temperature a larger degree of superheat must be given to avoid wet nozzle operation. This implies that in the system coupling process, progressively larger degrees of superheat must be used when the VT inlet temperature is increased. In addition, for some refrigerants, such as R32 and R41 (Figure 5.4e and f), their boundary line FDS are much farther away from their saturated vapour line (i.e. larger degree of superheat is needed), when compared to some other refrigerants, say R125 and R290 (Figure 5.4a and b). The main reason is that R32 and R41 have larger specific heat ratio *r*, and this leads to a lower nozzle outlet temperature (see Eq. 8.9 in Appendix 8.1) which results in a higher likelihood of wet nozzle operation, and hence a larger degree of superheat is needed.

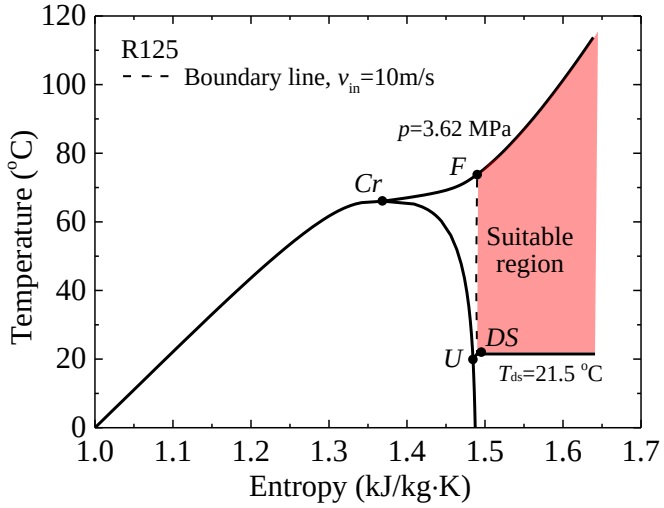

a

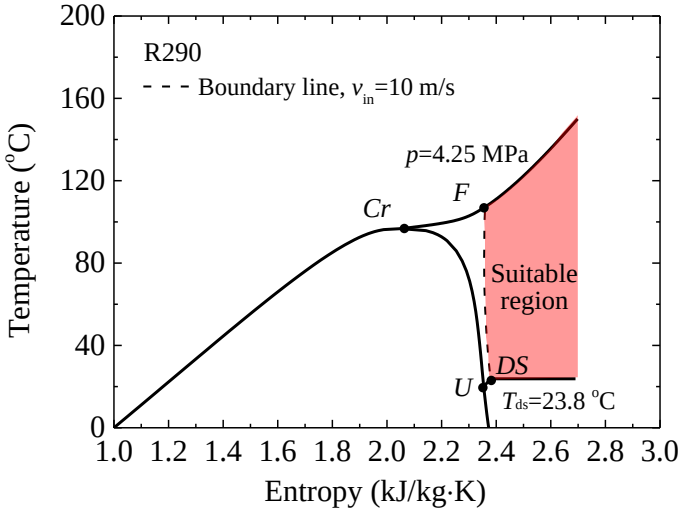

b

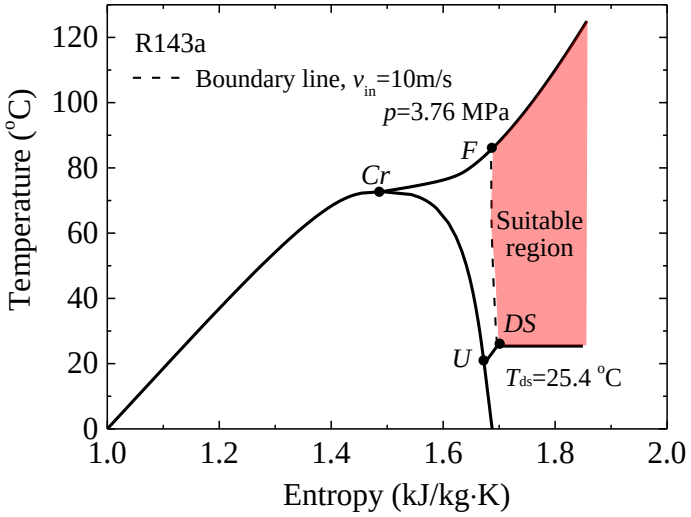
R143a
Boundary line, v_{in}=10m/s
p=3.76 MPa
F
Cr
Suitable region
DS
U
T_{ds}=25.4 °C
Temperature (°C)
Entropy (kJ/kg·K)
0
20
40
60
80
100
120
1.0
1.2
1.4
1.6
1.8
2.0

c

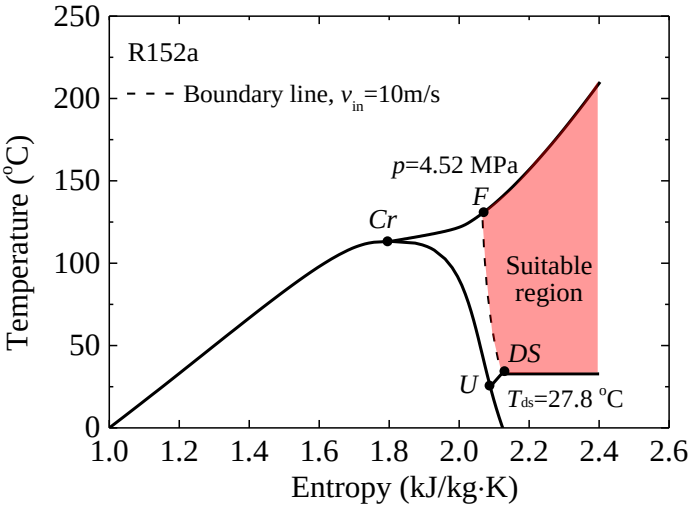
R152a
Boundary line, v_{in}=10m/s
p=4.52 MPa
F
Cr
Suitable region
DS
U
T_{ds}=27.8 °C
Temperature (°C)
Entropy (kJ/kg·K)
0
50
100
150
200
250
1.0
1.2
1.4
1.6
1.8
2.0
2.2
2.4
2.6

d

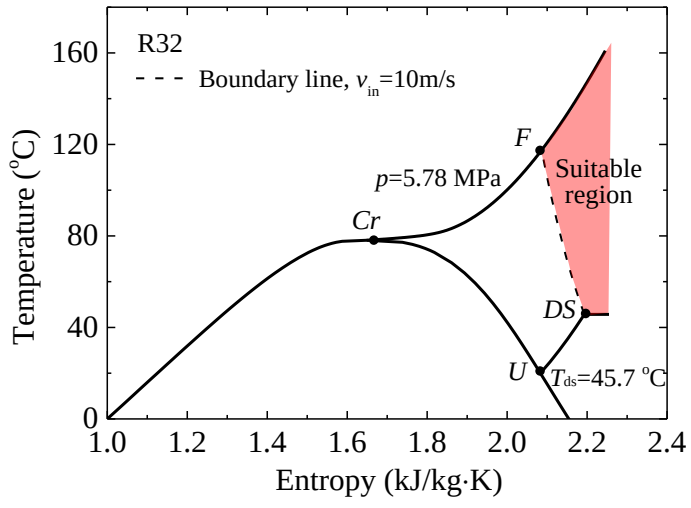
R32
Boundary line, v_{in}=10m/s
p=5.78 MPa
F
Cr
Suitable region
DS
U
T_{ds}=45.7 °C
Temperature (°C)
Entropy (kJ/kg·K)
0
40
80
120
160
1.0
1.2
1.4
1.6
1.8
2.0
2.2
2.4

e

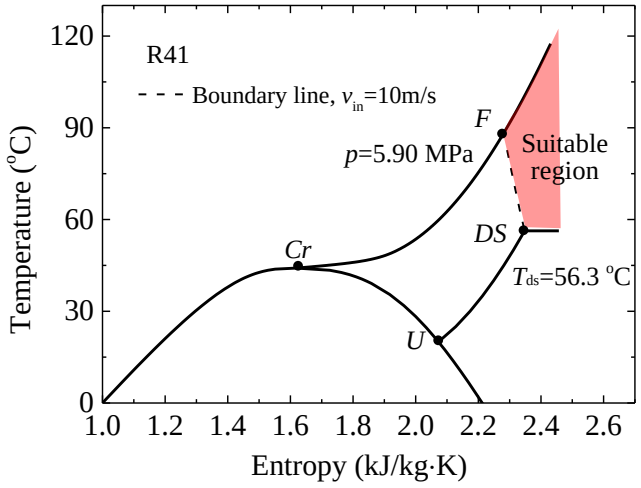

f

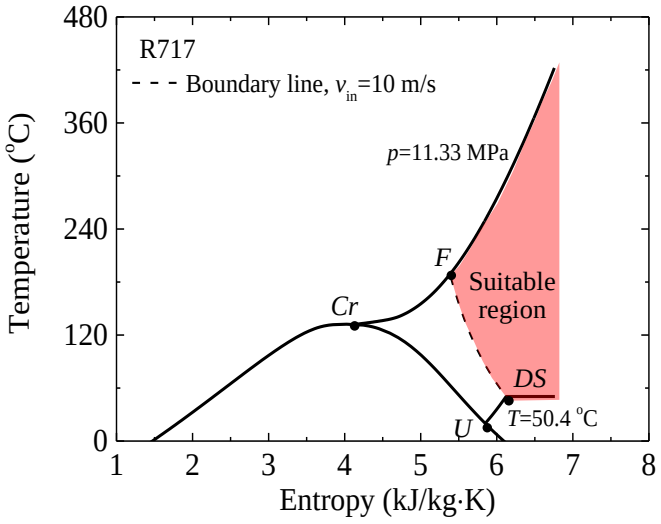

g

Figure 5.4 Established suitable VT entry regions for R125 (a), R290 (b), R143a (c), R152a (d), R32 (e), R41 (f) and R717 (g)

5.1.3 Sub-grouping refrigerants into small working ranges

Following the procedures presented in Section 3.2.3, the boundary lines for all the refrigerants are transported on a *T*-*p* diagram, as depicted on Figure 5.5. As previously explained, for a chosen refrigerant (or a chosen boundary line), within the specified temperature range, the region on the left of the line corresponds to the same suitable region on the *T*-*s* diagram, representing the suitable VT entry conditions for ensuring dry nozzle operation.

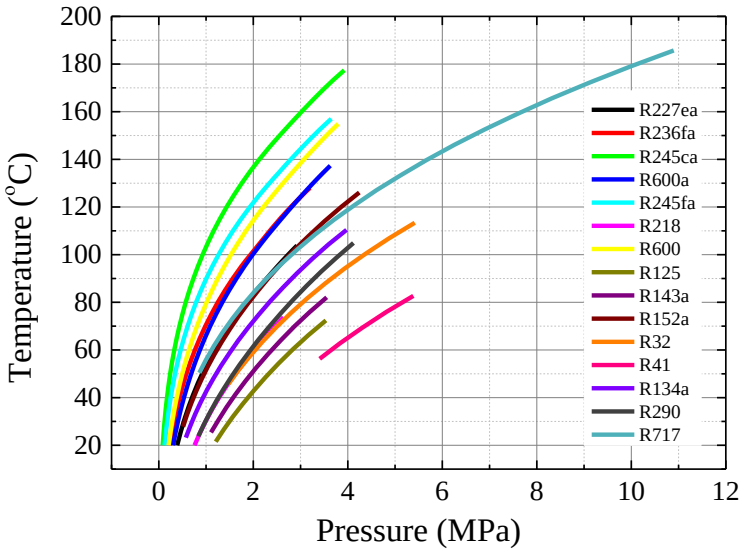

Figure 5.5 Boundary lines for both Group 1 and 2 refrigerants on the *T-p* diagram

Figure 5.5 represents a very useful set of data. For a chosen set of conditions (pressure and temperature), it enables us to decide easily which refrigerants could be selected for TSE comparison under these conditions. If the specified temperature and pressure point is on the right of the boundary line of a refrigerant that means this particular refrigerant should be excluded from the comparison exercise.

As discussed previously, the refrigerants are to be analysed and compared in seven temperature groups between 30 to 75 °C. As shown in Figure 5.5, R245ca is the furthest on the left, and for simplicity and illustration, the pressures on its boundary line are chosen as the pressure reference points; this would allow more refrigerants to be analysed in each of the sub-group.

For example, for the inlet temperature 30 °C, the corresponding pressure on the R245ca line is 0.12 MPa, and the refrigerants that could be included are R227a, R236fa, R245ca, R600a, R245fa, R218, R600, R134a, R290, R125, R143a and R152a. Coincidentally, for the chosen temperatures, each of Sub-groups 1 - 3 will have the same refrigerants included though they are compared at different temperature and pressure reference conditions, and as will be for individual Sub-groups 5 - 7. All seven Sub-groups are shown in Table 5.4. For a given temperature, if higher reference pressures were used, 2.0 or 3.0 MPa was used instead of 0.44 MPa for 70 °C, the numbers of refrigerants in individual groups would reduce accordingly, as exemplified in Table 5.5.

Table 5.4 Selected refrigerants within individual Sub-groups

No.	T_{in} °C	p_{in} MPa	Refrigerants
1	30	0.12	R227a, R236fa, R245ca, R600a, R245fa, R218, R600, R134a, R290, R125, R143a, R152a
2	35	0.15	R227a, R236fa, R245ca, R600a, R245fa, R218, R600, R134a, R290, R125, R143a, R152a
3	40	0.17	R227a, R236fa, R245ca, R600a, R245fa, R218, R600, R134a, R290, R125, R143a, R152a
4	60	0.33	R227a, R236fa, R245ca, R600a, R245fa, R218, R600, R134a, R290, R125, R143a, R152a, R717, R32
5	65	0.38	R227a, R236fa, R245ca, R600a, R245fa, R218, R600, R134a, R290, R125, R143a, R152a, R717, R32, R41
6	70	0.44	R227a, R236fa, R245ca, R600a, R245fa, R218, R600, R134a, R290, R125, R143a, R152a, R717, R32, R41
7	75	0.50	R227a, R236fa, R245ca, R600a, R245fa, R218, R600, R134a, R290, R125, R143a, R152a, R717, R32, R41

Table 5.5 Selected refrigerants at T_{in} = 70 °C and p_{in} = 2, 3 MPa

No.	T_{in} °C	p_{in} MPa	Refrigerants
6.1	70	2	R290, R143a, R218, R125, R32, R41
6.2	70	3	R125, R41

5.2 Analysis of thermal behaviour of refrigerants in VT

The TSE of the refrigerants in each of the Sub-groups are predicted using the established 2-D VT model (Section 3.1), and refrigerants are ranked according to their cooling or heating effect. The investigation focusses on relating their thermal-physical properties with their temperature separation performance. In addition, a couple of sub-groups are studied further for the influence of the VT inlet pressure/temperature conditions on the TSE.

5.2.1 Comparing the TSE of refrigerants in sub-groups

For the Sub-groups 1 to 3 (Section 5.1.3), the μ_c is varied from 0.1 to 0.9. For the Sub-groups 4 to 7, as the VT inlet temperatures are higher than 60 °C and there are small

possibilities of using these refrigerants for cooling applications under these conditions, therefore only the heating effect is considered and accordingly the μ_c is only varied between 0.6 and 0.9. All the μ_c are adjusted by controlling the hot end pressures p_h while the cold end pressure p_c is kept constant at 1 atm. The results of the cooling and heating effect are presented and discussed below.

1) The Sub-groups 1 - 3 refrigerants

Figure 5.6 presents the cooling effect of the Sub-group 1 refrigerants at the inlet condition of T_{in} = 30 °C, and p_{in} = 0.12 MPa.

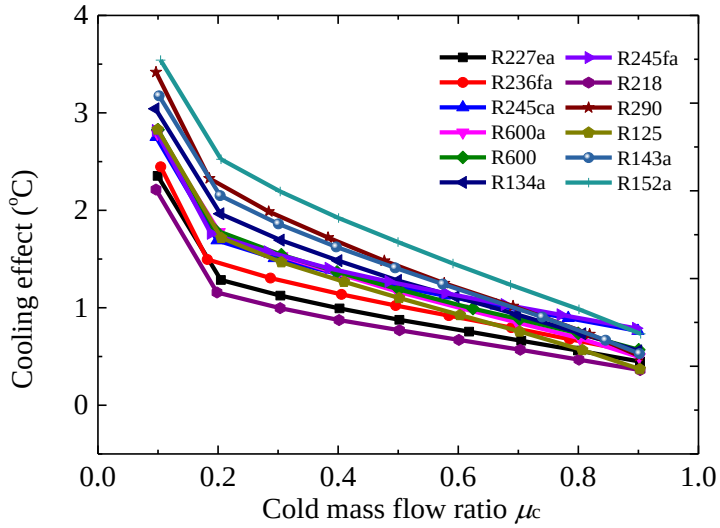

a. Cooling effect

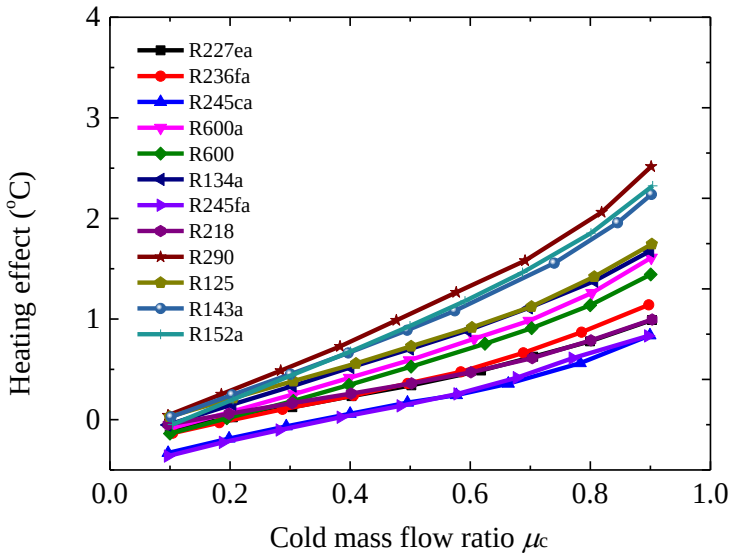

b. Heating effect

Figure 5.6 TSE of rerigerants in the Sub-group 1, T_{in} = 30 °C and p_{in} = 0.12 MPa

For all the refrigerants within this group, the results in general agree well with that observed from R134a and R600 in the previous chapter. The cooling effect decreases with increasing μ_c (Figure 5.6a) and this is due to having lower VT chamber inlet velocities $v_{cham,in}$ which are generated at higher values of μ_c, as seen in Figure 5.7, and thus producing a weaker rotation and hence a small temperature drop.

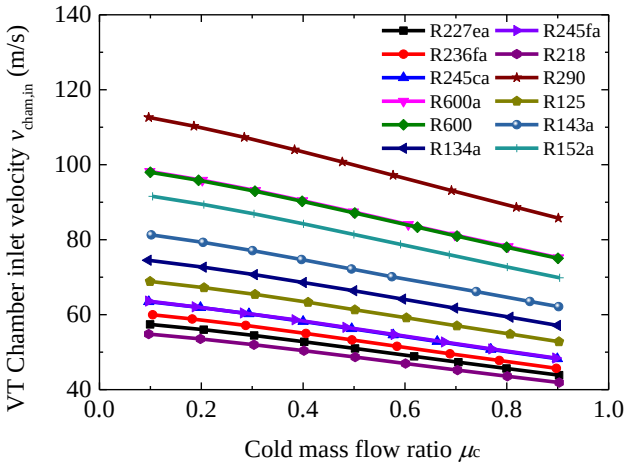

Figure 5.7 VT chamber inlet velocity $v_{cham,in}$ for the Sub-group 1 refrigerants

At the same time, the heating effect increases with increasing μ_c (Figure 5.6b); although the lower VT inlet velocities would result in smaller temperature increases, the lower pressure drops ($\Delta p_{in\text{-}h}$) at higher μ_c (Figure 5.8) would also lead to the smaller temperature drops, thus producing a net increase in heating effect. It is useful to point out at this stage that though all the refrigerants have similar $\Delta p_{in\text{-}h}$, the temperature drop associated with this expansion process varies among individual refrigerants, depending on their properties.

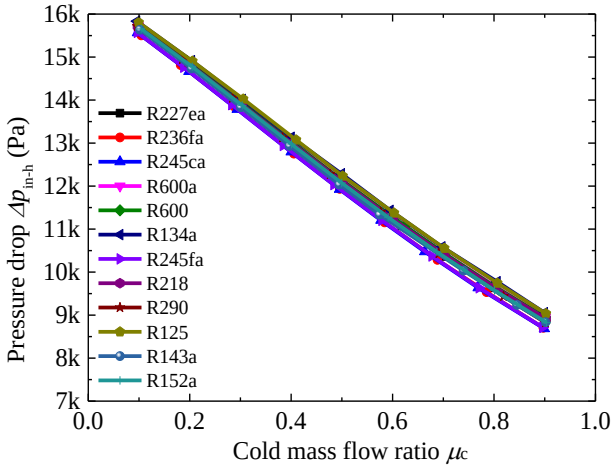

Figure 5.8 Pressure drop through the VT inlet and the hot end $\Delta p_{in\text{-}h}$ for the Sub-group 1 refrigerants

When the TSE of refrigerants in the Sub-group 1 are compared, their relative performance varies depending on the range of the μ_c. At a small μ_c, say less than around 0.5, R152a produces the largest cooling effect, followed by R290, R143a and R134a while R236fa, R227ea and R218 produce the smallest effect, and in between there is a group including R125, R600a, R600, R245fa and R245ca producing very much similar cooling effect.

However, at higher μ_c, say above 0.5, the trends become less clear as some refrigerants experience a bigger change in the gradient of the trend line, and as a result R245ca and R245fa join R152a as the top performers. For the rest of the refrigerants, both their cooling effect and their relative differences are rather small; as a VT will most likely be designed to function as a cooling device at low values of μ_c, any observations made at higher values of μ_c would have less practical relevance and significance.

Figure 5.9 displays the tangential velocities and the corresponding tangential shear stresses τ_{wy}[15] in the radial direction for three group members, R152a, R600a and R218, at two cross-sections CS1 and CS2 (at x_1 = 2 mm and x_2 = 90 mm, away from the chamber inlet in positive axial direction) for two values of μ_c (= 0.2 and 0.9) respectively. As expected, at any particular locations, higher stresses are usually associated steep velocity gradients as seen in Figure 5.9.

It can be noted that, though R600a (red lines) has a slightly stronger rotation (i.e. larger tangential velocities) than R152a (black lines), the latter has largest shear stresses which favour the generation of stronger temperature separation, as reflected in Figure 5.6. Among the three, it is apparent that R218 (blue lines) has the smallest TSE, as it has both smaller shear stresses and tangential velocities when compared to the other two refrigerants.

[15] τ_{wx} is not presented as it is much smaller than τ_{wy}, and it is expected to have negligible influence on the TSE

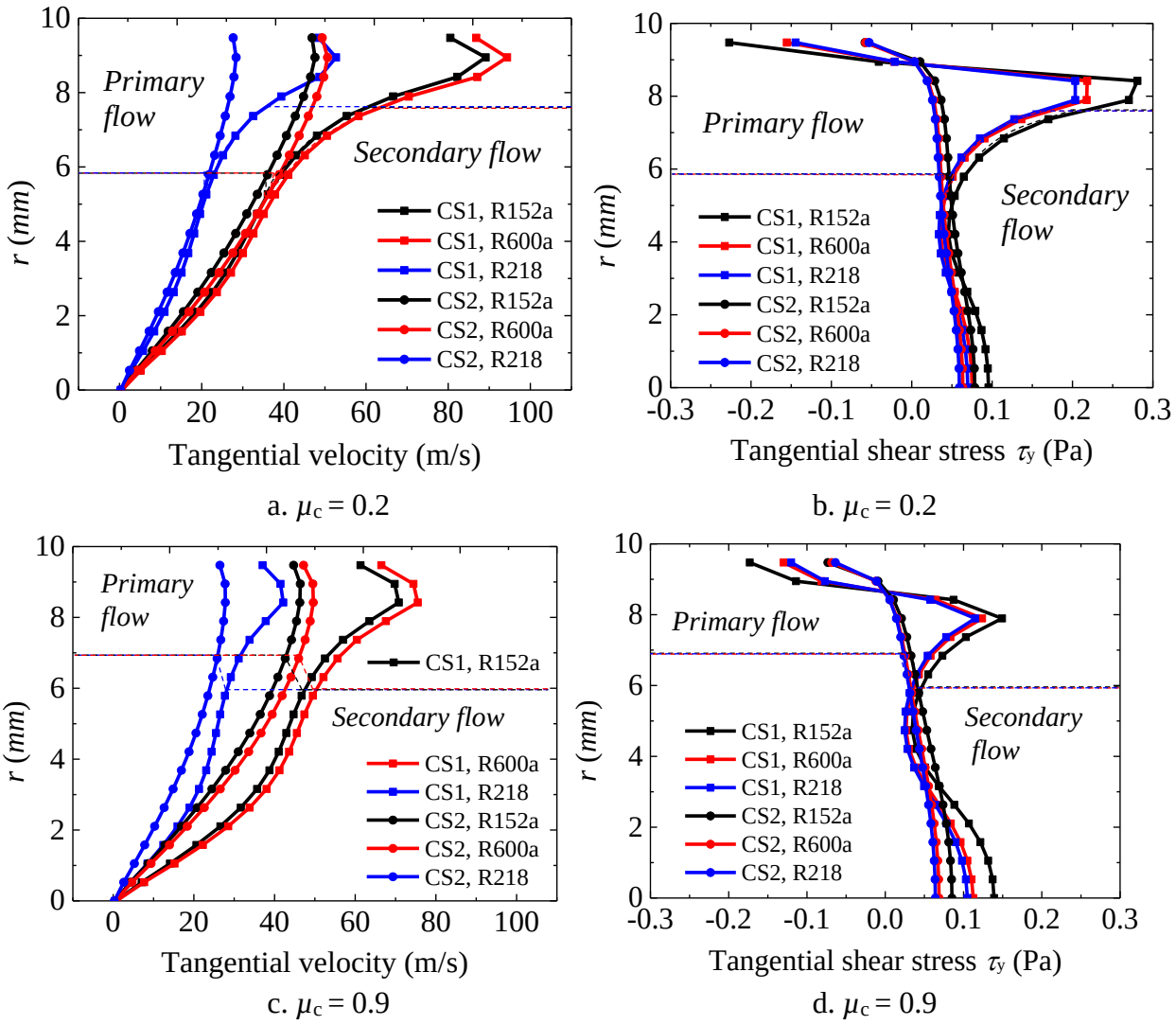

Figure 5.9 Tangential velocities and tangential shear stress τ_{wy} for R152a, R600a and R218 at two cross-sections (CS1: x_1 = 2 mm, CS2: x_2 = 90 mm), with μ_c = 0.2 for (a) and (b), μ_c = 0.9 for (c) and (d)

It has been suggested that the cooling effect is between the (J-T) isenthalpic and isentropic temperature drop. Table 5.6 presents the ranking order (in descending order) according to the magnitudes of the calculated isentropic and isenthalpic temperature drops of the Sub-group 1 refrigerants for the same $\Delta p_{in\text{-}c}$ (i.e. at a fixed VT inlet pressure of 0.12 MPa, inlet temperature of 30 °C and a cold end pressure of 0.10 MPa). It can be observed that they respectively follow closely the ranking of the refrigerants cooling effect at small and large μ_c values (as presented Figure 5.6). This observation suggests it may be possible to use isentropic expansion exponent[117, 124, 129] and J-T (Joule-Thomson) coefficient[130, 131] to rank their cooling performance. The J-T coefficient μ_{JT} expresses the rate of change of temperature with respect to the change of pressure at constant enthalpy, while, for a constant pressure ratio, in general a larger

isentropic expansion exponent would lead to a smaller outlet temperature (larger cooling effect). Both can be determined using relatively simple thermodynamics calculations.

Table 5.6 Ranking of isentropic and isenthalpic temperature drop for the Sub-group 1 refrigerants

Rank	Refrigerant	Isentropic temperature drop ΔT_s °C	Refrigerant	J-T Isenthalpic temperature drop ΔT_{JT} °C
1	R152a	6.95	R245fa	0.78
2	R290	6.32	R245ca	0.74
3	R143a	5.97	R152a	0.55
4	R134a	5.54	R600	0.50
5	R125	4.96	R236fa	0.46
6	R600a	4.92	R600a	0.43
7	R600	4.87	R134a	0.42
8	R245fa	4.32	R143a	0.36
9	R245ca	4.22	R227ea	0.35
10	R236fa	3.91	R290	0.33
11	R227ea	3.55	R125	0.27
12	R218	3.22	R218	0.25

Table 5.7 presents the ranking of the Sub-group 1 refrigerants based on the isentropic expansion exponent and J-T (Joule-Thomson) coefficient both are obtained at the same inlet conditions (p_{in} = 0.12 MPa and T_{in} = 30 °C). The ranking orders agree very well with that of Table 5.6 and Figure 5.6a (except for R245ca due to insufficient data points within the chosen range), confirming it is indeed possible to use these two parameters as the performance index to assess the relative cooling effect of individual refrigerants, thus reducing the reliance on CFD predictions. Practically, this offers convenience and simplicity.

Table 5.7 Ranking of isentropic expansion exponent and J-T coefficient based on the same VT inlet conditions for the Sub-group 1 refrigerants

Rank	Refrigerant	Isentropic expansion exponent	Refrigerant	J-T coefficient °C/MPa
1	R152a	1.13	R245fa	38.09
2	R290	1.11	R245ca	36.64
3	R143a	1.11	R152a	26.58
4	R134a	1.09	R600	24.19
5	R125	1.08	R236fa	21.58
6	R600a	1.07	R600a	20.91
7	R600	1.07	R134a	20.48
8	R245fa	1.05	R143a	17.79
9	R236fa	1.04	R227ea	17.25
10	R227ea	1.04	R290	16.31
11	R218	1.04	R125	13.20
12	R245ca	1.04	R218	12.07

Regarding the ranking of heating effect, the CFD results show that R290, R152a and R143a are the top performers, followed by R125, R134a, R600a and R600, R236fa, R218, R227ea, R245ca and R245fa have the smallest heating effect. This part of investigation looks into whether it is possible to use certain thermal-physical properties to predict the ranking of the heating effect of the refrigerants. As the VT temperature separation involves heat transfer and frictional shear forces between rotating fluid layers, thermal diffusivity and kinematic viscosity are main properties to consider.

Table 5.8 displays the thermal diffusivity (α) and kinematic viscosity (ν) of the Sub-group 1 refrigerants at the specified VT inlet conditions. The refrigerants are listed in the descending values of thermal diffusivity. The density (ρ) is also included, as a smaller density generally leads to a larger nozzle exit velocity under the same pressure differential across the nozzle, and thus a stronger rotational flow. The thermal diffusivity[66] represents the rate of heat transferring into the medium during changes in temperature with time, and a larger α corresponds to a faster propagation of heat into the medium. The kinematic viscosity[66] which can be called the diffusivity of momentum expresses the propagation of the movement by friction.

Table 5.8 Physical-thermal properties of the Sub-group 1 refrigerants at the specified VT inlet conditions (30 °C and 0.12 MPa), the refrigerants are ordered according to the decreasing values of thermal diffusivity

Refrigerant	Thermal diffusivity α cm^2/s	Kinematic viscosity ν cm^2/s	Density ρ kg/m^3
R290	0.051	0.038	2.17
R152a	0.042	0.031	3.27
R143a	0.039	0.027	4.14
R600a	0.035	0.026	2.89
R600	0.033	0.026	2.91
R134a	0.032	0.024	5.04
R125	0.030	0.022	5.90
R245ca	0.021	0.015	6.82
R245fa	0.021	0.015	6.79
R236fa	0.020	0.015	7.61
R227ea	0.020	0.014	8.47
R218	0.017	0.014	9.30

It is interesting to note that for the chosen refrigerants, both their thermal diffusivity (α) and kinematic viscosity (ν) follow the same listing order. Comparing the ranking order of α and ν of the refrigerants with the ranking of their heating effect (Figure 5.6b), they match fairly well, especially among the top performers. R290, having the highest values of both α and ν, and with the smallest density ρ, produces the highest heating effect. At the bottom end, R218, with the lowest values of α and ν, and the largest density ρ, has the lowest heating effect.

The "slight" mis-match between the two ranking orders, especially for refrigerants with weak heating effects, is attributed to the fact that the heating effect created from the rotation can be cancelled out by the temperature drop resulted from the adiabatic expansion through the VT. Figure 5.10 shows the J-T isenthalpic temperature drop based on the specified VT inlet and hot end pressures. It can be observed that R245ca and R245fa have the biggest isenthalpic temperature drop thus cancelling out a big part of the heating effect, and moving them to the bottom half of the heating effect ranking as seen in Figure 5.6b. As noted and explained previously, the ranking of the refrigerants' J-T coefficients (Table 5.7) can be used to predict the ranking of the isenthalpic temperature drop. This implies a refrigerant with a large J-T coefficient would lead to a smaller heating effect, as evident from the fact that R245ca and R245fa have the largest values of J-T coefficient.

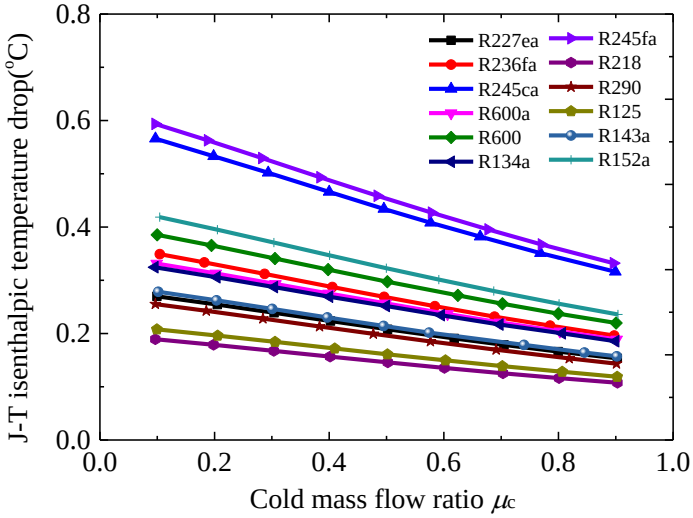

Figure 5.10 J-T isenthalpic temperature drop through the VT inlet and the hot end for the Sub-group 1 refrigerants

Based on the above observations and discussions, it can be preliminarily concluded that to achieve a better cooling effect, the fluid should have a large isentropic expansion exponent. On the other hand, to achieve a better heating effect, the fluid should have a small density and J-T coefficient, and a large thermal diffusivity and kinematic viscosity at the VT inlet conditions. In other words, isentropic expansion exponent, thermal diffusivity, kinematic viscosity, J-T coefficient and density can be used to assist in determining the temperature separation performance ranking of the refrigerants in VT.

Figure 5.11 presents the TSE of the Sub-groups 2 and 3 at respectively the inlet conditions T_{in} = 35 °C, p_{in} = 0.15 MPa and T_{in} = 40 °C, p_{in} = 0.17 MPa. Though referred as Sub-groups 2 and 3, both in fact comprise of the same refrigerants as the Sub-group 1. The same refrigerants are simply evaluated for their TSE under different inlet conditions, and it can be seen that in general they exhibit the same trends (with respect to μ_c) as the Sub-group 1 refrigerants, but at higher inlet temperatures and pressures, both their cooling and heating effects improve. However, it is important to assess if the same performance ranking orders are also preserved under different VT inlet conditions.

As Sub-groups 2 and 3 consist of the same refrigerants, then the key focus should be

(i) To see if the ranking (heating and cooling effects) changes when the inlet temperatures and pressures are raised.

(ii) To ensure the above conclusions drawn regarding isentropic expansion exponent, thermal diffusivity, kinematic viscosity, density and J-T coefficient remain valid under different inlet conditions.

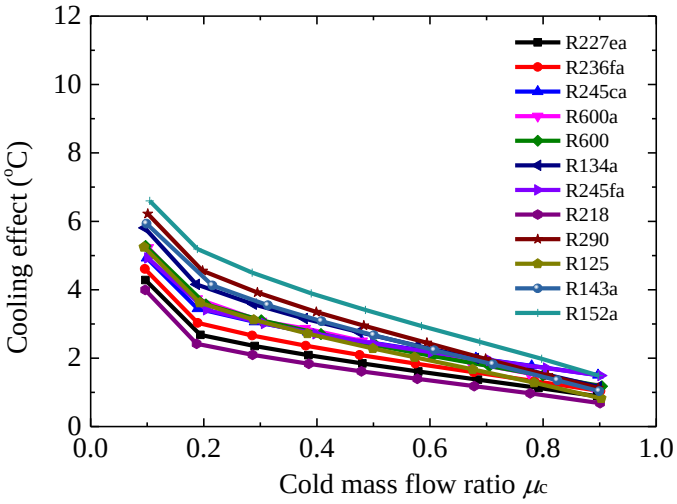

a. Cooling effect for the Sub-group 2 refrigerants

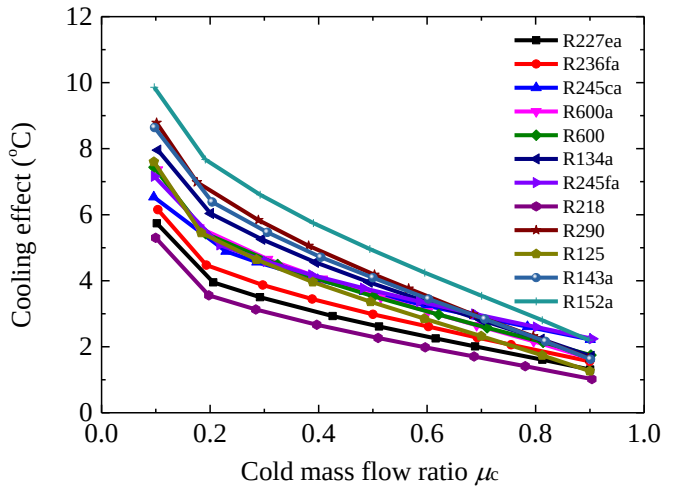

b. Cooling effect for the Sub-group 3 refrigerants

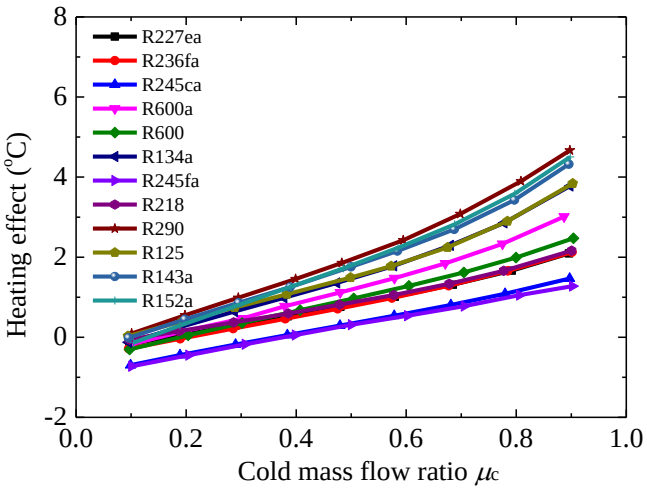

c. Heating effect for the Sub-group 2 refrigerants

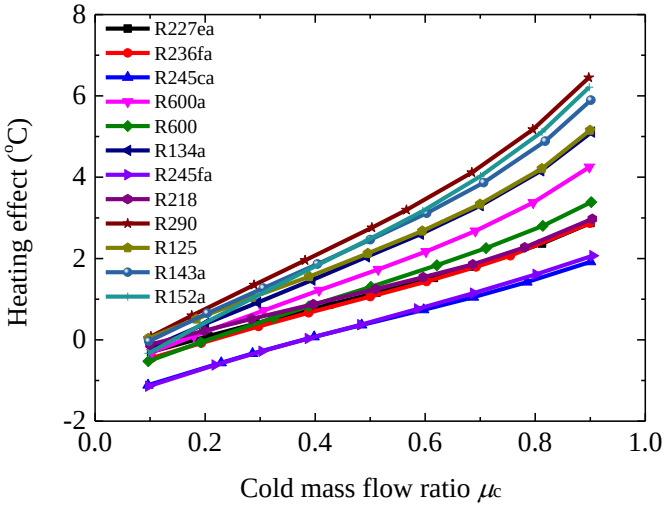

d. Heating effect for the Sub-group 3 refrigerants

Figure 5.11 TSE of the Sub-groups 2 and 3 rerigerants

Table 5.9 displays the ranking of isentropic and the isenthalpic temperature drops, and isentropic expansion exponent and J-T coefficient for the Sub-group 2 refrigerants, it can be observed that they follow the same order as that of the Sub-group 1 refrigerants. Same observations can be made for the Sub-group 3 refrigerants though their data are not presented. Based on the previous discussions, it came as no surprise that all the three groups have the same ranking of the cooling effects, as seen in Figure 5.6a and Figure 5.11a & b.

Table 5.9a Ranking of isentropic and isenthalpic temperature drops for the Sub-group 2 refrigerants

Rank	Refrigerant	Isentropic temperature drop / °C	Refrigerant	J-T isenthalpic temperature drop / °C
1	R152a	13.71	R245fa	1.57
2	R290	12.60	R245ca	1.52
3	R143a	11.94	R152a	1.12
4	R134a	11.08	R600	1.04
5	R125	9.91	R236fa	0.95
6	R600a	9.82	R600a	0.89
7	R600	9.73	R134a	0.86
8	R245fa	8.66	R143a	0.76
9	R245ca	8.46	R227ea	0.73
10	R236fa	7.84	R290	0.69
11	R227ea	7.11	R125	0.56
12	R218	6.45	R218	0.51

Table 5.9b Ranking of isentropic expansion exponent and J-T coefficient for the Sub-group 2 refrigerants

Rank	Refrigerant	Isentropic expansion coefficient	Refrigerant	J-T coefficient °C /MPa
1	R152a	1.12	R245fa	35.33
2	R290	1.11	R245ca	34.65
3	R143a	1.10	R152a	25.14
4	R134a	1.09	R600	23.12
5	R125	1.08	R236fa	20.52
6	R600a	1.07	R600a	20.00
7	R600	1.06	R134a	19.42
8	R245fa	1.04	R143a	16.85
9	R236fa	1.04	R227ea	16.40
10	R227ea	1.04	R290	15.58
11	R218	1.04	R125	12.57
12	R245ca	1.03	R218	11.50

Concerning the heating effect, Table 5.10 displays the chosen physical-thermal properties for the Sub-group 2 refrigerants and the ranking order of their thermal diffusivity matches exactly to that of the Sub-group 1 refrigerants. Similar observations can be made, that is the fluid producing the largest heating effect always has a relatively smaller density, larger kinematic viscosity and thermal diffusivity, all these contributing to a larger temperature increase arose from fluid rotating inside the VT.

Table 5.10 Thermal properties for the Sub-group 2 refrigerants

Refrigerant	Thermal diffusivity α cm^2/s	Kinematic viscosity ν cm^2/s	Density ρ kg/m^3
R290	0.044	0.033	2.56
R152a	0.036	0.027	3.86
R143a	0.033	0.023	4.89
R600a	0.030	0.023	3.43
R600	0.029	0.022	3.44
R134a	0.027	0.020	5.96
R125	0.026	0.019	6.97
R245ca	0.018	0.013	9.56
R245fa	0.018	0.013	8.05
R236fa	0.017	0.013	9.02
R227ea	0.017	0.012	10.03
R218	0.015	0.012	11.00

As explained previously, this temperature increase due to fluid rotation could be cancelled by the temperature drop resulting from the expansion process between the VT inlet and the hot end. Even though all refrigerants have similar pressure drop as shown in Figure 5.12, R245fa and R245ca have the highest isenthalpic temperature drop (Figure 5.13) and J-T coefficients (Table 5.9b), and these coupled with their relatively low values of kinematic viscosity and thermal diffusivity, and high density, put them at the bottom of the heating performance ranking (Figure 5.11c).

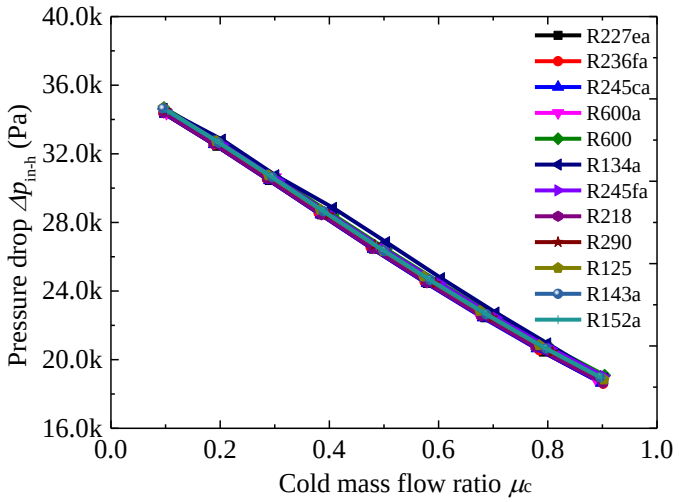

Figure 5.12 Pressure drop Δp_{in-h} for the Sub-group 2 refrigerants

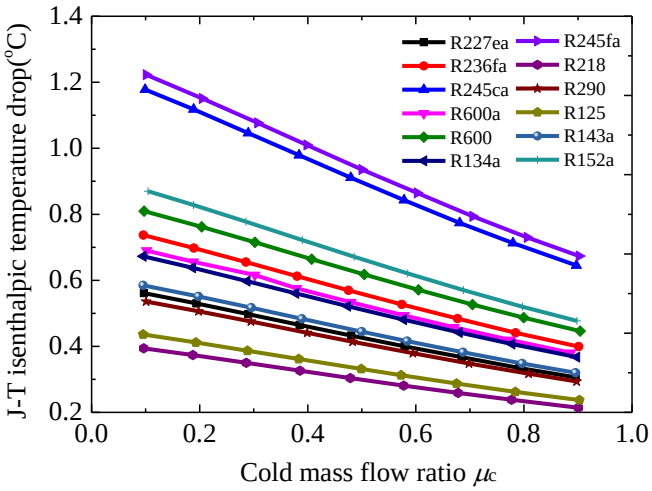

Figure 5.13 J-T isenthalpic temperature drop through the VT and the hot end for the Sub-group 2 refrigerants

Table 5.11 summarises the ranking of the refrigerants' cooling and heat effects. It appears that within the range of the inlet conditions considered, the ranking orders are not too significantly affected by the changes in the inlet temperatures and pressures. It can also be concluded that the proposed use of density, kinematic viscosity, thermal diffusivity, isentropic expansion exponent and J-T coefficient to predict the ranking of refrigerant's cooling and heating performance in a VT offers good reliability and accuracy.

Table 5.11 Ranking of the Sub-groups 1, 2 and 3 refrigerants for the cooling and heating effect

Rank	Sub-groups			
	Cooling effect / °C	Heating effect / °C		
	1~3	1	2	3
1	R152a	R290	R290	R290
2	R290	R152a	R152a	R152a
3	R143a	R143a	R143a	R143a
4	R134a	R125	R125	R125
5	R125	R134a	R134a	R134a
6	R600a	R600a	R600a	R600a
7	R600	R600	R600	R600
8	R245fa	R236fa	R218	R218
9	R245ca	R218	R236fa	R236fa
10	R236fa	R227ea	R227ea	R227ea
11	R227ea	R245ca	R245ca	R245fa
12	R218	R245fa	R245fa	R245ca

To achieve a large heating effect, a refrigerant should have a small density and J-T coefficient, and a large kinematic viscosity & thermal diffusivity at the VT inlet condition. The changes in the relative influence of these two groups of parameters make it harder to get a precise prediction of their ranking order, especially for those relatively weaker performers as seen in Table 5.11.

2) The Sub-groups 4 - 7 refrigerants

Figure 5.14 presents the heating effect of the Sub-group 4 refrigerants; the inlet conditions are now raised to T_{in} = 60 °C and p_{in} = 0.33 MPa, resulting in two more refrigerants R717 and R32 being included in this group. R41 is then added to create Sub-groups 5 - 7 which are evaluated respectively at T_{in} = 65 °C and p_{in} = 0.38 MPa, T_{in} = 70 °C and p_{in} = 0.44 MPa, and T_{in} = 75 °C and p_{in} = 0.50 MPa. The ranking of all the four Sub-groups are shown in Table 5.12.

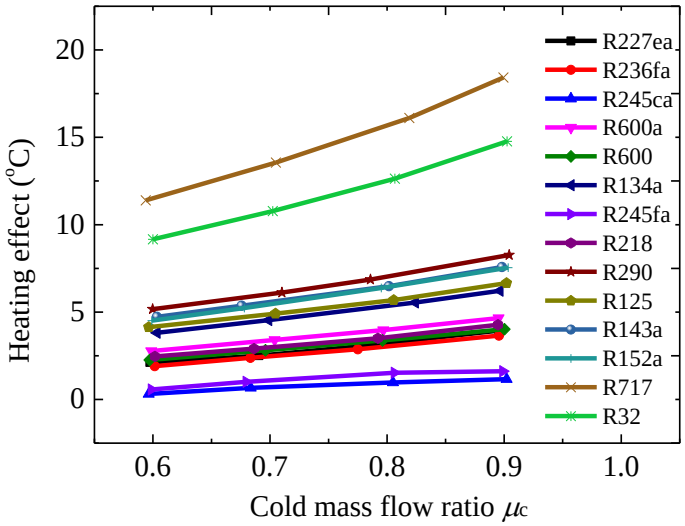

Figure 5.14 Heating effect of the Sub-group 4 refrigerants, T_{in} = 60 °C and p_{in} = 0.33 MPa

Table 5.12 Ranking of heating effect, in descending order, for Sub-groups 4 - 7 refrigerants

Rank	Sub-group			
	4	5	6	7
1		R41	R41	R41
2	R717	R717	R717	R717
3	R32	R32	R32	R32
4	R290	R290	R290	R290
5	R143a	R143a	R143a	R143a
6	R152a	R152a	R152a	R152a
7	R125	R125	R125	R125
8	R134a	R134a	R134a	R134a
9	R600a	R600a	R600a	R600a
10	R218	R218	R218	R218
11	R600	R600	R600	R600
12	R227ea	R227ea	R227ea	R227ea
13	R236fa	R236fa	R236fa	R236fa
14	R245fa	R245fa	R245fa	R245fa
15	R245ca	R245ca	R245ca	R245ca

It can be observed that in the Sub-group 4, R717 and R32 produce the largest heating effect, and the ranking order for the rest of refrigerants is quite similar to that of Sub-groups 1 - 3, with only very minor shifts of the orders.

Table 5.13 displays the chosen physical-thermal properties for refrigerants in the Sub-group 4. R717 and R32 have the largest kinematic viscosities and thermal diffusivities, and rather small densities at the VT entry, and thus a good heating performance is expected. Figure 5.15 shows that at $p_{in} = 0.33$ MPa, the spread of pressure drops among the refrigerants is relatively much bigger when compared to Sub-groups 1-3. Though R245fa and R245ca have the smallest pressure drops, associated with these pressure drops they still have the highest values of J-T isenthalpic temperature drop (Figure 5.16) and J-T coefficient (Table 5.14), and these coupled with their rather low values of α and ν, and large ρ, put them at the bottom of the ranking (Figure 5.14).

Table 5.13 Thermal-physical properties of the Sub-group 4 refrigerants

Refrigerant	Thermal diffusivity α cm^2/s	Kinematic viscosity ν cm^2/s	Density ρ kg/m^3
R717	0.061	0.055	2.06
R32	0.026	0.022	6.32
R290	0.022	0.017	5.42
R152a	0.019	0.014	8.20
R143a	0.017	0.012	10.32
R600a	0.015	0.011	7.32
R600	0.014	0.011	7.39
R134a	0.014	0.010	12.63
R125	0.013	0.010	14.69
R245fa	0.009	0.007	17.34
R245ca	0.009	0.006	17.62
R236fa	0.009	0.006	19.37
R227ea	0.009	0.006	21.41
R218	0.008	0.006	17.34

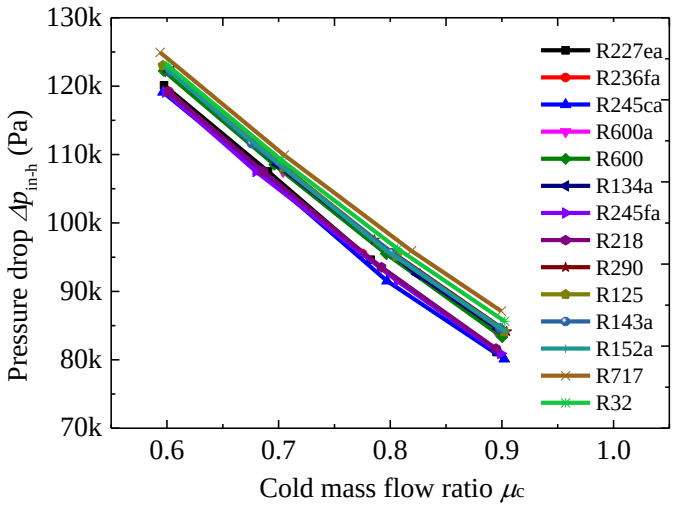

Figure 5.15 Pressure drop Δp_{in-h}, for the Sub-group 4 refrigerants, T_{in} = 60 °C and p_{in} = 0.33 MPa

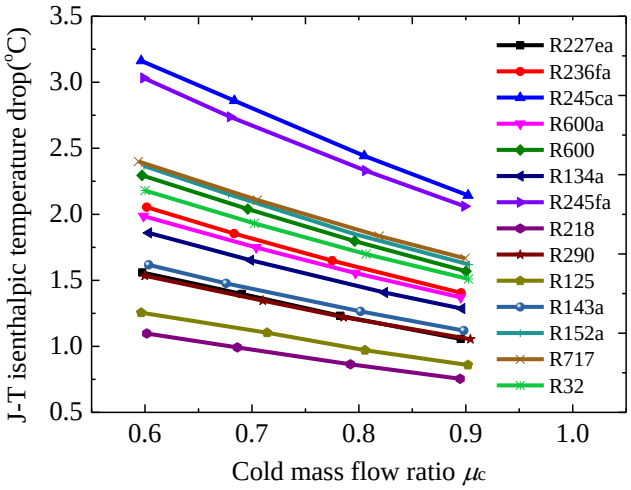

Figure 5.16 J-T isenthalpic temperature drop of the Sub-group 4 refrigerants, T_{in} = 60 °C and p_{in} = 0.33 MPa

Table 5.14 Ranking of J-T coefficient for the Sub-group 4 refrigerants

Rank	1	2	3	4	5	6	7
Refrigerants	R245ca	R245fa	R152a	R717	R600	R32	R236fa
J-T coefficient °C/MPa	27.15	25.50	19.41	18.93	18.93	17.49	16.51
Rank	8	9	10	11	12	13	14
Refrigerants	R600a	R134a	R143a	R227ea	R290	R125	R218
J-T coefficient °C/MPa	16.38	15.20	13.19	13.11	12.62	10.03	9.31

Figure 5.17 displays the heating effects of Sub-groups 5 to 7 refrigerants. When R41 is added, together with R717 and R32, they produce noticeably largest heating effect under all three Sub-group inlet conditions. Within this range of inlet conditions, the increase in inlet temperatures and pressures do not change the heating effects significantly. Some refrigerants experience a slight increase while some others undergo a small decrease, all depending on the relative changes of the involved thermal properties. However, the overall ranking orders do not change. In general one would expect the heating effect increases with increasing μ_c. However, under the range of inlet conditions considered, at high inlet pressures, R245fa and R245ca have their heating effect decreased when the μ_c exceeds certain value (Figure 5.17).

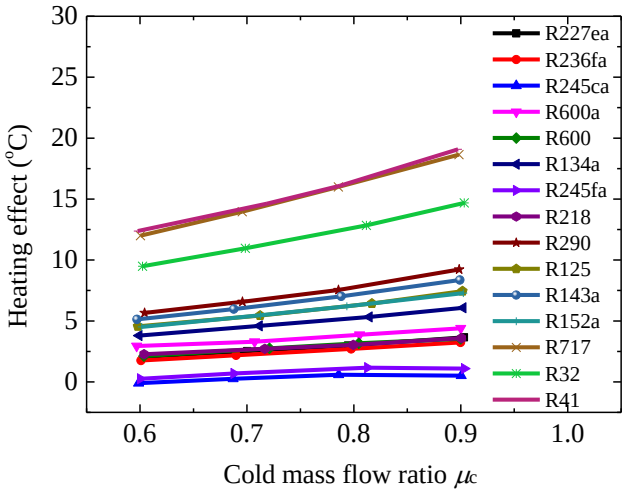

a. Sub-group 5 refrigerants, T_{in} = 65 °C and p_{in} = 0.38 MPa

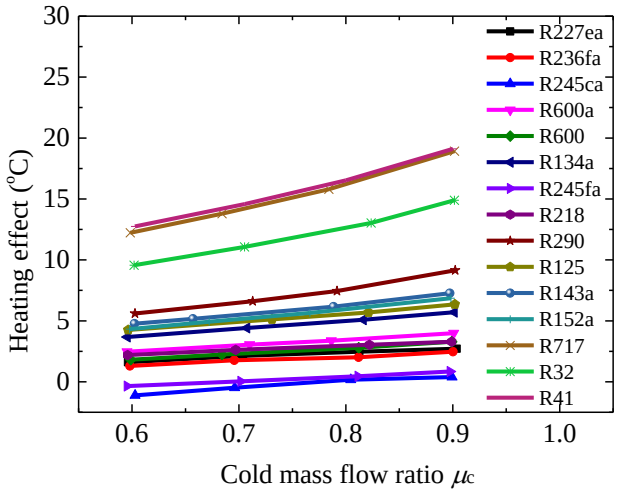

b. Sub-group 6 refrigerants, T_{in} = 70 °C and p_{in} = 0.44 MPa

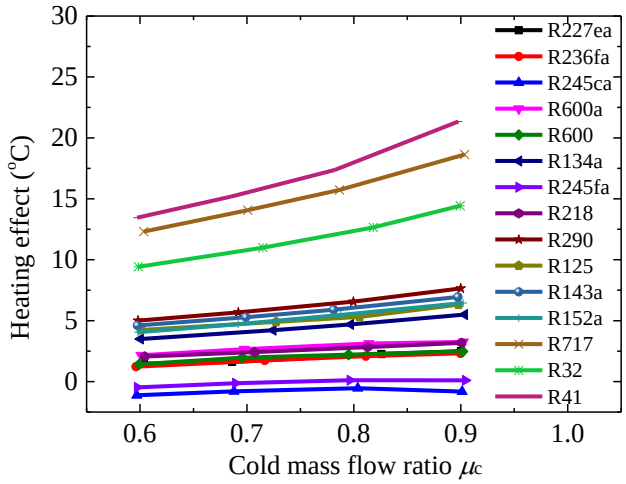

c. Sub-group 7 refrigerants, T_{in} = 75 °C and p_{in} = 0.50 MPa

Figure 5.17 Heating effect for Sub-groups 5 - 7 refrigerants

Table 5.15 presents the chosen thermal-physical properties for the Sub-group 5 refrigerants. Though R717 has a larger thermal diffusivity and kinematic viscosity, and a smaller density, than R41, the latter has a better heating effect particularly at higher inlet temperature/pressure. This is attributed to the fact that R41 has noticeably a lower J-T coefficient, and this coupled with a smaller pressure drop when compared to R717 (Figure 5.18) results in a smaller temperature drop from the expansion process.

Table 5.15 Thermal properties of the Sub-group 5 refrigerants

Refrigerant	Thermal diffusivity α cm^2/s	Kinematic viscosity ν cm^2/s	Density ρ kg/m^3	J-T coefficient μ_{JT} °C/MPa
R717	0.054	0.049	2.35	17.99
R41	0.036	0.026	4.68	12.74
R32	0.023	0.020	7.22	16.65
R290	0.020	0.015	6.20	12.13
R152a	0.016	0.012	9.38	18.51
R143a	0.015	0.011	11.81	12.62
R600a	0.013	0.010	8.40	15.81
R600	0.013	0.010	8.48	18.27
R134a	0.012	0.009	14.46	14.52
R125	0.012	0.009	16.79	9.62
R245ca	0.008	0.006	20.31	26.03
R236fa	0.008	0.006	22.25	15.92
R245fa	0.008	0.006	19.94	24.11
R227ea	0.008	0.005	24.56	12.60
R218	0.007	0.005	26.73	8.97

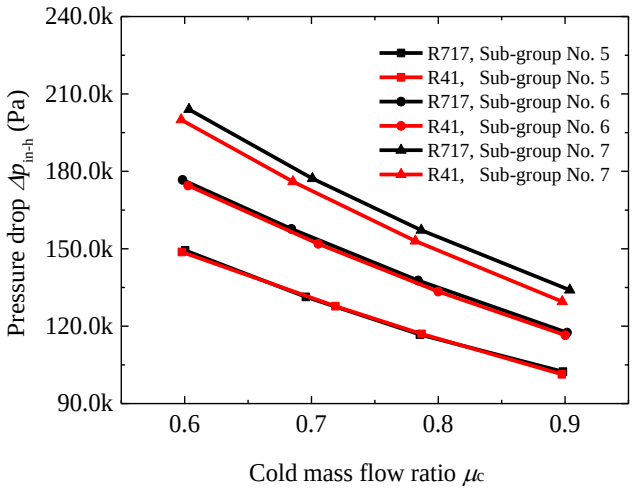

Figure 5.18 Pressure drop Δp_{in-h} for R41 and R717 in three Sub-groups

The observations and analysis reconfirm that various thermal-physical properties could be used effectively and reliably to predict the relative ranking of refrigerants over a range of VT inlet conditions.

5.2.2 Influence of VT inlet operating conditions on the TSE of the refrigerants

Section 4.2 provides some preliminary investigations into the influence of VT inlet temperature and pressure on both the variations of TSE and the VT hot end pressures for R134a and R600. When a VT is integrated into a closed system, these variations could significantly impact on the system performance. The same analysis is now applied to obtain detailed data for all the chosen refrigerants.

1) The influence of the inlet temperature

For the Sub-group 1 refrigerants, the inlet total temperature is increased from 30 °C to 40 °C at a 5 °C increment, and the hot end pressure is adjusted to achieve the required μ_c. The inlet and the cold end pressures are kept constant at 0.12 MPa and 0.101 MPa, respectively, unlike in Section 4.2.3 in which the inlet mass flow rates are kept constant instead. Figure 5.19 shows the effect of changing the inlet temperature on the cooling effect.

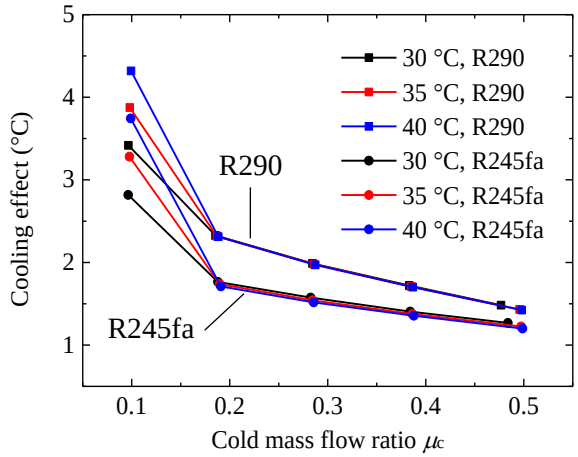

a

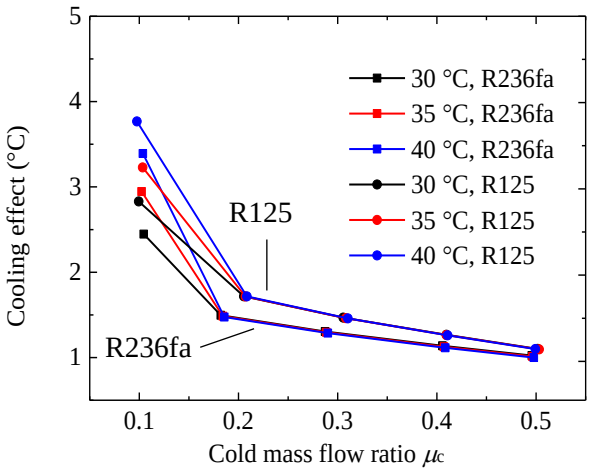

b

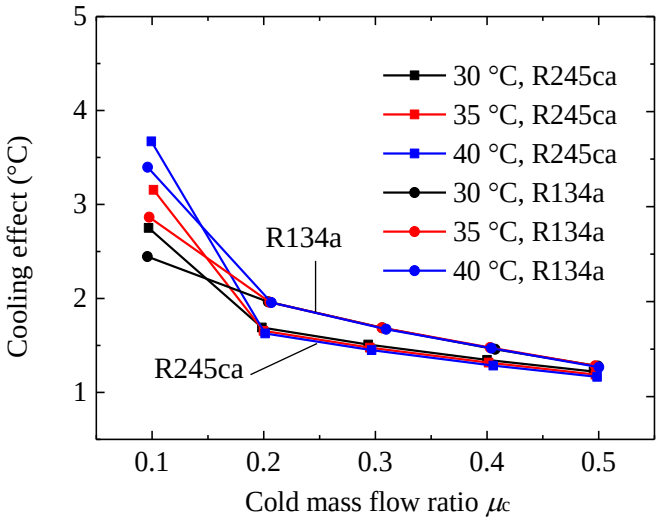
Cooling effect (°C)
Cold mass flow ratio μ_c
30 °C, R245ca
35 °C, R245ca
40 °C, R245ca
30 °C, R134a
35 °C, R134a
40 °C, R134a
R134a
R245ca

c

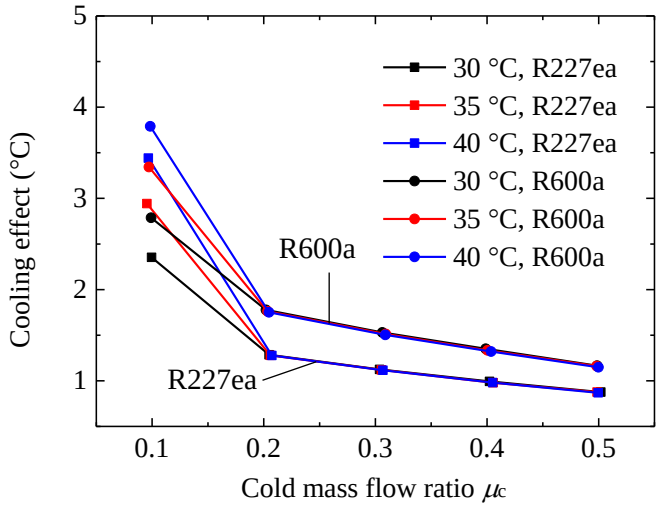
Cooling effect (°C)
Cold mass flow ratio μ_c
30 °C, R227ea
35 °C, R227ea
40 °C, R227ea
30 °C, R600a
35 °C, R600a
40 °C, R600a
R600a
R227ea

d

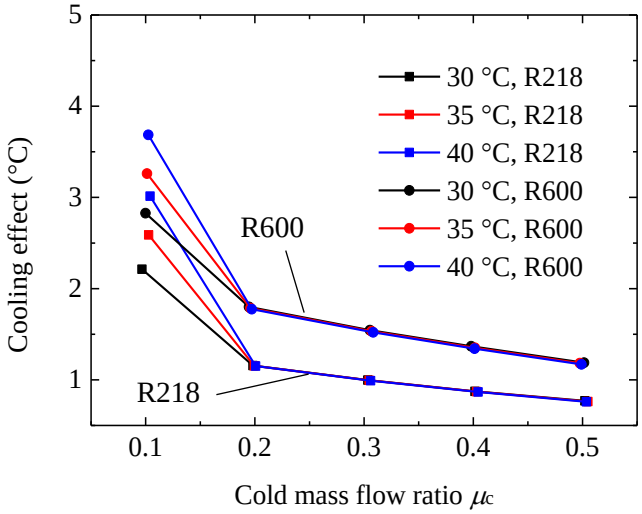
Cooling effect (°C)
Cold mass flow ratio μ_c
30 °C, R218
35 °C, R218
40 °C, R218
30 °C, R600
35 °C, R600
40 °C, R600
R600
R218

e

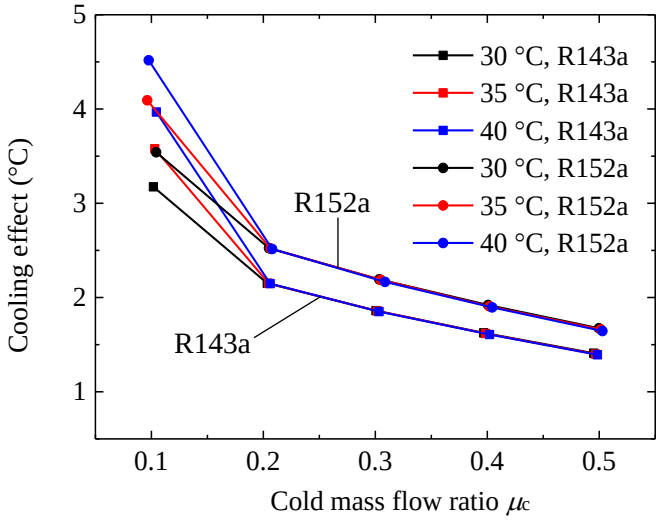

f

Figure 5.19 Effect of inlet temperature on the cooling effect for the Sub-group 1 refrigerants

It can be observed that within this range of inlet temperatures, the cooling effect is rather insensitive to the temperature at high values of μ_c. The increase of inlet temperature only leads to an increase of the cooling effect at μ_c smaller than 0.2. Such an increase of cooling effect is believed to be caused by a flow recirculation noted at the cold end exit for all the chosen refrigerants when $\mu_c = 0.1$, as illustrated in Figure 5.20 for R290. At the exit plane, the flow consists the main exiting flow and a flow recirculation (referred as the reversed flow in the CFD). The cold end temperature is calculated based on mass flow averaged temperature at the exit plane.

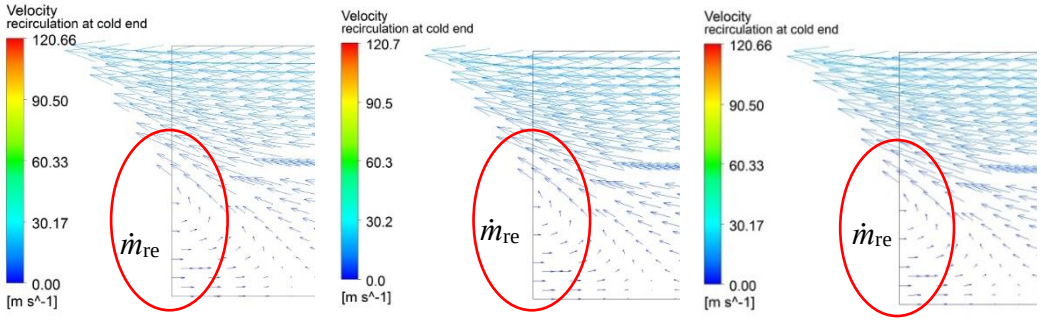

a. 30 °C b. 35 °C c. 40 °C

Figure 5.20 Flow velocity vectors at the cold end for R290 at different inlet temperatures ($\mu_c = 0.1$)

Since the reversed flow temperature is set to 20 °C ($\approx T_{atm}$), thus upon averaging, the exit temperature will acquire a lower value, when compared to a non-reversed flow situation. The would lead to an apparent improvement of cooling effect when the inlet temperature is increased; the cooling effects for R290 at $\mu_c = 0.1$, and 30 °C, 35 °C

and 40 °C are respectively 3.42 °C, 3.88 °C and 4.32 °C (Figure 5.19a). If using the trends for higher μ_c values to project the cooling effect at μ_c = 0.1, the cooling effect would be at a lower value of around 3 °C if no reversed flow was encountered. The practical implication of the above observation is to avoid running the VT at μ_c values too low to result in a flow recirculation at the cold end. The actual cooling effect at μ_c = 0.1 can be obtained by resetting the reversed temperature to the temperature of the main exiting flow; this would add complication to the CFD runs as each individual fluid will have a different main exit flow temperature.

Figure 5.21 presents the hot end pressures at different inlet temperatures. Across the entire range of μ_c, the increase of inlet temperature has hardly any influence on the hot end pressure within the range of inlet temperatures considered. In practical closed system operations, this implies that, in this range of inlet temperatures, a similar cold mass flow ratio can be obtained without adjusting the hot end throttle, thus reducing the need to keep manually adjusting the throttle.

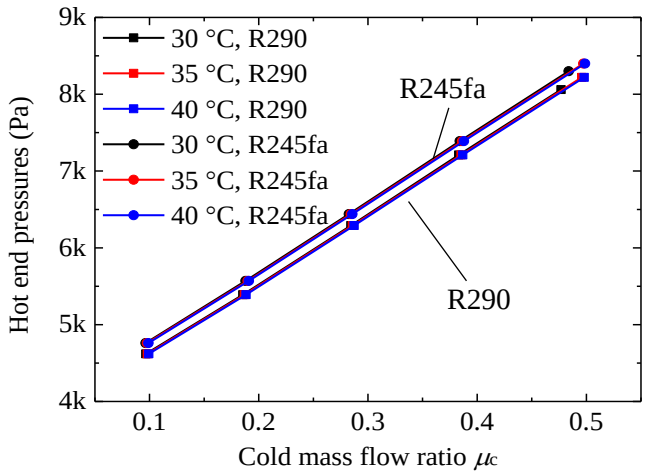

a

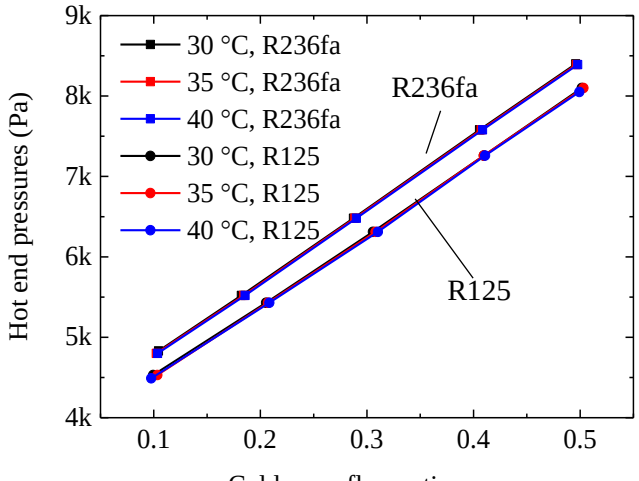

b

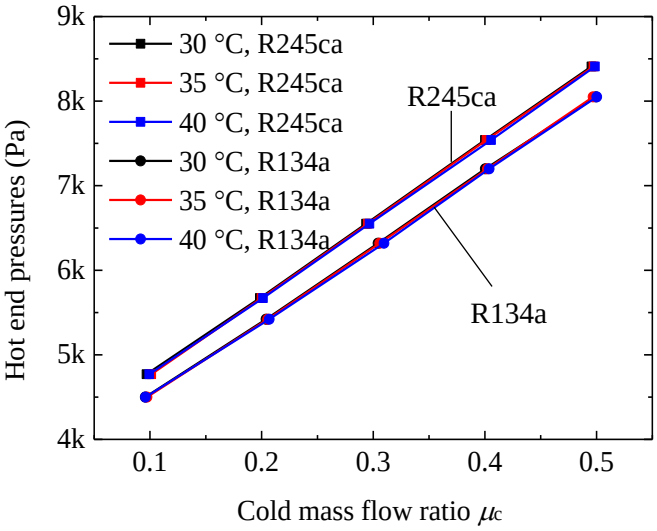
9k
8k
7k
6k
5k
4k
0.1
0.2
0.3
0.4
0.5
Hot end pressures (Pa)
Cold mass flow ratio μ_c
30 °C, R245ca
35 °C, R245ca
40 °C, R245ca
30 °C, R134a
35 °C, R134a
40 °C, R134a
R245ca
R134a

c

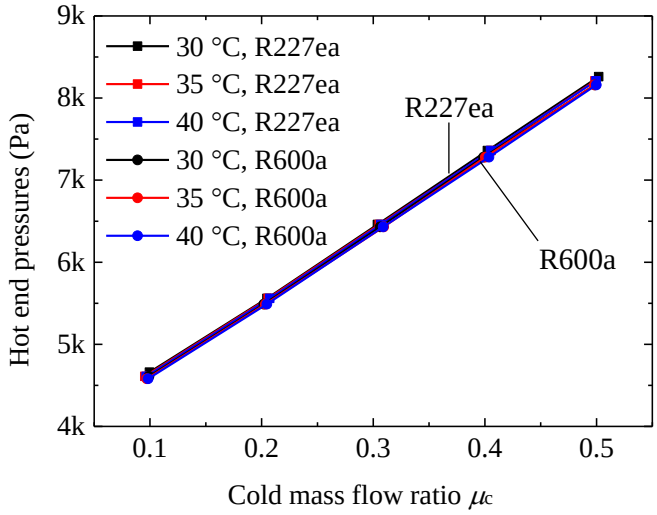
9k
8k
7k
6k
5k
4k
0.1
0.2
0.3
0.4
0.5
Hot end pressures (Pa)
Cold mass flow ratio μ_c
30 °C, R227ea
35 °C, R227ea
40 °C, R227ea
30 °C, R600a
35 °C, R600a
40 °C, R600a
R227ea
R600a

d

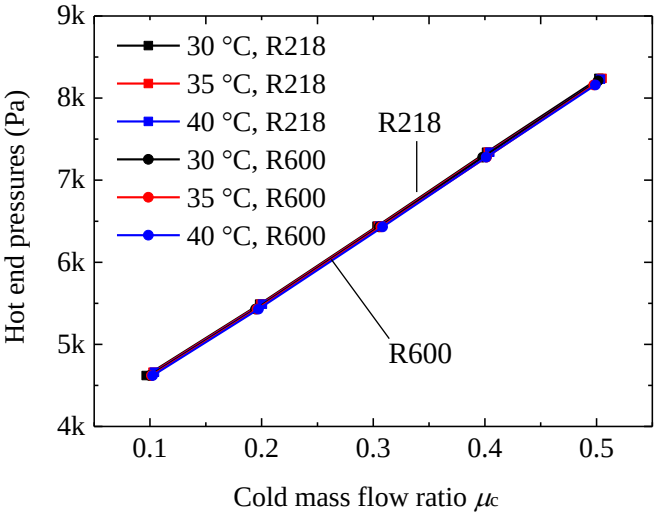
9k
8k
7k
6k
5k
4k
0.1
0.2
0.3
0.4
0.5
Hot end pressures (Pa)
Cold mass flow ratio μ_c
30 °C, R218
35 °C, R218
40 °C, R218
30 °C, R600
35 °C, R600
40 °C, R600
R218
R600

e

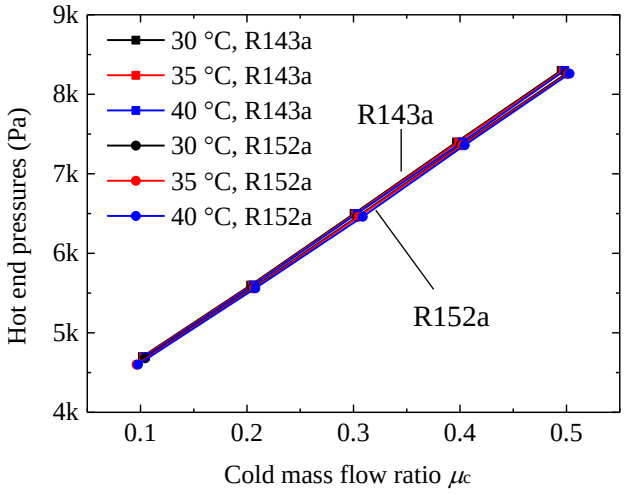

g

Figure 5.21 Hot end pressures (gauge) under different inlet temperatures for the Sub-group 1 refrigerants

Figure 5.22 presents the effect of inlet temperature on the heating effect for the Sub-group 4 refrigerants. The inlet pressure is fixed at 0.33 MPa, and the inlet temperature is increased from 60 °C to 85 °C at a 5 °C increment. The hot end pressures is varied to obtain the required μ_c (0.6 - 0.9), while the cold end pressure is kept at 1 atm.

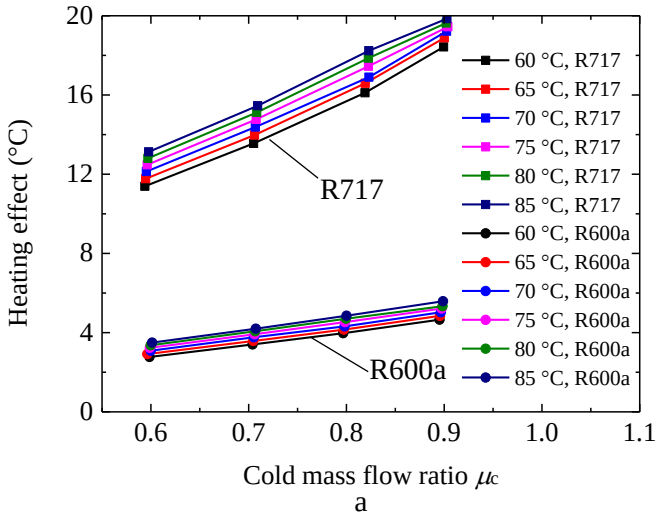

a

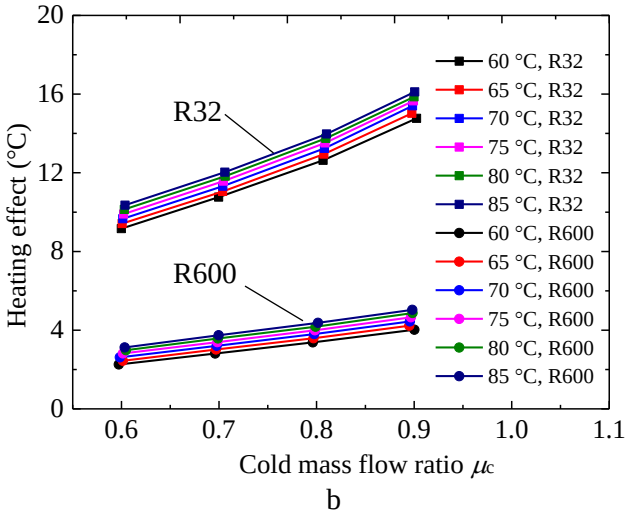

b

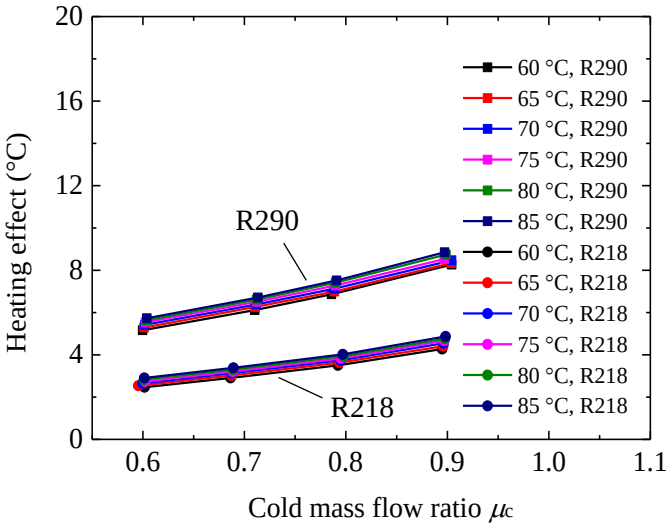
Heating effect (°C)
Cold mass flow ratio μ_c
R290
R218
60 °C, R290
65 °C, R290
70 °C, R290
75 °C, R290
80 °C, R290
85 °C, R290
60 °C, R218
65 °C, R218
70 °C, R218
75 °C, R218
80 °C, R218
85 °C, R218

c

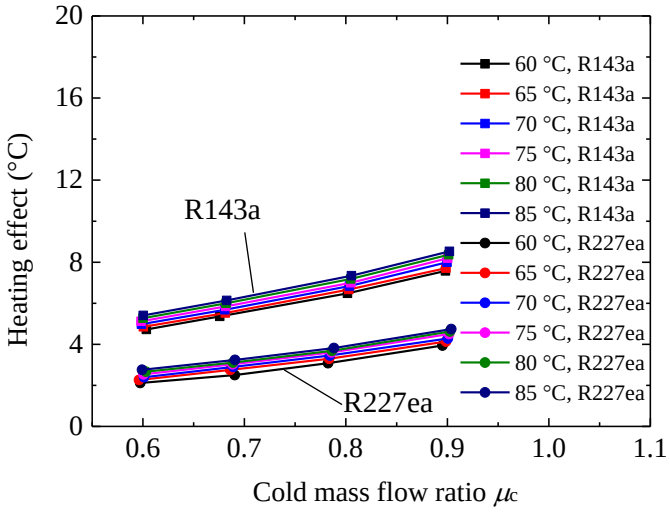
Heating effect (°C)
Cold mass flow ratio μ_c
R143a
R227ea
60 °C, R143a
65 °C, R143a
70 °C, R143a
75 °C, R143a
80 °C, R143a
85 °C, R143a
60 °C, R227ea
65 °C, R227ea
70 °C, R227ea
75 °C, R227ea
80 °C, R227ea
85 °C, R227ea

d

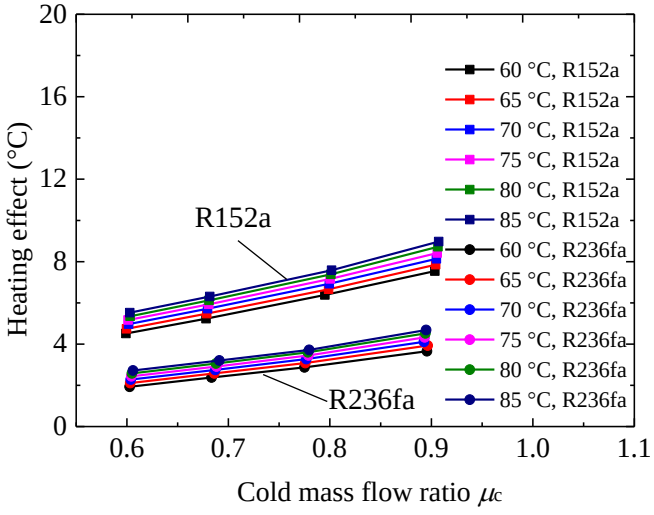
Heating effect (°C)
Cold mass flow ratio μ_c
R152a
R236fa
60 °C, R152a
65 °C, R152a
70 °C, R152a
75 °C, R152a
80 °C, R152a
85 °C, R152a
60 °C, R236fa
65 °C, R236fa
70 °C, R236fa
75 °C, R236fa
80 °C, R236fa
85 °C, R236fa

e

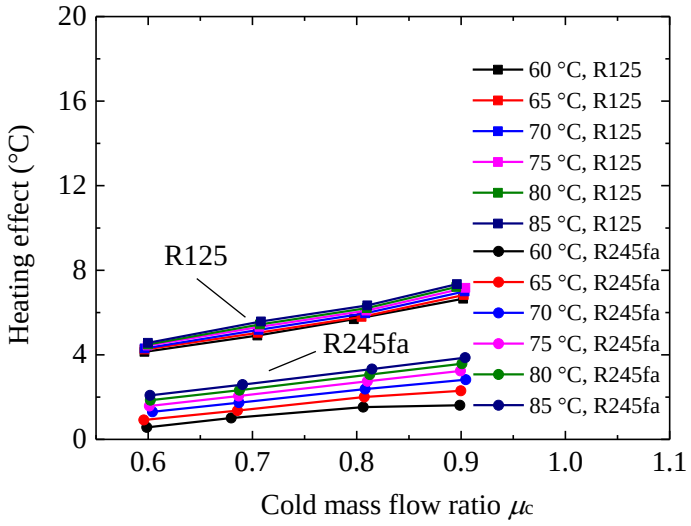

f

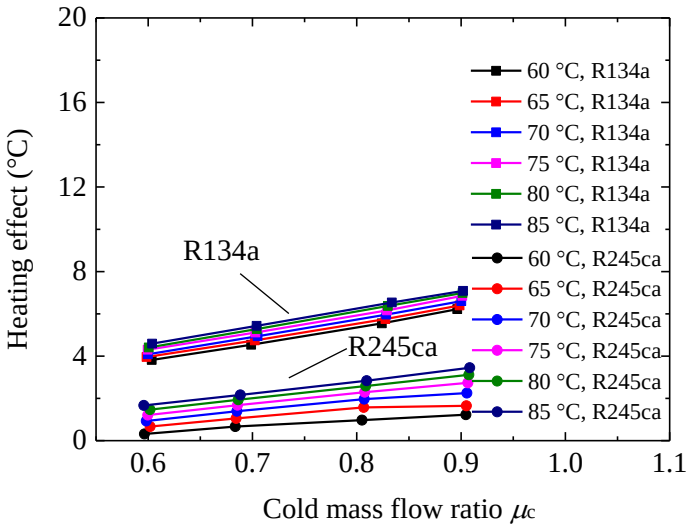

g

Figure 5.22 Heating effect at different inlet temperatures for the Sub-group 4 refrigerants

It can be noted that in general the heating effect improves when the inlet temperature is increased. Table 5.16 displays the thermal properties for R717 at different inlet temperatures. It can be observed that, as the inlet temperature is getting higher, the thermal diffusivity and kinetic viscosity both are getting larger, and the density is becoming smaller. At the same time, the associated J-T coefficient also becomes smaller. As explained previously, all these changes would lead to a larger heating effect.

Table 5.16 Properties for R717 at different inlet temperatures (p_{in} = 0.33 MPa)

T_{in} °C	Thermal diffusivity α cm^2/s	Kinematic viscosity ν cm^2/s	Density ρ kg/m^3	J-T coefficient μ_{JT} °C/MPa
60	0.061	0.055	2.06	18.93
65	0.063	0.057	2.03	18.02
70	0.066	0.059	1.99	17.18
75	0.068	0.061	1.96	16.40
80	0.071	0.063	1.93	15.66
85	0.073	0.065	1.91	14.98

Within this group of refrigerants, some have relatively higher sensitivities of heating effect to inlet temperature, e.g. R245ca (Figure 5.22g), while for a few others, such as R218 (Figure 5.22c), the inlet temperature has hardly any influence of the heating effect. For comparison purpose, Table 5.17 shows the thermal properties of R245ca and R218 at the same inlet conditions. These two refrigerants have similar heating values. It is clear that R245ca has a larger rate of increase of α and ν with respect to increase in inlet temperature than R218, and at the same time R245ca also has a larger rate of decrease of J-T coefficient, resulting in the former having a higher sensitivity of heating effect to inlet temperature.

Table 5.17a Properties for R245ca at different inlet temperatures (p_{in} = 0.33 MPa)

T_{in} °C	α cm^2/s	Δ%	ν cm^2/s	Δ%	ρ kg/m^3	Δ%	μ_{JT} °C/MPa	Δ%
60	0.0090	+5.39%	0.0064	+4.00%	17.62	-2.19%	27.15	-7.74%
65	0.0094	+4.99%	0.0067	+3.86%	17.23	-2.08%	25.05	-7.12%
70	0.0099	+4.69%	0.0069	+3.73%	16.87	-2.00%	23.26	-6.62%
75	0.0104	+4.44%	0.0072	+3.61%	16.54	-1.93%	21.72	-6.22%
80	0.0108	+4.25%	0.0074	+3.50%	16.22	-1.87%	20.37	-5.90%
85	0.0113		0.0077		15.91		19.17	

Table 5.17b Properties for R218 at different inlet temperatures (p_{in} = 0.33 MPa)

T_{in} °C	α cm^2/s	Δ%	ν cm^2/s	Δ%	ρ kg/m^3	Δ%	μ_{JT} °C/MPa	Δ%
60	0.00770	+3.84%	0.0060	+3.28%	23.34	-1.75%	9.31	-4.90%
65	0.00799	+3.74%	0.0063	+3.21%	22.93	-1.70%	8.85	-4.74%
70	0.00829	+3.66%	0.0064	+3.14%	22.54	-1.67%	8.43	-4.59%
75	0.00860	+3.58%	0.0066	+3.07%	22.17	-1.63%	8.05	-4.46%
80	0.00890	+3.50%	0.0068	+3.01%	21.81	-1.60%	7.69	-4.33%
85	0.00921		0.0070		21.46		7.35	

Figure 5.23 presents the hot end pressures at different inlet temperatures. It can be noted that, for all the Sub-group 4 refrigerants, the increase in inlet temperatures has negligible impact on the hot end pressures. Once again, in practise, this means the position of the hot throttle often needs no adjustment to achieve the same cold mass flow ratio within the examined range of VT inlet temperatures.

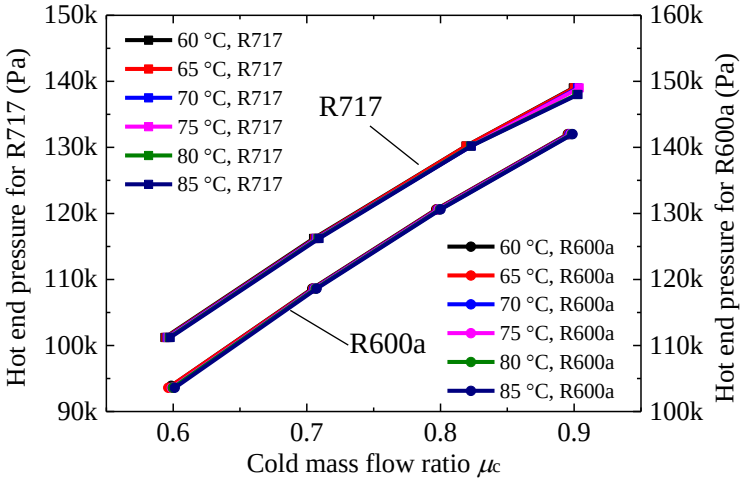

a

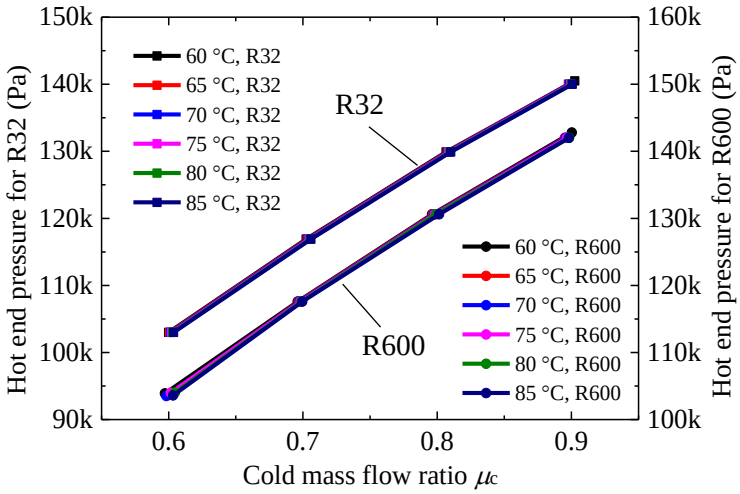

b

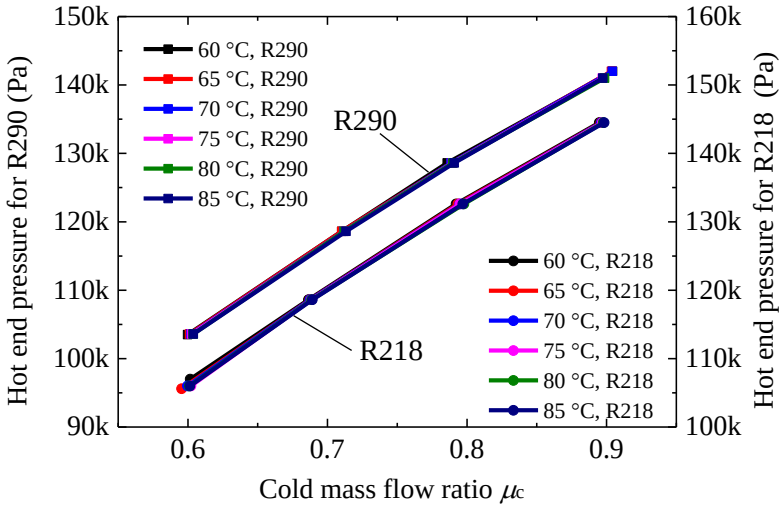
Hot end pressure for R290 (Pa)
Hot end pressure for R218 (Pa)
Cold mass flow ratio μ_c
60 °C, R290
65 °C, R290
70 °C, R290
75 °C, R290
80 °C, R290
85 °C, R290
R290
R218
60 °C, R218
65 °C, R218
70 °C, R218
75 °C, R218
80 °C, R218
85 °C, R218
150k
140k
130k
120k
110k
100k
90k
160k
150k
140k
130k
120k
110k
100k
0.6
0.7
0.8
0.9

c

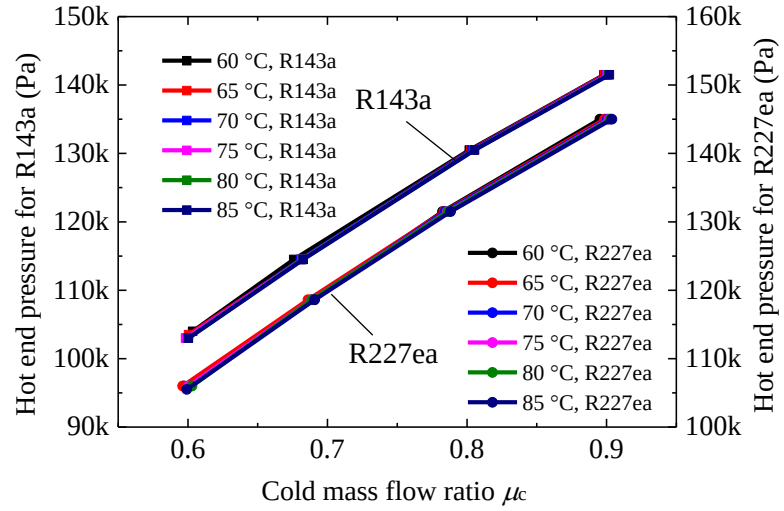
Hot end pressure for R143a (Pa)
Hot end pressure for R227ea (Pa)
Cold mass flow ratio μ_c
60 °C, R143a
65 °C, R143a
70 °C, R143a
75 °C, R143a
80 °C, R143a
85 °C, R143a
R143a
R227ea
60 °C, R227ea
65 °C, R227ea
70 °C, R227ea
75 °C, R227ea
80 °C, R227ea
85 °C, R227ea
150k
140k
130k
120k
110k
100k
90k
160k
150k
140k
130k
120k
110k
100k
0.6
0.7
0.8
0.9

d

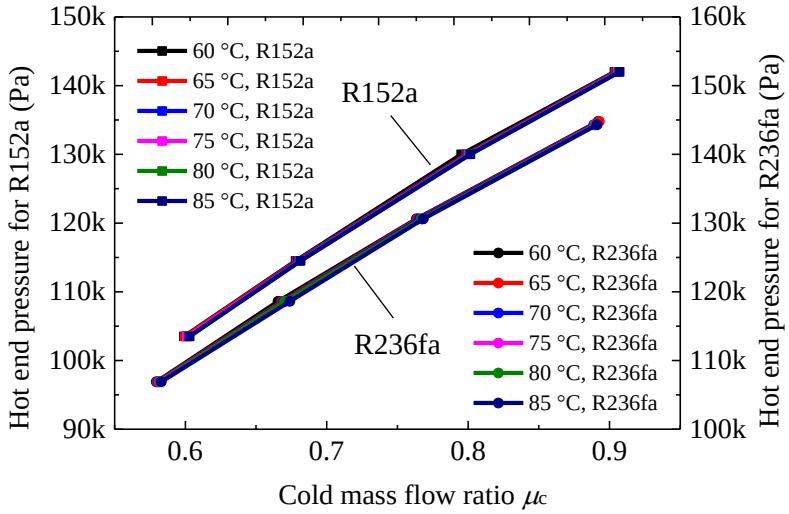
Hot end pressure for R152a (Pa)
Hot end pressure for R236fa (Pa)
Cold mass flow ratio μ_c
60 °C, R152a
65 °C, R152a
70 °C, R152a
75 °C, R152a
80 °C, R152a
85 °C, R152a
R152a
R236fa
60 °C, R236fa
65 °C, R236fa
70 °C, R236fa
75 °C, R236fa
80 °C, R236fa
85 °C, R236fa
150k
140k
130k
120k
110k
100k
90k
160k
150k
140k
130k
120k
110k
100k
0.6
0.7
0.8
0.9

e

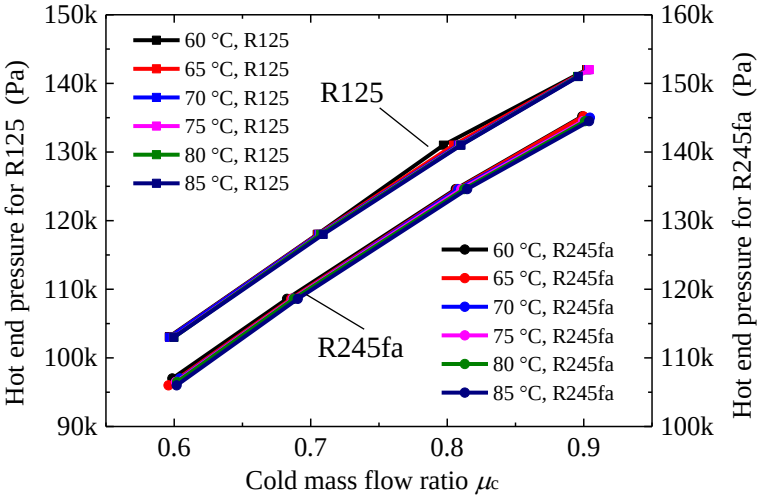

f

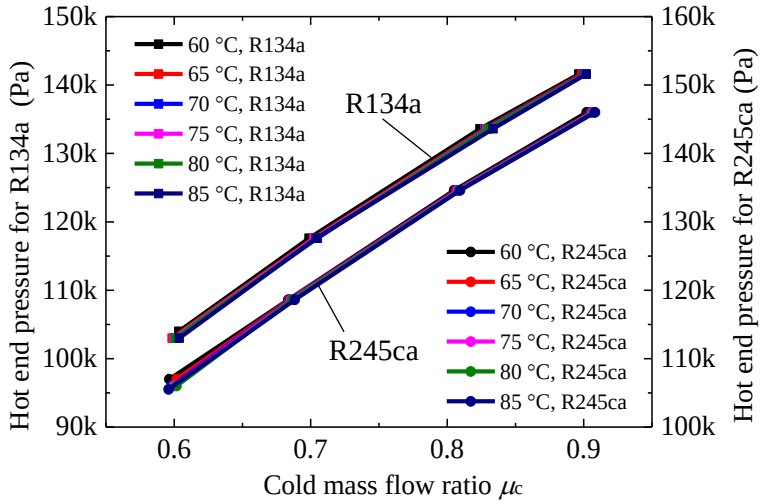

g

Figure 5.23 Hot end pressure (gauge) at different inlet temperatures for the Sub-group 4 refrigerants

The influence of the VT inlet temperatures on the heating effect is also investigated for Sub-groups 5, 6 and 7 refrigerants, which have an additional refrigerant R41. As similar to previous observations are made for all the refrigerants, and only representative results of R41 are shown. Figure 5.24 and Figure 5.25 display the heating effect and the hot end pressures at different inlet temperatures, respectively. All previous discussions also apply here.

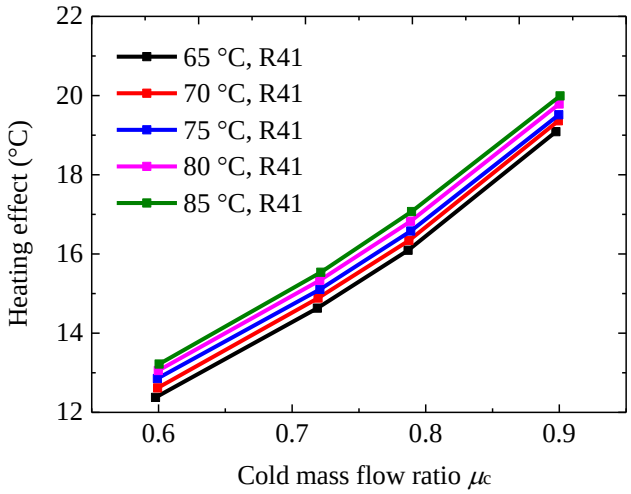

Figure 5.24 Heating effect at different inlet temperatures for R41 (p_{in} = 0.38 MPa)

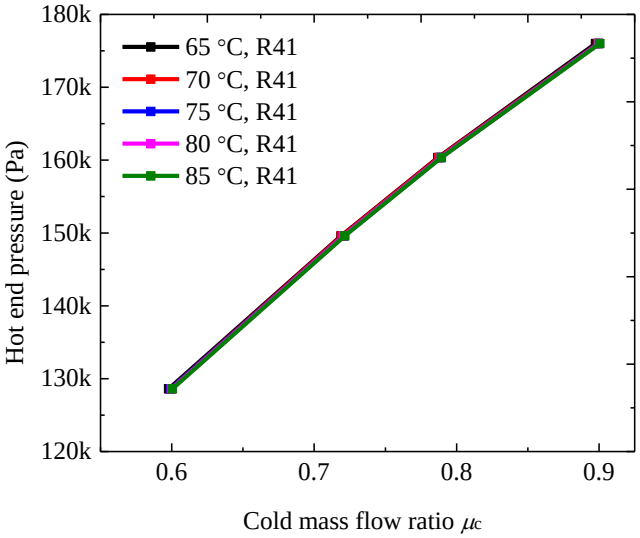

Figure 5.25 Hot end pressure (gauge) at different inlet temperatures for the R41 (p_{in} = 0.38 MPa)

2) The influence of the inlet pressure

Figure 5.26 shows how the cooling effect varies with the inlet pressures for the Sub-group 1 refrigerants, when the inlet temperature is kept constant at 40 °C. As previously explained, in general a higher inlet pressure would lead to a larger chamber inlet velocity and thus a stronger rotation flow, resulting in a larger cooling effect. This section is therefore only presenting the data for all the refrigerants within this Sub-group.

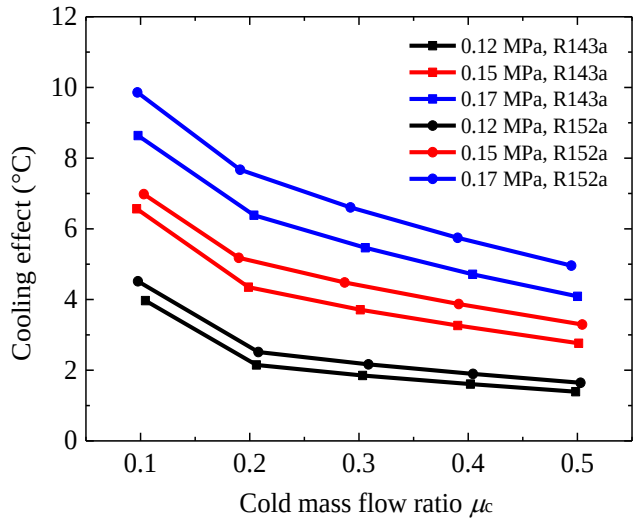
Cooling effect (°C)
Cold mass flow ratio μ_c
0.12 MPa, R143a
0.15 MPa, R143a
0.17 MPa, R143a
0.12 MPa, R152a
0.15 MPa, R152a
0.17 MPa, R152a

a

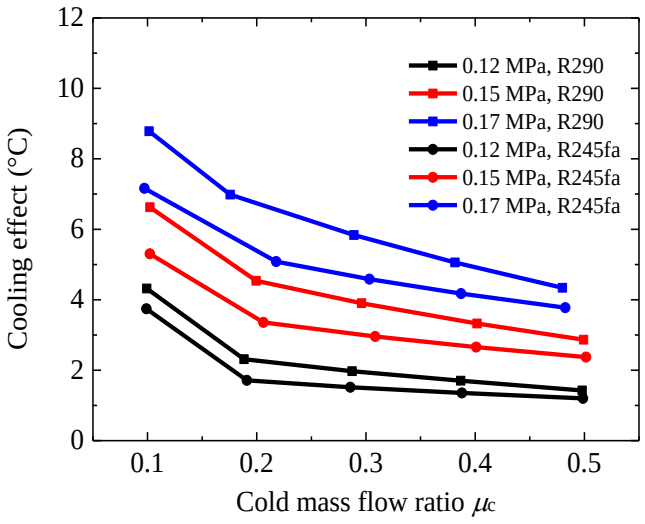
Cooling effect (°C)
Cold mass flow ratio μ_c
0.12 MPa, R290
0.15 MPa, R290
0.17 MPa, R290
0.12 MPa, R245fa
0.15 MPa, R245fa
0.17 MPa, R245fa

b

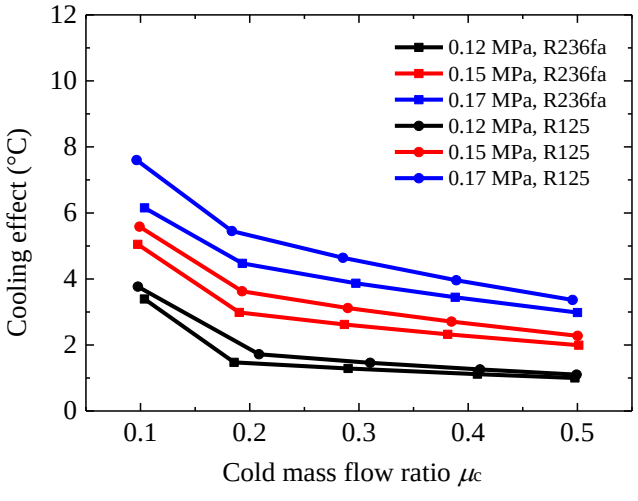
Cooling effect (°C)
Cold mass flow ratio μ_c
0.12 MPa, R236fa
0.15 MPa, R236fa
0.17 MPa, R236fa
0.12 MPa, R125
0.15 MPa, R125
0.17 MPa, R125

c

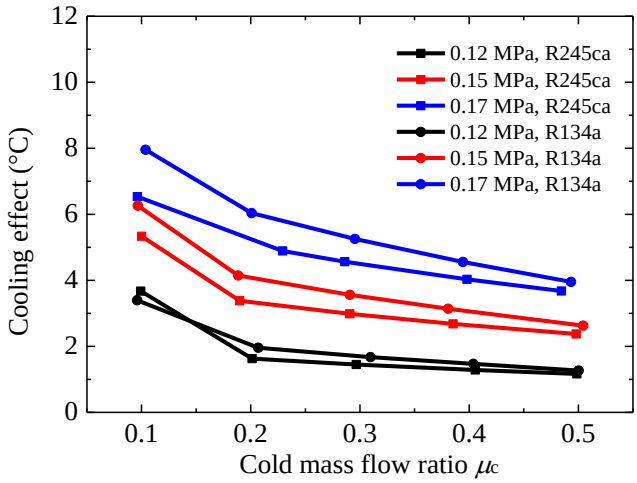

d

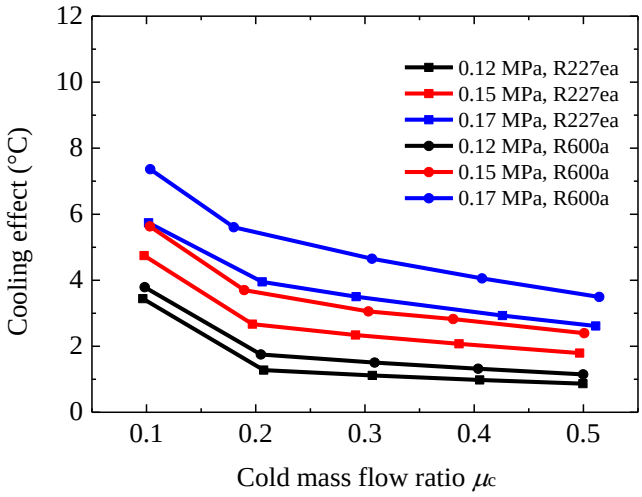

e

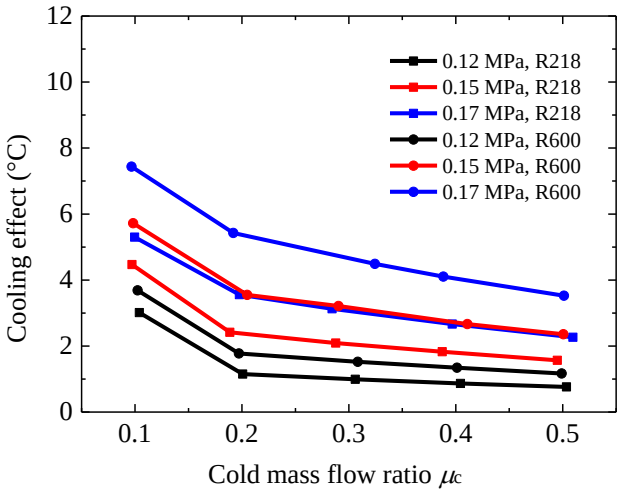

f

Figure 5.26 Variations of cooling effect with inlet pressures for the Sub-group 1 refrigerants at T_{in} = 40 °C

Figure 5.27 presents the influence of inlet pressures on the heating effect for the Sub-group 4 refrigerants at 75 °C VT inlet temperature. Within the pressure range considered (0.33 MPa ~ 0.50 MPa), for certain refrigerants including R717, R32, R125, R290, R143a and R600a, the heating effect could reach a peak value when the inlet pressure is increased, and any further increase in pressure would lead to the heating effect falling. Similar to the explanations put forward for R134a and R600 in Chapter 4, a larger inlet pressure leads to a higher tangential velocity (illustrated by R290, Figure 5.28) which is expected to produce a higher shear stress and a stronger rotation, as well as a higher temperature increase. But the rate of velocity increase drops when p_{in} is reaching certain peak value. At the same time, a larger p_{in} would give rise to a larger $\Delta p_{in\text{-}h}$, resulting in a bigger temperature drop that would cancel out a bigger portion of heating effect.

On the other hand, for R134a, R245fa, R245ca, R236fa, R152a, R227ea, R600 and R218, an increase of the inlet pressures would only lead to a decrease in heating effect. The pressure corresponding to the peak heating effect is probably below the pressure range considered.

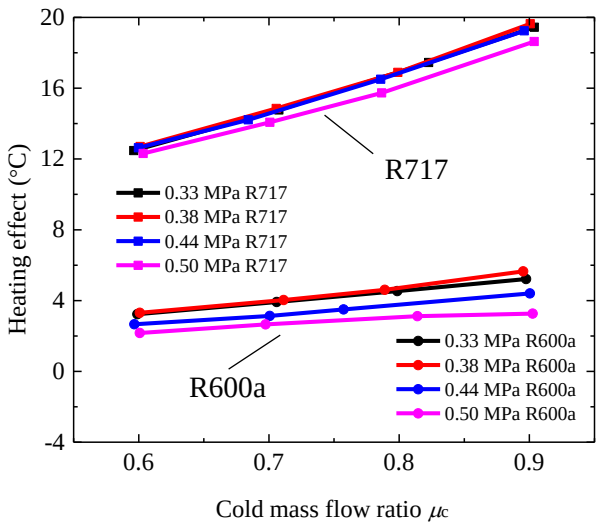

a

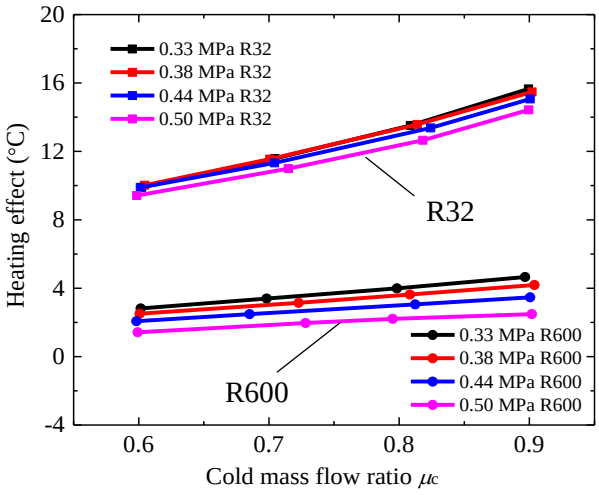
0.33 MPa R32
0.38 MPa R32
0.44 MPa R32
0.50 MPa R32
R32
R600
0.33 MPa R600
0.38 MPa R600
0.44 MPa R600
0.50 MPa R600
Heating effect (°C)
Cold mass flow ratio μc

b

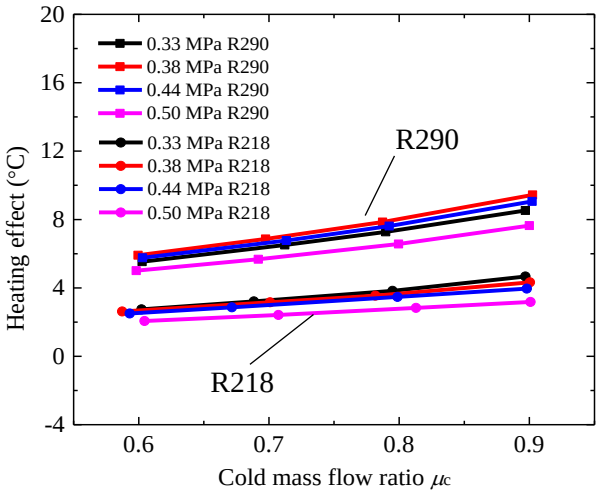
0.33 MPa R290
0.38 MPa R290
0.44 MPa R290
0.50 MPa R290
0.33 MPa R218
0.38 MPa R218
0.44 MPa R218
0.50 MPa R218
R290
R218
Heating effect (°C)
Cold mass flow ratio μc

c

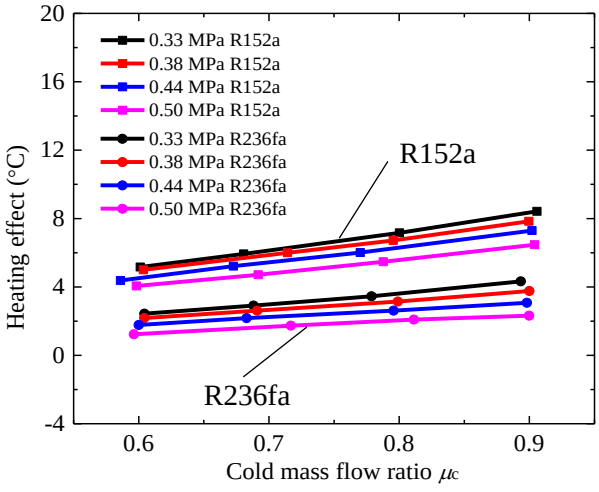
0.33 MPa R152a
0.38 MPa R152a
0.44 MPa R152a
0.50 MPa R152a
0.33 MPa R236fa
0.38 MPa R236fa
0.44 MPa R236fa
0.50 MPa R236fa
R152a
R236fa
Heating effect (°C)
Cold mass flow ratio μc

d

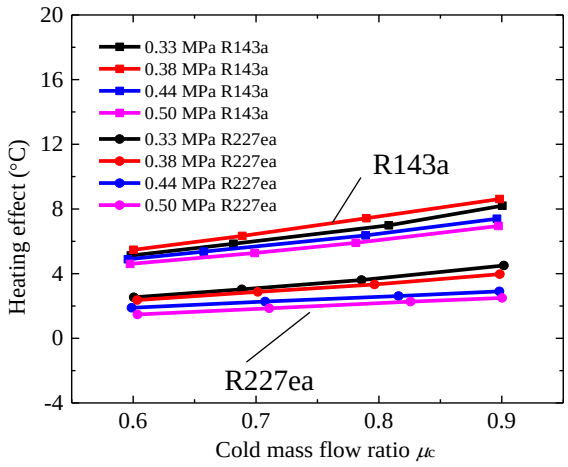

e

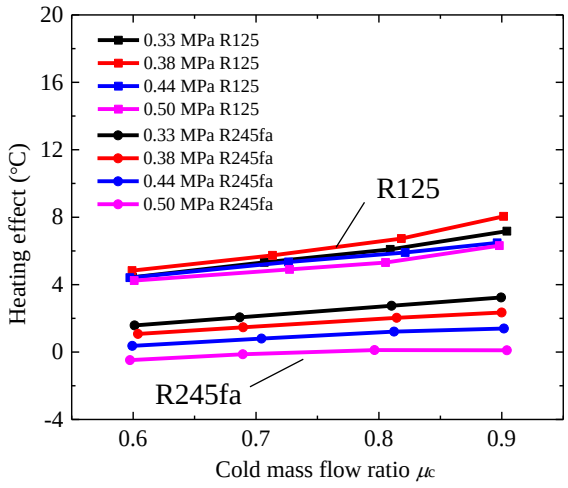

f

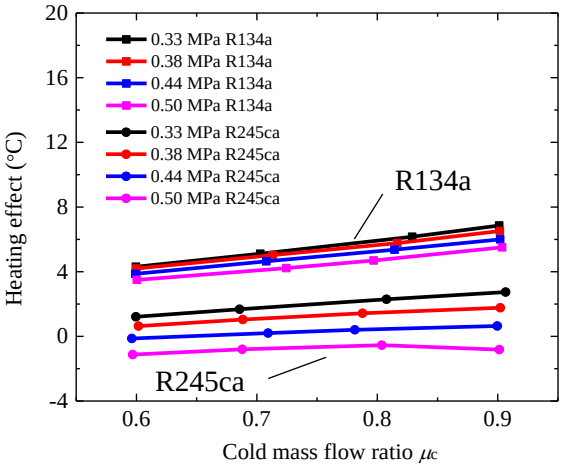

g

Figure 5.27 Variations of heating effect with inlet pressures effect for the Sub-group 4 refrigerants (T_{in} = 75 °C)

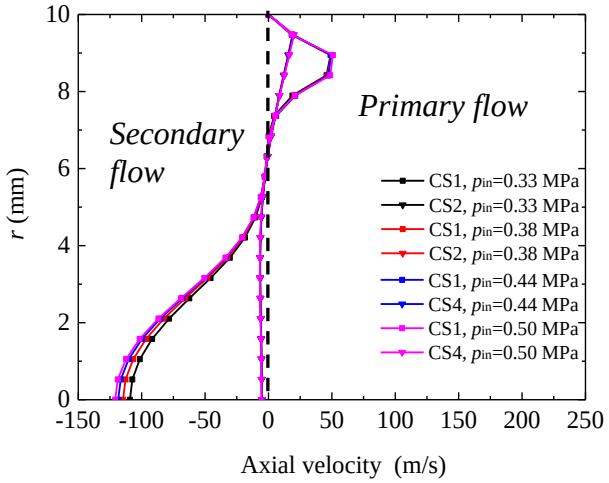

a

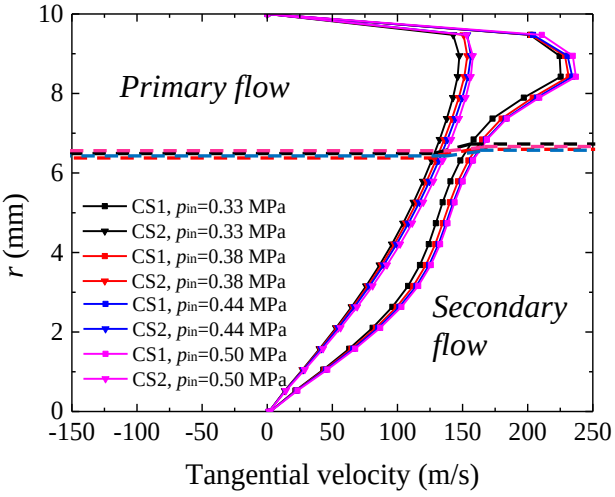

b

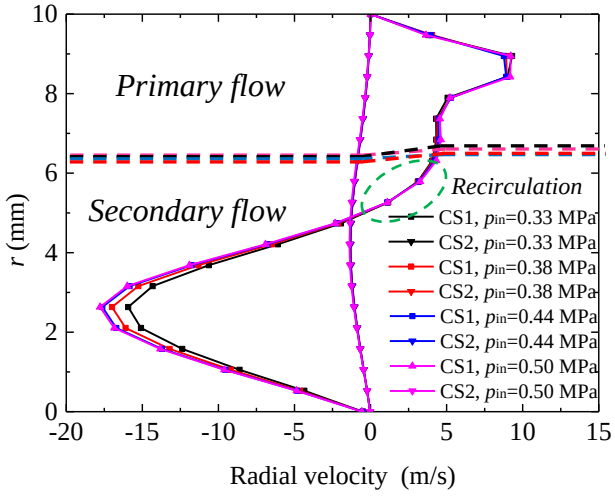

c

Figure 5.28 Axial (a), tangential (b) and radial (c) velocity profiles at two cross-sections (x_1 = 2 mm, x_2 = 90 mm) at different inlet pressures for R290 (μ_c = 0.6)

This chapter presented the details of constructing boundary lines for chosen refrigerants in each of the two groups, followed by further sub-grouping them based on the likely VT inlet pressure/temperature in system environment. The influence of the VT inlet temperature/pressure on the TSE for two sub-groups refrigerants were examined. The influence of thermal-physical properties (e.g. thermal diffusivity) on TSE was discussed.

To summarise, using the boundary line (FU or FDS) the VT inlet condition/state to ensure dry nozzle operation can be easily "read" from the *T*-*s* diagram. Noting that the positions of the line remains relatively stationary when low VT inlet velocities are involved has a practical implication; that is for a given refrigerant, one boundary line can be used to determine the VT inlet pressure during system integration, for a range of VT inlet velocities.

The analysis and comparison of the relative TSE of individual refrigerants in different Sub-groups enhance significantly our understanding of how their TSE is affected by various thermal-physical properties, suggesting these properties could be initially used to rank refrigerants' VT temperature separation performance.

The findings from the investigation into the influence of the VT inlet temperature/pressure on the TSE provide a useful platform for developing the system integration procedure. Within the range of p_{in} and T_{in} considered, the cooling effect is mainly affected by the p_{in}, suggesting that the VT inlet pressure should be chosen on the boundary line FU (Group 1 refrigerants) or FDS (Group 2 refrigerants) to achieve the best cooling effect, for a specified VT inlet temperature. On the other hand, the heating effect of the examined refrigerants are found to be influenced by both p_{in} and T_{in}, suggesting that there is a combination of the p_{in} and T_{in} generating the largest heating effect.

In the next chapter, the system integration procedure will be detailed and applied for certain refrigerants. The cooling system will be firstly integrated, then followed by the heating system. The possibility of using different refrigerant choices or the re-dimensioning the VT to achieve the required heating temperature will be assessed.

6 VT system integration with refrigerants

This chapter presents the application/implementation details of the procedures outlined in Section 3.3, for integrating a VT in the chosen cooling and heating systems, also taking into account of the refrigerant choices. The refrigerants are chosen initially based on the ranking of their cooling/heating effect, when the VT is assessed in isolation as described in Section 5.2. The main purpose of the integration process is therefore to establish if any of the chosen refrigerants could provide the required cooling or heating temperature, under the system operating conditions.

The integration procedures include:

- Since various key system design temperatures (e.g. T_{in} to the VT, condensing temperature) are already specified, for a chosen refrigerant, this step involves relating the temperatures, via the boundary line conditions and the refrigerant properties, to the refrigerant pressures.
- Taking the refrigerant pressures as the VT operating pressures, the VT heating or cooling temperature is predicted using the established CFD model and compared/ matched to the required system heating or cooling temperature.
- If no match could be found, another potential refrigerant choice or a possible re-dimensioning of the VT geometries, based on its thermal-physical properties at the system operating conditions, could be then suggested.
- The VT system performance is then evaluated thoroughly over a range of operating conditions/requirements. This is equivalent to typical system simulations, but with additional data input from CFD.

The coverage on the cooling system integration is presented in Section 6.1, also including a discussion on coefficient of performance (*COP*) when different refrigerant choices are made. Section 6.2 presents the heating system integration which also discusses the VT re-dimensioning requirements.

6.1 Coupling of refrigerants with the VT cooling system

R152a, R600a and R227ea are initially chosen representing respectively the top, middle and bottom ranking performers according to their cooling effect (Table 5.11), to compare how well they meet the cooling temperature requirement. The first is a

Group 2 refrigerant and the last two belong to Group 1.

It should be noted that the starting saturation temperature (T_u) for the construction of the boundary line was set at 20 °C, and to allow for the required superheat for Group 2 refrigerants, the boundary line actually starts at a temperature (i.e. T_{ds}) larger than 20 °C (e.g. T_{ds} = 27.8 °C for R152a).

In the chosen system, if the VT T_{in} is lower than T_{ds}, it is not possible to use the boundary line to read off the VT inlet pressure. In such case, the boundary line should be extended until the start point T_{ds} is at the required T_{in} (i.e. to have a lower corresponding saturated temperature to start the construction of the boundary line). The extension can be implemented also if one would like to bring in additional Group 2 refrigerants for evaluation, such as R717 and R41, which have much higher T_{ds}.

6.1.1 Preparation for system integration

Previously, the analysis concludes that for a given refrigerant, when the VT inlet pressure is kept constant, the inlet temperature only has minimal impact on the cooling effect. On the other hand, at a constant inlet temperature, a higher inlet pressure would produce a larger cooling effect. Therefore, to achieve a better cooling effect, the VT inlet conditions (location 3 on Figure 3.14) should have a larger pressure at the design temperature.

In the integration, the VT inlet temperature T_3 is varied from 20 °C to 30 °C then to 40 °C. The procedure for locating the VT inlet state (T_3, p_3) on the *T*-*s* diagram in the cooling system integration is applied to R152a, R600a, R227ea, R717 and R41. The last two are added as they have large isentropic expansion exponents and are worth to be considered/compared too.

To illustrate, for R600a (Group 1 refrigerant) when the VT inlet T_3 is 40 °C which is smaller than T_p (~ 107.79 °C), the pressure p_3 at position 3 can be found, based on Figure 3.18i from Figure 3.7, to be 0.53 MPa. Similarly for R717 (a Group 2 refrigerant), p_3 (0.63 MPa, T_3 = 40 °C) can be decided based on Figure 3.18iii (from Figure 5.4g). Accordingly, the inlet pressures for other chosen refrigerants at the specified VT inlet temperatures are shown in Table 6.1.

Table 6.1 VT inlet pressures (within the system) for the chosen refrigerants at three inlet temperatures

Refrigerant \ T_3 (°C) / p_3 (MPa)	20	30	40
R41	1.58	2.00	2.47
R152a	0.40	0.55	0.74
R227ea	0.39	0.53	0.70
R717	0.32	0.46	0.63
R600a	0.30	0.40	0.53

In the simulation, only the cold mass flow ratio μ_c in the range between 0.2 and 0.5 are considered as explained previously; this is achieved by adjusting the VT hot end and the cold end pressures to ensure reaching a Mach number as close to 1 as possible.

The thermodynamic performance of the cooling system is analysed based on the following general assumptions:

- The pressure drops and the heat loss in the connecting pipes are negligible.
- The total efficiency of the compressor η_C is assumed at 0.98.

The thermodynamic performance is analysed based on the system flow process shown on the *p-h* diagram; only a *p-h* diagram (Figure 6.1, Group 2 refrigerants) is shown for illustration purpose, which is corresponding to the *T-s* diagram shown on Figure 3.18iii.

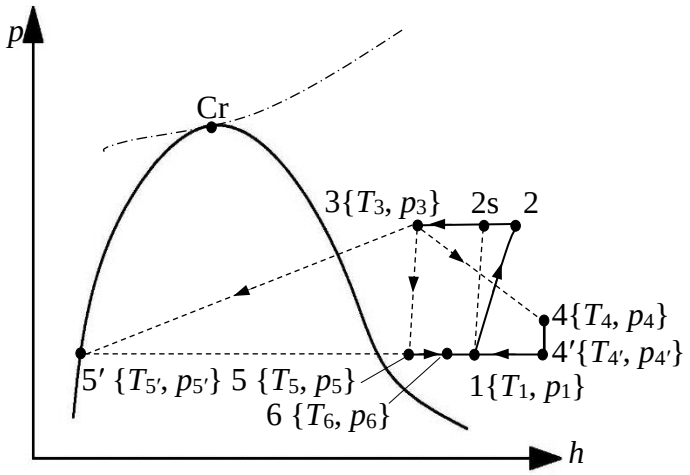

Figure 6.1 *p-h* diagram for the Group 2 refrigerants in the system based on Figure 3.18iii

For the heat exchanger Hx2 (Figure 3.14), the cooling capacity (Q_2) is defined as

$$Q_2 = \dot{m}_c \times (h_6 - h_5) \tag{6.1}$$

where $\dot{m}_c$ is the mass flow rate from the VT cold end (= $\mu_c \cdot \dot{m}_{in}$), The states at 5 and 6 are acquired from the CFD simulation. If liquid is produced and leaving the cold end, the equation will be revised accordingly to include 5′. The enthalpy at the compressor outlet is:

$$h_2 = \frac{h_{2s} - h_1}{\eta_c} + h_1 \tag{6.2}$$

2s is the compressor outlet for constant entropy compression to p_3.

The enthalpy at 1 can be given by

$$h_1 = \frac{\dot{m}_c \times h_6 + (\dot{m}_{in} - \dot{m}_c) \times h_4}{\dot{m}_{in}} \tag{6.3}$$

where $\dot{m}_{in}$ is the inlet mass flow rate to the VT. The compressor power consumption (W_{Co}) is taken as

$$W_{Co} = \dot{m}_{in} \times (h_2 - h_1) \tag{6.4}$$

The rejected heat from the refrigerant in Hx1 is given as

$$Q_1 = \dot{m}_{in} \times (h_3 - h_2) \tag{6.5}$$

The efficiency for the system (COP_C) is defined as

$$COP_C = \frac{Q_2}{W_{Co}} \tag{6.6}$$

6.1.2 Evaluation of system performance

The refrigerant R717 is examined first and Figure 6.2 presents the VT cold end temperature T_5 under T_3 = 20 °C, 30 °C and 40 °C. It can be noted that, at the same T_3 (or p_3), a larger μ_c leads to a higher T_5 (i.e. a smaller VT cooling effect) in the system; the same observation is made in Section 4.2 and Section 5.2.

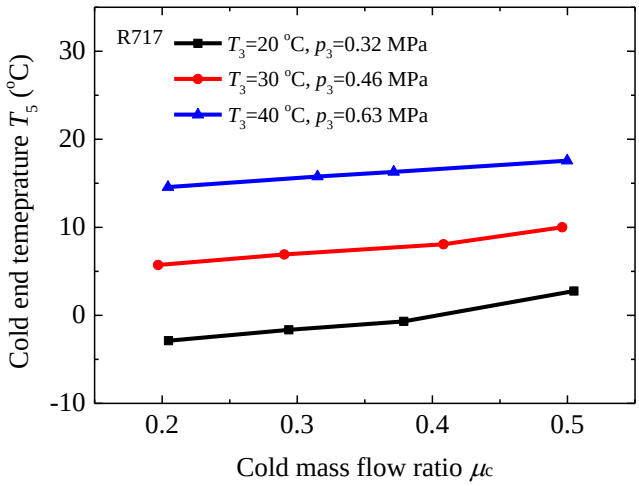

Figure 6.2 VT cold end temeprature T_5 for R717 under different inlet conditions

At the same μ_c, T_5 is found to increase at the same rate as T_3 (or p_3), leaving the cooling effect practically unchanged. It indicates that in the system, the increase of the pressure does not bring a significant improvement of the cooling effect for VT because the chamber inlet velocities (Figure 6.3) do not change significantly, hence little impact of the temperature drop from the rotation process. Looking from another angle, though a higher inlet pressure (temperature) is expected to produce a larger pressure drop $\Delta p_{in\text{-}c}$ (Figure 6.4), the isentropic expansion exponent (Table 6.2) gets smaller. The combined influence is therefore to have the cooling effect practically unaffected.

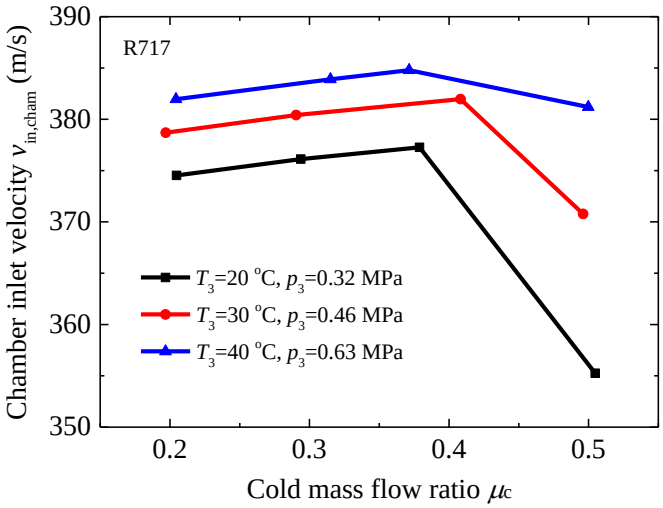

Figure 6.3 Chamber inlet velocities for R717 at different system operating conditions

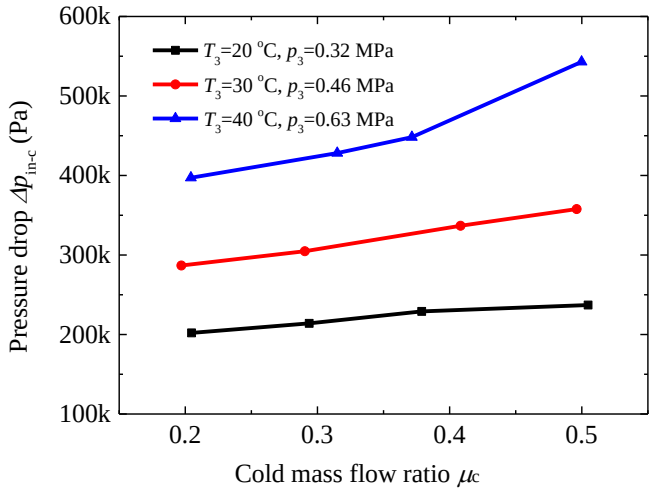

Figure 6.4 Pressure drop $\Delta p_{in\text{-}c}$ between the VT inlet and the cold end for R717 at different system operating conditions

Table 6.2 Isentropic expansion exponent for R717 at different system conditions

T_3 °C	p_3 MPa	Isentropic expansion exponent
20	0.32	1.297
30	0.46	1.293
40	0.63	1.288

Also observed from Figure 6.2 is that, when T_3 is above 40 °C, heat exchanger Hx2 cannot perform any cooling duties, as the initial design temperature range at the Hx2 exit (i.e. T_6) is set at between -5 °C and 15 °C (an interval of 5 °C), which is below T_5. When T_3 is set at 30 °C, the cooling function can only be achieved when T_6 is specified between 10 ~ 15 °C; a lower T_6 (0 ~ 15 °C) is only possible when T_3 is 20 °C.

Figure 6.5 presents the system COP_C for R717. At a given VT inlet T_3, the COP_C increases with increasing T_6, as a result of having the cooling capacity increased (with respect T_6) at a faster rate than that of compressor power consumption (Table 6.3). Additionally, at the same T_3, there appears to have an optimal μ_c leading to the largest COP_C at relatively high T_6 values, reflecting the balance between the relative changes in the cold end mass flow rate and cooling effect when μ_c is varied from low to high values. At a fixed T_6, a lower T_3 would lead to a higher COP_C, as a result of having a larger cooling capacity produced by Hx2.

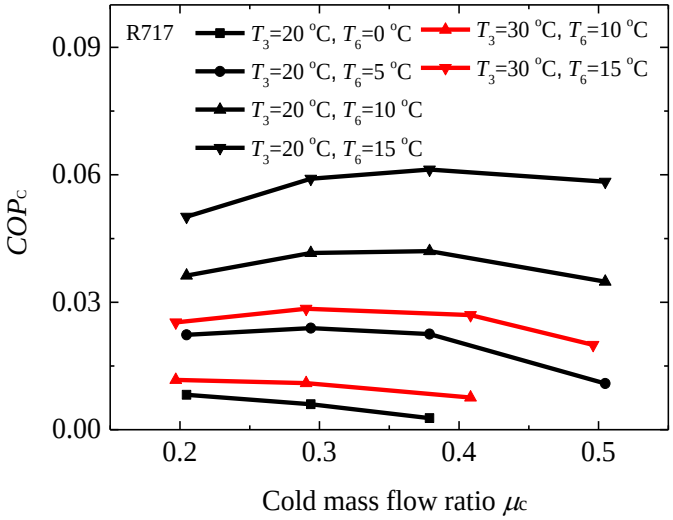

Figure 6.5 COP_c of the cooling system under different conditions for R717

Table 6.3 Comparison of the cooling capacity and the comsumed compressor power at different cooling temeprature T_6 (T_3 = 20°C)

T_6 °C	Cooling capacity Q_E kW	Δ%	Compressor power W_{Co} kW	Δ%
0	0.012	+172.88%	1.405	+0.43%
5	0.031	+63.16%	1.411	+0.35%
10	0.051	+38.63%	1.416	+0.35%
15	0.071		1.421	

Figure 6.6 displays the enthalpy at the VT inlet (location 3) and the cold end exit (location 5) in the system under different operating conditions. It can be seen that, h_5 is always smaller than h_3 at any conditions, suggesting when compared to a simple throttle, a VT could produce a colder exit. Therefore potentially there are opportunities in replacing throttling devices in thermal systems by VT to achieve both pressure and temperature reductions requirements.

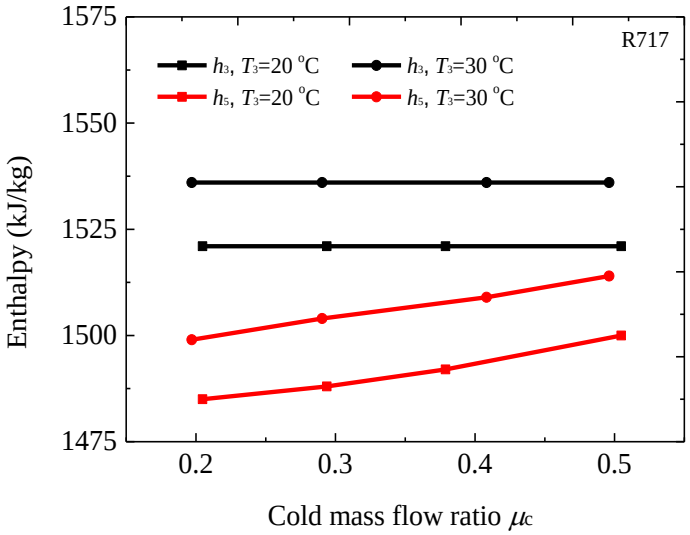

Figure 6.6 Enthalpy at VT inlet (location 3) and the cold end exit (location 5) in the system (Figure 3.14) under different operating conditions for R717

Figure 6.7 presents the variations of the Mach number at the VT chamber inlet for R717. It can be noted that, under the examined conditions, the largest Mach number achieved is around 0.95, above which choked flow will occur and the simulation could not reach convergence. In addition, Mach number of 0.95 could not be maintained at all μ_c, as both hot end and cold end pressures need to be adjusted to achieve certain μ_c values. This implies that in a system, if a VT is to operate at the largest Mach number at all μ_c values, a variable nozzle geometry may be more desirable.

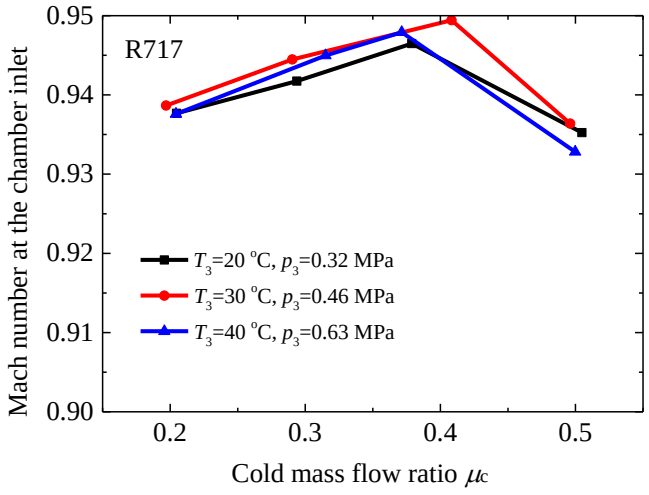

Figure 6.7 Mach number at the chamber inlet with R717

The same system integration procedure is also applied to R41, R227ea, R152a and R600a. The VT cold end temperature T_5 for these refrigerants are shown in Figure 6.8. It can be noted that for all refrigerants, at the same μ_c, an increase of T_3 leads to an

increase of T_5 by a similar amount. This again implies in the system, both the increase of VT inlet pressure and temperature could not bring a significant increase of the cooling effect (lower cooling temperature). As explained by R717, this is due to the fact that chamber inlet velocities are rather similar at different T_3 and p_3 for a given refrigerant, and at a higher T_3 and p_3 the refrigerant has a smaller isentropic expansion exponent even it has a larger pressure drop $\Delta p_{\text{in-c}}$. For R41 and R227ea, the cold end temperature T_5 decreases with increasing μ_c from 0.2 to 0.5, and it (results not presented) reaches a minimum value at μ_c of around 0.6, suggesting that in the system, the largest cooling effect is acquired at μ_c of around 0.6.

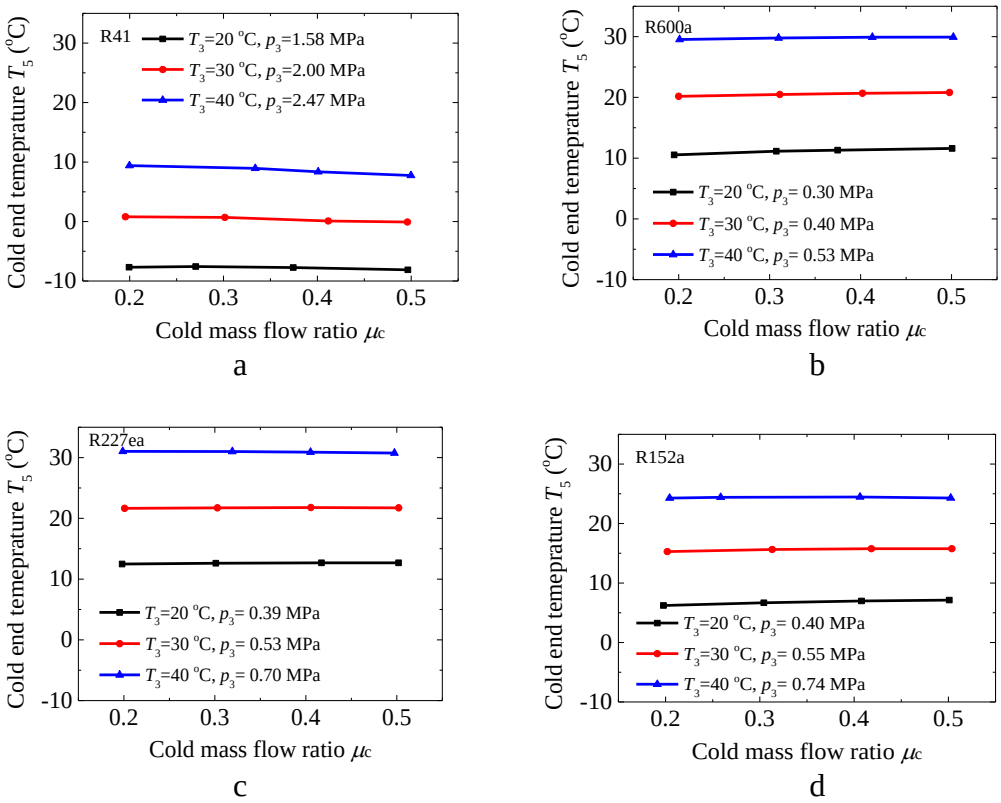

Figure 6.8 VT cold end temeprature T_5 for refrigerants under different inlet temperatures: R41 (a), R600a (b), R227ea (c), R152a (d)

Figure 6.9 displays the COP_c of the chosen refrigerants under the specified operating conditions. As previously noted for R717, for a given cooling temperature T_6, a smaller T_3 will lead to a larger COP_c, which is a result of having a larger cooling capacity provided by the heat exchanger Hx2. The optimal value of μ_c for delivering the largest COP_c is found to be dependent on both the refrigerant choices/properties (e.g. the isentropic expansion exponent) and the operating conditions, and at optimal μ_c, p_c reaches the lowest value for individual refrigerants.

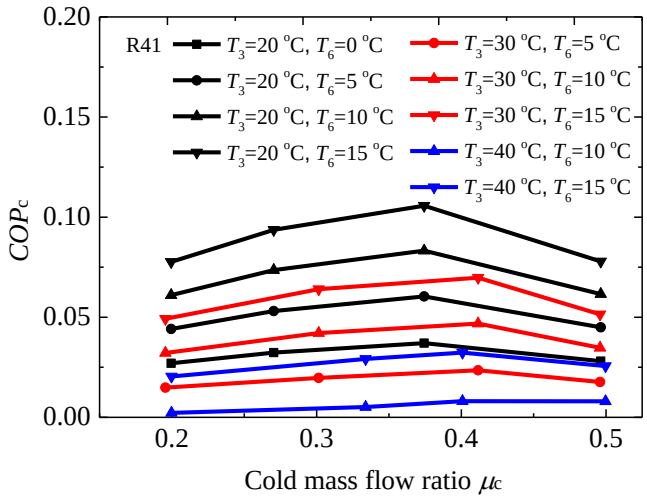

a. R41, T_3 = 20 - 40 °C, T_6 = 0 - 15 °C

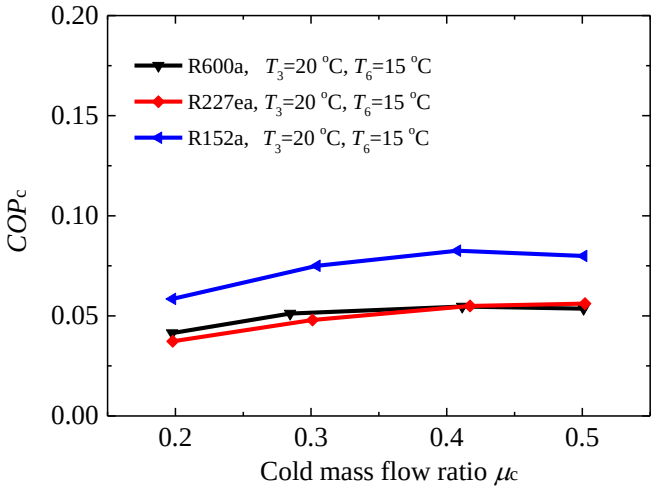

b. R600a, R227ea and R152a, T_3 = 20 °C, T_6 = 15 °C

Figure 6.9 COP_C of the cooling system under different operating conditions with refrigerants: a. R41, b.R600a, R227ea and R152a

6.1.3 Comparison of the system performance for different refrigerants

Figure 6.10 compares the VT cold end temperature (T_5) in the system for the chosen refrigerants at three VT inlet temperatures (T_3 = 20 °C, 30 °C and 40 °C).

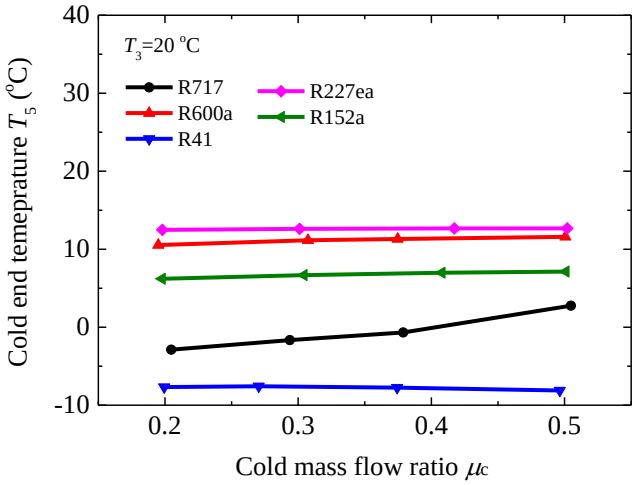

a

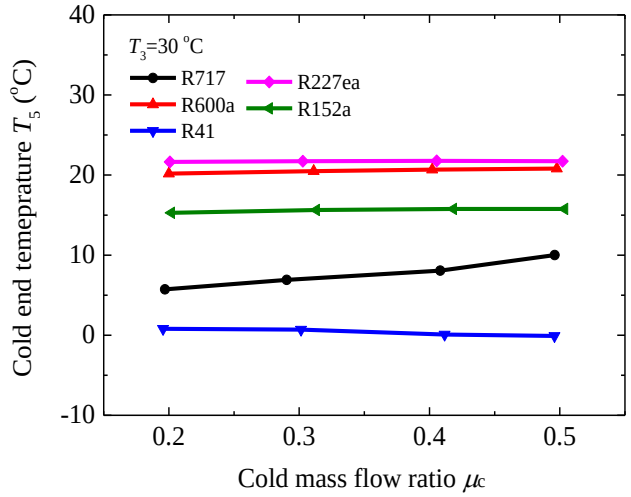

b

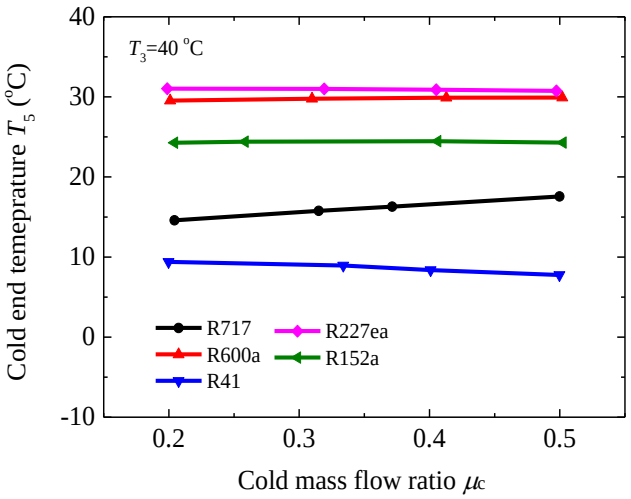

c

Figure 6.10 Comparison of the cold end temperatures for refrigerants under different inlet conditions

It can be seen that, R41 always generates the lowest VT cold end temperature T_5 (i.e. the largest cooling effect ΔT_c) than R717 and R152a, whereas R227ea and R600a produce the highest T_5. This observation deviates from the trends observed in Section 5.2.1; as R41 has a smaller isentropic expansion exponent than R717 (see illustrated in Table 6.4 for T_3 = 20 °C) and is thus expected to produce a larger T_5 (smaller ΔT_c). However, the observation in Section 5.2.1 is made when the same pressure drop $\Delta p_{in\text{-}c}$ can be set for all the examined refrigerants, when they are evaluated for an "isolated" VT. In the system, R41 experiences a larger pressure drop $\Delta p_{3\text{-}5}$ ($\Delta p_{in\text{-}c}$), which is expected to bring a bigger temperature drop through the VT, thus generating a lower VT cold end temperature. R600a has a larger isentropic expansion exponent but a smaller $\Delta p_{3\text{-}5}$ than R227ea, and therefore they end up of having similar T_5 (cooling effect).

Table 6.4 Isentropic expansion exponent and pressure drop $\Delta p_{3\text{-}5}$ for chosen refrigerants at the system operating conditions (T_3 = 20 °C)

Refrigerants	p_3 MPa	Isentropic expansion exponent	$\Delta p_{3\text{-}5}$ (μ_c = 0.2) MPa
R717	0.32	1.297	0.20
R41	1.58	1.255	1.00
R152a	0.40	1.094	0.23
R600a	0.30	1.029	0.17
R227ea	0.39	0.965	0.21

Figure 6.11 presents the comparison of the system *COP*c for different refrigerants, at T_3 = 20 °C and T_6 = 15 °C. In general, the refrigerant that produces the coldest temperature T_5 is expected to have the largest *COP*c. However the *COP*c is also influenced by the compressor power consumption. R717 has a higher specific work of compression than R152a thus a smaller *COP*c.

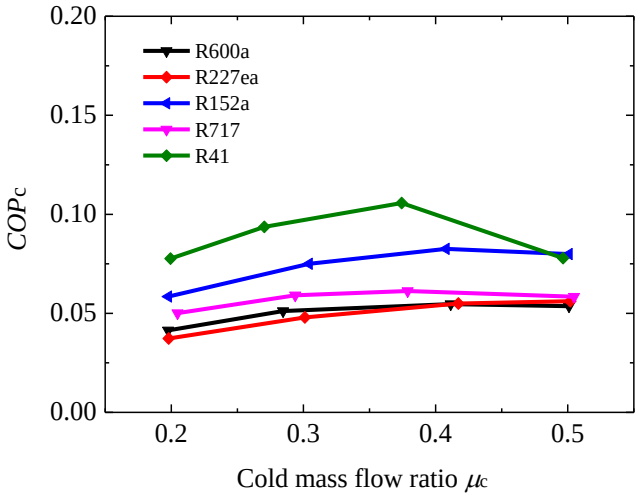

Figure 6.11 the comparison of *COP*c under the system temperature

Compared to conventional vapour compression refrigeration systems, the VT system has much smaller *COP* values (less than 0.15), though they are of similar values to that of VT *COP*[54]. In the VT system, the fluid exiting the cold end is always in the superheated vapour state whereas in the former, latent heat is always involved.

In a system it is possible to produce liquid at the VT cold end to improve system *COP*c by:

1. Choosing a refrigerant which has relatively a larger isentropic expansion exponent, and has a higher pressure at a given temperature on the boundary line. These help to generate larger temperature drop from the VT inlet.

2. Replacing the VT with a liquid VT which is designed to produce liquid inside the VT[16].

6.2 Integration of the liquid pump heating system

Based on the ranking of the heating effect in Section 5.2.1, R41, R717, R600a and R227ea are chosen for evaluation. R41 and R717 are chosen as they are found to generate the largest heating effect, and have quite different saturated pressure (at the same temperature). R600a and R227ea[17] are chosen for comparison purpose as they are sitting at the middle and bottom of the rank.

[16] Liquid VT is not simulated in this part as the research/design about it is rather limited
[17] R227ea is chosen, instead of R236fa, R245fa and R245ca which are the last three refrigerants in the heating rank, as it also consumes much less computer running time

6.2.1 Preparation for the system integration

In the liquid pump VT heating system (as shown in Figure 3.16, for readers' convenience the figure together with the associated *T*-*s* diagram, Figure 3.20iii, are reproduced below), the pressure p_4 at the VT inlet is the same as the boiler pressure (p_3) which is controlled by the boiler heat input. The p_4 could in theory take up any value between the condensing pressure p_8 (= VT cold end pressure, p_6 which is governed by the condensing temperature T_8) and the saturated pressure $p_{sat\text{-}4}$ for T_4 which is the boiler exit temperature. T_4 - T_3 is the degree of superheat ΔT_{sh} at boiler exit.

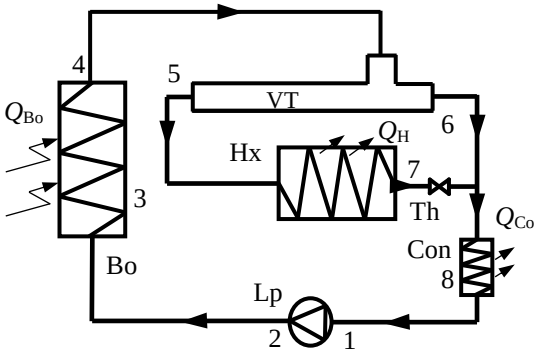

Figure 3.16 Schematic diagram of the closed liquid-pump VT heating system[94] (Lp-Liquid pump, Bo-Boiler, Con-Condenser, Hx-Heat exchanger, Th-Throttle, VT-Vortex tube)

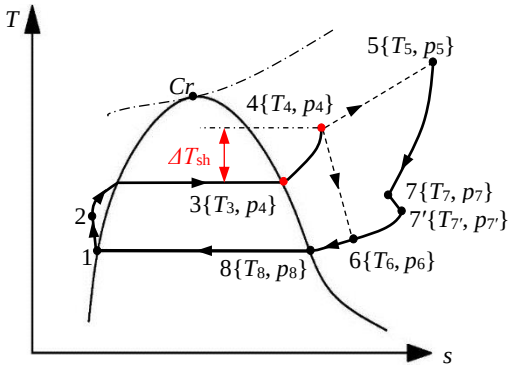

iii

Figure 3.20 Key state points (●) used in the coupling process for the specified heating system

Based on the observations from the Chapter 5, at a constant p_{in} and μ_c, an increase in inlet temperature T_{in} (i.e. a larger ΔT_{sh}) would lead to an increase in heating effect. At a constant T_{in} and μ_c, the maximum heating effect is achieved when the inlet pressure p_{in} reaches a certain value, above which any further increase of p_{in} would result in a drop in the heating effect.

Taking into account the above observations, the system integration procedure proposed in Section 3.3.2 is applied accordingly. The key aim is to identify the best combination of the VT inlet pressure p_4 and the associated ΔT_{sh} to produce the largest heating effect, and at the same time examine whether the VT hot end temperature T_5 (based on this largest heating effect) is larger than the specified required temperature T_7; if not either a VT re-dimensioning or/and switching refrigerant choices could be considered.

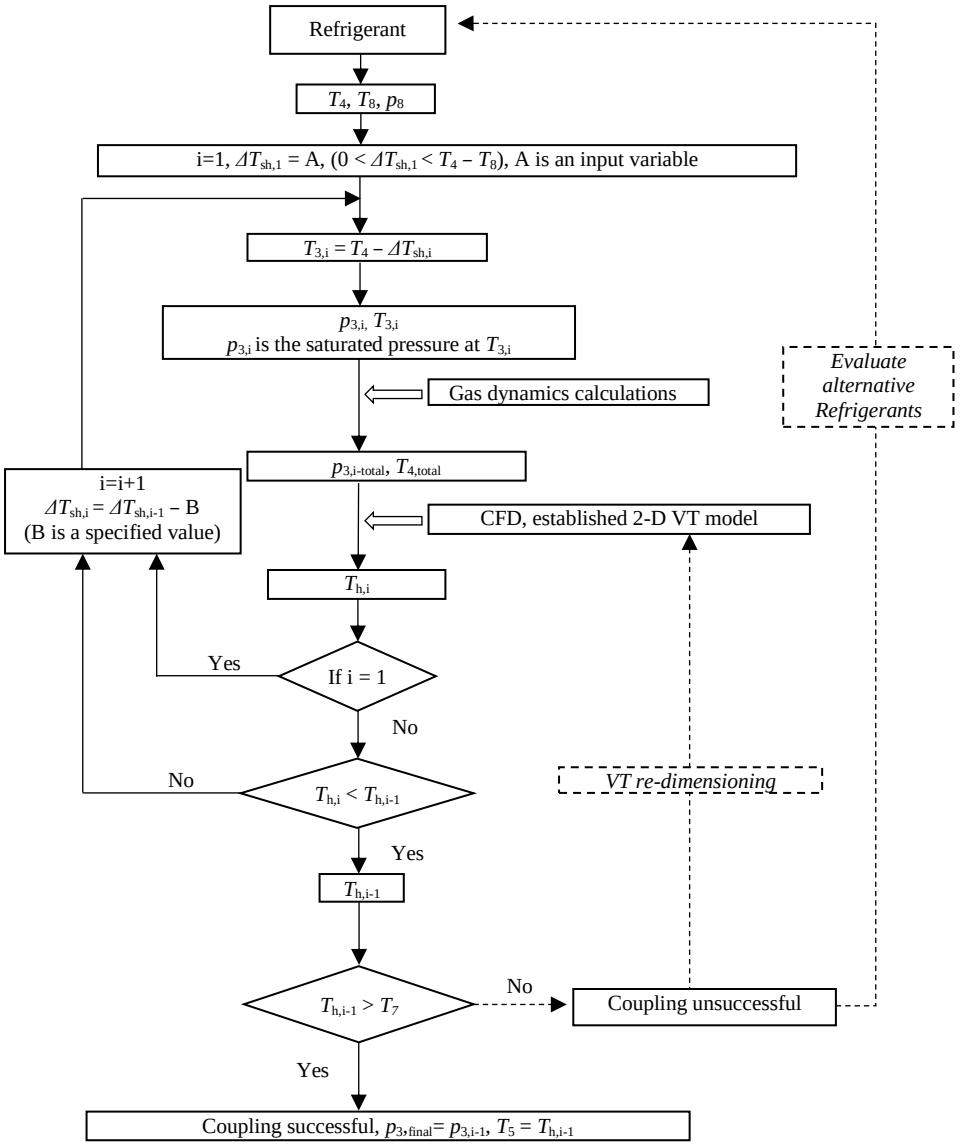

Figure 3.21 Procedure of coupling the heating system with the refrigerant for a given VT

The temperature T_4 is varied from 60 to 80 °C (at a 5 °C increment), the condensing temperature T_8 from 20 to 30 °C (at a 5 °C increment). Setting an initial ΔT_{sh} of 30, 40 or 50 °C (Figure 3.21, also reproduced above for readers' convenience), the possible T_{3i} and ΔT_{shi} for T_8 = 20 °C, T_4 = 60 °C, 70 °C and 80 °C are shown in Table 6.5.

Table 6.5 T_{3i}, p_4 and ΔT_{shi} for T_8 = 20 °C, and T_4 = 60, 70 and 80 °C

T_8	i	T_{3i}	p_4[18]	T_4	ΔT_{shi}	T_4	ΔT_{shi}	T_4	ΔT_{shi}
°C		°C	MPa	°C	°C	°C	°C	°C	°C
	1	30	$p_{4,sat-30}$		30		40		50
	2	40	$p_{4,sat-40}$	60	20		30		40
20	3	50	$p_{4,sat-50}$		10	70	20	80	30
	4	60	$p_{4,sat-60}$				10		20
	5	70	$p_{4,sat-70}$						10

Starting with, say, a T_4 = 60 °C (highlighted), the heating effect for each individual combination of pressure p_4 and the associated degree of superheat ΔT_{shi}, starting from i = 1, 2, 3…, is determined and compared to the next one until the combination that would produce the largest heating effect is identified. Let's say the heating effect for i = 2 (i.e. $p_{4, sat-40,}$ T_{3i} = 40 °C and ΔT_{sh2} = 20 °C) is compared to the case i = 3 (i.e. $p_{4,sat-50,}$ T_{3i} = 50 °C and ΔT_{sh3} = 10 °C). If the latter is found to produce less heating effect, then the former is taken as the best combination. Otherwise, cases i = 3 and 4 are compared next until the conditions to achieve the maximum heating effect are identified; for i = 4 and T_4 = 60 °C, a smaller than 10 °C ΔT_{shi} is input. The steps are repeated to identify the best combination at T_4 = 70 and 80 °C.

For illustration, for R717, at T_4 = 60 °C, T_8 = 20 °C, ΔT_{sh} = 30, 20 and 10 °C, the combinations for p_4 and ΔT_{sh} are respectively 1.17 MPa (ΔT_{sh1} = 30 °C), 1.56 MPa (ΔT_{sh2} = 20 °C) and 2.03 MPa (ΔT_{sh3} = 10 °C); for the rest of chosen refrigerants at the same T_4 (= 60 °C), their details are also included (Table 6.6[19]).

[18] The actual value of these p_4 are varied for different refrigerants, $p_{4,sat-30}$ represents the pressure at the saturated temperature 30 °C for a chosen refrigerant

[19] R41 has a different T_3 to R717, R600a and R227ea, as the critical temperature of R41 is 44.13 °C (less than 50 °C), hence two separate tables

Table 6.6a VT inlet conditions at corresponding degree of superheat for R717, R600a and R227ea, T_4 = 60 °C

T_8	i	T_{3i}	p_4, R717	p_4, R600a	p_4, R227ea	T_4	ΔT_{shi}
°C		°C	MPa	MPa	MPa	°C	°C
	1	30	1.17	0.40	0.53		30
20	2	40	1.56	0.53	0.70	60	20
	3	50	2.03	0.68	0.92		10
	1	30	1.17	0.40	0.53		30
25	2	40	1.56	0.53	0.70	60	20
	3	50	2.03	0.68	0.92		10
	1	35	1.35	0.46	0.61		25
30	2	45	1.78	0.60	0.80	60	15
	3	55	2.31	0.77	1.04		5

Table 6.6b VT inlet conditions at corresponding degree of superheat for R41, T_4 = 60 °C

T_8	i	T_{3i}	p_4, R41	T_4	ΔT_{shi}
°C		°C	MPa	°C	°C
	1	30	4.30		30
20	2	40	5.39	60	20
	3	44	5.90		16
	1	30	4.30		30
25	2	40	5.39	60	20
	3	44	5.90		16
	1	35	4.82		25
30	2	40	5.39	60	20
	3	44	5.90		16

The thermodynamic performance of the heating system is analysed based on the following general assumptions:

- The pressure drops and the heat loss/gain in the connecting pipe are negligible
- The degree of superheat for the refrigerants can be controlled by in the superheating section of the boiler
- The liquid pump work is negligible

The system flow processes are shown on the *p-h* diagram (Figure 6.12), as an illustration, for a Group 2 refrigerant, which is corresponding to the *T-s* diagram shown on Figure 3.20iii. The conditions to achieve max heating effects are identified and used to acquire the relevant enthalpy values in the thermal analysis.

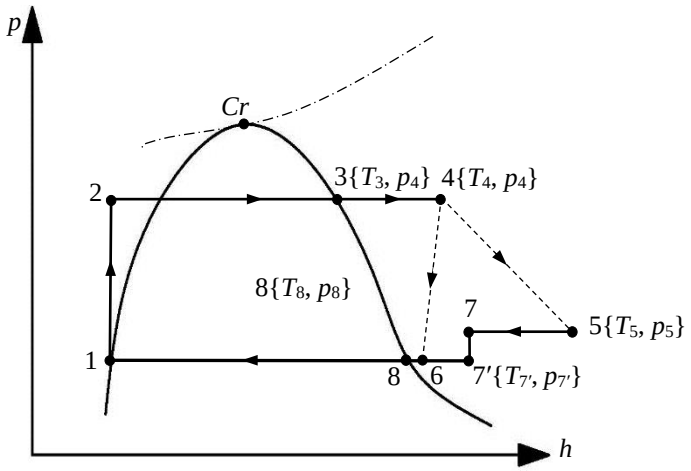

Figure 6.12 *p-h* diagram for the Group 2 refrigerants in the system based on Figure 3.20iii

The boiler heating capacity is given as,

$$Q_{\mathrm{Bo}} = \dot{m}_{\mathrm{in}} \times (h_4 - h_2) \tag{6.7}$$

The enthalpy h_2 is equalled to h_1, where h_1 is the enthalpy of the saturated liquid at T_1 ($T_1 = T_8$). The h_4 is the enthalpy at the VT inlet state 4.

The heating capacity of heat exchanger Hx1 is:

$$Q_{\mathrm{H}} = (\dot{m}_{\mathrm{in}} - \dot{m}_{\mathrm{c}}) \times (h_5 - h_7) \tag{6.8}$$

The refrigerant heat rejection rate in the condenser is given by:

$$Q_{\mathrm{Con}} = (\dot{m}_{\mathrm{in}} - \dot{m}_{\mathrm{c}}) \times (h_{7'} - h_1) + \dot{m}_{\mathrm{c}} \times (h_6 - h_1) \tag{6.9}$$

As the fluid always experiences an isenthalpic process in the throttle, the enthalpy $h_{7'}$

equals to h_7.

The COP_H of the heating system is defined as

$$COP_H = \frac{Q_H}{Q_{Bo}} \tag{6.10}$$

6.2.2 Comparison of the system performance of the chosen refrigerants

This section presents and discusses the results for the four chosen refrigerants, R227ea, R600a, R717 and R41. For three individual condensing temperatures (T_8 = 20, 25 and 30 °C), the maximum (i.e. heating effect) hot end temperature and the corresponding system conditions (p_4 and ΔT_{sh}) to achieve them are shown in Figure 6.13, the results are all for a VT inlet temperature of T_4 = 60 °C.

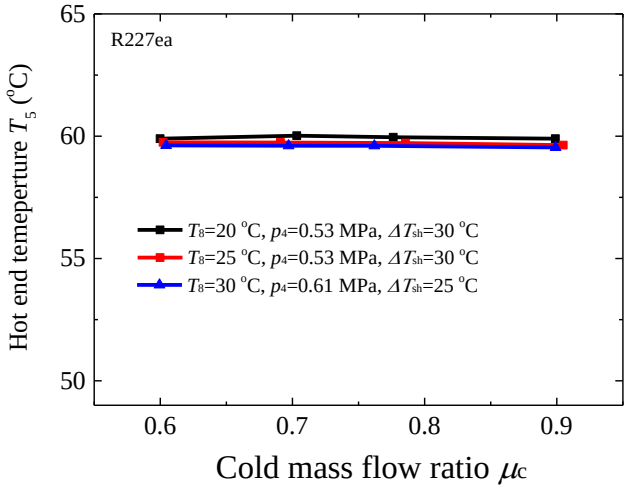

a

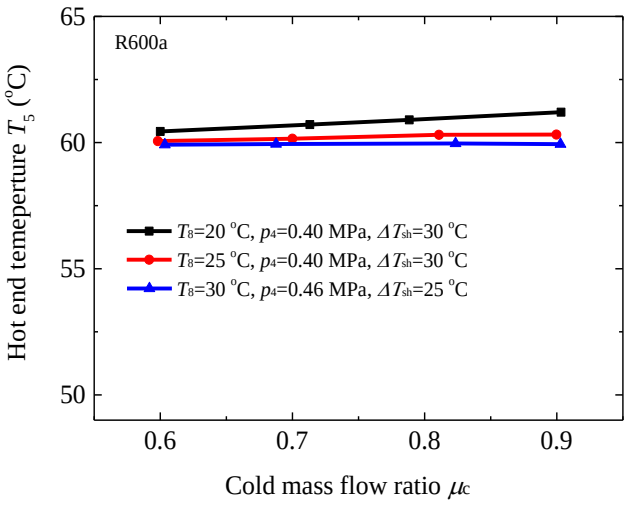

b

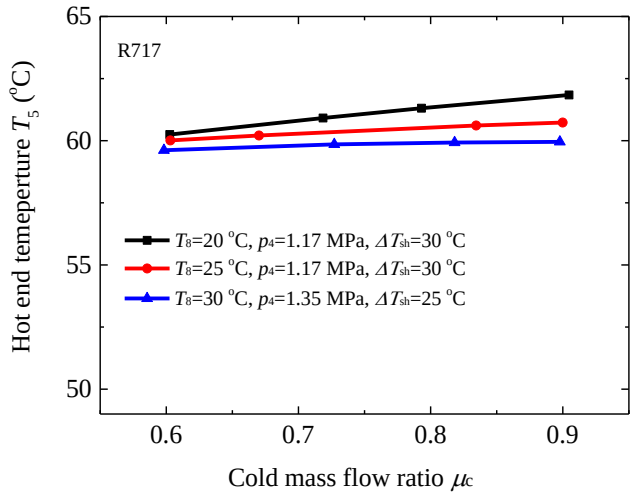

c

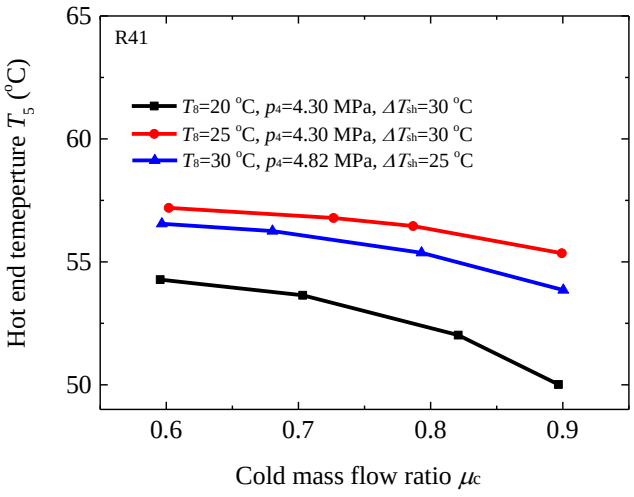

d

Figure 6.13 Maximum heating temperature T_5 at different cold mass flow ratios for T_4 = 60 °C, R227ea (a), R600a (b), R717 (c) and R41 (d)

It can be observed that none of the four chosen refrigerants is able to produce a T_5 temperature greater than the specified required T_7 (set at 80 ~ 100 °C); only two of them (R600a and R717) are able to produce a small positive heating effect, and R41 in fact produces a negative heating effect. The combination of condensing temperature and degree of superheat to produce the highest heating temperature (T_5) for R227ea, R600a and R717 are same (T_8 = 20 °C, ΔT_{sh} = 30 °C), whereas R41 requires to operate at a higher condensing temperature (T_8 = 25 °C, ΔT_{sh} = 30 °C) to achieve the best result. The heating temperature for R227ea appears to be rather insensitive to changes of combinations of system operating parameters. For R600a and R717, the changes in heating temperature are believed to be mainly influenced by the systems pressure

which affects R41 most.

Figure 6.14 and Figure 6.15 present the VT chamber inlet velocity $v_{cham,in}$, and the pressure drop between the VT inlet and the hot end $\Delta p_{4\text{-}5}$ (i.e. $\Delta p_{in\text{-}h}$) respectively. In general, for a constant p_4, the increase of T_8 would lead to a decrease of the $v_{cham,in}$ and $\Delta p_{4\text{-}5}$. The former ($v_{cham,in}$) is expected to generate a weaker rotation and a smaller temperature increase, while the latter ($\Delta p_{4\text{-}5}$) leads to a smaller temperature cancellation to the temperature increase, and thus an optimal combination of T_8 = 20 °C (for R227ea, R600a and R717) or 25 °C (for R41), and ΔT_{sh} = 30 °C exits.

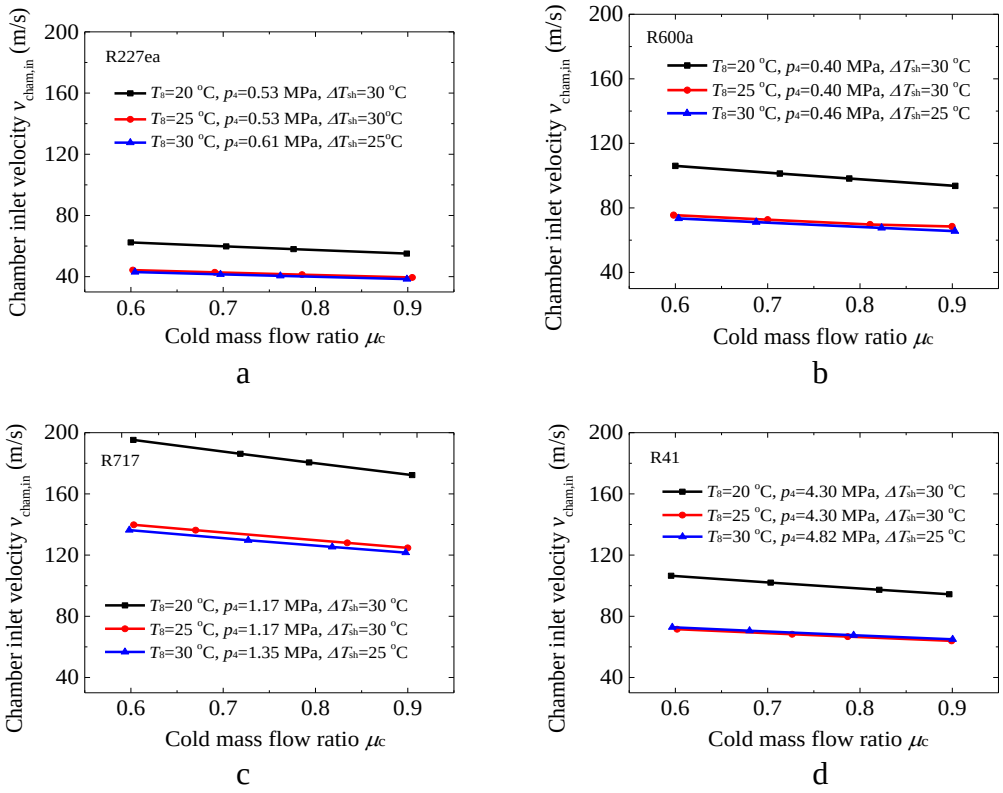

Figure 6.14 Chamber inlet velocities for four refrigerants at T_4 = 60 °C, R227ea (a), R600a (b), R717 (c) and R41 (d)

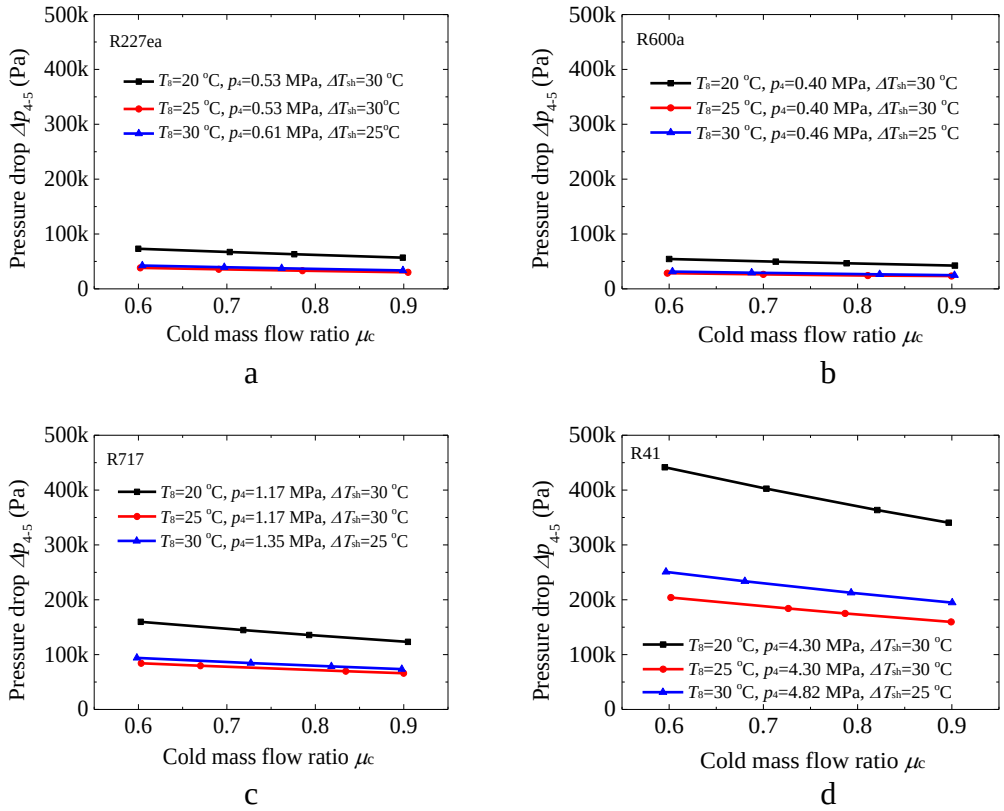

Figure 6.15 Pressure drops $\Delta p_{4\text{-}5}$ ($\Delta p_{\text{in-h}}$) between the VT inlet and the hot end for four refrigerants in the system operating conditions (T_4 = 60 °C), R227ea (a), R600a (b), R717 (c) and R41 (d)

When comparing different combinations of T_3 and T_8, the results show that the maximum heating effect always occurs at condensing temperature (T_8) of 20 °C (except for R41, the maximum occurs at 25 °C) and boiler temperature (T_3) of 30 °C. Figure 6.16[20] presents the maximum heating effect[21] for R717, R227ea, R600a and R41 when T_4 is set respectively at 60, 65, 70, 75 and 80 °C.

In the system, the increase of VT inlet temperature leads a higher heating effect, and R717 and R41 are shown to have a relatively higher sensitivity towards the changes in the boiler outlet temperature. This can be explained by looking at the rates of changes of their properties with respect to the changes in T_4. As compared in Table 6.7 showing the relevant properties for R717 and R600a. The percentage increase of α and ν for R717 with respect to T_4 is larger than that of R600a, though the percentage change of density for two refrigerants are quite similar.

[20]For comparison purpose, the heating temperature (or heating effect) for four refrigerants are presented at the same system operating temperature condition, i.e. T_8 = 20 °C

[21] Heating effect is used here instead of heating temperature, as it can directly reflect the variation of VT performance with respect to the change of VT inlet temperature

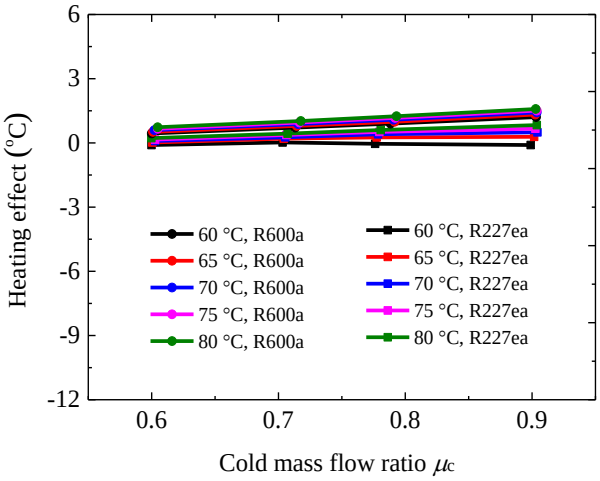

a

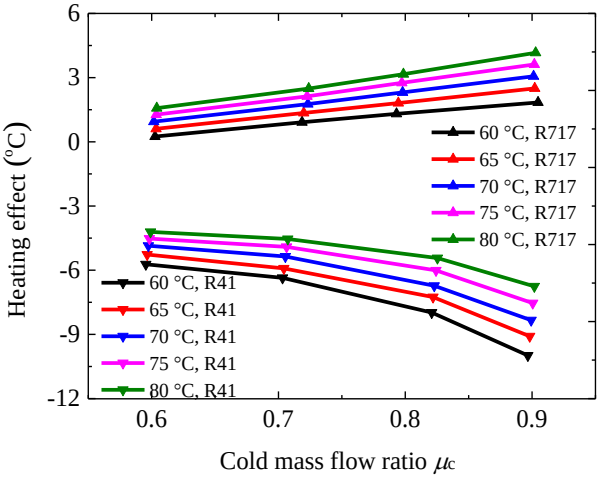

b

Figure 6.16 Heating effect for R600a, R227ea, R717 and R41 at T_8 = 20 °C, at T_3 = 30 °C, T_4 = 60 ~ 80 °C

Table 6.7a Thermal-physical properties for R717 at different inlet temperatures T_4 (p_4 = 1.17 MPa)

T_4 °C	α cm^2/s	Δ%	ν cm^2/s	Δ%	ρ kg/m^3	Δ%
60	0.014	+5.65%	0.014	+3.92%	7.84	-2.02%
65	0.015	+5.35%	0.015	+3.80%	7.68	-1.95%
70	0.016	+5.08%	0.015	+3.70%	7.53	-1.89%
75	0.016	+4.86%	0.016	+3.60%	7.39	-1.83%
80	0.017		0.017		7.25	

Table 6.7b Thermal-physical properties for R600a at different inlet temperatures T_4 (p_{in} = 0.40 MPa)

T_4 °C	α cm^2/s	Δ%	ν cm^2/s	Δ%	ρ kg/m^3	Δ%
60	0.012	+3.85%	0.009	+3.42%	9.21	-1.90%
65	0.012	+3.74%	0.009	+3.34%	9.03	-1.85%
70	0.013	+3.61%	0.010	+3.26%	8.87	-1.80%
75	0.013	+3.51%	0.010	+3.19%	8.71	-1.75%
80	0.014		0.010		8.55	

It is important to point out that when incorporating the VT into the system, none of the four chosen refrigerants can generate a heating effect larger than 5 °C, but when evaluating the VT in isolation (Chapter 5), a 20 °C heating effect is possible.

To explain, Figure 6.17 and Figure 6.18 present respectively VT chamber inlet velocity $v_{in,cham}$ and the pressure drop $\Delta p_{in\text{-}h}$. The data are presented based on two conditions, referred as the "VT alone" and "VT system"

- VT alone: T_{in} = 70 °C, p_{in} = 0.44 MPa (chosen according the Sub-Group 6 conditions), p_c fixed at 0.10 MPa.
- VT system: $T_{in} = T_4$ = 70 °C, p_{in} = saturated pressure corresponding to T_3 = 30 °C, p_c is the condensing pressure at 20 °C.

The relevant thermal-physical properties of the refrigerants at these two conditions are displayed in Table 6.8.

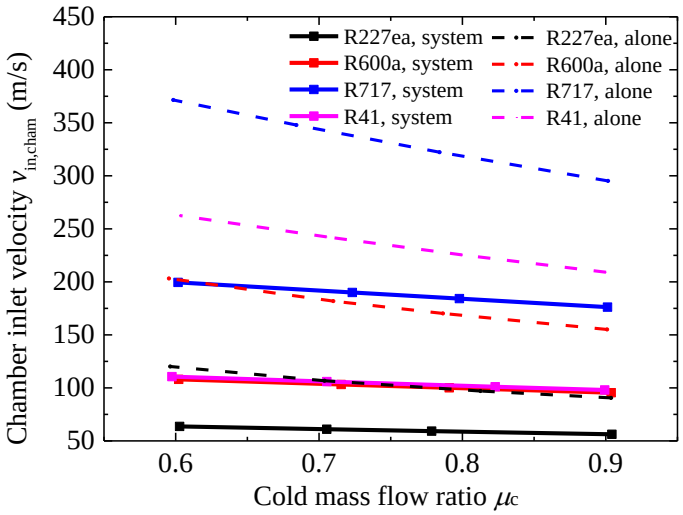

Figure 6.17 Chamber inlet velocities based on VT system and VT alone conditions

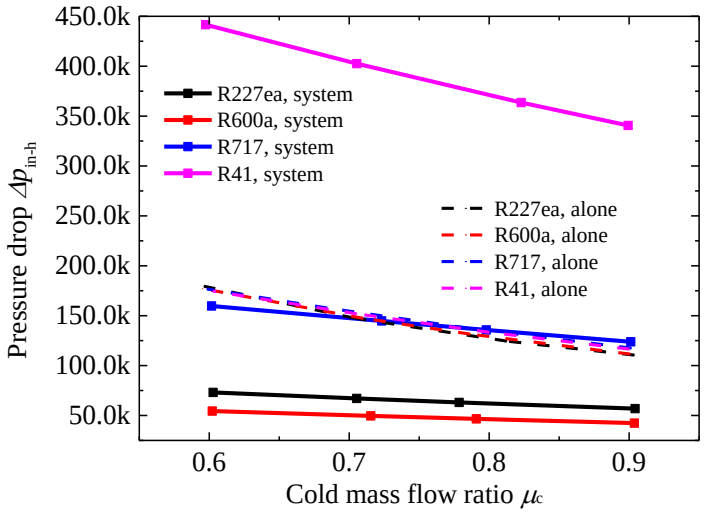

Figure 6.18 Pressure drops between VT inlet and the hot end ($\Delta p_{\text{in-h}}$) based on VT system and VT alone conditions

Table 6.8 Releavnt thermal-pysical properties at VT system and VT alone conditions

Refrigerants	α (cm^2/s)		ν (cm^2/s)		ρ (kg/m^3)		μ_{JT} (°C/MPa)	
	Alone	System	Alone	System	Alone	System	Alone	System
R717	0.048	0.016	0.044	0.015	2.67	7.5285	17.11	16.61
R41	0.032	0.002	0.024	0.002	5.32	68.105	12.20	10.78
R600a	0.012	0.013	0.009	0.010	9.61	8.8651	15.28	15.14
R227ea	0.007	0.005	0.005	0.004	28.05	34.647	12.13	12.46

When operating in the system, all refrigerants have lower chamber inlet velocities than when the VT is operating on its own, resulting in a weaker rotation in the VT chamber. One of the main reasons that chamber inlet velocity in the system is so much smaller than that in the VT alone conditions because a much smaller pressure ratio is encountered in the system, as shown in Figure 6.19. On the other hand, R717, R41 and R227ea have smaller thermal diffusivities and kinematic viscosities but larger densities under the system conditions, and all of which contribute to a smaller temperature increase from the rotation process. Having similar α, v, and ρ in both conditions, due to the lower pressure ratio in the system, R600a has a much smaller chamber inlet velocity thus producing a rather small system heating effect.

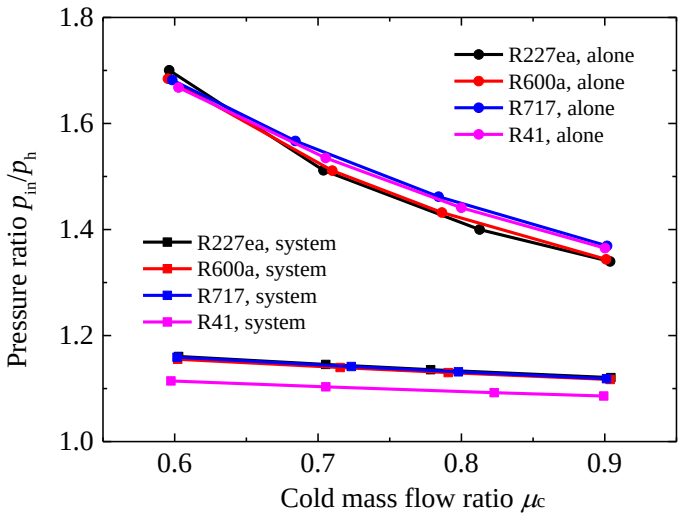

Figure 6.19 Ratio of the VT inlet pressure to the hot end pressure, based on VT system and VT alone conditions.

R717, R600a and R227ea have less pressure drop $\Delta p_{\text{in-h}}$ in the VT when operating in the system than when operating in the VT alone, resulting in a small temperature cancellation. The net combined consequence of a smaller heating effect for the VT system suggests that the influence of the rotating velocity is stronger than that of the pressure drop in the system. On the other hand, R41 has a larger $\Delta p_{\text{in-h}}$ in the system than in the VT alone, resulting in a larger temperature cancellation, and thus a smaller heating effect in the system.

6.2.3 Suggesting the potential refrigerant and re-dimensioning the VT to achieve the aimed heating temperature

1) Changing the refrigerants

In previous section, the results show that all four chosen refrigerants fail to generate satisfactory heating temperature because when operating under the prescribed system temperatures, they have small chamber inlet velocities, thermal diffusivities and kinematic viscosities. Therefore a revised procedure is needed to improve the refrigerant choices for closed VT system integration. The ranking from Chapter 5 cannot be used to assess/rank the refrigerants' heating effect under the system conditions, as the pressure drop through VT may be quite different among different refrigerants. However, the ranking from Chapter 5 help to establish how various chosen properties are related to the VT heating effect.

Based on the previous discussion, it is important to identify the refrigerants which may produce a higher chamber inlet velocity $v_{cham,in}$ in the VT. Using gas dynamic theories, the possible largest outlet velocity (v_{in} = 0 m/s) of a convergent nozzle for a superheated refrigerant can be approximated[118] by

$$v = \left\{ \frac{2r}{r-1} \cdot \frac{p_{in}}{\rho} \left[1 - \left(\frac{p_c}{p_{in}} \right)^{\frac{r-1}{r}} \right] \right\}^{0.5} \tag{6.11}$$

The equation shows that the velocity is a function of specific heat ratio r, VT inlet p_{in} (= p_4) and cold end p_c[22](= p_6), as well as the fluid density ρ. Table 6.9 presents the rank of the approximated nozzle outlet velocities in the order of descending values for 15 refrigerants (as chosen in Chapter 5); the velocities are calculated based on p_4 = $p_{30°C}$, p_6 = $p_{20°C}$, and T_4 = 60 °C. The thermal diffusivities, the kinematic viscosities, J-T coefficients and pressure drops Δp (= $\Delta p_{in\text{-}c}$[23]) for these 15 refrigerants under system conditions (T_4 = 60 °C, p_4 = $p_{30°C}$ and p_6 = $p_{20°C}$) are presented in Table 6.10 in the descending order for α.

[22] Nozzle outlet pressure is usually not available and therefore a VT exit pressure is used instead; p_c is chosen instead of p_h, as p_c is always smaller than p_h for the VT

[23] $\Delta p_{in\text{-}c}$ is chosen instead of $\Delta p_{in\text{-}h}$, as $\Delta p_{in\text{-}h}$ is generated by the CFD and could not be calculated directly based on the VT inlet and hot end conditions. $\Delta p_{in\text{-}c}$ can be calculated directly as p_{in} and p_c can be mathematically calculated based on system conditions

Table 6.9 Nozzle outlet velocities, specific heat ratios and densities when $p_4 = p_{30°C}$, $p_6 = p_{20°C}$, $T_4 = 60$ °C

Rank	Refrigerants	Velocity m/s	$p_{30°C}$ (p_{in}) MPa	$p_{20°C}$ (p_c) MPa	Specific heat ratio r	Density ρ kg/m^3
1	R717	296.47	1.17	0.86	1.40	7.84
2	R600	165.69	0.28	0.21	1.11	6.32
3	R290	164.64	1.08	0.84	1.20	19.84
4	R41	161.37	4.30	3.41	1.80	73.52
5	R600a	159.00	0.40	0.30	1.12	9.21
6	R32	150.29	1.93	1.47	1.46	43.85
7	R152a	147.37	0.69	0.51	1.21	18.36
8	R245ca	122.80	0.12	0.08	1.08	6.10
9	R245fa	120.19	0.18	0.12	1.09	9.01
10	R134a	118.58	0.77	0.57	1.17	31.95
11	R143a	117.03	1.43	1.11	1.25	53.14
12	R236fa	105.75	0.32	0.23	1.09	18.96
13	R125	98.58	1.57	1.21	1.22	83.09
14	R227ea	93.95	0.53	0.39	1.10	36.14
15	R218	80.99	0.99	0.76	1.13	80.18

Table 6.10 Thermal-pyiscal properties and pressure drops for 15 refrigerants ($p_4 = p_{30°C}$ and $p_6 = p_{20°C}$, $T_4 = 60$ °C) in the descending order for α

Refrigerants	Thermal diffusivity α cm^2/s	Kinematic viscosity ν cm^2/s	J-T coefficient μ_{JT} K/MPa	Pressure drop $\Delta p_{in\text{-}c}$ MPa
R245ca	0.0275	0.0187	23.56	0.039
R245fa	0.0178	0.0128	24.01	0.055
R600	0.0167	0.0131	18.62	0.076
R717	0.0139	0.0143	18.21	0.310
R600a	0.0117	0.0091	16.82	0.103
R236fa	0.0090	0.0065	16.47	0.091
R152a	0.0079	0.0062	20.06	0.177
R290	0.0057	0.0047	14.31	0.243
R134a	0.0052	0.0041	16.24	0.198
R227ea	0.0049	0.0036	14.03	0.139
R32	0.0031	0.0033	16.78	0.453
R143a	0.0030	0.0024	14.56	0.329
R218	0.0022	0.0018	11.45	0.234
R125	0.0021	0.0018	11.91	0.363
R41	0.0016	0.0018	11.61	0.899

It can be seen that R717 has a considerable larger inlet velocity than the others. The differences in velocities among the others are relatively small, suggesting that the influence on the heating effect caused by their velocities differences should not be too significant, except for R717. As for the properties, R245ca, R245fa, R600 and R717 have larger α and v than other refrigerants, and they have smaller pressure drops (except R717 which has the largest velocity and a large pressure too). Combining the above two factors, the potential refrigerants (among the 15 refrigerants) which could be expected to perform well under the system conditions are R245ca, R245fa, R600 and R717.

Though R717 has the largest velocity, when compared to R245ca, its thermal diffusivity is about half and pressure drop ($\Delta p_{\text{in-c}}$) 8 times that of R245ca, resulting in R717 having potentially a relatively poorer heating performance. When R717 is compared to R600, though similar properties but 4 times pressure drop ($\Delta p_{\text{in-c}}$) of R600 suggests R717 may produce a smaller heating effect. R245fa and R600 have rather similar thermal properties, but the former has a much smaller nozzle outlet velocity (Table 6.9) while the latter has a smaller pressure drop $\Delta p_{\text{in-c}}$, suggesting they may have similar heating effect.

On the other hand, when comparing R600 and R245ca, despite R245ca having a smaller nozzle outlet velocity (26% smaller), it has a higher thermal diffusivity (65% higher) and a higher kinematic viscosity (43% higher). Therefore, relatively a higher heating effect for R245ca could be expected. For R245ca and R245fa, the former has a larger α, v and velocity, but a smaller μ_{JT} and $\Delta p_{\text{in-c}}$, suggesting R245ca would definitely produce a better heating effect.

Based on above discussion (and Table 6.9 and Table 6.10), an estimated rank of the heating effect under the specified system conditions (T_4 = 60 °C, $p_{\text{in}} = p_4 = p_{30°\text{C}}$ and $p_{\text{c}} = p_6 = p_{20°\text{C}}$) could be made as R245ca > R245fa ≈ R600 > R717.

To validate the discussion, further analysis on the heating effect of R245ca, R245fa and R600 are performed. Figure 6.20 presents the results of their heating effect; for comparison purpose previous results of R717 are also included. The results reflect very well the logic and rationale put behind the discussion, showing R245ca indeed has a better heating effect, followed by R245fa, R600 and R717.

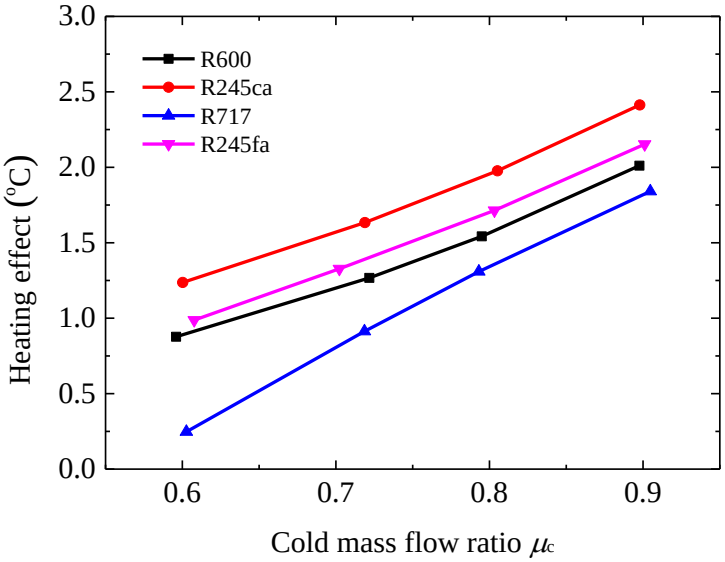

Figure 6.20 Heating effect for R600, R245ca and R717 under the specified system conditions

2) Re-dimensioning process

For VT, increasing its length or chamber diameter has a potential effect on the rotational strength of the flow and hence its heating effect. In the following studies, the VT length L_{VT} is increased from 50 to 175 mm, and the VT diameter Φ_{cham} is increased from 16 to 22 mm. To assess the influence of re-dimensioning the VT on the heating effect, R600[24] is chosen as the refrigerant, and the VT inlet and cold end conditions are specified as $p_{in} = p_{30°C}$ (= 0.28 MPa), $p_c = p_{20°C}$ (= 0.21 MPa), $T_{in} = T_4 =$ 60 °C.

Figure 6.21 presents the heating effect when the chamber diameter is fixed at 20 mm and chamber inlet area A_{cham} at 60 mm^2. It can be observed that the VT has the largest heating effect when its length reaches 150 mm, and any further increase in length would reduce the heating effect.

[24] R600 is chosen instead of R245ca which generates a larger heating effect at the chosen conditions, because it uses less pc running time than R245ca

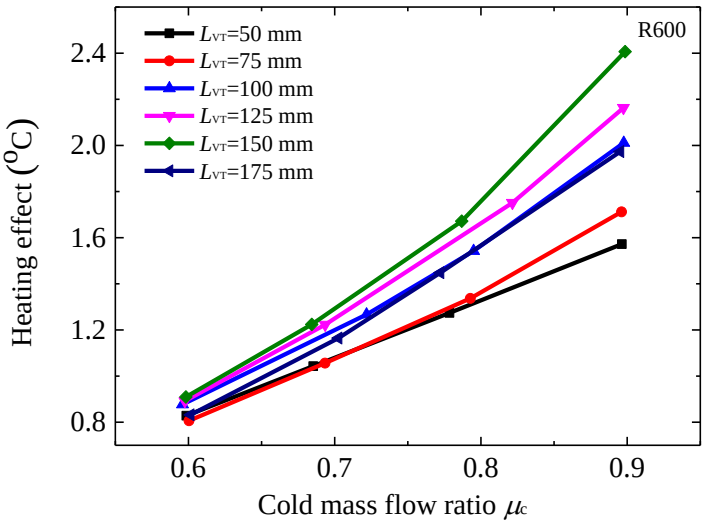

Figure 6.21 Heating effect for six VT lengths

Figure 6.22 displays the flow streamlines within the VT for these six different lengths. It can be seen that as the length increases, the recirculation becomes larger, suggesting that the fluid experiences a longer rotation distance before it turns back, and this would lead to generate more friction and energy transferred from the centre to the outer of the rotation. The influence of the length on the growth of this recirculation stops when the VT reaches 150mm.

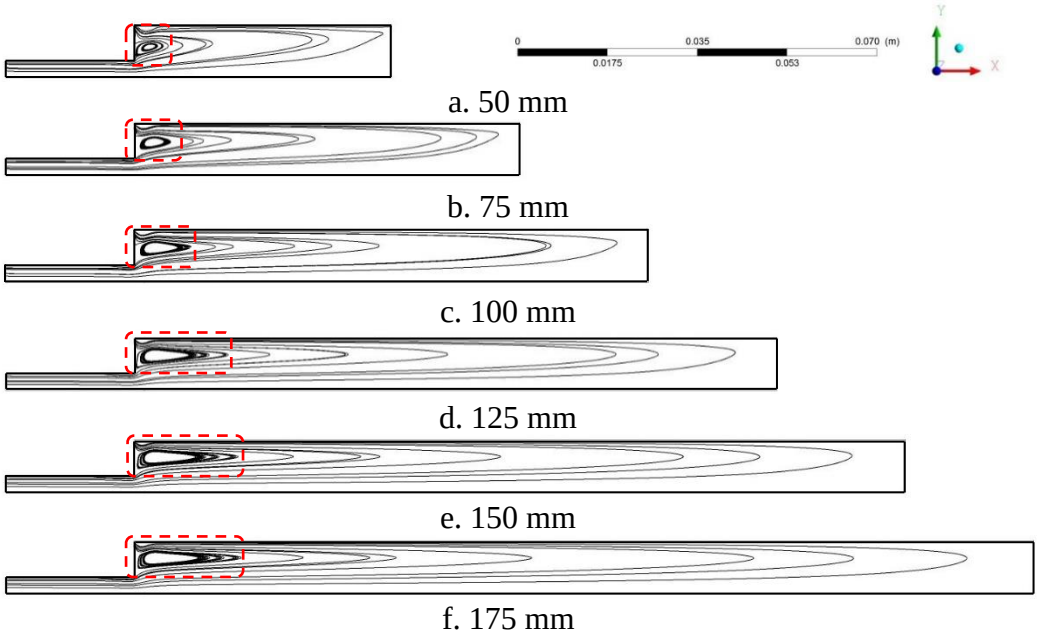

Figure 6.22 Streamline through the VT for six lengths VT (μ_c= 0.9)

Figure 6.23 shows the chamber inlet velocities $v_{cham,in}$ and pressure drops $\Delta p_{in\text{-}h}$ at six different lengths. It can be observed that a longer VT length would lead to a higher $v_{cham,in}$ and a larger $\Delta p_{in\text{-}h}$. The former (a higher $v_{cham,in}$) contributes to stronger rotation and a higher heating temperature, while the later (a larger $\Delta p_{in\text{-}h}$) would cancel out some of this temperature rise, suggesting there could be an optimum VT length.

Also seen in the results that the $v_{cham,in}$ reaches a maximum when the VT length is increased to 150 mm, and at the same time the rate of increase in pressure drop $\Delta p_{in\text{-}h}$ with respect to the increase in VT length also decreases to a rather small value when VT length goes beyond 150 mm. All these reflect well that there is indeed an optimum length of around 150 mm to produce the maximum heating effect for R600 under the specified system conditions, as shown in Figure 6.21.

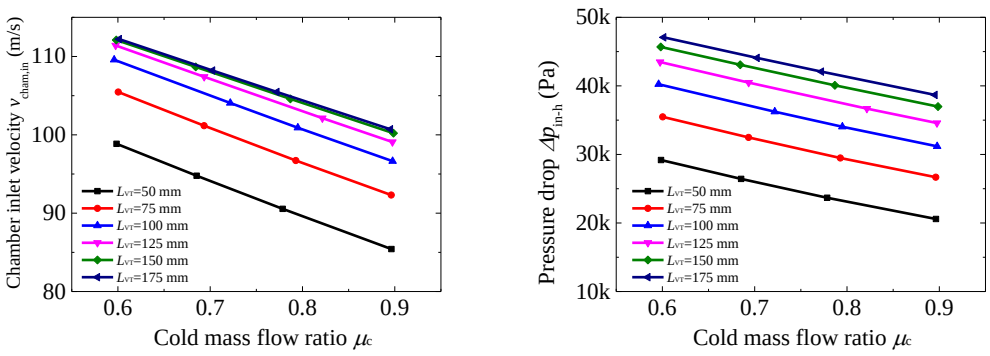

a b

Figure 6.23 VT chamber inlet velocities (a), pressure drop $\Delta p_{in\text{-}h}$ (b) for R600 at six different VT lengths

Figure 6.24 shows the tangential velocities and the associated shear stresses in both radial and axial directions at the cross-sections (x = 30 mm and x = 90 mm). At x = 30 mm (for L_{VT} of 50 mm to 175 mm) and 90 mm (for L_{VT} of 100 mm to 175 mm), the tangential velocities become smaller as the VT length increases. In addition, when assessing the velocities at these two cross-sections, the decrease of velocities per unit length is larger for the longer VTs; this is also reflected by the higher tangential shear stresses in axial direction for the longer VTs. The tangential shear stresses of the primary flow in radial direction are getting larger as the length increases, agreeing with the trends that the heating effect caused by the rotational friction is getting larger at the same time. Again, this suggests there is a VT length which leads to the optimal combination of the shear stresses in axial direction for creating pressure drop and in the radial direction for producing a heating effect.

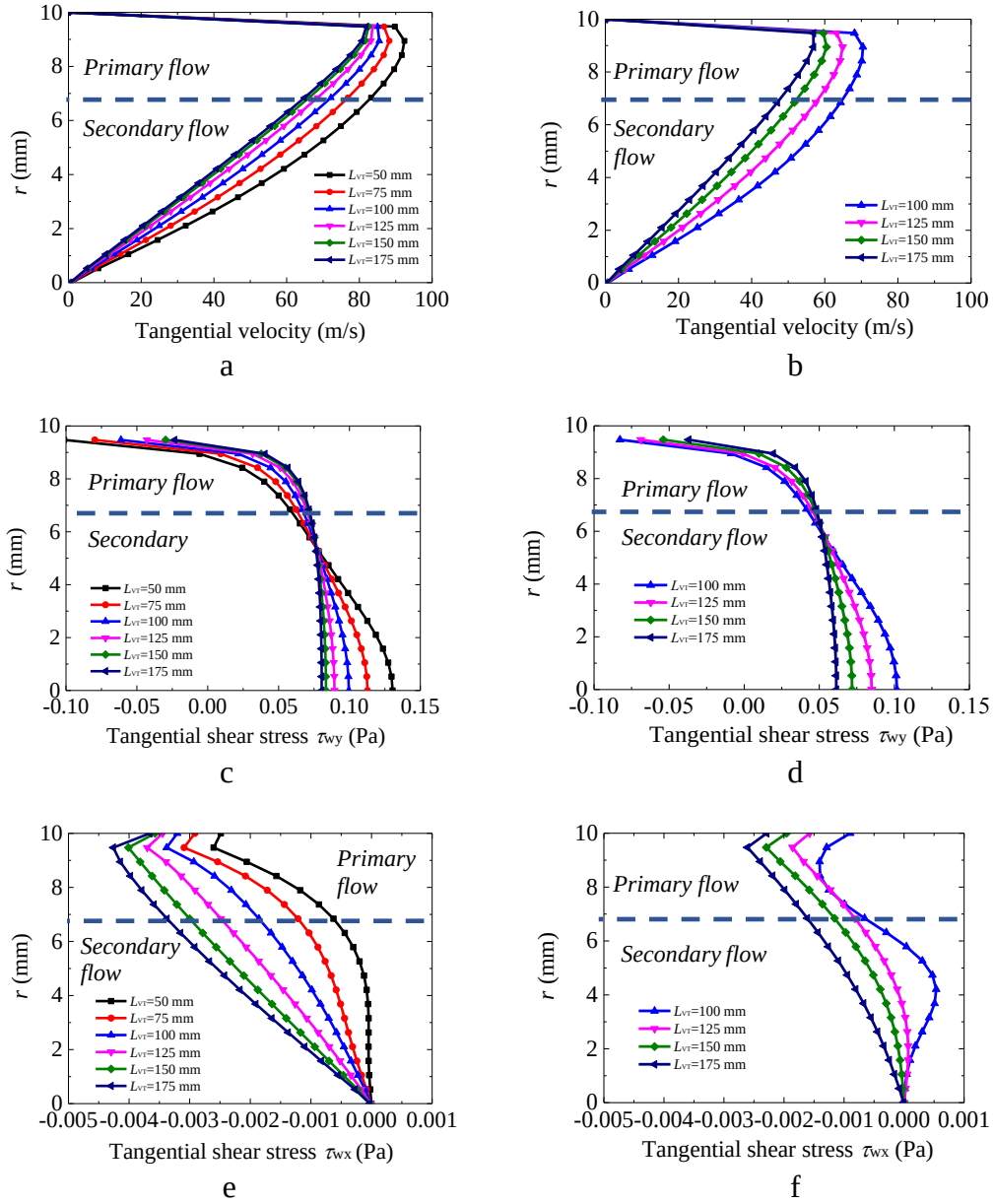

Figure 6.24 Tangential velocities at cross sections x = 30 mm (a) and x = 90 mm (b); shear stresses in the y/radial direction at x = 30 mm (c) and x = 90 mm (d); shear stresses in the x/axial direction at x = 30 mm (e) and x = 90 mm (f) for various VT lengths (μ_c= 0.9)

Figure 6.25 presents the heating effect when the chamber diameter is varied from 16 to 22 mm (16, 18, 20 and 22 mm) when the VT length is kept constant at 150 mm and the chamber inlet area is fixed at 60 mm^2. It can be seen that the largest heat effect is generated when the diameter reaches 20 mm, though the differences among various diameters are noticeably quite small.

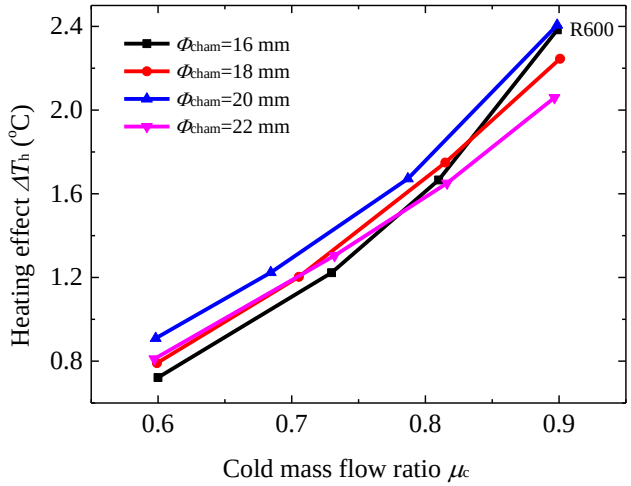

Figure 6.25 Heating effect for chamber diameter varied from 16 and 22 mm, at L_{VT} = 150 mm, A_{noz} = 60 mm^2

Figure 6.26 shows the chamber inlet velocity $v_{cham,in}$ and pressure drop $\Delta p_{in\text{-}h}$. It can be seen that the VT chamber inlet velocity ($v_{cham,in}$) increases with increasing chamber diameter but the pressure drops $\Delta p_{in\text{-}h}$ remain fairly constant. The increase of $v_{cham,in}$ is due to an increase of pressure drop across the nozzle, and there must be a smaller pressure drop from the nozzle outlet to the hot end, as supported by the fact that τ_{wx} (Figure 6.27) is decreasing with increasing chamber diameter.

Unlike previously noted that a higher $v_{cham,in}$ would generally lead to a higher heating effect. However, for the current results, the heating effect does not continue to go up with increasing $v_{cham,in}$, because the tangential velocities and shear stresses, τ_{wy} and τ_{wx}, (at the same ratio r_i/r) are getting smaller (Figure 6.27), thus leading to a smaller friction/heating effect. One the other hand, a larger chamber diameter represents a longer rotational distance for fluid elements to travel, and this could generate more friction and lead to more energy transferred from the centre towards the outer layers.

As a result, there could be a chamber diameter for an optimal combination of the shear stresses and rotational distances to produce the largest heating effect. However, all the changes involved are relatively small, suggesting the influence of diameters is less critical, within the considered range.

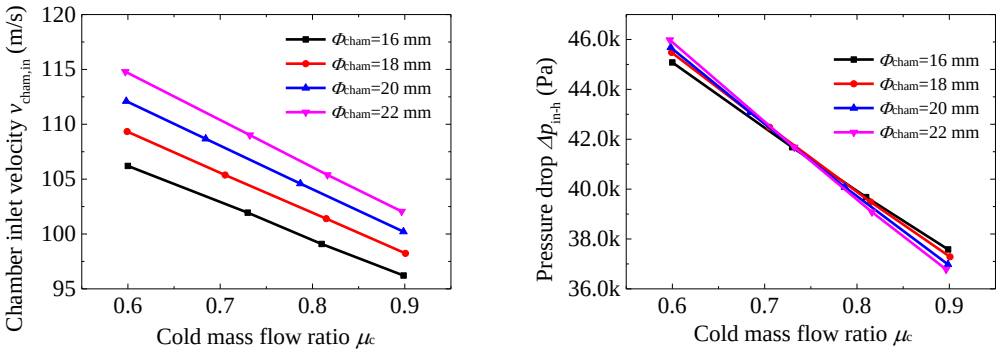

Figure 6.26 VT chamber inlet velocity (a), pressure drop $\Delta p_{\text{in-h}}$ (b) for four chamber diameters

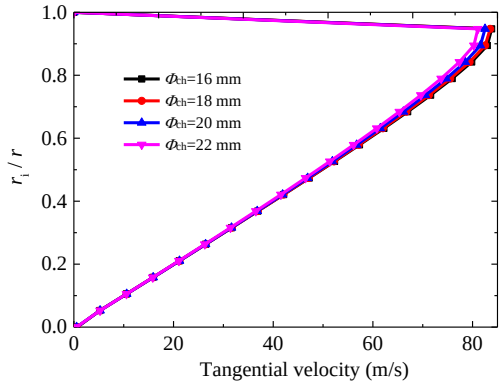

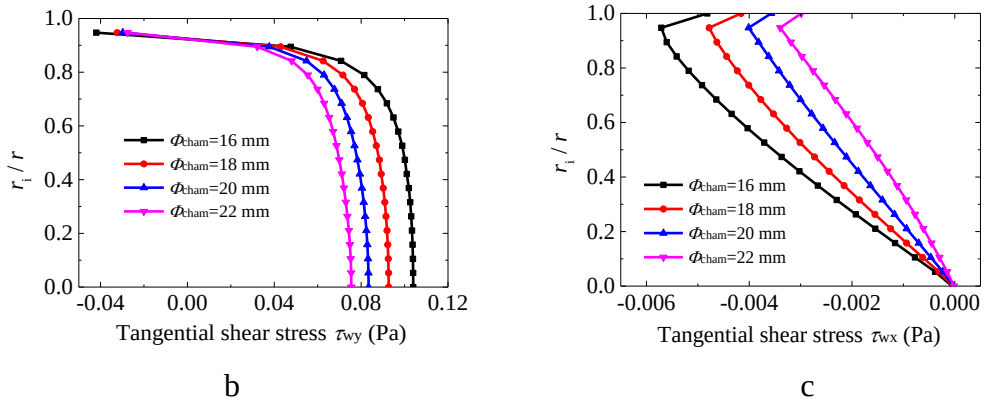

Figure 6.27 Tangential velocities (a) and shear stresses in y/radial direction (b) and x/axial direction (c) at the same normalised radial locations (x = 30 mm) for four chamber diameters (μ_c = 0.9)

Decreasing the nozzle inlet area is another way to increase the chamber inlet velocity. Figure 6.28 presents the heating effect when the chamber inlet area is varied between 40 and 60 mm^2 when the chamber diameter is kept constant at 20 mm and the VT length at 150 mm. It can be shown that the area has little influence on the heating effect under the specified system conditions. Figure 6.29 shows both the chamber inlet

velocity and pressure drop ($\Delta p_{\text{in-h}}$) decrease with increasing inlet flow area, thus balancing out their influence on the heating effect, resulting in rather little overall changes.

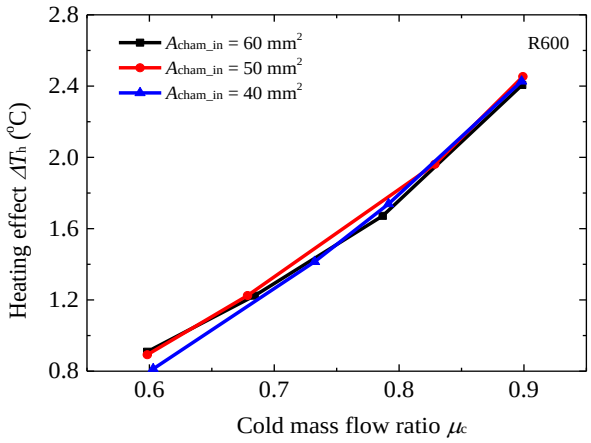

Figure 6.28 Heating effect for three different chamber inlet areas

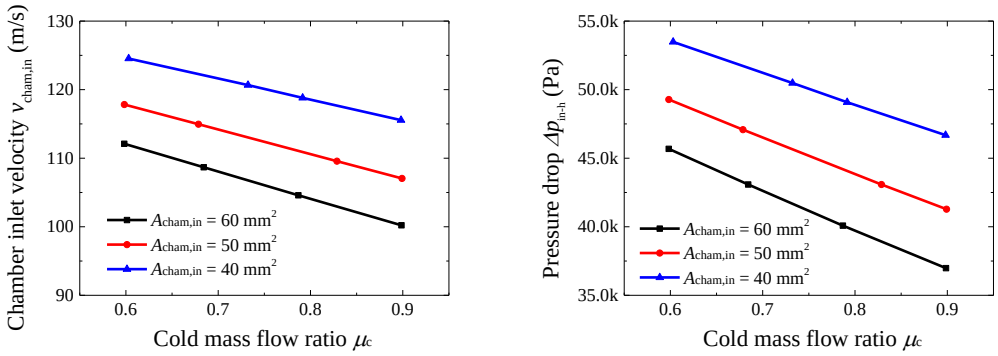

a b

Figure 6.29 Chamber inlet velocities $v_{\text{cham,in}}$ (a), pressure drops $\Delta p_{\text{in-h}}$ for three different chamber inlet areas (b)

For a given VT and refrigerant at certain specified system operating conditions, even though results on the flow streamline (Figure 6.22), and the chamber inlet velocity and the pressure drop (Figure 6.23) can be acquired from the CFD runs, it is still not straight forward to determine the optimal L_{VT} that would produce the largest heating effect.

However, the results suggest that it is possible to get an indication as if it is necessary to re-dimension the VT to achieve a better heating effect, by using the distribution of the shear stress (τ_{wy} in the radial direction) of the secondary flow (Figure 6.24). The longer VT is shown to have a rather uniform τ_{wy} in the center core region than that of a shorter VT at both x = 30 mm or 90 mm, suggesting that using the shear stress distribution over the half length of the VT to assess if it is necessary to re-dimension

the VT to a shorter length to improve the heating effect. On the other hand, when a non-uniform τ_{wy} distribution in the center core region is noted, one could consider extending the VT length. This re-dimensioning approach could be applied when other refrigerants are being considered and assessed.

Based on the results (Figure 6.21, Figure 6.25 and Figure 6.28), it appears that the L_{VT} has a stronger influence than the Φ_{cham} and $A_{cham,in}$ on the heating effect, thus, re-dimensioning based on the length is considered a more practical and cost effective means of achieving a better heating effect, without replacing the VT.

Previously, the performance of the four chosen refrigerants (R600, R245ca, R245fa and R717) were assessed for L_{VT} = 100mm, Φ_{cham} = 20 mm and $A_{cham,in}$ = 60 mm^2, and none of them could achieve the required T_7 temperature. All these refrigerants are now reassessed for their heating effect based on the new VT geometries, i.e. L_{VT} = 150 mm, Φ_{cham} = 20 mm and $A_{cham,in}$ = 50 mm^2, which have been identified as the optimum VT dimensions for R600. The results (heating effect) are shown in Figure 6.30, indicating that with VT re-dimensioning it is now possible to achieve the required T_7 temperature when T_4 = 80 °C, $p_4 = p_{30°C}$ (= 1.17 MPa) and $p_8 = p_{20°C}$ (= 0.86 MPa) for R717.

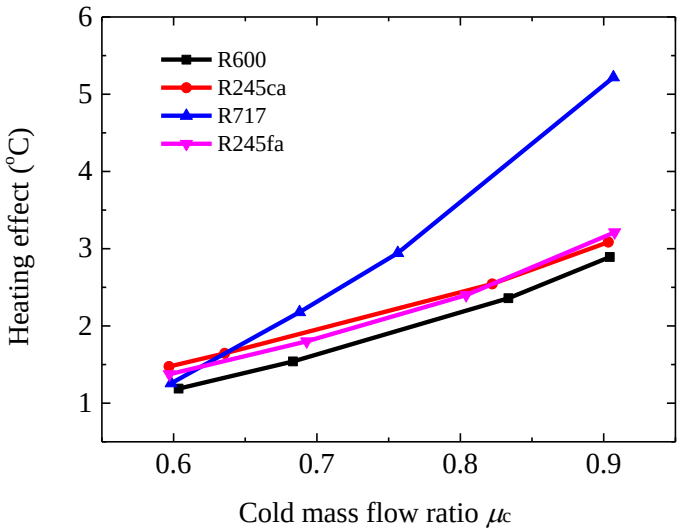

Figure 6.30 Hot end temperature for R600, R245ca and R717 at T_4 = 80 °C for L_{VT} = 150 mm, Φ_{cham} = 20 mm and $A_{cham,in}$ = 50 mm^2, $p_4 = p_{30°C}$ and $p_8 = p_{20°C}$

Based on the discussion, in order to further increase the VT hot end temperature (or the heating effect), two factors could be considered.

- To consider using another refrigerant that has a larger thermal diffusivity and kinematic viscosity, a smaller J-T coefficient, and could potentially produce a larger chamber inlet velocity and smaller pressure drop ($\Delta p_{\text{in-c}}$).
- To re-dimension the VT length for the replacement refrigerant, based on a preliminary CFD run at the specified system conditions to acquire information on τ_{wy} at a suitable axial position.

To summarise, the developed integration procedure for matching of the working fluid, VT dimensions and system configuration for specified systems is found to be effective. The results and discussion enable us to understand how the relative TSE of refrigerants under the system conditions are influenced by larger number of factors.

In the specified cooling system, relative VT cooling effect (ranking) of different working fluids can be evaluated by considering the value of the isentropic expansion exponent at VT inlet, and the pressure drop $\Delta p_{\text{in-c}}$ in the system. The same ranking can also be obtained when they are assessed in isolation.

However, the relative heating effect (ranking) of the working fluids is found to be different when the VT is examined alone or within the system. It should be assessed by examining the relative values of the chosen properties (e.g. thermal diffusivity) at the VT inlet conditions, together with the pressure drop $\Delta p_{\text{in-h}}$ within the system.

7 Conclusions

This chapter provides an overall conclusion of the research, presenting first a summary of the main work, followed by the main contributions and key research findings, and ended with some proposed future work.

Summary of main work

- A comprehensive literature has been carried out, which shows that when the potential benefits of using the temperature separation effect of a VT in closed thermal systems are being assessed by researchers, there are knowledge gaps in how to match the VT design with properties of working fluids in a closed system environment.
- A systematic refrigeration screening approach and a closed VT system integration procedure, coupling the thermodynamics and numerical CFD analysis, have been proposed and developed. The development work is based on a large number of commercially available refrigerants.
- The CFD code Fluent is chosen as the main numerical tool to predict the TSE of the chosen refrigerants. Significant amount of time was used to perform the CFD runs for refrigerants, and a very thorough and comprehensive analysis on the data has been carried out.
- A VT CFD model is successfully established. An axisymmetric 2-D geometry is defined, the optimal meshing elements number for providing a good compromise between the simulation accuracy and the calculation time is chosen. Having assessed various choices of turbulence models, the *standard k-ε* turbulence model is selected. The model is as far as practically possible both quantitatively and qualitatively validated.
- The influence of operating conditions (T_{in}, p_{in}, μ_c and $\dot{m}_{in}$) on refrigerants' VT performance are fully investigated. The variations of thermofluid-dynamic characteristics (temperature and pressure distributions, shear stresses, flow streamlines, velocity components profiles and pressure drops) inside the VT under different conditions are carefully analysed and discussed. (Note: it

should be stressed that this research is not to develop new theories to explain the mechanism of TSE in VT, but to acquire a better understanding of the dependence of the refrigerant's TSE on key operation parameters, properties of working fluids and VT design.)

- As far as the author is aware, this is the first time a large number of refrigerants are collectively assessed and compared for their VT temperature separation performance, and the data are analysed and correlated to their key thermal-physical properties.

- Two VT systems, one for cooling and one for heating, have been chosen to illustrate, step-by-step in details, the application of the newly developed system integration procedure. The author also explained how to adapt and apply the procedure to other system configurations. (Note: it must be emphasised that it is not the aim of this research to develop/propose new VT systems, but for any proposed system configurations, to provide a methodology to evaluate choices of working fluids and VT design for optimum cooling/heating effect.)

Main contributions

- A novel screening approach consisting of grouping the refrigerants based on their shape on *T-s* diagrams and assessing their relative TSE has been developed. Two refrigerant groups are identified according to their potential for cooling or heating applications. A new boundary line concept is introduced to identify a suitable VT entry region on the *T-s* diagram to ensure dry nozzle operation. However, the method for constructing the boundary line is only for pure refrigerant, when mixtures are involved, this method should be changed.

- The research successfully demonstrates that, for cooling, the isentropic expansion exponent can be used as the index to assess relative TSE of individual refrigerants. For heating, a relatively large thermal diffusivity α and kinematic viscosity v, and a small density ρ and J-T coefficient μ_{JT} would produce a large TSE. However, the gravity of fluid is not considered in the modelling as a very small VT is employed in the simulation; it may affect TSE for heavier fluids in some large VTs when low velocities are encountered.

- This is the first time that a systematic closed VT integration procedure has been developed and applied successfully to evaluate VT effectiveness in closed system environment, and to match the refrigerant choice, the VT geometry with the system operation. Essentially the procedure can be used to provide full system simulations, which have not been possible previously by using only energy balance in thermodynamics analysis. It is particularly useful to apply the boundary line concept to determine the VT inlet pressure in a cooling system. The originally developed iteration procedure to determine the best combination of VT inlet pressure and degree of superheat for the heating system is also proved valuable.

- An original idea for considering if re-dimensioning of the VT length is necessary to improve the heating effect has been put forward. Though simple, it still requires some preliminary CFD runs to provide results of shear stresses in the secondary flow. Changing the length appears to be the most effective and practical ways to alter the VT performance. (Note: It should be pointed out that it is not possible to use this idea to determine exactly the optimum length; it just gives us an indication as whether we should increase or decrease the length of the VT.)

Overall, it can be concluded the following three set objectives are fulfilled satisfactorily, and the study is considered unique and novel.

- An accurate VT CFD model for analysing the influence of various operating parameters on the VT thermal and flow behaviour, and for predicting the TSE of different refrigerants under specified working conditions has been created.

- A refrigerant screening methodology for evaluating the suitability of various refrigerants, to achieve the desired VT operation and performance has been developed and successfully applied.

- A procedure for examining the matching of refrigerant properties, VT design, and the system operating conditions has been established and effectively implemented, in order to assess whether a chosen refrigerant could perform satisfactorily in a prescribed practical situation.

Key findings

- The influences of the VT inlet temperature and pressure on the TSE of various refrigerants are thoroughly studied. For each individual refrigerant, at a specified inlet pressure, the effect of inlet temperature T_{in} has a stronger influence on the heating effect than on the cooling effect. On the other hand, at a given T_{in}, the heating effect will reach a maximum value when p_{in} is increased to a certain value, as the larger pressure drop associated with the larger p_{in} will cancel out a greater amount of heating effect.

- Air and refrigerants are found to have rather similar trends in their VT cooling effect. At a given μ_c and a cold end pressure, an increase in p_{in} (or mass flow rate $\dot{m}_{in}$) generally leads to an increase in cooling effect, though the rate of increase is diminishing when the chamber inlet velocities approach the sonic or chocked condition.

- Air and refrigerants are found to have unique differences in the trends of their VT heating effect; the analysis shows the pressure drop in the VT plays a much stronger and important role in determining the heating effect for refrigerants than for air.

- For individual refrigerants, the positions of the boundary lines are insensitive to inlet velocities unless reaching very high velocities. For some refrigerants, it is necessary to use large degrees of superheat to move the boundary line away from the saturated vapour line. Both have useful practical implications.

- The inlet temperature is found to have very little influence on the hot end pressure, unless the temperature is varied over a large range. In practice, this implies in a closed system it is not necessary to adjust the hot end throttle position to maintain a certain cold mass flow ratio when the inlet temperature is varied, thus offering convenience in terms of control.

- The work shows that the ranking of refrigerants' TSE by considering the VT in isolation or within a system environment will produce different results, and it is therefore important to evaluate their performance under correct conditions. In a cooling system, if the cold end pressure cannot be controlled, the ranking of cooling effect of different working fluids will be the same regardless

whether they are assessed in isolation or under system conditions, as in both conditions the relative isentropic temperature drops among the refrigerants are found to be the same.

- The relative heating effect (ranking) of the working fluids is found to be different when the VT is examined alone or within the system. It should be assessed by examining the relative values of the chosen properties (e.g. thermal diffusivity) at the VT inlet conditions, together with the pressure drop $\Delta p_{\text{in-h}}$ within the system. The J-T coefficient is found to be an effective index to represent the temperature cancelling effect when assessing refrigerants' VT heating effect.

Future work

- Using CFD simulations, lots of data can be generated and based on them it is possible to develop some kind of numerical correlations (perhaps, based on non-dimensional approach) to relate VT dimensions/geometries and operating conditions, refrigerant thermal-physical properties and TSE. This can potentially eliminate the need for running the time-consuming CFD simulations in future when evaluating new refrigerant choices for specific VT applications. To establish this kind of correlations could be a major future work.

- In our research, only vapour phase is exiting both hot and cold ends. In certain applications, however it would be beneficial to have liquid refrigerant to exit the cold end, in order to utilize the refrigerant's latent heat in the system. It is proposed future research looks into VT design to achieve liquid formation within the VT main body and existing the cold end. To achieve that, the secondary flow must be able to transfer more energy to the outer layers. For the future VT design, the focus should be on optimizing structure to improve the energy transfer in the secondary flow. The study of two-phase rotating flow would also be a big challenge.

- Based on the results from this research and observations from the published work, it is noted that both the primary flow towards the hot end and secondary flow towards the cold end often have the same rotational direction. It is suggested that further work could explore different hot end throttle design to see if it is possible to create counter-rotating flows, to achieve better TSE.

References

1. Eiamsa-ard, S. and P. Promvonge, Review of Ranque-Hilsch effects in vortex tubes. Renewable & Sustainable Energy Reviews, 2008. 12(7): p. 1822-1842.
2. Choi, H.Z., S.W. Lee, and H.D. Jeong, A comparison of the cooling effects of compressed cold air and coolant for cylindrical grinding with a CBN wheel. Journal of Materials Processing Technology, 2001. 111(1-3): p. 265-268.
3. Baz, A. and D. Uhler, A compressed gas-powered heating-system for underwater divers. Ocean Engineering, 1986. 13(3): p. 273-290.
4. Hilsch, R., The use of the expansion of gases in a centrifugal field as cooling process. Review of Scientific Instruments, 1947. 18(2): p. 108-113.
5. Michalski, L., K. Eckersdorf, J. Kucharski, and J. McGhee, Temperature measurement of fluids, in Temperature Measurement. 2001, John Wiley & Sons, Ltd. p. 361-380.
6. Pinar, A.M., O. Uluer, and V. Kirmaci, Optimization of counter flow Ranque-Hilsch vortex tube performance using Taguchi method. International Journal of Refrigeration, 2009. 32(6): p. 1487-1494.
7. Behera, U., P.J. Paul, K. Dinesh, and S. Jacob, Numerical investigations on flow behaviour and energy separation in Ranque-Hilsch vortex tube. International Journal of Heat and Mass Transfer, 2008. 51(25-26): p. 6077-6089.
8. Kassner, R. and E. Knoernschild, Friction laws and energy transfer in circular flow. Part 1-the law of shear stresses in circular flow. Part 2-energy transfer in circular flow and possible applications (explanation of the Hilsch or Ranque effect). 1948, DTIC Document.
9. Chang, T.H. and H.Y. Kim, An investigation of swirling flow in a cylindrical tube. Ksme International Journal, 2001. 15(12): p. 1892-1899.
10. Yilmaz, M., Ö. Çomakli, and S. Yapici, Enhancement of heat transfer by turbulent decaying swirl flow. Energy Conversion and Management, 1999. 40(13): p. 1365-1376.
11. Saraç, B.A. and T. Bali, An experimental study on heat transfer and pressure drop characteristics of decaying swirl flow through a circular pipe with a vortex generator. Experimental Thermal and Fluid Science, 2007. 32(1): p. 158-165.
12. Gulyaev, A.I., Ranque effect at low temperatures. Journal of engineering physics, 1965. 9(3): p. 242-244.
13. Ding, Y., Research of application of vortex tube in light hydrocarbon recovery technology. Master Thesis, 2006. Beijing University of Technology, Beijing, China.
14. Shannak, B.A., Temperature separation and friction losses in vortex tube. Heat and Mass Transfer, 2004. 40(10): p. 779-785.
15. Amitani, T., T. Adachi, and T. Kato, Thermal separation in a large vortex tube. Transactions of the Japan Society of Mechanical Engineers Series B, 1983. 49(440): p. 877-884.
16. Gao, C., Experimental study on the Ranque-Hilsch vortex tube. PhD Thesis, 2005. Eindhoven University of Technology, Eindhoven, Netherlands.
17. Hamdan, M.O., B. Alsayyed, and E. Elnajjar, Nozzle parameters affecting vortex tube energy separation performance. Heat and Mass Transfer, 2013. 49(4): p. 533-541.
18. Dincer, K., S. Baskaya, and B.Z. Uysal, Experimental investigation of the effects of length to diameter ratio and nozzle number on the performance of counter flow Ranque-Hilsch vortex tubes. Heat and Mass Transfer, 2008. 44(3): p. 367-373.
19. Aydin, O. and M. Baki, An experimental study on the design parameters of a counterflow vortex tube. Energy, 2006. 31(14): p. 2763-2772.
20. Martynovskii, V. and V. Alekseev, Investigation of the vortex thermal separation effect for gases and vapors. Soviet Physics-Technical Physics, 1956. 1(10): p. 2233-2243.

21. Han, X., N. Li, K. Wu, Z. Wang, L. Tang, G. Chen, and X. Xu, The influence of working gas characteristics on energy separation of vortex tube. Applied Thermal Engineering, 2013. 61(2): p. 171-177.
22. Akhesmeh, S., N. Pourmahmoud, and H. Sedgi, Numerical study of the temperature separation in the Ranque-Hilsch vortex tube. American Journal of Engineering and Applied Sciences, 2008. 1(3).
23. Tlili El May, O., I. Mokni, H. Mhiri, and P. Bournot, CFD investigation of a vortex tube: effect of the cold end orifice in the temperature separation mechanism. Science Academy Transactions on Renewable Energy Systems Engineering and Technology, 2011. 1(3).
24. Lorey, M., J. Steinle, and K. Thomas. Industrial application of vortex tube separation technology utilizing the Ranque-Hilsch effect. in European Petroleum Conference. 1998. The Hague, Netherlands: Society of Petroleum Engineers.
25. Xue, Y., M. Jafarian, A. Choudhry, and M. Arjomandi, The expansion process in a counter flow vortex tube. Journal of Vortex Science and Technology, 2015. 2(1).
26. Nellis, G.F. and S.A. Klein, The application of vortex tubes to refrigeration cycles, in International Refrigeration and Air Conditioning Conference. 2002: Purdue Univeristy, USA. p. 537.
27. Prabakaran, J. and S. Vaidyanathan, Effect of orifice and pressure of counter flow vortex tube. Indian Journal of Science and Technology, 2010. 3(4): p. 374-376.
28. Cao, Y., Theoretical and experimental study on the performance of a small flow vortex tube. Ph.D. Thesis, 2003. Zhejiang University, Hangzhou, China.
29. Saidi, M.H. and M.S. Valipour, Experimental modeling of vortex tube refrigerator. Applied Thermal Engineering, 2003. 23(15): p. 1971-1980.
30. Wang, Z., K. Wu, G. Chen, and X. Han, The experimental study on different ratios of vortex tube hot end pressure and cold end pressure. Journal of Engineering Thermophysics, 2013. 34(8): p. 1407-1410.
31. Takahama, H. and H. Yokosawa, Energy separation in vortex tubes with a divergent chamber. Journal of Heat Transfer, 1981. 103(2): p. 196-203.
32. Xue, Y.P. and M. Arjomandi, The effect of vortex angle on the efficiency of the Ranque-Hilsch vortex tube. Experimental Thermal and Fluid Science, 2008. 33(1): p. 54-57.
33. Markal, B., O. Aydin, and M. Avci, An experimental study on the effect of the valve angle of counter-flow Ranque-Hilsch vortex tubes on thermal energy separation. Experimental Thermal and Fluid Science, 2010. 34(7): p. 966-971.
34. Chang, K., Q. Li, G. Zhou, and Q.A. Li, Experimental investigation of vortex tube refrigerator with a divergent hot tube. International Journal of Refrigeration, 2011. 34(1): p. 322-327.
35. Im, S.Y. and S.S. Yu, Effects of geometric parameters on the separated air flow temperature of a vortex tube for design optimization. Energy, 2012. 37(1): p. 154-160.
36. Devade, K. and A. Pise, Effect of cold orifice diameter and geometry of hot end valves on performance of converging type Ranque Hilsch vortex tube. 4 International Conference on Advances in Energy Research (Icaer 2013), 2014. 54: p. 642-653.
37. Cebeci, I., V. Kirmaci, and U. Topcuoglu, The effects of orifice nozzle number and nozzle made of polyamide plastic and aluminum with different inlet pressures on heating and cooling performance of counter flow Ranque-Hilsch vortex tubes: An experimental investigation. International Journal of Refrigeration, 2016. 72: p. 140-146.
38. Kirmaci, V., O. Uluer, and K. Dincer, An experimental investigation of performance and exergy analysis of a counterflow vortex tube having various nozzle numbers at different inlet pressures of air, oxygen, nitrogen, and argon. Journal of Heat Transfer, 2010. 132(12).
39. Collins, R. and R. Lovelace, Experimental study of two-phase propane expanded through the Ranque-Hilsch tube. Journal of Heat Transfer, 1979. 101(2): p. 300-305.
40. Kirmaci, V. and O. Uluer, An experimental investigation of the cold mass fraction,

nozzle number, and inlet pressure effects on performance of counter flow vortex tube. Journal of Heat Transfer-Transactions of the Asme, 2009. 131(8): p. 081701.
41. Eiamsa-ard, S., Experimental investigation of energy separation in a counter-flow Ranque-Hilsch vortex tube with multiple inlet snail entries. International Communications in Heat and Mass Transfer, 2010. 37(6): p. 637-643.
42. Ahlborn, B., J. Camire, and J.U. Keller, Low-pressure vortex tubes. Journal of Physics D-Applied Physics, 1996. 29(6): p. 1469-1472.
43. Ahlborn, B., J.U. Keller, R. Staudt, G. Treitz, and E. Rebhan, Limits of temperature separation in a vortex tube. Journal of Physics D-Applied Physics, 1994. 27(3): p. 480-488.
44. Rattanongphisat, W. and K. Thungthong, Improvement vortex cooling capacity by reducing hot tube surface temperature: Experiment. Energy Procedia, 2014. 52: p. 1-9.
45. Stephan, K., S. Lin, M. Durst, F. Huang, and D. Seher, An investigation of energy separation in a vortex tube. International Journal of Heat and Mass Transfer, 1983. 26(3): p. 341-348.
46. Promvonge, P. and S. Eiamsa-ard, Investigation on the vortex thermal separation in a vortex tube refrigerator. ScienceAsia, 2005. 31(3): p. 215-23.
47. Rafiee, S.E. and M. Rahimi, Experimental study and three-dimensional (3D) computational fluid dynamics (CFD) analysis on the effect of the convergence ratio, pressure inlet and number of nozzle intake on vortex tube performance-Validation and CFD optimization. Energy, 2013. 63: p. 195-204.
48. Mohammadi, S. and F. Farhadi, Experimental analysis of a Ranque-Hilsch vortex tube for optimizing nozzle numbers and diameter. Applied Thermal Engineering, 2013. 61(2): p. 500-506.
49. Farzaneh-Gord, M. and M. Kargaran, Recovering energy at entry of natural gas into customer premises by employing a counter-flow vortex tube. Oil & Gas Science and Technology-Revue D Ifp Energies Nouvelles, 2010. 65(6): p. 903-912.
50. Takahama, H., H. Kawamura, S. Kato, and H. Yokosawa, Performance characteristics of energy separation in a steam-operated vortex tube. International Journal of Engineering Science, 1979. 17(6): p. 735-744.
51. Fulton, C., Ranques tube. Journal of the ASRE, 1950. 58: p. 473-478.
52. Fulton, C., Comments on the vortex tube. J ASRE Refrig Eng, 1951. 59: p. 984.
53. Gutsol, A. and J.A. Bakken, A new vortex method of plasma insulation and explanation of the Ranque effect. Journal of Physics D-Applied Physics, 1998. 31(6): p. 704-711.
54. Ahlborn, B.K. and J.M. Gordon, The vortex tube as a classic thermodynamic refrigeration cycle. Journal of Applied Physics, 2000. 88(6): p. 3645-3653.
55. Liew, R., J.C.H. Zeegers, J.G.M. Kuerten, and W.R. Michalek, Maxwell's demon in the Ranque-Hilsch vortex tube. Physical Review Letters, 2012. 109(5): p. 054503.
56. Deemter, J.J., On the theory of the Ranque-Hilsch cooling effect. Applied Scientific Research, Section A, 1952. 3(3): p. 174-196.
57. Polihronov, J.G. and A.G. Straatman, The vortex tube effect without walls. Canadian Journal of Physics, 2015: p. 1-5.
58. Liu, X.W. and Z.L. Liu, Investigation of the energy separation effect and flow mechanism inside a vortex tube. Applied Thermal Engineering, 2014. 67(1-2): p. 494-506.
59. Chu, J.Q., Acoustic streaming as a mechanism of the Ranque–Hilsch Effect. PhD Thesis, 1982. University of Tennessee, Knoxville, USA.
60. Reynolds, A.J., Studies of rotating fluids: I. Plane axisymmetric flow. II. The Ranque–Hilsch vortex. Ph.D. Thesis, 1961. University of London (Imperial College of Science and Technology).
61. Deissler, R.G. and M. Perlmutter, Analysis of the flow and energy separation in a turbulent vortex. International Journal of Heat and Mass Transfer, 1960. 1(2): p. 173-191.

62. Kurosaka, M., Acoustic Streaming in Swirling Flow and the Ranque-Hilsch (Vortex-Tube) Effect. Journal of Fluid Mechanics, 1982. 124(Nov): p. 139-172.
63. Polihronov, J.G. and A.G. Straatman, Thermodynamics of angular propulsion in fluids. Physical Review Letters, 2012. 109(5): p. 054504.
64. Xue, Y., M. Arjomandi, and R. Kelso, Visualization of the flow structure in a vortex tube. Experimental Thermal and Fluid Science, 2011. 35(8): p. 1514-1521.
65. Lewins, J. and A. Bejan, Vortex tube optimization theory. Energy, 1999. 24(11): p. 931-943.
66. Ghoshdastidar, P.S., Heat transfer (2nd Edition). 2012, Oxford University Press.
67. Bovand, M., M.S. Valipour, K. Dincer, and A. Tamayol, Numerical analysis of the curvature effects on Ranque–Hilsch vortex tube refrigerators. Applied Thermal Engineering, 2014. 65(1–2): p. 176-183.
68. Kazantseva, O.V., S.A. Piralishvili, and A.A. Fuzeeva, Numerical simulation of swirling flows in vortex tubes. High Temperature, 2005. 43(4): p. 608-613.
69. Dutta, T., K.P. Sinhamahapatra, and S.S. Bandyopadhyay, Numerical investigation of gas species and energy separation in the Ranque-Hilsch vortex tube using real gas model. International Journal of Refrigeration, 2011. 34(8): p. 2118-2128.
70. Thakare, H.R. and A.D. Parekh, Computational analysis of energy separation in counter-flow vortex tube. Energy, 2015. 85: p. 62-77.
71. Bej, N. and K.P. Sinhamahapatra, Exergy analysis of a hot cascade type Ranque-Hilsch vortex tube using turbulence model. International Journal of Refrigeration, 2014. 45: p. 13-24.
72. Bruun, H.H., Experimental investigation of the energy separation in vortex tubes. Journal of Mechanical Engineering Science, 1969. 11(6): p. 567-582.
73. Frohlingsdorf, W. and H. Unger, Numerical investigations of the compressible flow and the energy separation in the Ranque-Hilsch vortex tube. International Journal of Heat and Mass Transfer, 1999. 42(3): p. 415-422.
74. Karimi-Esfahani, M., A. Fartaj, and G. Rankin. Predicting optimum vortex tube performance using a simplified CFD model. in Twelfth annual conference of the CFD Society of Canada. 2004. Ottawa, Canada.
75. Keyes Jr, J. An experimental study of gas dynamics in high velocity vortex flow. in Proceedings of the 1960 Heat Transfer and Fluid Mechanics Institute. 1960. Stanford University Press.
76. Kandil, H.A. and S.T. Abdelghany, Computational investigation of different effects on the performance of the Ranque–Hilsch vortex tube. Energy, 2015. 84(0): p. 207-218.
77. Aljuwayhel, N.F., G.F. Nellis, and S.A. Klein, Parametric and internal study of the vortex tube using a CFD model. International Journal of Refrigeration, 2005. 28(3): p. 442-450.
78. Skye, H.M., G.F. Nellis, and S.A. Klein, Comparison of CFD analysis to empirical data in a commercial vortex tube. International Journal of Refrigeration, 2006. 29(1): p. 71-80.
79. Shamsoddini, R. and A.H. Nezhad, Numerical analysis of the effects of nozzles number on the flow and power of cooling of a vortex tube. International Journal of Refrigeration, 2010. 33(4): p. 774-782.
80. Farouk, T. and B. Farouk, Large eddy simulations of the flow field and temperature separation in the Ranque-Hilsch vortex tube. International Journal of Heat and Mass Transfer, 2007. 50(23-24): p. 4724-4735.
81. Behera, U., P.J. Paul, S. Kasthurirengan, R. Karunanithi, S.N. Ram, K. Dinesh, and S. Jacob, CFD analysis and experimental investigations towards optimizing the parameters of Ranque-Hilsch vortex tube. International Journal of Heat and Mass Transfer, 2005. 48(10): p. 1961-1973.
82. Dutta, T., K.P. Sinhamahapatra, and S.S. Bandyopdhyay, Comparison of different turbulence models in predicting the temperature separation in a Ranque-Hilsch vortex tube. International Journal of Refrigeration, 2010. 33(4): p. 783-792.

83. Dincer, K., S. Baskaya, B.Z. Uysal, and I. Ucgul, Experimental investigation of the performance of a Ranque-Hilsch vortex tube with regard to a plug located at the hot outlet. International Journal of Refrigeration, 2009. 32(1): p. 87-94.
84. Baghdad, M., A. Ouadha, O. Imine, and Y. Addad, Numerical study of energy separation in a vortex tube with different RANS models. International Journal of Thermal Sciences, 2011. 50(12): p. 2377-2385.
85. Bruno, T.J., Laboratory applications of the vortex tube. Journal of Chemical Education, 1987. 64(11): p. 987-988.
86. Singh, M. and K.G. Narayankhedkar, Personal cooling belt. International Journal of Refrigeration, 1982. 5(5): p. 314-315.
87. Reddy, B.S.K. and K. Govindarajulu, Air cooling in automobiles using vortex tube refrigeration system. International Journal of Engineering Science & Technology, 2013. 5(2).
88. Arkharov, I.A., E.S. Navasardyan, and P.A. Luk'yanov, Equipment for biomaterial storage systems. Chemical and Petroleum Engineering, 2001. 37(7): p. 428-433.
89. Martin, R.W. and K.W. Zilm, Variable temperature system using vortex tube cooling and fiber optic temperature measurement for low temperature magic angle spinning NMR. Journal of Magnetic Resonance, 2004. 168(2): p. 202-209.
90. Zhongtao, H. and L. Guanwei, Automobile rinse method based on vortex tube making heating principle. Chinese Journal of Mechanical Engineering, 2005. 41(5): p. 157-160.
91. Baz, A., J. Gilheany, and A. Kalvaitis, Feasibility of vortex tube-assisted environmental control of a manned underwater research habitat. Ocean Engineering, 1988. 15(1): p. 33-54.
92. Arslan, S., B. Mitrovic, and M.R. Muller. Vortex tube applications in micro-power generation. in 2002 International Joint Power Generation Conference. 2002. Phoenix, USA: American Society of Mechanical Engineers.
93. Xiong, C., C. Chen, K. Yi, L. Feng, T. Wang, and X. Jian, Application of vortex tube heating technique in gas Industry. Oil & Gas Storage and Transportation, 2009. 28(6): p. 69-72.
94. Wang, Z., The research of the vortex tube performance and the coupling characteristics with the responding refrigeration system. Master Thesis, 2013. Zhejiang University, Hangzhou, China.
95. Zhang, X., S. Yao, and Z. Ma, Experimental study on the performance of a minitype vortex tube for electronic component cooling. Science Technology and Engineering, 2007. 7(10): p. 2340-2342,2353.
96. Wang, Z., T. Li, K. Wu, G. Chen, and X. Han, The new refrigeration system with vortex tube and ejector. Journal of Engineering Thermophysics, 2012. 33(11): p. 1843-1848.
97. Dubey, A.M., G. Das Agrawal, and S. Kumar, Performance evaluation and optimal configuration analysis of a transcritical carbon dioxide/propylene cascade system with vortex tube expander in high-temperature cycle. Clean Technologies and Environmental Policy, 2016. 18(1): p. 105-122.
98. Chen, G., K. Wu, Q. Wang, Z. Wang, and T. Li, An auto-cascade System with Vortex Tube. Patent 201110159357.0, China, 2013.
99. Sarkar, J., Cycle parameter optimization of vortex tube expansion transcritical CO2 system. International Journal of Thermal Sciences, 2009. 48(9): p. 1823-1828.
100. Maurer, T., Entspannungseinrichtung. Patent DE 197 48 083 A1, 1999.
101. Farouk, T., B. Farouk, and A. Gutsol, Simulation of gas species and temperature separation in the counter-flow Ranque-Hilsch vortex tube using the large eddy simulation technique. International Journal of Heat and Mass Transfer, 2009. 52(13-14): p. 3320-3333.
102. Ameri, M. and B. Behnia, The study of key design parameters effects on the vortex tube performance. Journal of Thermal Science, 2009. 18(4): p. 370-376.
103. Thakare, H.R. and A.D. Parekh, Computational analysis of energy separation in

counter—flow vortex tube. Energy, 2015. 85: p. 62-77.
104. Thakare, H.R. and A.D. Parekh, Experimental investigation & CFD analysis of Ranque–Hilsch vortex tube. Energy, 2017. 133: p. 284-298.
105. Shamsoddini, R. and A.F. Khorasani, A new approach to study and optimize cooling performance of a Ranque-Hilsch vortex tube. International Journal of Refrigeration, 2012. 35(8): p. 2339-2348.
106. Gulyaev, A.I., Investigation of conical vortex tubes. Journal of Engineering Physics, 1966. 10(3): p. 193-195.
107. Pinar, A.M., O. Uluer, and V. Kirmaci, Statistical assessment of counter-flow vortex tube performance for different nozzle numbers, cold mass fractions, and inlet pressures Via Taguchi method. Experimental Heat Transfer, 2009. 22(4): p. 271-282.
108. Avci, M., The effects of nozzle aspect ratio and nozzle number on the performance of the Ranque-Hilsch vortex tube. Applied Thermal Engineering, 2013. 50(1): p. 302-308.
109. Hirsch, C., Numerical computation of internal & external flows: fundamentals of numerical discretization, ed. H. Charles. 1988: John Wiley & Sons, Inc.
110. Eiamsa-ard, S. and P. Promvonge, Numerical investigation of the thermal separation in a Ranque-Hilsch vortex tube. International Journal of Heat and Mass Transfer, 2007. 50(5-6): p. 821-832.
111. Rafiee, S.E. and M. Sadeghiazad, Three-dimensional and experimental investigation on the effect of cone length of throttle valve on thermal performance of a vortex tube using k-ε turbulence model. Applied Thermal Engineering, 2014. 66(1): p. 65-74.
112. Eiamsa-ard, S. and P. Pongjet, Numerical prediction of vortex flow and thermal separation in a subsonic vortex tube. Journal of Zhejiang University Science A, 2006. 7(8): p. 1406-1415.
113. ANSYS, I. ANSYS Fluent Theory Guide, Release 15.0. 2013.
114. Khazaei, H., A.R. Teymourtash, and M. Malek-Jafarian, Effects of gas properties and geometrical parameters on performance of a vortex tube. Scientia Iranica, 2012. 19(3): p. 454-462.
115. Li, N., Internal report: experimental research of R134a in vortex tube, 2015. Institute of Refrigeration and Cryogenics, Zhejiang University, China, unpublished.
116. Keller, J. and M. Göbel, Die thermodrossel: eine anlage zur entspannung komprimierter flüssigkeiten unter wärmeabgabe. KI. Luft-und Kältetechnik, 1997. 33(2): p. 57-60.
117. Lemmon, E.W., M.L. Huber, and M.O. McLinden;, NIST Standard Reference Database 23: Reference Fluid Thermodynamic and Transport Properties-REFPROP, Version 8.0. 2007, National Institute of Standards and Technology, Standard Reference Data Program: Gaithersburg.
118. Ascher H, S., The dynamics and thermodynamics of compressible fluid flow. 1953, New York: Ronald Press.
119. Li, N., Z.Y. Zeng, Z. Wang, X.H. Han, and G.M. Chen, Experimental study of the energy separation in a vortex tube. International Journal of Refrigeration, 2015. 55: p. 93-101.
120. Ahlborn, B. and S. Groves, Secondary flow in a vortex tube. Fluid Dynamics Research, 1997. 21(2): p. 73-86.
121. Ahlborn, B.K., J.U. Keller, and E. Rebhan, The heat pump in a vortex tube. Journal of Non-Equilibrium Thermodynamics, 1998. 23(2): p. 159-165.
122. Xue, Y.P., M. Arjomandi, and R. Kelso, A critical review of temperature separation in a vortex tube. Experimental Thermal and Fluid Science, 2010. 34(8): p. 1367-1374.
123. Xue, Y.P., M. Arjomandi, and R. Kelso, The working principle of a vortex tube. International Journal of Refrigeration, 2013. 36(6): p. 1730-1740.
124. Klein, S.A. EES – Engineering Equation Solver, V10. 2017, F-Chart Software, http://fchart.com.
125. Manimaran, R., Computational analysis of flow features and energy separation in a counter-flow vortex tube based on number of inlets. Energy, 2017. 123: p. 564-578.

126. Schaschke, C., Dictionary of Chemical Engineering. 2014, Oxford University Press.
127. Barin, I., Thermodynamic functions and relations, in Thermochemical Data of Pure Substances. 2008, Wiley-VCH Verlag GmbH. p. 1-20.
128. American Society of Heating, R. and I. Air-Conditioning Engineers, 2014 ASHRAE Handbook - Refrigeration (SI Edition). 2014 American Society of Heating, Refrigerating and Air-Conditioning Engineers, Inc.
129. Maric, I., A. Galovic, and T. Smuc, Calculation of natural gas isentropic exponent. Flow Measurement and Instrumentation, 2005. 16(1): p. 13-20.
130. Han, K.H., S.P. Noh, I.K. Hong, and K.A. Park, Cooling domain prediction of HFCs and HCFCs refrigerant with Joule-Thomson coefficient. Journal of Industrial and Engineering Chemistry, 2012. 18(2): p. 617-622.
131. Abbas, R., C. Ihmels, S. Enders, and J. Gmehling, Joule-Thomson coefficients and Joule-Thomson inversion curves for pure compounds and binary systems predicted with the group contribution equation of state VTPR. Fluid Phase Equilibria, 2011. 306(2): p. 181-189.

8 Appendix

8.1 Gas dynamics calculations in VT nozzle analysis

Typically, convergent nozzles are used in VTs, in which the velocity of the fluid increases with an associated drop in their temperature. Classic gas dynamics theories have been established to calculate the fluid states inside the nozzle. For a given refrigerant, the temperature drop is a function of nozzle geometry and fluid initial velocity, temperature and pressure.

For a convergent nozzle and assuming a Mach number of 1 is achieved, the status of the fluid at the outlet can be got according to the gas dynamics theory[118]. The fluid is assumed as the ideal gas in all the calculation below.

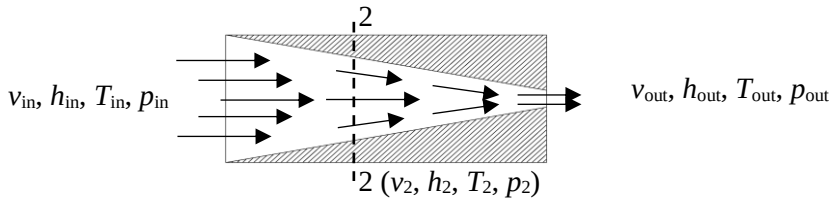

Figure 8.1 One-dimensional ideal gas isentropic flow process in a convergent nozzle

For the one-dimensional ideal gas isentropic flow process in a stream tube (as shown in Figure 8.1), according to the first law of thermodynamics, the enthalpy and velocity in different places can be got:

$$h_{in} + \frac{v_{in}^2}{2} = h_2 + \frac{v_2^2}{2} \tag{8.1}$$

When the velocity of the fluid in the tube is zero, the kinetic energy is transferred to internal energy, and this state is the stagnation point. The stagnation state is always used as a reference state in the analysis of the flow in a stream tube. According to equation (8.1), the stagnation enthalpy of the fluid is

$$h_{stag} = h_{in} + \frac{v_{in}^2}{2} \tag{8.2}$$

Correspondingly, the stagnation temperature and pressure of the fluid are

$$T_{stag} = T_{in} + \frac{v_{in}^2}{2c_p} \tag{8.3}$$

For the perfect gas,

$$\Delta h = c_{\mathrm{p}} \Delta T \tag{8.4}$$

$$c_p = \frac{\gamma}{\gamma - 1} R_{\mathrm{g}} \tag{8.5}$$

According to equation (8.3-8.5), the velocity of the fluid at any constant cross sectional area in the stream tube can be got:

$$v = \sqrt{2c_p(T_{\mathrm{stag}} - T)} = \sqrt{\frac{2\gamma}{\gamma - 1} R_{\mathrm{g}}(T_{\mathrm{stag}} - T)} \tag{8.6}$$

The speed of sound at the stagnation temperature is

$$c_{\mathrm{stag}} = \sqrt{\gamma R_{\mathrm{g}} T_{\mathrm{stag}}} \tag{8.7}$$

At the outlet of the nozzle, a Mach number of 1 is regarded the optimal value for the VT to operate work efficiently With $v^* = c^*$, according to equation (8.6-8.7), the temperature and of the fluid at the outlet when Mach number is 1 is follow:

$$T^* = \frac{2}{\gamma + 1}\left(T_{\mathrm{in}} + \frac{v_{\mathrm{in}}^2}{2c_p}\right) \tag{8.9}$$

8.2 *Standard k-ε* model turbulence model

The *standard k-ε* model[113] is wildly accepted engineering turbulence model, the turbulence kinetic energy *k* and the rate of dissipation *ε*, can be got from the following transport equations:

$$\frac{\partial(\rho k)}{\partial t} + \frac{\partial(\rho k u_{\mathrm{i}})}{\partial x_{\mathrm{i}}} = \frac{\partial}{\partial x_{\mathrm{j}}}\left[\left(\mu + \frac{\mu_t}{\sigma_k}\right)\frac{\partial k}{\partial x_{\mathrm{j}}}\right] + G_k + G_b - \rho\varepsilon - Y_M + S_k \tag{8.10}$$

$$\frac{\partial(\rho \varepsilon)}{\partial t} + \frac{\partial(\rho \varepsilon u_{\mathrm{i}})}{\partial x_{\mathrm{i}}} = \frac{\partial}{\partial x_{\mathrm{j}}}\left[\left(\mu + \frac{\mu_t}{\sigma_e}\right)\frac{\partial \varepsilon}{\partial x_{\mathrm{j}}}\right] + C_{1\varepsilon}\frac{\varepsilon}{k}(G_k + C_{3\varepsilon}G_b) - C_{2\varepsilon}\rho\frac{\varepsilon^2}{k} + S_\varepsilon \tag{8.11}$$

In it, G_k is the generation of turbulence kinetic energy from the mean velocity gradients; G_b is the generation of turbulence kinetic energy from buoyancy; Y_M is the contribution of the fluctuating dilatation in compressible turbulence to the overall dissipation rate; $C_{1\varepsilon}$, $C_{2\varepsilon}$, $C_{3\varepsilon}$ are constants; σ_k and σ_ε are the turbulent Prandtl numbers for *k* and *ε*; S_k

and S_ε are user-defined source terms.

μ_t is the turbulent viscosity, which can be calculated by k and ε as follows:

$$\mu_t = \rho C_\mu \frac{k^2}{\varepsilon} \tag{8.12}$$

$C_\mu = 0.09$, $C_{1\varepsilon} = 1.44$, $C_{2\varepsilon} = 1.92$, $\sigma_k = 1.0$, $\sigma_\varepsilon = 1.3$

8.3 States of refrigerant at the nozzle outlet for different inlet conditions

Table 8.1 States of R290 at the nozzle outlet for different inlet conditions (V-Vapour, L-Liquid) for different inlet conditions, $v_{in} = 10$m/s

T_{sat} °C	p_{sat} MPa	ΔT_{sh} °C												
		3.6	3.7	3.8	3.9	4.1	4.5	4.9	5.5	6.2	7	7.9	8.8	9.9
95	4.12	--	--	--	--	--	--	--	--	--	--	--	L	V
90	3.76	--	--	--	--	--	--	--	--	--	--	L	V	--
85	3.44	--	--	--	--	--	--	--	--	--	L	V	--	--
80	3.13	--	--	--	--	--	--	--	--	L	V	--	--	--
75	2.85	--	--	--	--	--	--	--	L	V	--	--	--	--
70	2.59	--	--	--	--	--	--	L	V	--	--	--	--	--
65	2.34	--	--	--	--	--	L	V	--	--	--	--	--	--
60	2.12	--	--	--	--	L	V	--	--	--	--	--	--	--
55	1.91	--	--	--	L	V	--	--	--	--	--	--	--	--
50	1.71	--	L	--	V	--	--	--	--	--	--	--	--	--
45	1.53	L	V	--	--	--	--	--	--	--	--	--	--	--
40	1.37	V	--	--	--	--	--	--	--	--	--	--	--	--
35	1.22	V	--	--	--	--	--	--	--	--	--	--	--	--
30	1.08	V	--	--	--	--	--	--	--	--	--	--	--	--
25	0.95	L	V	--	--	--	--	--	--	--	--	--	--	--
20	0.84	--	L	V	--	--	--	--	--	--	--	--	--	--

Table 8.2 States of R143a at the nozzle outlet for different inlet conditions (V-Vapour, L-Liquid) for different inlet conditions, v_{in} = 10 m/s

T_{sat} °C	p_{sat} MPa	ΔT_{sh} °C										
		5.4	5.6	6.0	6.4	6.9	7.5	8.2	9.0	10.0	11.0	12.1
70	3.55	--	--	--	--	--	--	--	--	--	L	V
65	3.20	--	--	--	--	--	--	--	--	L	V	--
60	2.87	--	--	--	--	--	--	--	L	V	--	--
55	2.58	--	--	--	--	--	--	L	V	--	--	--
50	2.31	--	--	--	--	--	L	V	--	--	--	--
45	2.06	--	--	--	--	L	V	--	--	--	--	--
40	1.83	--	--	--	L	V	--	--	--	--	--	--
35	1.62	--	--	L	V	--	--	--	--	--	--	--
30	1.43	--	L	V	--	--	--	--	--	--	--	--
25	1.26	L	V	--	--	--	--	--	--	--	--	--
20	1.11	V	--	--	--	--	--	--	--	--	--	--

Table 8.3 States of R152a at the nozzle outlet for different inlet conditions (V-Vapour, L-Liquid) for different inlet conditions, v_{in} = 10 m/s

T_{sat} °C	p_{sat} MPa	ΔT_{sh} °C															
		7.8	7.9	8.0	8.2	8.4	8.7	9.1	9.5	10.0	10.7	11.4	12.2	13.0	14.0	15.0	16.1
110	4.24	--	--	--	--	--	--	--	--	--	--	--	--	--	--	L	V
105	3.86	--	--	--	--	--	--	--	--	--	--	--	--	--	L	V	--
100	3.51	--	--	--	--	--	--	--	--	--	--	--	--	L	V	--	--
95	3.18	--	--	--	--	--	--	--	--	--	--	--	L	V	--	--	--
90	2.88	--	--	--	--	--	--	--	--	--	--	L	V	--	--	--	--
85	2.60	--	--	--	--	--	--	--	--	--	L	V	--	--	--	--	--
80	2.34	--	--	--	--	--	--	--	--	L	V	--	--	--	--	--	--
75	2.11	--	--	--	--	--	--	--	L	V	--	--	--	--	--	--	--
70	1.89	--	--	--	--	--	--	L	V	--	--	--	--	--	--	--	--
65	1.69	--	--	--	--	--	L	V	--	--	--	--	--	--	--	--	--
60	1.50	--	--	--	--	L	V	--	--	--	--	--	--	--	--	--	--
55	1.33	--	--	--	L	V	--	--	--	--	--	--	--	--	--	--	--
50	1.18	--	--	L	V	--	--	--	--	--	--	--	--	--	--	--	--
45	1.04	--	L	V	--	--	--	--	--	--	--	--	--	--	--	--	--
40	0.91	L	V	--	--	--	--	--	--	--	--	--	--	--	--	--	--
35	0.79	V	--	--	--	--	--	--	--	--	--	--	--	--	--	--	--
30	0.69	V	--	--	--	--	--	--	--	--	--	--	--	--	--	--	--
25	0.60	V	--	--	--	--	--	--	--	--	--	--	--	--	--	--	--
20	0.51	V	--	--	--	--	--	--	--	--	--	--	--	--	--	--	--

Table 8.4 States of R32 at the nozzle outlet for different inlet conditions (V-Vapour, L-Liquid) for different inlet conditions, v_{in} = 10 m/s

T_{sat} °C	p_{sat} MPa	ΔT_{sh} °C										
		25.7	26.6	27.4	28.4	29.4	30.5	31.7	32.9	34.2	35.5	36.9	38.4
75	5.42	--	--	--	--	--	--	--	--	--	--	L	V
70	4.88	--	--	--	--	--	--	--	--	--	L	V	--
65	4.38	--	--	--	--	--	--	--	--	L	V	--	--
60	3.93	--	--	--	--	--	--	--	L	V	--	--	--
55	3.52	--	--	--	--	--	--	L	V	--	--	--	--
50	3.14	--	--	--	--	--	L	V	--	--	--	--	--
45	2.79	--	--	--	--	L	V	--	--	--	--	--	--
40	2.48	--	--	--	L	V	--	--	--	--	--	--	--
35	2.19	--	--	L	V	--	--	--	--	--	--	--	--
30	1.93	--	L	V	--	--	--	--	--	--	--	--	--
25	1.69	L	V	--	--	--	--	--	--	--	--	--	--
20	1.47	V	--	--	--	--	--	--	--	--	--	--	--

Table 8.5 States of R125 at the nozzle outlet for different inlet conditions (V-Vapour, L-Liquid) for different inlet conditions, v_{in} = 10 m/s

T_{sat} °C	p_{sat} MPa	ΔT_{sh} °C									
		1.5	1.7	2.0	2.4	2.9	3.6	4.4	5.3	6.3	7.4
65	3.54	--	--	--	--	--	--	--	--	L	V
60	3.17	--	--	--	--	--	--	--	L	V	--
55	2.84	--	--	--	--	--	--	L	V	--	--
50	2.54	--	--	--	--	--	L	V	--	--	--
45	2.26	--	--	--	--	L	V	--	--	--	--
40	2.01	--	--	--	L	V	--	--	--	--	--
35	1.78	--	--	L	V	--	--	--	--	--	--
30	1.57	--	L	V	--	--	--	--	--	--	--
25	1.38	L	V	--	--	--	--	--	--	--	--
20	1.21	V	--	--	--	--	--	--	--	--	--

Table 8.6 States of R41 at the nozzle outlet for different inlet conditions (V-Vapour, L-Liquid) for different inlet conditions, v_{in} = 10 m/s

T_{sat} °C	p_{sat} MPa	ΔT_{sh} °C				
		36.3	37.8	39.4	41.0	42.7
40	5.39	--	--	--	L	V
35	4.82	--	--	L	V	--
30	4.30	--	L	V	--	--
25	3.83	L	V	--	--	--
20	3.41	V	--	--	--	--

Table 8.7 States of R717 at the nozzle outlet for different inlet conditions (V-Vapour, L-Liquid) for different inlet conditions, v_{in} = 10 m/s

T_{sat} °C	p_{sat} MPa	ΔT_{sh} °C																						
		30.4	31.0	31.7	32.4	33.1	33.9	34.7	35.6	36.5	37.5	38.6	39.7	40.8	42.1	43.3	44.7	46.1	47.5	49.0	50.6	52.2	53.9	55.7
130	10.90	--	--	--	--	--	--	--	--	--	--	--	--	--	--	--	--	--	--	--	--	--	L	V
125	9.97	--	--	--	--	--	--	--	--	--	--	--	--	--	--	--	--	--	--	--	--	L	V	--
120	9.11	--	--	--	--	--	--	--	--	--	--	--	--	--	--	--	--	--	--	--	L	V	--	--
115	8.32	--	--	--	--	--	--	--	--	--	--	--	--	--	--	--	--	--	--	L	V	--	--	--
110	7.58	--	--	--	--	--	--	--	--	--	--	--	--	--	--	--	--	--	L	V	--	--	--	--
105	6.89	--	--	--	--	--	--	--	--	--	--	--	--	--	--	--	--	L	V	--	--	--	--	--
100	6.26	--	--	--	--	--	--	--	--	--	--	--	--	--	--	--	L	V	--	--	--	--	--	--
95	5.66	--	--	--	--	--	--	--	--	--	--	--	--	--	--	L	V	--	--	--	--	--	--	--
90	5.12	--	--	--	--	--	--	--	--	--	--	--	--	--	L	V	--	--	--	--	--	--	--	--
85	4.61	--	--	--	--	--	--	--	--	--	--	--	--	L	V	--	--	--	--	--	--	--	--	--
80	4.14	--	--	--	--	--	--	--	--	--	--	--	L	V	--	--	--	--	--	--	--	--	--	--
75	3.71	--	--	--	--	--	--	--	--	--	--	L	V	--	--	--	--	--	--	--	--	--	--	--
70	3.31	--	--	--	--	--	--	--	--	--	L	V	--	--	--	--	--	--	--	--	--	--	--	--
65	2.95	--	--	--	--	--	--	--	--	L	V	--	--	--	--	--	--	--	--	--	--	--	--	--
60	2.62	--	--	--	--	--	--	--	L	V	--	--	--	--	--	--	--	--	--	--	--	--	--	--
55	2.31	--	--	--	--	--	--	L	V	--	--	--	--	--	--	--	--	--	--	--	--	--	--	--
50	2.03	--	--	--	--	--	L	V	--	--	--	--	--	--	--	--	--	--	--	--	--	--	--	--
45	1.79	--	--	--	--	L	V	--	--	--	--	--	--	--	--	--	--	--	--	--	--	--	--	--
40	1.56	--	--	--	L	V	--	--	--	--	--	--	--	--	--	--	--	--	--	--	--	--	--	--
35	1.36	--	--	L	V	--	--	--	--	--	--	--	--	--	--	--	--	--	--	--	--	--	--	--
30	1.17	--	L	V	--	--	--	--	--	--	--	--	--	--	--	--	--	--	--	--	--	--	--	--
25	1.00	L	V	--	--	--	--	--	--	--	--	--	--	--	--	--	--	--	--	--	--	--	--	--
20	0.86	V	--	--	--	--	--	--	--	--	--	--	--	--	--	--	--	--	--	--	--	--	--	--